

**Some pages of this thesis may have been removed for copyright restrictions.**

If you have discovered material in Aston Research Explorer which is unlawful e.g. breaches copyright, (either yours or that of a third party) or any other law, including but not limited to those relating to patent, trademark, confidentiality, data protection, obscenity, defamation, libel, then please read our [Takedown policy](#) and contact the service immediately (openaccess@aston.ac.uk)

# **Experimental Demonstration of Performance Enhancement in Non-Linearity Limited Optical Fibre Systems**

Mohammad Ahmad Zaki Al-Khateeb

*Doctor of Philosophy*

Aston University

January 2018

©Mohammad Ahmad Zaki Al-Khateeb, 2018

Mohammad asserts his moral right to be identified as the author of this thesis

This copy of the thesis has been supplied on condition that anyone who consults it is understood to recognise that its copyright rests with its author and that no quotation from the thesis and no information derived from it may be published without appropriate permission or acknowledgement.



Aston University

# **Experimental Demonstration of Performance Enhancement in Non-Linearity Limited Optical Fibre systems**

Mohammad Ahmad Zaki Al-Khateeb

Doctor of Philosophy

2018

## **Summary**

This thesis presents a study of the nonlinear limits of coherent, long-haul, optical fibre transmission systems and studies the capabilities of digital and all-optical nonlinearity compensation techniques to enhance their performance. By deriving the theoretical description of optical fibre nonlinear Kerr effects, this thesis presents theoretical, numerical, and experimental evidence showing that the compensation efficiency of deterministic nonlinear impairments in OPC assisted transmission system is highly dependent on the span length. This document shows that the deployment of multiple OPCs, in a system limited by deterministic signal-signal nonlinear interactions, can negate the performance enhancement achieved by a single OPC. I have derived, and verified by simulations, closed form equations that accurately represent the ultimate nonlinear threshold of the nondeterministic nonlinear signal-noise interaction limit in discretely amplified and quasi-lossless Raman optical fibre transmission systems. This nondeterministic nonlinear threshold can be unveiled when deploying ideal nonlinearity compensation techniques and can be minimised by deploying multiple OPCs.

In this thesis, I have experimentally shown that the performance enhancement achieved by mid-link OPC when deployed in discretely amplified transmission system is highly dependent on the bandwidth of the signals propagating along the system. The experimental results have shown that the OPC enhances the reach of discretely amplified transmission system by 43%, 32%, and 24% for 2x28Gbaud, 4x28Gbaud, and 8x28Gbaud of PM-QPSK signals, respectively. Also, I have experimentally demonstrated the highest reported reach enhancement of 72% (compared to EDC system) for 3.6Tbps (30x30Gbaud PM-QPSK, spectral efficiency of 3.6bps/Hz); when deploying a mid-link OPC in distributed Raman system.

Keywords: Coherent optical fibre communication systems, optical fibre nonlinearities, Kerr effects, nonlinearity mitigation techniques, Optical Phase Conjugation, Digital Backpropagation.





## Acknowledgements

I would like to thank my supervisor Prof. Andrew Ellis for the constant support, encouragement, and fruitful discussions during my research at Aston University. Also, I would like to extend my appreciation to the researchers, postdocs, and staff members at AIPT for the collaborations and support that inspired great contributions to the scientific community. Also, I would like to thank EPSRC (projects: UNLOC (EP/J017582/1) and PEACE (EP/L000091/1)) for providing the financial support towards my research.

Finally, I wish to thank my parents for the constant support during my studies.



# Contents

Summary.....	3
Acknowledgements .....	5
Abbreviations .....	9
List Symbols.....	11
List of Tables .....	13
List of Figures.....	13
Chapter 1 : Introduction.....	19
1.1 Thesis Organization .....	20
1.2 Collaboration Acknowledgments .....	23
1.3 Publication Summary.....	24
Chapter 2 : Background.....	29
2.1 Optical Fibre as a Transmission Medium .....	29
2.1.1 Optical Fibre Attenuation .....	29
2.1.2 Optical Fibre Dispersion.....	30
2.1.3 Optical Fibre Nonlinearities .....	31
2.2 Optical Amplifiers .....	34
2.2.1 Noise Accumulation in Discretely Amplified Systems.....	37
2.2.2 Noise Accumulation Distributed Raman Amplified Systems .....	39
2.3 Optical Fibre Communication Systems .....	41
2.3.1 Optical Transmitter.....	42
2.3.2 Coherent Optical Receivers .....	43
2.3.3 Optical Transmission Performance Merits .....	45
2.4 Optical Fibre Nonlinearity Compensation Techniques .....	46
2.4.1 Digital Backpropagation.....	47
2.4.2 Optical Phase Conjugation .....	49
Chapter 3 : Optical Nonlinear Kerr Effects in Optical Transmission Systems .....	53
3.1 Nonlinear Kerr Effects in Discretely Amplified Transmission Systems .....	55
3.2 Nonlinear Kerr Effects in Distributed Raman Transmission Systems .....	60
3.3 Nonlinear Kerr Effects in OPC-Assisted Discretely Amplified Transmission Systems.....	68
3.4 Nonlinear Kerr Effects in OPC-Assisted Distributed Raman Amplified Transmission Systems.....	76
Summary and Conclusions .....	82
Chapter 4 : Nonlinear Performance Limits of Optical Transmission Systems .....	84

4.1	Nonlinear Noise Generation Efficiency .....	85
4.2	Nonlinear Noise Due to Signal-Noise Interactions.....	94
4.3	Performance of Coherently Detected Optical Modulated Signals .....	102
4.4	Simulations, Verification, and Analysis .....	103
4.4.1	Discretely Amplified Systems .....	104
4.4.2	Distributed Raman Transmission Systems .....	112
	Summary and Conclusions .....	117
Chapter 5 : Nonlinear Optical Fibre Devices .....		119
5.1	Dual-Band Optical Phase Conjugator, Design and Characterisation .....	120
5.1.1	Counter Dithering and SBS Characterisation .....	122
5.1.2	Polarisation Dependency of the Optical Phase Conjugator.....	125
5.1.3	Performance of Conjugated Modulated Optical Signals .....	128
5.2	Comb Generator, Dispersion Optimisation Technique.....	137
	Summary and Conclusions .....	145
Chapter 6 : Experimental Demonstration of Performance Enhancement in OPC-Assisted Transmission Systems .....		147
6.1	OPC-Assisted Discretely Amplified Transmission System .....	148
6.2	OPC-Assisted Distributed Raman Transmission System .....	154
	Summary and Conclusion: .....	161
Chapter 7 : Conclusions.....		163
	Future Work.....	165
References: .....		167

## Abbreviations

Abbreviation	Phrase
ADC	Analog to Digital Converters
ASE	Amplified Spontaneous Emission
AWG	Arbitrary Wave generator
AWGN	Additive White Gaussian Noise
BER	Bit Error Rate
BPD	Balanced Photo-Detector
BPF	Band Pass Filter
CW	Continuous Wave
DBP	Digital Back Propagation
DCF	Dispersion Compensating fibre
DDG	Digital Delay Generators
DP-QAM	Dual-Polarisation Quadrature Amplitude Modulation
DSP	Digital Signal Processing
EDC	Electronically Dispersion Compensated
EDFA	Erbium Doped Fibre Amplifiers
EVM	Error Vector Magnitude
FBG	Fibre Bragg Grating
FEC	Forward Error Correction
FFT	Fast Fourier Transform
FOPA	fibre Optical Parametric Amplifiers
FWM	Four Wave Mixing
FWM	Four Wave Mixing
GFF	Gain Flattening Filter
HNLF	Highly Nonlinear Fibre
iFFT	inverse Fast Fourier Transform
MZM	Mach–Zehnder Modulator
NF	Noise Figure
NLSE	Nonlinear Schrodinger Equation

NZDSF	Non-Zero Dispersion Shifted Fibre
OBP	Optical Back Propagation
OFDM	Orthogonal Frequency Division Multiplexed
OPC	Optical Phase Conjugation
OSA	Optical Spectrum Analyzer
OSNR	Optical Signal to Noise Ratio
OTDR	Optical Time-Domain Reflectometer
PBC	Polarisation Beam Combiner
PBS	Polarisation Beam Splitters
PCP	Phase Conjugated Pilot
PCTW	Phase Conjugated Twin Wave
PM	Polarisation Maintaining
PMD	Polarisation Mode Dispersion
PPLN	Periodically Poled Lithium-Niobate
PSA	Phase Sensitive Amplifiers
RIN	Relative Intensity Noise
SBS	Stimulated Brillouin Scattering
SNR	Signal to Noise Ratio
SOA	Semiconductor Optical Amplifiers
SPM	Self-Phase Modulation
SRS	Stimulated Raman Scattering
SSMF	Standard Single Mode Fibre
VOA	Variable Optical Attenuator
WDM	Wavelength Division Multiplexed
WSS	Wavelength Selective Switch
XPM	Cross Phase Modulation
ZDW	Zero Dispersion Wavelengths

## List Symbols

<b>Symbol (unit)</b>	<b>Representation</b>
$P(W)$	Optical power
$\alpha(Np/m)$	Optical fibre attenuation coefficient
$E(V/m)$	Optical field
$\beta^k(s^k/m)$	Propagation constant of the $k^{th}$ order (as a function of radial frequency)
$D_c(ps/[nm.km])$	Chromatic dispersion
$S(ps/[nm^2.km])$	Dispersion slope
$\lambda(m)$	Wavelength
$\omega(rad/s)$	Radial frequency
$f(Hz)$	Frequency
$L(m)$	Optical fibre length
$D_p(s/m^{0.5})$	PMD factor
$\chi(m^2/W)$	Optical fibre third order susceptibility
$c(m/s)$	Speed of light
$\Delta\beta(rad/m)$	Phase mismatching
$D(unitless)$	Degeneracy factor
$g_B(1/[W.m])$	Brillouin gain coefficient
$g_r(1/[W.m])$	Raman gain coefficient
$P_{fw}(W)$	Forward Raman pumping power
$P_{bw}(W)$	Backward Raman pumping power
$P_o(W)$	Total Raman pumping power
$r_f(unitless)$	Forward Raman pumping power ratio
$I(W/Hz)$	Power spectral density
$B_w(Hz)$	Bandwidth
$n_{sp}(unitless)$	Spontaneous emission factor
$h(m^2.kg/s)$	Planck constant
$\nu(Hz)$	Optical frequency
$N(unitless)$	Number of spans
$T(Kelvin)$	Temperature
$k_B(m^2.kg.s^{-2}.K^{-1})$	Boltzmann constant
$R(bit/s)$	Total bit rate



$\eta_s(\text{bit/s/Hz})$	Spectral efficiency
$H(f)(\text{rad/m})$	Phase correction to compensate for dispersion
$BER(\text{unitless})$	Bit Error Rate
$EVM(\text{unitless})$	Error Vector Magnitude
$M(\text{unitless})$	Number of points in QAM modulation
$\gamma_0(1/[W.m])$	Intrinsic nonlinear coefficient of optical fibre
$A_{\text{eff}}(m^2)$	Effective area of the fibre core
$\delta(\text{unitless})$	Ratio of the residual dispersion in dispersion managed system
$N_{\text{seg}}(\text{unitless})$	Number of segments
$\eta(1/W^2)$	Nonlinear noise generation efficiency
$\kappa(\text{unitless})$	Residual nonlinear noise ratio (OPC assisted system to EDC system)
$N_{\text{OPC}}(\text{unitless})$	Number of OPCs

## List of Tables

Table 6.1: Experimental demonstrations of OPC assisted discretely amplified transmission systems. ....	154
Table 6.2: Experimental demonstrations of OPC assisted distributed Raman amplified transmission systems. ....	160

## List of Figures

Figure 1.1: Performance improvement ( $\Delta Q^2$ ) in reported OPC assisted system deployed in EDFA (discretely amplified) and distributed Raman amplified transmission systems. (a) the performance improvement as a function of maximum EDC distance, (b) the performance improvement as a function of the net bitrate-distance product. *Different experiments have used various Forward Error Correction (FEC) thresholds. ....	23
Figure 2.1: Optical fibre output power and SBS Back scattering as a function of the total input power to SSMF. CW linewidth=1Hz, L=15km, $\alpha=0.2\text{dB/km}$ , Effective core area= $80 \times 10^{-12}\text{m}^2$ , SBS gain coefficient ( $g_B$ )= $4.6 \times 10^{-11}\text{m/W}$ .....	34
Figure 2.2: Raman gain coefficient in SSMF, CW Raman pump located at 1455nm. The data set extracted from simulation results using VPITransmissionMaker 9.8.....	35
Figure 2.3: Schematic diagram of distributed Raman amplified fibre span.....	36
Figure 2.4: Signal power profile as a function of distance for 100km SSMF span. $\alpha=0.2\text{dB/km}$ , $g_r=0.37\text{W/km}$ , $P_0$ was calibrated to have 0dB net Raman gain. ....	37
Figure 2.5: Noise Figure as a function of EDFA's gain. ....	38
Figure 2.6: Total ASE power spectral density, as a function of amplifier spacing, for a 2000km transmission system that deploys EDFAs with fixed ideal spontaneous emission factor ( $n_{sp}=1$ ). ....	39
Figure 2.7: ASE power spectral density (accumulated along a 100km link) as a function of the forward pumping ratio for various span lengths (100km, 2x50km, 10x10km, and quasi-lossless Raman). $\alpha=0.2\text{dB/km}$ , $g_r(\text{peak})=0.37\text{W/m}$ , $n_{Rm}=1.14$ . ....	40
Figure 2.8: Optical fibre communication system. ....	41
Figure 2.9: Optical transmitter of N WDM channels. PBS: Polarisation Beam Splitter, MZM: Mach-Zehnder modulator, PS: Phase Shifter, PBC: Polarisation Beam Combiner, WDM: Wavelength Division Multiplexer. ....	43
Figure 2.10: Coherent optical receiver. BPD: Balanced Photo-Detector, ADC: Analog to Digital Converter. ....	43
Figure 2.11: DBP assisted optical fibre transmission system. ....	48
Figure 2.12: DBP using split-step Fourier method.....	49

Figure 2.13: The concept of OPC.....	50
Figure 3.1: (a) 100km span optical system transmitting two CW lasers (0dBm each, spectrally located at 1555nm) through Non-Zero-Dispersion Fibre (NZDSF) or Standard Single Mode Fibre (SSMF). (b) The nonlinear Kerr product power as a function of frequency separation between the mixing CWs. [X1] .....	55
Figure 3.2: Nonlinear Kerr field accumulation map for multi-span optical transmission system. [X1].....	57
Figure 3.3: (a) 5x100km optical system transmitting two CW lasers (0dBm each, spectrally located at 1555nm) through NZDSF and SSMF. (b) Nonlinear Kerr product power as a function of frequency separation between the mixing components. [X1].....	58
Figure 3.4: Nonlinear Kerr power as a function of the frequency separation between two CW lasers. (a) 100km system, (b) 2x100km system [X15].....	59
Figure 3.5: (a) Dispersion managed 5x100km optical system transmitting two CW lasers (0dBm each, spectrally located at 1555nm). (b) Nonlinear Kerr product power as a function of frequency separation between the mixing components, the different curves show various values of residual dispersion $\delta$ . (solid lines) theoretical predictions, (open circles) simulation results. [X1].....	60
Figure 3.6: Nonlinear Kerr product power as a function of frequency separation between two CW lasers (0dBm each, spectrally located at 1555nm) propagating through single span (a) and two spans (b), each span is 62km that deploy 1 <sup>st</sup> order bidirectional Raman pumping (100% $>r_f>0\%$ ). (Solid lines) theoretical predictions resulted from equation 3.9, (open circles) simulation results. The color code represents different forward Raman pumping ratio ( $r_f$ ). [X4] .....	62
Figure 3.7: RMS error of nonlinear Kerr power as a function of forward Raman pumping ratio ( $r_f$ ). The RMS was calculated in reference to the calculation of ( $M=31$ ) over 50GHz bandwidth for different number of sections $M=2, 4, 6, 8, 10$ , and 12.....	63
Figure 3.8: Two section approximation for distributed Raman power profile: (left) power profile in the case of dominating backward pump ( $r_f<0.25$ ), and (right) is the case of dominating forward pump ( $r_f>0.75$ ). [X18].....	64
Figure 3.9: (a) Nonlinear Kerr product power as a function of frequency separation, (b) signal power profile. (solid lines) 31-section approximation, (dashed lines) two-section approximation.....	66
Figure 3.10: Experimental setup of 2 <sup>nd</sup> order distributed Raman span, the table shows the pumping powers, forward pumping ratio ( $r_f$ ), and the power of input CW lasers. [X18].....	66
Figure 3.11: (a) Nonlinear Kerr product power as a function of frequency separation, (b) correspondent power profile along the distributed Raman span. (Solid lines) experimental measurement, (dashed lines) assumed power profile for the two-section approximation of profiles 1 to 4. [X18] .....	67

Figure 3.12: Nonlinear Kerr product power as a function of frequency separation between two CW lasers passing through 62km second order Raman pumped (at 1366nm) span with different $r_f$ values listed in figure 3.10. [X18].....	67
Figure 3.13: OPC deployment techniques. (top) single segment spaced OPCs, (bottom) double segment spaced OPCs.....	69
Figure 3.14: Nonlinear Kerr product power as a function of frequency separation between two CW lasers (0dBm each, spectrally located at 1555nm) propagating through 200km lumped transmission system (with different span length). (left column) fully dispersion compensated system with 0% residual dispersion, (right column) dispersion uncompensated system. (red) without OPC, (blue) with mid-link OPC. (solid lines) theory, (open circles) simulation results. [X4].....	73
Figure 3.15: Nonlinear Kerr product power as a function of frequency separation between two CW lasers (0dBm each, spectrally located at 1555nm) propagating through 24x100km lumped transmission system with different number of equally spaced and symmetrically located OPCs (1OPC, 3OPCs, 5OPCs, and 7OPCs). (red) without OPC, (blue) with OPCs. [X4].....	75
Figure 3.16: Nonlinear Kerr power as a function between two CW lasers (5dBm each, spectrally located at 1553nm) passing through 2x100km transmission system. (a) without OPC, (b) with OPC. [X4] [X15] .....	76
Figure 3.17: (left column) power profiles of distributed Raman with $r_f$ ranging from $r_f=0\%$ to 100% with a step of 20%. (right column) Nonlinear Kerr product power as a function of frequency separation between two CW lasers (0dBm each, spectrally located at 1555nm) propagating through 200km 1 <sup>st</sup> order distributed Raman transmission system (with different span lengths). (solid lines) without mid-link OPC, (dashed lines) with mid-link OPC, the colour code indicates the power profile shown in the left column of the figure. [X4].....	78
Figure 3.18: Verification of the curves in figure 3.17 using simulation results (with mid-link OPC). (solid lines) theoretical predictions, (open circles) simulation results. [X4].....	80
Figure 3.19: Nonlinear Kerr product power as a function of frequency separation between two CW lasers (0dBm each, spectrally located at 1555nm) propagating through 24x50km distributed Raman transmission system with different number of equally spaced and symmetrically located OPCs (1OPC, 3OPCs, 5OPCs, and 7OPCs). Colours represent different $r_f$ values, same colour code as figure 3.16. [X4] .....	81
Figure 3.20: Experimental setup to measure the nonlinear Kerr product power generated in 2x50km 1 <sup>st</sup> order distributed Raman amplified system (with $r_f=0\%$ ). Inset shows the theoretical and measured power profile of both 50km spans. [X4] .....	82
Figure 3.21: The nonlinear Kerr power as a function between two CW lasers passing through 2x50km backward pumped 1 <sup>st</sup> order distributed Raman transmission system without OPC (a) with mid-link OPC (b). [X4] .....	82
Figure 4.1: Nonlinear Kerr power ratio between discretely amplified system with mid-link OPC and a system without OPC. (N=30, fibre type: SSMF) [X12] .....	92

Figure 4.2: Residual nonlinear noise ratio (in dB) as a function the modulated signal bandwidth. ....	93
Figure 4.3: Kerr nonlinear noise accumulation in discretely amplified optical transmission system that deploys full field DBP. [X1] .....	96
Figure 4.4: Kerr nonlinear noise accumulation in discretely amplified optical transmission system that deploys a single OPC (a) and two OPCs (b). ....	99
Figure 4.5: $Q^2$ as a function of signal power for discretely amplified 2400km transmission system that deploys various uniform span lengths and number of OPCs. [X2].....	106
Figure 4.6: (a) The maximum $Q^2$ factor, as a function of span length, can be achieved by single channel (28Gbaud) propagating through 2400km discretely amplified EDC system. (b) The improvement in the maximum $Q^2$ factor can be achieved by 1-OPC, 2-OPCs, and 3-OPCs. [X2] .....	107
Figure 4.7: (a) Maximum $Q^2$ factor, as a function of span length and bandwidth, can be achieved by the end of 2400km discretely amplified system without OPC. (b) Improvement in the maximum $Q^2$ factor can be achieved by 1-OPC. [X2] .....	108
Figure 4.8: (a) $Q^2$ as a function of signal power in 24x100km discretely amplified system. (b) maximum $Q^2$ achieved by EDC system as a function of signal bandwidth, (c) the improvement in $Q^2$ of mid-link OPC system as a function of signal bandwidth. [X2].....	110
Figure 4.9: $Q^2$ as a function of the total launched optical signal power into a 12x100km discretely amplified system (EDFA noise figure of 6dB, $B_w=224\text{GHz}$ ) with different dispersion maps: SSMF, NZDSF, SSMF+DCP with 5% residual dispersion. [X1,X5] .....	111
Figure 4.10: $Q^2$ as a function of distance (at optimum power identified by figure 4.9) of a discretely amplified system with $L=100\text{km}$ with different dispersion maps: SSMF, NZDSF, SSMF+DCP with 5% residual dispersion. [X1,X5].....	112
Figure 4.11: Normalised signal power as a function of span length, where the span is pumped with backward Raman pump achieving 0dB net gain. ....	113
Figure 4.12: $Q^2$ as a function of signal power for distributed Raman amplified 2400km transmission system that deploys various span length and number of OPCs. [X2].....	114
Figure 4.13: (a) The maximum $Q^2$ factor, as a function of span length, can be achieved by 2400km distributed Raman amplified EDC system. (b) The improvement in the maximum $Q^2$ factor can be achieved by 1-OPC, 2-OPCs, and 3-OPCs. [X2] .....	115
Figure 4.14: (a) Maximum $Q^2$ factor, as a function of span length and bandwidth, can be achieved by the end of 2400km distributed Raman amplified system without OPC. (b) Improvement in the maximum $Q^2$ factor can be achieved by 1-OPC. [X2].....	116
Figure 4.15: $Q^2$ as a function of signal power for distributed Raman amplified 1200km transmission system that deploys various span length and number of OPCs. NLC: Nonlinearity Compensation (DBP or OPC). [X7].....	117

Figure 5.1: Experimental setup of dual band, polarisation insensitive, dual pump OPC.....	120
Figure 5.2: Frequency response of dithered OPC pumps. The x-axis represents the frequency relative to the CW laser frequency. ....	123
Figure 5.3: (a) SBS measurement setup, (b) SBS power as a function of pump power at the input of the HNLF. ....	124
Figure 5.4: The frequency response of conjugated CW lasers (1550nm and 1560.5nm). ....	125
Figure 5.5: Polarisation independency calibration and testing setup. ....	125
Figure 5.6: Optical spectrum observed at 1% monitor (of OPC1 and OPC2) when the input signal is depolarised ASE band. (red solid lines) indicates the spectrum as the pumps were turned off, (solid green lines) HOLD MIN optical spectrum with the pumps turned on after PC0 was randomly changed, (dashed blue lines) HOLD MAX optical spectrum with the pumps turned on after PC0 was randomly changed. ....	127
Figure 5.7: Optical spectrum observed at the OPC output 1% monitors (OPC1 and OPC2) when the input signal is polarised ASE band. (red solid lines) indicates the spectrum as the pumps were turned off, (solid green lines) HOLD MIN optical spectrum with the pumps turned on as PC0 was randomly changed, (dashed blue lines) HOLD MAX optical spectrum with the pumps turned on and PC0 was randomly changed. ....	128
Figure 5.8: Optical spectrum (resolution: 0.02nm) at the output 1% monitor of the OPC, when a 10dBm CW laser is injected at the input of the OPC. ....	129
Figure 5.9: Optical spectrum (resolution: 0.02nm) at the output 1% monitor of the OPC, when a 10dBm CW laser is injected at the input of the OPC. CW laser was swept from 1544nm to 1567nm with 0.8nm (100GHz) step, the color code indicates the CW peaks resulted for each step. ....	130
Figure 5.10: Interference-free conjugation (by limiting the signal bandwidth) tested by 10dBm CW laser. (a) central band (1552nm-1560nm), (b) outer band (1546nm-1550nm & 1551nm-1565nm). ....	131
Figure 5.11: Back to back performance measurement setup, (with and without OPC). ....	132
Figure 5.12: Optical spectrum at the input and output monitor points of the OPC (for both bands: OPC1 and OPC2). [X2] ....	132
Figure 5.13: Receiver $Q^2$ factor(a) and BER(b) as a function of OSNR. ....	133
Figure 5.14: Received Q factor as a function of input power to the OPC. ....	134
Figure 5.15: Experimental setup for spectrally efficient, comb-based transmitter system. [X3] ....	135
Figure 5.16: Optical spectrum at the output monitor points of the OPC (on both bands). [X3] ....	135
Figure 5.17: Receiver $Q^2$ factor(a) and BER(b) as a function of OSNR. ....	136

Figure 5.18: (a) Optical spectrum with and without OPC, at maximum OSNR. (b) $Q^2$ of the individual channels with and without OPC, at maximum OSNR. [X3].....	137
Figure 5.19: Experimental setup of comb regenerator. [X13].....	138
Figure 5.20: (left) Input Comb lines with the phase profile applied to the optical spectrum using the interferometric WSS. (right) output optical spectrum of the HNLF (1%). .....	140
Figure 5.21: (left) Input Comb lines with the phase profile applied to the optical spectrum using the interferometric WSS. (right) the output optical spectrum of the HNLF (1%). .....	141
Figure 5.22: Regenerated comb lines (at the 1% output of the HNLF) for different input powers. ....	143
Figure 5.23: (a) phase profile applied to seed comb lines which was optimised to generate flat comb lines, (b) input and output spectrum of the comb generator, (c) the OSNR of input and output comb lines. ....	144
Figure 6.1: Experimental setup of OPC assisted discretely amplified transmission system.	149
Figure 6.2: $Q^2$ as a function of signal power (left column) and the received constellation at the optimum signal power (right column) measured at 3000km with and without OPC. The figure contains the results for 2 channels (a), 4 channels (b), and 8 channels (c). ....	150
Figure 6.3: (left column) $Q^2$ as a function of distance, (right column) received constellation at selected distance (the maximum of EDC system). The figure contains the results for 2 channels (a), 4 channels (b), and 8 channels (c). ....	152
Figure 6.4: Optical spectrum and BER per channel at the maximum distance (at which $BER > 2 \times 10^{-3}$ ), for 2-channel system (a), 4-channel system (b), and 8-channel system (c); with and without OPC. ....	153
Figure 6.5: Comparison of improvement in $Q^2$ of experimental coherent transmission systems, shown in table 6.1, that use mid-link OPC. [2] .....	154
Figure 6.6: Experimental setup of OPC assisted distributed Raman amplified transmission system. ....	155
Figure 6.7: $Q^2$ as a function of signal power and the received constellation at the optimum signal power measured at 2400km without OPC, 1-OPC, 2-OPC, and 3-OPC. ....	156
Figure 6.8: $Q^2$ as a function of distance and received constellation at 4400km (the maximum of EDC system). ....	158
Figure 6.9: Optical spectrum (resolution 0.1nm) and BER per channel of the received signals at the maximum distance of EDC system and mid-link OPC assisted system. [X3] .....	159
Figure 6.10: Comparison of improvement in $Q^2$ of experimental coherent transmission systems, shown in table 6.2, that use optical phase conjugation. [X3] .....	160

# Chapter 1 : Introduction

Today, coherent Wavelength Division Multiplexed (WDM) long-haul optical transmission systems are considered to be the backbone to global communication systems. Due to their significant cost, telecom operators design and deploy optical links that serve their customers and accommodate a projection of their future needs to avoid bottleneck state in their communication networks. The exponential growth in demand for optically delivered digital communication [1] and the saturation in delivered capacity (per fibre) reported by hero research experiments [2] have lead the research and industrial communities to recognise and predict a future “*Capacity Crunch*” [3]; where optical fibre networks reach a state at which it cannot accommodate the growth capacity demand. Recent hero transmission experiments (that use single mode fibre) have reported an exhaustion of the capacity dimensions of the fibre, achieved by: the deployment of dual polarisation modulation and coherent detection [4,5], full utilisation of the low loss bandwidth of the fibre [6], innovations to build low noise optical amplifiers [7–11], high spectral efficiency modulation [12], digital signal processing [13], and optical fibre nonlinearity compensation techniques [14–19]. While some of these solutions have been fully developed and commercially deployed, other innovations can deliver a temporary solution to postpone the predicted effects of capacity crunch, and provide mature solutions to the optical links to be deployed in the future.

Long-haul optical fibre transmission systems are designed to achieve a target distance reach and maximum capacity throughput. During the design of long haul optical links, both linear and nonlinear noise accumulation along the transmission system must be taken into consideration; these noise terms will limit the maximum achievable capacity or distance reach of optical signals (with a resilient Bit Error Rate, BER). This limit has been commonly called the “*nonlinear Shannon limit*” [20,21] which defines the digital capacity to optical bandwidth ratio (bps/Hz) as a function of the Signal to Noise Ratio (SNR) of the received optical signals [22].



The maximum achievable SNR in a long-haul optical transmission system is limited by the linear Amplified Spontaneous Emission (ASE) noise, generated from inline amplifiers, and the nonlinear inter-/intra-channel interference, generated along the optical fibre. An optimisation of optical signal power is always required to operate at the maximum SNR which trades-off between the linear ASE noise (dominant at low signal power) and the nonlinear noise (dominant at high signal power). The intensity of the linear ASE noise generated in optical amplifiers (that compensates for the signal power loss due to optical fibre attenuation) can vary based on the amplification phenomenon occurring inside the amplifier [10,23,24]. This ASE noise is added at the end of each span in discretely amplified systems or continuously along the span in distributed Raman transmission systems. On the other hand, the susceptibility of the optical fibre generates noise-like interference among the signals propagating along the fibre, this nonlinear interference grows cubically with the signal power. The accumulation of this nonlinear noise depends on the design of the optical transmission link: span length, properties of the fibre, and amplification scheme.

## 1.1 Thesis Organization

This thesis reports on the theoretical definition of nonlinear limits for various optical transmission systems that deploy nonlinearity compensation techniques, especially Digital Back Propagation (DBP) and Optical Phase Conjugation (OPC).

In **chapter 2**, I will recall basic literature that present the basic implications of signals propagating through optical fibres, optical amplifiers, point to point optical fibre communication systems, and nonlinearity compensation techniques.

**Chapter 3** reports on the derivation and verification, using simulation and experimental results, of theoretical models that describe nonlinear interactions (Kerr effects) occurring in discretely amplified and distributed Raman amplified transmission systems that deploy single or multiple OPCs. This chapter compares the frequency response of Kerr product generation in systems without OPC, with mid-link OPC, and with multiple OPCs; to calculate the achievable nonlinearity compensation efficiency by OPC assisted systems. The theoretical analysis, backed by simulation results and experimental verifications, will show that the nonlinearity compensation efficiency achieved in OPC assisted distributed Raman system is superior to the compensation efficiency achieved by OPC assisted discretely amplified transmission link. Also, I will show that the compensation efficiency achieved by OPC in both systems can be enhanced by shortening the span length in a uniform optical transmission link. Furthermore,

chapter 3 shows that the deployment of multiple OPCs along any optical transmission system enhances the nonlinear interactions (compared to a system that uses only a single OPC) among signals propagating through the system. This reduction in compensation efficiency of nonlinearities when deploying multiple OPC is explained by the fact that each OPC in the system will act as periodic dispersion compensator that enhances the efficiency of the nonlinear interactions along the system.

**Chapter 4** extends chapter 3's theoretical nonlinear Kerr product generation models to identify the nonlinear noise generation (nonlinear performance limit) among modulated signals propagating through the previously described systems. I will show that deploying mid-link OPC in discretely amplified transmission system will lead to a partial compensation of the deterministic signal-signal nonlinear interactions. By compensating only for intra-channel interference (among strongly phase matched signals), the mid-link OPC leaves the system limited by the nonlinear noise generated due the inter-channel interference (among weakly phase matched signals). This chapter presents a closed form equation, verified by simulation results, that identifies the nonlinear noise compensation efficiency achieved by mid-link OPC when deployed in discretely amplified system with long span length. This equation will show that the nonlinear noise compensation efficiency, achieved by mid-link OPC, is highly dependent on the bandwidth of the modulated signals propagating along the system. I will present a reference numerical analysis that shows the expected performance ( $Q^2$ ) enhancement, as a function of span length and signal bandwidth, achieved by a single OPC deployed in discretely amplified and distributed Raman systems. The simulation results and numerical analysis conducted in this chapter confirms the message carried in chapter 3, if a mid-link OPC assisted system is limited by deterministic nonlinear signal-signal interactions, then deploying multiple OPCs will degrade the level of performance enhancement achieved by a single, mid-link, OPC. I will also present an accurate theoretical description of the ultimate nonlinear limit of ideal nonlinearity compensated, PMD free, transmission systems which are limited by the non-deterministic signal-noise interactions; when using full-field DBP (unbounded by computational load) or when using single or multi OPC deployed in ideal lossless distributed Raman systems (lossless OPCs).

**Chapter 5** presents the experimental implementation and characterisation of dual band, dual pump, polarisation insensitive OPC as well as the experimental implementation of comb generator that uses Wavelength Selective Switch (WSS) as a dispersion management tool. This chapter characterises the dual band OPC in terms of counter dithering, polarisation dependent

loss, and the performance of modulated signals (8x28Gbaud PM-QPSK, and 30x30Gbaud PM-QPSK) conjugated by the dual band OPC. The implemented OPC will be used in the following chapter to demonstrate nonlinearity compensation and performance enhancement of modulated signals propagating along optical transmission systems. Also, this chapter studies the parametric comb generation technique that uses WSS to control the phase matching among seed comb lines to expand the number of comb lines (with restricted flatness) generated by the end of Highly Nonlinear Fibre (HNLF).

In **chapter 6**, I will experimentally deploy the dual band OPC in discretely amplified and distributed Raman optical fibre transmission system. This chapter shows that the nonlinearity compensation efficiency achieved by OPC assisted discretely amplified transmission system is highly dependent on the bandwidth of the modulated signals of the number of channels propagating along the system. These experimental results verify the closed form equation reported in chapter 4 which identifies the nonlinearity compensation efficiency achieved by mid-link OPC deployed in discretely amplified transmission system. The experimental results have shown that employing a mid-link OPC in discretely amplified transmission system with 100km amplifier spacing achieves reach enhancement of 43%, 32%, and 24% for 2x112Gbps, 4x112Gbps, and 8x112Gbps (each 28Gbaud, PM-QPSK) signals. In this chapter, I will deploy the dual band OPC to compensate nonlinearities among 30x30Gbaud PM-QPSK (15ch/Band) propagating along distributed Raman amplified transmission system with Raman pump spacing of 50km. In this experiment, I will report on the highest reported performance enhancement (or distance enhancement) of 72% achieved by mid-link OPC assisted long-haul transmission system that propagates large bandwidth optical signals (3.6Tbps/1THz). Figure 1.1 shows the performance enhancement (in  $Q^2$ ) achieved in our experimental results compared with key experimental demonstrations reported in literature (EDFA systems [25–29], distributed Raman systems [27,30–35] [X8]), as a function of the maximum distance achieved by Electronically Dispersion Compensated (EDC) distance (a) and as a function of the total bitrate-distance product (b). The figure shows that the deployment of OPC in discretely amplified (EDFA amplified) transmission system achieves moderate performance enhancement for single channel system, these reported performance improvements of single channel systems slowly vanishes as the number of channels increases. The figure also shows that our OPC assisted distributed Raman system has achieved the largest reported performance improvement in long-haul optical transmission systems (>1000km).

Finally, **chapter 7** will provide the conclusions and suggested future work.

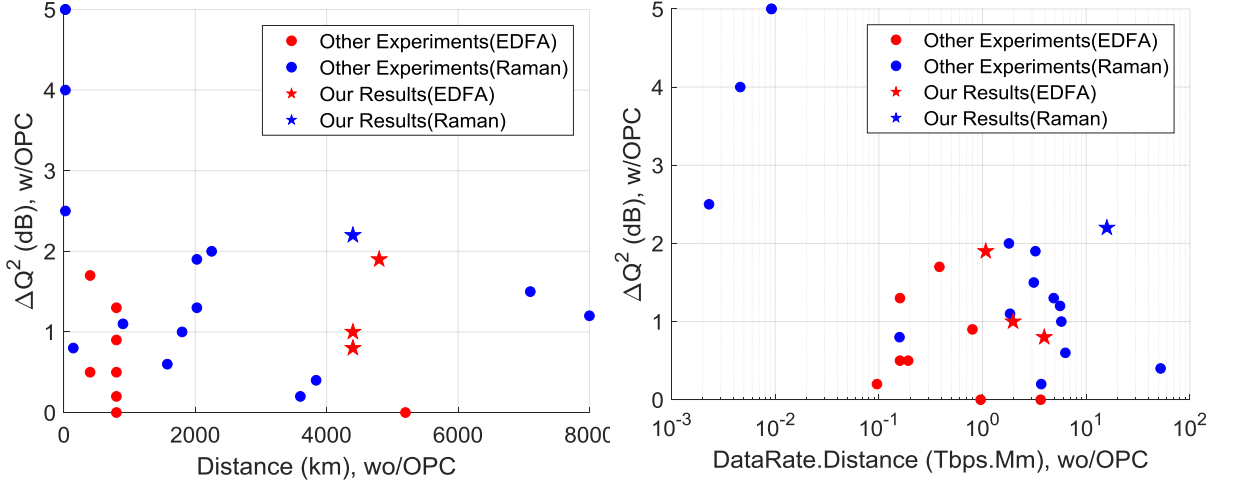


Figure 1.1: Performance improvement ( $\Delta Q^2$ ) in reported OPC assisted system deployed in EDFA (discretely amplified) and distributed Raman amplified transmission systems. (a) the performance improvement as a function of maximum EDC distance, (b) the performance improvement as a function of the net bitrate-distance product. \*Different experiments have used various Forward Error Correction (FEC) thresholds.

## 1.2 Collaboration Acknowledgments

The work reported in this thesis would not be possible without the collaborations established with colleagues working here at AIPT. As I have conducted all the simulations and experimental demonstrations reported across this thesis (chapter 3-7), my supervisor (Prof. Andrew Ellis) has contributed to improve the reported results by guiding my research direction and challenging my ideas to report polished research. The simulations of coherent optical systems conducted in chapter 4 have used the Digital Signal Processing (DSP) provided by Dr. Christian Sánchez. While I have operated the offline DSP (with DBP functionality implemented by me), Dr. Christian Sánchez has always provided me with his support. Dr. Mary McCarthy, Dr. Paul Harper, and Dr. Marc Stephens have trained me in the lab to operate the instrumentations correctly and safely. The experimental training and support from my lab supervisors has enabled me to use: lasers, high power amplifiers, splicing, optical transmitters, coherent receiver, offline DSP, recirculating loops, and Raman lasers. As a result of this training, I have been able to build and conduct my own experiments (reported in chapter 3, 5, 6). In the reported Raman related experiments, I have worked with Dr. Mingming Tan and Md. Asif Iqbal, both have supplied me with the Raman pumps, helped me measure signal's power profile, and allowed me to use one of their novel distributed Raman systems (Raman Fibre Laser [36]) to measure the nonlinear Kerr frequency response for various power profiles (reported in chapter 3).

While this thesis mainly contains my own research (published or to be published as a first author), I have contributed (as a co-author) to other published research conducted by my colleagues. For example, I have conducted simulations (validated by theory) that show the performance limits of dispersion uncompensated, dispersion managed, and Dispersion Shifted Fibre (DSF) deployed in PMD free discretely amplified transmission system (with and without DBP) [X5]; which will be reported in chapter 4. I have derived a simple closed form theoretical expression, validated by simulation results, that describes the nonlinear signal-noise interaction limits of ideal lossless Raman systems that deploy DBP, mid-link OPC, multiple OPCs [X5, X6]; which will be reported in chapter 4. I have provided the theoretical support to polish the closed form equations that describe the nonlinear signal-noise interaction limit for various systems [X9, X10, X21], and supported the first author of [X16] to obtain his simulation results. In the lab and during my training stage, I have helped during the design and implementation stages of the experiments reported in [X8, X11, X20], where I have conducted simulations to predict systems performance and helped to automate some aspects of the experiment, capturing spectrums, programming the recirculating loop.

### 1.3 Publication Summary

Book Chapter:

- [X.1] **Mohammad Ahmad Zaki Al-Khateeb**, Abdallah Ali, Andrew D. Ellis, ‘Chapter 2: Basic Optical Fibre Nonlinear Limits’, in *The Potential for Networks with Capacities Exceeding the Nonlinear-Shannon Limit*, Pan Stanford Publishing Pte Ltd, (to be submitted).

Journal Papers:

- [X.2] **Mohammad A. Z. Al-Khateeb**, Christian Sánchez, Mary E. McCarthy, Andrew D. Ellis, “Nonlinearity compensation using Optical Phase Conjugation deployed in discretely amplified transmission systems”, *Optics Express*, (submitted).
- [X.3] **Mohammad A. Z. Al-Khateeb**, Mingming Tan, Md. Asif Iqbal, Abdallah Ali, Christian Sánchez, Mary E. McCarthy, Paul Harper, Andrew D. Ellis, “Experimental demonstration of 72% reach enhancement of 3.6Tbps optical transmission system using mid-link Optical Phase Conjugation”, *Optics Express*, (submitted).
- [X.4] **Mohammad A. Z. Al-Khateeb**, Md. Asif Iqbal, Mingming Tan, Abdallah Ali, Mary McCarthy, Paul Harper, and Andrew D. Ellis, "Analysis of the nonlinear Kerr effects

- in optical transmission systems that deploy optical phase conjugation," *Opt. Express* 26, 3145-3160 (2018).
- [X.5] A. D. Ellis, M. E. McCarthy, **M. A. Z. Al Khateeb**, M. Sorokina, and N. J. Doran, "Performance limits in optical communications due to fibre nonlinearity," *Adv. Opt. Photon.* 9, 429-503 (2017).
  - [X.6] Andrew D. Ellis, **Mohammad Ahmad Zaki Al Khateeb**, and Mary E. McCarthy, "Impact of Optical Phase Conjugation on the Nonlinear Shannon Limit," *J. Lightwave Technol.* 35, 792-798 (2017).
  - [X.7] **Mohammad A. Z. Al-Khateeb**, Mary McCarthy, Christian Sánchez, and Andrew Ellis, "Effect of second order signal–noise interactions in nonlinearity compensated optical transmission systems," *Opt. Lett.* 41, 1849-1852 (2016).
  - [X.8] Andrew D. Ellis, Mingming Tan, Md Asif Iqbal, **Mohammad Ahmad Zaki Al-Khateeb**, Vladimir Gordienko, Gabriel Saavedra Mondaca, Simon Fabbri, Marc F. C. Stephens, Mary E. McCarthy, Andreas Perentos, Ian David Phillips, Domaniç Lavery, Gabriele Liga, Robert Maher, Paul Harper, Nick Doran, Sergei K. Turitsyn, Stylianos Sygletos, and Polina Bayvel, "4 Tb/s Transmission Reach Enhancement Using  $10 \times 400$  Gb/s Super-Channels and Polarization Insensitive Dual Band Optical Phase Conjugation," *J. Lightwave Technol.* 34, 1717-1723 (2016).
  - [X.9] M. E. McCarthy, **M. A. Z. Al Kahteeb**, F. M. Ferreira, and A. D. Ellis, "PMD tolerant nonlinear compensation using in-line phase conjugation," *Opt. Express* 24, 3385-3392 (2016).
  - [X.10] A. D. Ellis, M. E. McCarthy, **M. A. Z. Al-Khateeb**, and S. Sygletos, "Capacity limits of systems employing multiple optical phase conjugators," *Opt. Express* 23, 20381-20393 (2015).
  - [X.11] Son Thai Le, Mary E. McCarthy, Naoise Mac Suibhne, **Mohammad A. Z. Al-Khateeb**, Elias Giacomidis, Nick Doran, Andrew D. Ellis, and Sergei K. Turitsyn, "Demonstration of Phase-Conjugated Subcarrier Coding for Fibre Nonlinearity Compensation in CO-OFDM Transmission," *J. Lightwave Technol.* 33, 2206-2212 (2015).

Conference Proceedings:

- [X.12] **Mohammad Ahmad Zaki Al-Khateeb**, Mary Elizabeth Mccarthy, Andrew Ellis, "Performance Enhancement Prediction for Optical Phase Conjugation in Systems with

- 100km Amplifier Spacing”, in *European Conference on Optical Communication*, Gothenburg (2017), pp. 1-3 (Th.1.F.4).
- [X.13] **M. Al-Khateeb**, M. E. McCarthy, M. D. G. Pascual, F. Smyth, and A. D. Ellis, "Optimization of Parametric Comb Generation Using Interferometric Wavelength Selective Switch," in *Conference on Lasers and Electro-Optics*, OSA Technical Digest (online) (Optical Society of America, 2017), paper JW2A.31.
- [X.14] M. Kamalian Kopae, J. E. Prilepsky, S. A. Derevyanko, S. T. LE, S. Turitsyn, and **M. Al-Khateeb**, "Nonlinear Fourier Based Spectral Filtering," in *Conference on Lasers and Electro-Optics*, OSA Technical Digest (online) (Optical Society of America, 2017), paper JTh2A.135.
- [X.15] **M. Al-Khateeb**, M. E. McCarthy, and A. D. Ellis, "Experimental Verification of Four Wave Mixing in Lumped Optical Transmission Systems that Employ Mid-Link Optical Phase Conjugation," in *Conference on Lasers and Electro-Optics*, OSA Technical Digest (online) (Optical Society of America, 2017), paper JTh2A.64.
- [X.16] A. A. I. Ali, C. S. Costa, **M. A. Z. Al-Khateeb**, F. M. Ferreira and A. D. Ellis, "Four-wave mixing in optical phase conjugation system with pre-dispersion," 2017 Opto-Electronics and Communications Conference (OECC) and Photonics Global Conference (PGC), Singapore, 2017, pp. 1-3.
- [X.17] **M. Al-Khateeb**, M. McCarthy, C. S. Costa, and A. D. Ellis, "Mid-Link Optical Phase Conjugation in Lumped Optical Transmission Systems," in *Asia Communications and Photonics Conference 2016*, OSA Technical Digest (online) (Optical Society of America, 2016), paper AS2B.5.
- [X.18] **M. A. Z. Al-Khateeb**, M. Tan, M. A. Iqbal, M. McCarthy, P. Harper and A. D. Ellis, "Four wave mixing in distributed Raman amplified optical transmission systems," *2016 IEEE Photonics Conference (IPC)*, Waikoloa, HI, 2016, pp. 795-796.
- [X.19] A. D. Ellis, **M. A. Z. A. Khateeb** and M. E. McCarthy, "Impact of optical phase conjugation on the nonlinear shannon limit," 2016 Optical Fibre Communications Conference and Exhibition (OFC), Anaheim, CA, 2016, pp. 1-3.
- [X.20] A. D. Ellis, I. D. Phillips, M. Tan, M. F. C. Stephens, M. E. McCarthy, **M. A. Z. Al Kahteeb**, M. A. Iqbal, A. Perentos, S. Fabbri, V. Gordienko, D. Lavery, G. Liga, M. G. Saavedra, R. Maher, S. Sygletos, P. Harper, N. J. Doran, P. Bayvel, and S. K. Turitsyn, "Enhanced superchannel transmission using phase conjugation," in *Proc. European Conference and Exhibition on Optical Communication (ECOC, 2015)*, paper We2.6.4.

[X.21] A. D. Ellis, S. T. Le, **M. A. Z. Al-Khateeb**, S. K. Turitsyn, G. Liga, D. Lavery, T. Xu, and P. Bayvel, “The impact of phase conjugation on the nonlinear-shannon limit: The difference between optical and electrical phase conjugation,” in IEEE Summer Topicals Meeting Series (IEEE, 2015), pp. 209–210.

In this thesis, I will address in more details to my contribution to:

- Chapter 3: [X4], [X15], and [X18].
- Chapter 4: [X1], [X2], [X5], [X6], [X7], [X12], [X17], and [X19].
- Chapter 5: [X13].
- Chapter 6: [X2], [X3], and [X12].





# Chapter 2 : Background

This chapter reviews background literature that will be used throughout the following chapters.

## 2.1 Optical Fibre as a Transmission Medium

Optical fibres are silica-based transmission media that permits light to propagate through it. There are many types of optical fibres that have been used and currently under development, such as: single mode fibres, multi-mode fibres, and various types of multicore fibres [37]. Multi-mode fibres suffer from intermodal dispersion that degrades the quality of signals propagating through it, which restricts the maximum achievable reach and capacity of those fibres. Multi-mode fibres can be found in short reach (access) networks and datacentres. Standard Single Mode Fibres (SSMF), unlike the multi-mode fibres, permit the propagation of a single mode (dual polarisation modes). Such fibres are widely used in metro and long-haul optical communication systems.

Multicore fibres are new trending solution to tackle the capacity limits of SSMF fibres and provide cost efficient system integration solutions. In this thesis, I will concentrate on the properties of the SSMF since it stands as a mature transmission medium in long-haul optical transmission systems. Optical fibres impose physical alterations on the signals propagating through it, such as: attenuation, dispersion, and nonlinear effects.

### 2.1.1 Optical Fibre Attenuation

Optical fibre's attenuation is one of the parameters that limits the maximum achievable distance by optical communication systems, as optical amplifiers (that emit noise) are needed to compensate for this attenuation. Due to Rayleigh scattering, light absorption, impurities, and waveguide imperfections [38]; signals propagating along the optical fibre lose a portion of their power. The optical power of signals propagating along the optical fibre can be written as:

$$P(z) = P(0)e^{-\alpha(\lambda)z} \quad (2.1)$$

where  $P(z)$  is the optical signal power after propagation through  $z$  fibre length,  $\alpha(\lambda)$  is the attenuation coefficient of the fibre (in Neper/m). The attenuation coefficient of optical fibre is wavelength dependent as different spectral optical bands suffer from different power degrading effects (scattering, absorption, or impurities) [38].

The optical bands C (1530nm to 1565nm) and L (1565nm to 1625nm) are commonly used for the purposes of long-haul optical communications; due to fact that SSMF have their minimum attenuation coefficient at these bands (ranging around 0.19dB/km[4.6e<sup>-5</sup>Neper/m], and can get as low as 0.1419dB/km [39]).

### 2.1.2 Optical Fibre Dispersion

Optical fibre dispersion causes pulse broadening (in time domain) or differential phase shift (in frequency domain) of optical signals propagating through it. Different spectral components of optical light propagate along the optical fibre with different speeds; these speeds are governed by the frequency dependent propagation coefficient  $\beta(\omega)$ :

$$E(z, \omega) = E(0, \omega) e^{(-i\omega t)} e^{\left[\left[-\frac{\alpha}{2} + i\beta(\omega)\right]z\right)} \quad (2.2)$$

$$\beta(\omega) = \beta + \omega\beta' + \frac{\omega^2}{2}\beta'' + \frac{\omega^3}{6}\beta''' + \dots + \frac{\omega^k}{k!}\beta^{(k)}$$

where  $E(z, \omega)$  is the optical field measured at fibre length  $z$  and propagating at radial frequency  $\omega$ ,  $\beta(\omega)$  is the propagation constant of optical spectral tone  $\omega$ ,  $\beta$  (1/km) is a constant phase shift,  $\beta'$  (ps/km) is the group time delay,  $\beta''$  (ps<sup>2</sup>/km) is the time broadening which relates to the optical fibre chromatic dispersion  $D_c$  (ps/km/nm) coefficient as:

$$\beta'' = -\frac{\lambda^2}{2\pi c} D_c \quad (2.3)$$

and  $\beta'''$  (ps<sup>3</sup>/km) is the third order propagation constant that relates to dispersion slope  $S$  (ps/km/nm<sup>2</sup>) coefficient as:

$$S = \frac{4\pi c}{\lambda^3} \beta'' + \left(\frac{2\pi c}{\lambda^3}\right)^2 \beta''' \quad (2.4)$$

The chromatic dispersion of the SSMF, ranges around 16ps/km/nm, is considered to be the major dispersive coefficient of modulated signal propagating in a long-haul transmission system; whereas dispersion slope of the SSMF, ranging around 0.08ps/km/nm<sup>2</sup>, can be significant over large bandwidth (higher than 10nm) and long propagation distances. The higher order (third order, fourth order, ...) propagation coefficients are insignificant over the C and L optical bands and often are ignored.

SSMF inherently supports the propagation of two orthogonal signal polarisation modes, where the two polarisations may face different refractive index (propagation constants) due to the imperfections in the fabrication of the optical fibre and the random anisotropic stress along the fibre [38]. These imperfections also lead to the randomisation of the polarisation state of signals propagating along the fibre. Polarisation Mode Dispersion (PMD) occurring in SSMF causes the two polarisations to propagate with different speeds; which results a differential time delay between the two polarisation states that can be approximated as [38]:

$$\Delta t_p = D_p \sqrt{L} \quad (2.5)$$

where  $D_p$  is the PMD factor of the optical fibre measured in  $\text{ps}(\text{km})^{-0.5}$ .

### 2.1.3 Optical Fibre Nonlinearities

Optical fibre nonlinearities are induced from the third order susceptibility of the fibre from electronic and stimulated scattering [38] effects. These nonlinearities can be constructive or destructive factor in the implementation of long-haul optical communication systems. For example, the nonlinear index (susceptibility) of the optical fibre can be used to realise optical devices that achieve parametric signal amplification [10], all-optical signal processing [16,40], and optical comb generators [41]. At the same time, these nonlinearities, often called “*Kerr effects*” [42], cause an unwanted interference among signals propagation along the system. The stimulated nonlinear scattering that occurs in optical fibres also can be used to realise optical amplification [24] and signal filtering [43], and also can cause nonlinear signal-signal interference.

#### 2.1.3(a) *Kerr Optical Fibre Nonlinearities*

The propagation of up to three optical waves (spectrally located at  $\omega_q$ ,  $\omega_r$ , and  $\omega_s$ ), in optical fibres, generate a nonlinear optical field (spectrally located at  $\omega_F = \omega_q + \omega_r - \omega_s$ ) which is governed by the inhomogeneous wave equation [44] (simplified according to slowly varying envelope approximation and assuming no depletion: high signal to nonlinear product power ratio):

$$\frac{\partial E_F(z)}{\partial z} = -\frac{\alpha}{2} E_F(z) + i \frac{2\pi\omega_F D\chi}{nc} E_q(0) E_r(0) E_s^*(0) e^{\left[\left[-\frac{3}{2}\alpha + i\Delta\beta\right]z\right]}$$

where :

$$(2.6)$$

$$E_{q,r,s}(z, \omega_{q,r,s}) = E_{q,r,s}(0) e^{(-i\omega_{q,r,s}t)} e^{\left[\left[-\frac{\alpha}{2} + i\beta_{q,r,s}\right]z\right]}$$

$$\Delta\beta = \beta_F + \beta_s - \beta_q - \beta_r$$

where  $D$  is the degeneracy factor,  $n$  is the refractive index of the optical fibre,  $c$  is the speed of light,  $\chi$  is the third order nonlinear susceptibility [38],  $\Delta\beta$  is the phase mismatching between the mixing components (defined as a function of the propagation constants of the involved optical waves, shown in equation 2.2), and the (\*) indicates the optical field conjugate. The differential equation (2.6) can be solved to result an equation that describes the generated nonlinear optical field ( $E_F$ ) [44]:

$$E_F(z) = i \frac{2\pi\omega_F D\chi}{nc} E_q(0) E_r(0) E_s^*(0) e^{\left(\frac{\alpha}{2}z\right)} \left[ \frac{e^{[-\alpha + i\Delta\beta]z} - 1}{-\alpha + i\Delta\beta} \right] \quad (2.7)$$

The process that generates the nonlinear field (at  $\omega_F$ ) is commonly known as the nonlinear Kerr product which can be categorised into three types: Self-Phase Modulation (SPM), Cross Phase Modulation (XPM), and Four Wave Mixing (FWM). The distinction between SPM, XPM, and FWM corresponds to the number of optical waves involved in the nonlinear Kerr process where: SPM is generated from a single wave ( $\omega_q = \omega_r = \omega_s$ ), XPM is generated from two waves ( $\omega_q = \omega_r \neq \omega_s$ ), and FWM is generated from three waves ( $\omega_q \neq \omega_r \neq \omega_s$ ). The degeneracy factor  $D$  represents the number of permutations of nonlinear Kerr products results from SPM, XPM, and FWM and takes values of 1, 3, or 6, respectively [44]. The newly generated nonlinear product is still subjected to the attenuation of the optical fibre ( $\exp(-\alpha z/2)$ ), as seen in equation 2.6. The nonlinear product generation is highly dependent on the susceptibility of the fibre, the intensity of the source optical fields ( $q, r, s$ ), the properties of the fibre ( $z$  and  $\alpha$ ), and the phase mismatching accumulated along the optical fibre. The phase mismatching ( $\Delta\beta$ ) among the mixing components (spectrally located at  $\omega_q, \omega_r, \omega_s$ , and  $\omega_F$ ) arise from the mismatching of propagation constants along the fibre (for each component wave, as seen in equation 2.6), and can be theoretically defined as [45] (when ignoring the propagation constants above the third order) :

$$\Delta\beta = \frac{2\pi\lambda_F^2}{c} (f_q - f_s)(f_r - f_s) \left[ D_c + \frac{\lambda_F^2}{2c} (f_q + f_r - 2f_s) S \right] \quad (2.8)$$

This nonlinear process introduces a degrading effect to the modulated signals propagating along the transmission system, as the newly generated nonlinear products are viewed as a noise-like interfering products [46–48].

### ***2.1.3(b) Stimulated Optical Fibre Nonlinearities***

The stimulated nonlinear effects occur in optical fibres are categorised into two types: Stimulated Raman Scattering (SRS) and Stimulated Brillouin Scattering (SBS). Unlike Kerr effects, SRS and SBS impose an energy exchange between the optical wave and the transmission medium (optical fibre) causing frequency down conversion of energy from the pump wave [38]. The newly generated photons from the stimulated nonlinear process cause a spectral gain stokes that travel: in both direction (forward and backward, relative to the pump propagation direction) in the case of SRS, and only in the backward direction (opposite to the direction of pump propagation) in the case of SBS [38]. The gain coefficients of SRS and SBS are highly dependent on the properties of the fibre (the effective core area and core dopants [24,38]).

SRS is an attractive phenomenon that can be utilised to amplify broadband optical signals that are spectrally located at approximately -13THz away from a Raman pump [24,38], I will discuss this amplification scheme in more details in the next section. On the other hand, SBS generates a narrow band gain (in the order of MHz, located at approximately -10GHz away from the pump [38]) which can be used for ultra-narrow band filtering (amplification) [43]. SBS can also be considered as a limiting phenomenon, especially in the context of parametric amplifiers [10], as it limits the maximum pump power that can be injected into the fibre (typically HNLF) by reflecting the pump energy in the backward direction. As the parametric process (based on fibres susceptibility) amplify signals copropagating with the pump, the limit that SBS imposes on the maximum injected pump power restricts the maximum gain that can be achieved in the parametric amplifier. SBS stokes generation efficiency can be minimised by reducing the Brillouin gain coefficient ( $g_B$ ) through: linearly straining the fibre [49], changing the temperature [50], changing core dopants [51], increasing core area [52], or by distribution of the optical power over larger bandwidth (dithering) [53].

Figure 2.1 shows simulation results conducted in VPITransmissionMaker v9.8 displaying optical fibre output power and the reflected SBS power as a function of the input power of Continuous Wave (CW) laser propagating through 15km of SSMF (parameters are in the caption). At low input CW laser power (<-10dBm), the reflected light is dominated by Rayleigh scattering which is a constant portion of the forward propagating power. When the CW laser

power ranges between -5dBm and 5dBm, the backscattered light become dominated by SBS which manifests as growth in the reflected power as a function of the input CW power. At high CW laser power (>5dBm), the CW laser that reaches the output of the fibre saturates (at 8dBm) and all the excessive input power will be reflected as SBS.

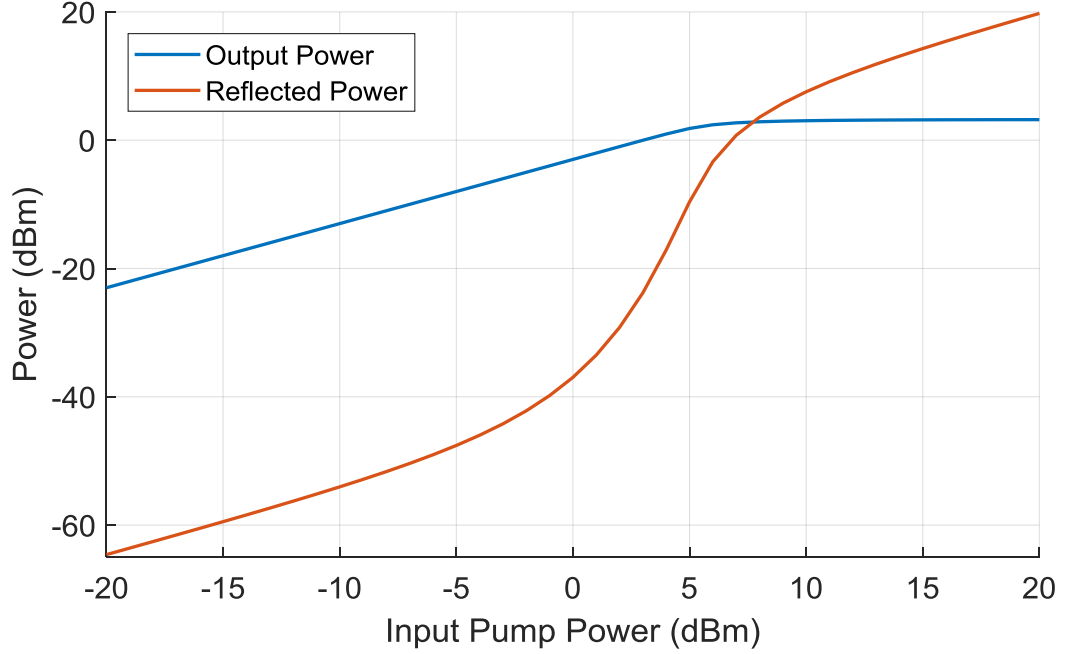


Figure 2.1: Optical fibre output power and SBS Back scattering as a function of the total input power to SSMF. CW linewidth=1Hz,  $L=15\text{km}$ ,  $\alpha=0.2\text{dB/km}$ , Effective core area= $80 \times 10^{-12}\text{m}^2$ , SBS gain coefficient ( $g_B$ )= $4.6 \times 10^{-11}\text{m/W}$ .

## 2.2 Optical Amplifiers

As they compensate for the optical signal loss, optical amplifiers are essential to enable long-haul optical transmission systems. Optical amplifiers generate ASE noise that degrades the performance of signals propagating along the systems. There are many types of optical amplifiers, such as: Doped Fibre Amplifiers (DFA) [7], Raman Amplifiers [8,24,38], Fibre Optical Parametric Amplifiers (FOPA) [9,10], Phase Sensitive Amplifiers (PSA) [40], Semiconductor Optical Amplifiers (SOA) [11]. Each one of these amplification techniques has its own: properties, amplification mechanism, gain flatness, amplification bandwidth, and the noise generated within the amplifier. In this thesis, I will restrict my study to long-haul optical transmission systems that deploy DFAs [23] and Distributed Raman amplification [24], remarks about the other types of amplifiers is not the focus of this thesis thus not much emphasis will be placed on them.

Optical amplification in long-haul optical transmission systems can be deployed periodically by the end of each fibre span to compensate for its loss; these links are normally referred to as

discretely amplified systems (lumped system). Also, optical amplification can be distributed along the transmission fibre itself, this type of amplification can exploit the nonlinear stimulated Raman scattering [24] or the nonlinear parametric Kerr properties [54] of the SSMF. DFA is optical amplification technique that utilises the stimulated scattering phenomenon in optical fibres doped with rare-earth elements. The dopants infused in the fibre core of the DFA identify the band of amplification (and the required pump wavelength), for example: Praseodymium DFA amplifies the O band, and Erbium DFA (EDFA) amplifies the C and L bands [23].

Distributed Raman amplification utilises the SRS nonlinear process to amplify optical signals that co-propagate and/or counter-propagate with Raman pump [24]. The gain (and its flatness) of Raman amplifiers is restricted by the Raman gain coefficient ( $g_r(\lambda_s)$ ) of the fibre, the power and spectral width of the Raman pump. The typical frequency response of the Raman gain coefficient ( $g_r(\lambda_s)$ ) in SSMF can be seen in figure 2.2, where the Raman pump is a CW laser spectrally located at 1455nm (to amplify signals spectrally located at 1555nm). The frequency response of Raman gain is not flat, but flattened Raman gain spectrum can be realised by using broadband Raman pump [55] or multiple Raman pumps located on different wavelengths [56].

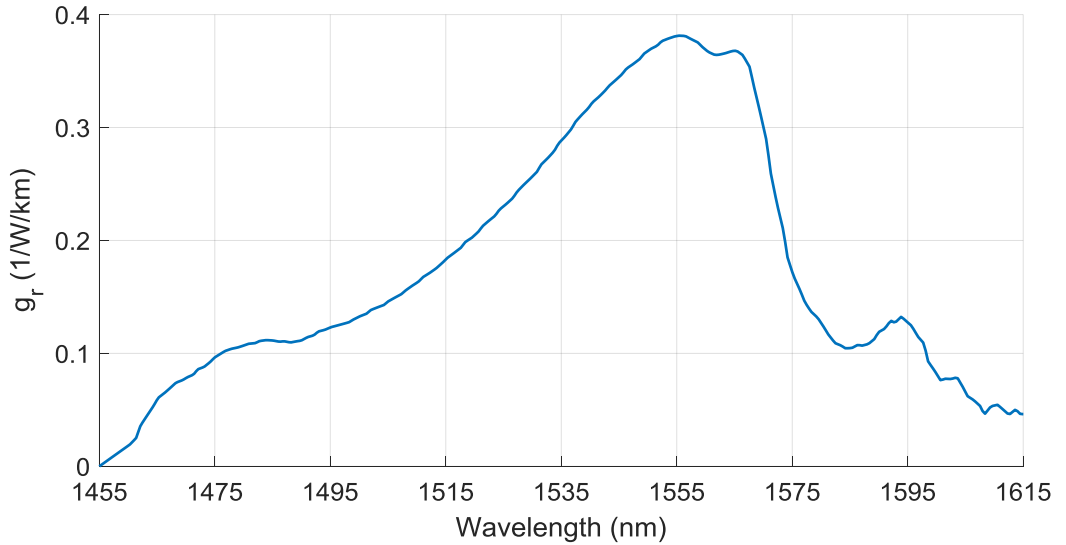


Figure 2.2: Raman gain coefficient in SSMF, CW Raman pump located at 1455nm. The data set extracted from simulation results using VPITransmissionMaker 9.8.

Raman amplifiers do not have restrictions on the wavelength of operation, that is why it is possible to realise broadband 200nm flat amplification bandwidth [56]. The low  $g_r$  value of SSMF (approximated as 0.37/W/km) requires high pumping power spectrally located at 14xxnm [57] to amplify signals in the low loss bands (C and L-bands). Figure 2.3 shows a schematic diagram of a distributed Raman amplified optical fibre span that deploys counter



propagating pumps. The figure shows that the signals co-propagate with the forward Raman pump ( $P_{fw}$ ) and counter-propagate with the backward Raman pump ( $P_{bw}$ ), both  $P_{fw}$  and  $P_{bw}$  are propagating on the same wavelength (approximately -100nm away from the signal wavelength). Optical isolators (or circulators) are used at the output of each Raman pump to prevent the Raman pump damage due to the remaining pump power from the counter-propagating pump.

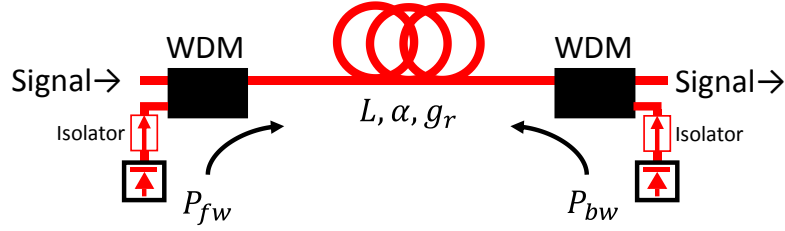


Figure 2.3: Schematic diagram of distributed Raman amplified fibre span.

The total pumping power can be theoretically modelled (along the fibre) as [24]:

$$P_p(z) = P_0 \left[ r_f e^{-\alpha_p z} + (1 - r_f) e^{-\alpha_p (L-z)} \right] \quad (2.9)$$

where  $P_p(z)$  is the total Raman pump power as a function of fibre length  $z$ ,  $P_0$  is the total pumping power ( $P_{fw} + P_{bw}$ ) injected to the span on both directions,  $r_f$  is the ratio of the forward pump power to the total pump power ( $P_{fw}/P_0$ ),  $\alpha_p$  is the fibre attenuation factor at the pump wavelength ( $\lambda_p$ ), and  $L$  is the total span length. The first term in the squared brackets represents the power evolution of the forward pump, while the second term represents the backward propagating pump. The gain evolution of the signal propagating through the span can be written as, assuming no pump depletion (high pump to signal power ratio) and 0dB net gain [24]:

$$G(z) = \frac{P_s(z)}{P_s(0)} = e^{\left( g_r(\lambda_s) \int_0^z P_p(z) dz - \alpha_s z \right)} \quad (2.10)$$

where  $P_s(z)$  is the signal power as a function of distance,  $g_r(\lambda_s)$  is the Raman gain coefficient for signal propagating at wavelength  $\lambda_s$  (shown in figure 2.2),  $\alpha_s$  is the fibre attenuation coefficient at the signal band. Figure 2.4 shows signal power profile as a function of distance (calculated from equation 2.10) for a distributed Raman amplified 100km SSMF span; where the total pumping power  $P_0$  was calibrated to achieve 0dB net signal gain ( $P_s(L) = P_s(0)$ ). The figure differentiates between the power profile of lossy (unpumped,  $P_0 = 0W$ ) span and distributed Raman amplified span (with different forward pumping ratios,  $r_f$ ). As  $r_f$  goes to zero (fully backward pumped span), the signal experiences an attenuation close to 0.2dB/km as it

propagates through the first 20km of the span (due to the low backward pumping power arriving to that region). As the signal propagates towards the end of the span the Raman pump power starts show full compensation of the fibre attenuation coefficient (around  $60\text{km} < z < 80\text{km}$ ) and gain factor around  $+0.5\text{dB/km}$  towards the last 10km of the span. On the other hand, fully forward pumped span ( $r_f=1$ ) would provide signals with gain factor of  $+0.5\text{dB/km}$  in the first 10km; this gain will fade away to reach the normal fibre attenuation factor by the end of the span. Equal powered counter-propagating Raman pumps ( $r_f=0.5$ ) causes the signals to be amplified equally on both ends of the span whilst it shows attenuation in the mid-region of the span (crossing the  $0\text{dB}$  gain at the midpoint of the span).

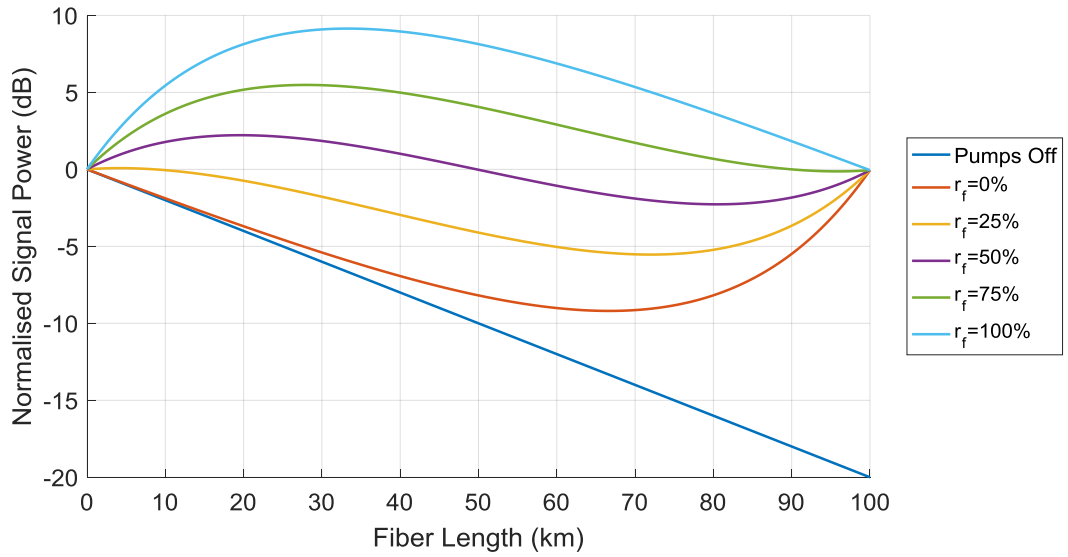


Figure 2.4: Signal power profile as a function of distance for 100km SSMF span.  $\alpha=0.2\text{dB/km}$ ,  $g_r=0.37\text{W/km}$ ,  $P_0$  was calibrated to have  $0\text{dB}$  net Raman gain.

### 2.2.1 Noise Accumulation in Discretely Amplified Systems

Optical amplifiers generate ASE noise across their amplification bandwidth due to quantum fluctuations, this noise is statistically random both in frequency and polarisation and will be superimposed over the amplified signals. The power spectral density of ASE noise generated in an EDFA (on both polarisations) can be analytically described as [23]:

$$I_{ASE} = \frac{P_{ASE}}{B_w} = 2n_{sp} h\nu (G-1) \quad (2.11)$$

where  $G$  is the gain of the EDFA,  $h$  is the Planck constant,  $\nu$  is the optical frequency,  $n_{sp}$  is the spontaneous emission factor, and  $B_w$  is the bandwidth at which the total power of ASE noise was measured. Ideally, the spontaneous emission factor ( $n_{sp}$ ) would be equal to 1, which can be realised when that amplifier is in the state of full population inversion, i.e. electrons in the

dopant ions are fully inverted to the metastable state due to the transferred pump energy. Noise Figure ( $NF$ ) is a common used parameter to identify the power spectral density of the generated ASE noise ( $I_{ASE}=h\nu[NF.G-1]$ ).  $NF$  can be identified as the ratio between the input  $SNR$  to the EDFA (assuming  $SNR$  at the input is limited by shot noise= $h\nu$ ) and the output  $SNR$  as [23]:

$$NF = \frac{SNR_{in}}{SNR_{out}} = \frac{I_s/(h\nu)}{GI_s/(h\nu + I_{ASE})} = \frac{2n_{sp}(G-1)}{G} + \frac{1}{G} \quad (2.12)$$

The minimum value of  $n_{sp}$  ( $=1$ ) suggests that the noise figure ( $NF$ ) is equal to 2 (3dB) when the net gain provided by the EDFA is large ( $G \gg 1$ ). The noise figure can drop below 2 ( $<3$ dB) as the gain of the EDFA approaches the transparency state ( $G \rightarrow 1$ ), assuming that the doped fibre length and pumping power were optimised [23]. Figure 2.5 shows the achievable noise figure as a function of the total gain provided by the EDFA with constant spontaneous emission factor ( $n_{sp}=1$ ). The figure shows that the noise figure of the EDFA does not change significantly when the total gain provided by the EDFA is higher than 15dB. On the other hand, the noise figure of the EDFA significantly degraded when the total gain is lower than 10dB.

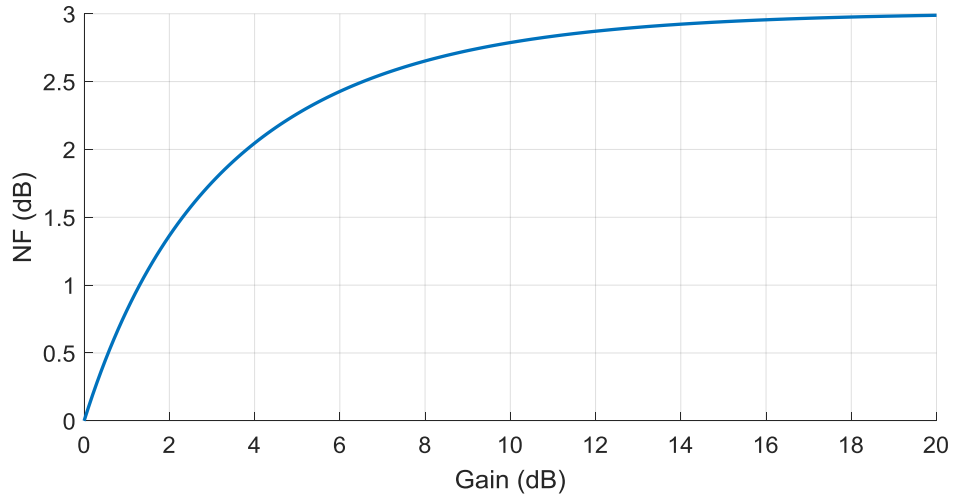


Figure 2.5: Noise Figure as a function of EDFA's gain.

In a uniform multi-span optical transmission system, an EDFA is deployed by the end of each fibre span to compensate for its total loss, thus the gain of EDFA can be written as:

$$G = \frac{1}{e^{(-\alpha L)}} = e^{(\alpha L)} \quad (2.13)$$

As a result, the total accumulated power spectral density of ASE noise along a system of  $N$  spans can be written as:

$$NI_{ASE} = 2Nn_{sp}h\nu(e^{\alpha L} - 1) \quad (2.14)$$

Figure 2.6 shows the total ASE power spectral density, as a function of the span length, accumulated along 2000km transmission system that deploys EDFAs (that compensate for the insertion loss of the span) with fixed ideal spontaneous emission factor ( $n_{sp}=1$ ). From the figure, it can be seen that reducing the span length (amplifier spacing or total gain per EDFA) along the system results in a reduction in the accumulated ASE noise to reach its minimum when the system deploys infinite number of EDFAs with infinitely small span length.

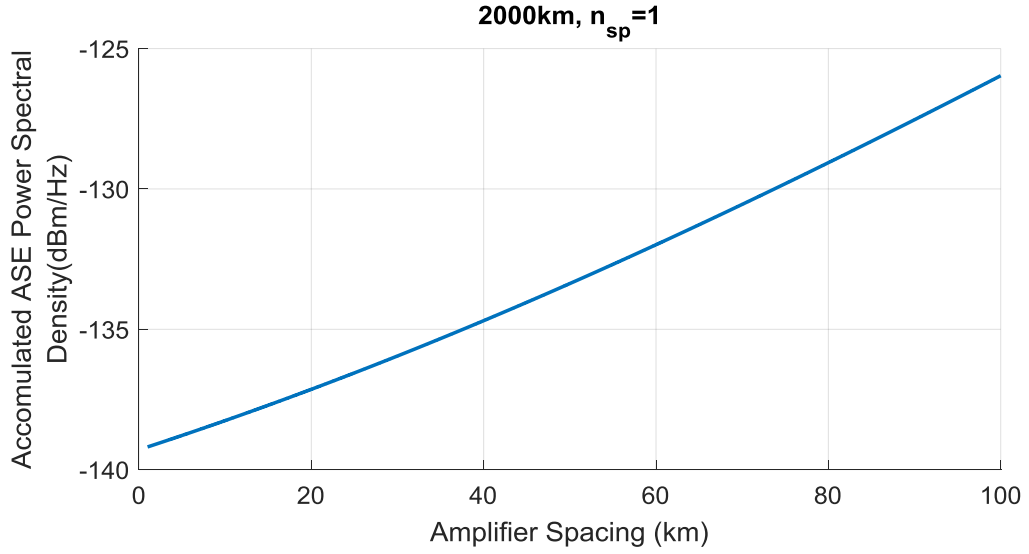


Figure 2.6: Total ASE power spectral density, as a function of amplifier spacing, for a 2000km transmission system that deploys EDFAs with fixed ideal spontaneous emission factor ( $n_{sp}=1$ ).

### 2.2.2 Noise Accumulation Distributed Raman Amplified Systems

Distributed Raman amplification, as the EDFA, generates ASE noise that degrades the SNR of optical signals propagating through it. The accumulation of the ASE noise in distributed Raman depends on the evolution of signal and pump power across the amplified span, a transmission system of  $N$  spans can be written (assuming 0dB net signal gain) as [24]:

$$NI_{ASE} = Nn_{sp}h\nu_s g_r \int_0^L \frac{P_p(z)}{G(z)} \partial z \quad (2.15)$$

where  $n_{sp}$  is the Raman spontaneous emission generation factor which can be described as [58]:

$$n_{sp} = 1 + \frac{1}{\exp[h\Delta\nu/(k_B T)] - 1} \quad (2.16)$$

where  $\Delta\nu$  is the frequency separation between the pump and signal,  $k_B$  is the Boltzmann constant,  $T$  is the temperature in kelvin. In a room temperature of 25°C, the Raman spontaneous emission generation factor  $n_{sp}$  can range around 1.14 (at the peak of Raman gain frequency response) [59]. Reducing the distributed Raman span length tends to reduce the signal power variation along the span, and an infinitely short span length reaches the state of ideal lossless distributed Raman system where the signals maintain a constant power as they propagate along the fibre. Such quasi-lossless transmission links can also be realised at sensible span lengths (25km,  $r_f=0.5$ , [59]) by deploying higher order Raman pumping, where the  $n^{\text{th}}$  order Raman pump is spectrally located  $n \times 100\text{nm}$  below the signal band to be amplified [59,60]. The power spectral density of ASE generated in such a quasi-lossless Raman link (total length= $L_{\text{Total}}$ ) can be written as [61]:

$$I_{\text{ASE}} = n_{sp} \alpha N L h \nu_s \quad (2.17)$$

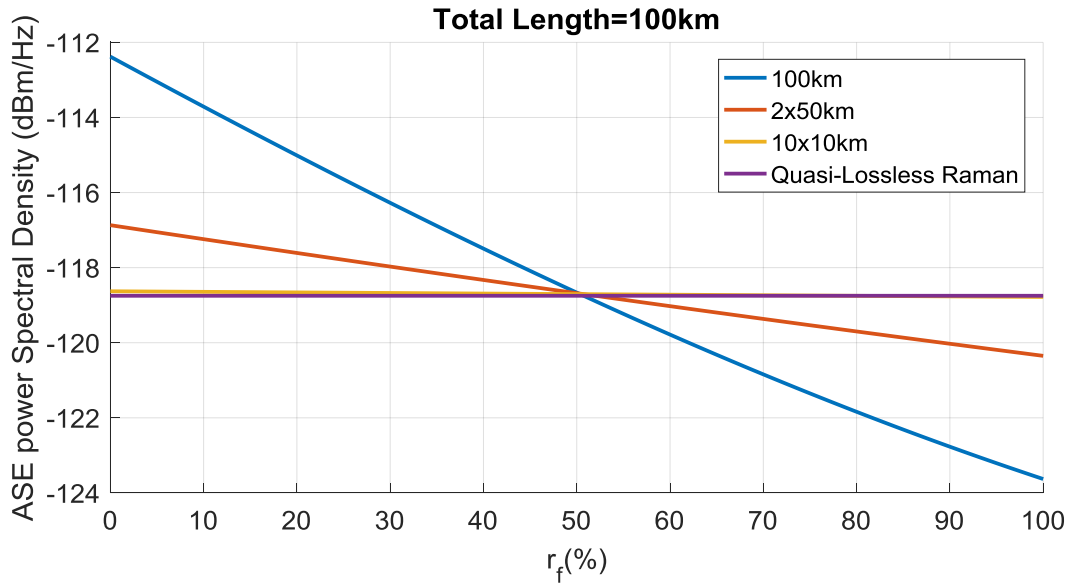


Figure 2.7: ASE power spectral density (accumulated along a 100km link) as a function of the forward pumping ratio for various span lengths (100km, 2x50km, 10x10km, and quasi-lossless Raman).  $\alpha=0.2\text{dB/km}$ ,  $g_{\text{r}}(\text{peak})=0.37\text{W/m}$ ,  $n_{\text{Rm}}=1.14$ .

Figure 2.7 shows the ASE power spectral density (accumulated along a 100km link) as a function of the forward pumping ratio for various span lengths (100km, 2x50km, 10x10km, and quasi-lossless Raman). The curves in figure 2.7 were calculated from equation 2.15 (for non- quasi-lossless) and 2.17 (for quasi-lossless Raman), the parameters are displayed in the caption of the figure. It can be seen from figure 2.7 that the power spectral density of ASE noise generated in distributed Raman link is highly dependent on the span length and the forward pumping ratio ( $r_f$ ). For example, the ASE power spectral density accumulated over a

100km span shows 11.2dB variance as a function of the forward pumping ratio ( $r_f$ ) due to the signal power variation along the span ( $G(z)$ , which can be seen in figure 2.4). Deploying a shorter span length results a reduction in the signal power variation along the transmission link, hence the reduction in the variance ASE noise (3.4dB for 2x50km, and 0.15dB for 10x10km) as a function of the forward pumping ratio ( $r_f$ ). Figure 2.7 shows that by shortening the span length, the total ASE noise accumulated along the distributed Raman system converges to match the ASE noise accumulated in ideal quasi-lossless distributed Raman (described by equation 2.17).

### 2.3 Optical Fibre Communication Systems

Figure 2.8 shows the physical layer of a point-to-point optical fibre communication link. The link delivers the modulated optical signals generated from the transmitter to the receiver, the system can deploy discrete optical amplifiers or distributed Raman amplification.

IQ modulation based optical transmitters and coherent receivers are essential to accommodate the increasing capacity demand from optical transmission systems. IQ modulator-based transmitters can carry higher data rates by exploiting multi-level modulation formats carried on the four dimensions available by the SSMF based transmission medium (amplitude, phase, and both optical polarisations).  $M$ -points Dual-Polarisation Quadrature Amplitude Modulation ( $M$ -ary DP-QAM) is one of many modulation formats available to carry digital data on an analog signals, where the higher number of constellation points increase the capacity of each transmitted symbol by a factor of  $2\log_2(M)$  when compared to the classical On-Off keying modulation. Coherent receivers enable the detection of dual polarisation IQ modulated optical signals and the compensation of various distortions generated from propagation through optical fibre, in the digital domain.

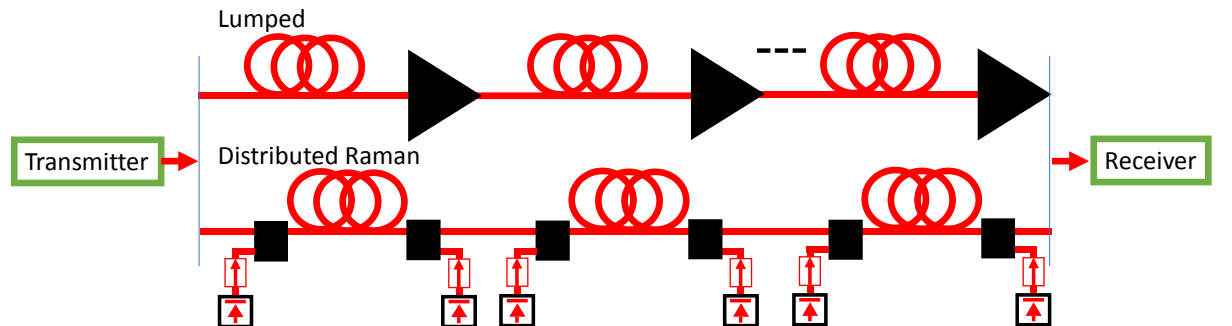


Figure 2.8: Optical fibre communication system.

### 2.3.1 Optical Transmitter

$M$ -ary QAM [62] assigns binary digital bits (symbol) to a constellation of contain  $M$  points. The spectral efficiency  $\eta_s$  (in bps/Hz) of  $M$ -ary PM-QAM can be written as:

$$\eta_s = 2 \frac{R}{B_w} \log_2(M) \quad (2.18)$$

where  $R$  is the baud rate (symbol rate) of the modulated signal,  $B_w$  is the bandwidth of the optical signal. Figure 2.9 shows a WDM transmitter configuration that generates  $N$ -channels each modulated by an IQ modulator-based transmitter module. A set of CW lasers spectrally located on wavelength grid ( $\lambda_1, \lambda_2, \dots, \lambda_N$ ) act as carriers for different WDM channels. Each one of the lasers is injected into a transmitter module where it will be split into two orthogonal polarisations (x and y), then each polarisation is fed into an IQ modulator that translates two RF waveforms (one for each quadrature) onto single polarisation optical field. The optical transmitter module is supplied by a stream of digital information bits that pass through an encoder that is responsible for the addition of Forward Error Correction (FEC) [63] bits, those extra added bits will help correcting bit errors at the receivers decoder to establish resilient communication system. The digital modulator is responsible for the conversion of digital bit stream to a four analog RF signals (to cover the four dimensions of the modulation,  $I_x, Q_x, I_y, Q_y$ ) that represent dual polarisation constellation. The digital modulator can also enforce RF pulse shaping [62] to construct spectrally efficient modulation and minimise inter-channel interference in ultra-dense WDM systems. Mach–Zehnder Modulators (MZM) [64] are used to convert the four RF signals into the optical domain by modulating the laser. The MZM on each arm of the IQ modulator utilises the electro-absorption of the MZM waveguide which changes the refractive index of the waveguide when external electrical voltage is applied [64]; the change in refractive index results a phase change of the optical field passing through the two paths inside the MZM which will later add up constructively or destructively to generate each quadrature of the optical signal ( $I_x, Q_x, I_y, Q_y$ ). The second MZM (that modulates  $Q_x$  and  $Q_y$ ) in the IQ modulator is followed by a Phase Shifter to convert the modulated light into the correct quadrature dimension. Finally, the two quadratures of modulated light are combined to create single polarisation QAM. A Polarisation Beam Combiner (PBC) combines the two polarised and modulated optical fields to form dual polarisation modulated signal.

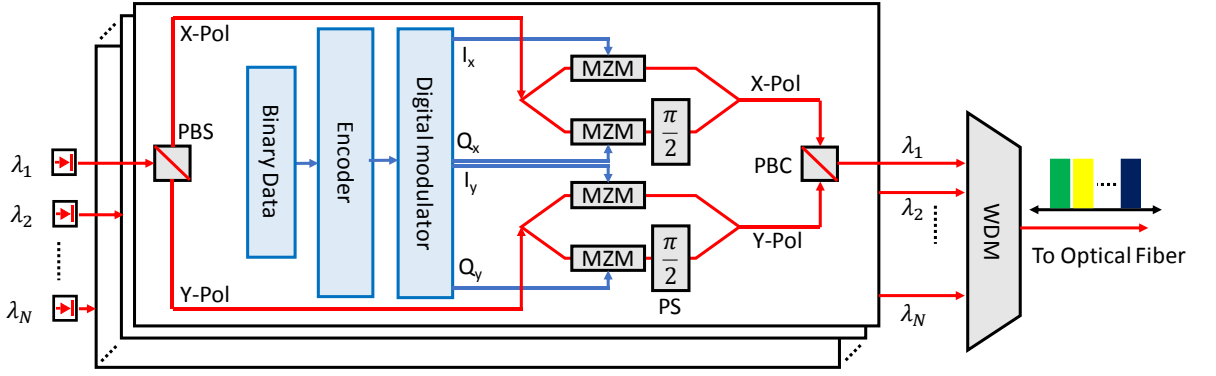


Figure 2.9: Optical transmitter of  $N$  WDM channels. PBS: Polarisation Beam Splitter, MZM: Mach-Zehnder modulator, PS: Phase Shifter, PBC: Polarisation Beam Combiner, WDM: Wavelength Division Multiplexer.

### 2.3.2 Coherent Optical Receivers

Coherent detection ensures the detection of the complex envelope of the optical field with linear transformation of both amplitude and phase of the optical field on both polarisation, this detection technique uses a local oscillator laser that beats with the modulated channel to be detected [65]. Analog to Digital Converters (ADC) [66] in coherent receivers allow the implementation of CMOS based DSP to compensate for the optical fibre dispersive impairments (Chromatic dispersion and PMD) in the electrical domain. Figure 3.8 shows the basic building blocks of coherent receiver that is capable of receiving dual polarisation modulated optical signals.

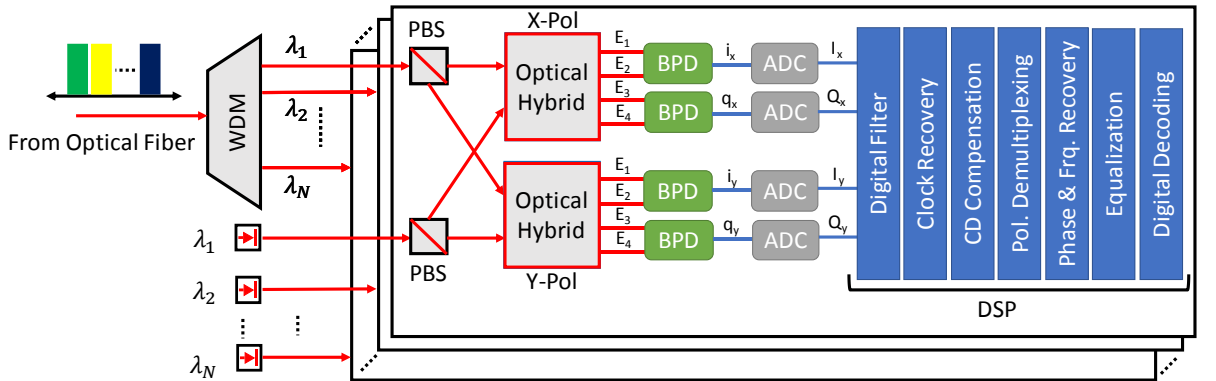


Figure 2.10: Coherent optical receiver. BPD: Balanced Photo-Detector, ADC: Analog to Digital Converter.

The coherent optical receivers use local oscillator laser spectrally located on the centre frequency of the modulated WDM channel to be detected. Both the signal and the local oscillator are split into the basic two polarisation modes (x and y) using Polarisation Beam Splitters (PBS), then the polarised signal and local oscillator are fed into an optical hybrid that is used to interfere both optical fields to generate four fields (as shown in the figure) that can be written as [65]:



$$\begin{bmatrix} E_1 \\ E_2 \\ E_3 \\ E_4 \end{bmatrix} = \frac{1}{2} \begin{bmatrix} E_{LO}(t) + E_{sig}(t) \\ E_{LO}(t) + iE_{sig}(t) \\ E_{LO}(t) - E_{sig}(t) \\ E_{LO}(t) - iE_{sig}(t) \end{bmatrix} \quad (2.19)$$

where  $E_{sig}$  is the signal optical field and  $E_{LO}$  is the optical field of the local oscillator. A Balanced Photo-Detector (BPD) is used after the hybrid to convert the optical field to an electrical RF waveform which can be written as [65]:

$$\begin{aligned} i &= R \left[ E_1(t) E_1^*(t) - E_2(t) E_2^*(t) \right] \\ &= R \sqrt{P_{sig} P_{LO}} u_{IQ}(t) \cos \left[ (\omega_{sig} - \omega_{LO})t + (\theta_{sig} - \theta_{LO})t + \theta_{IQ}(t) \right] \\ q &= R \left[ E_3(t) E_3^*(t) - E_4(t) E_4^*(t) \right] \\ &= R \sqrt{P_{sig} P_{LO}} u_{IQ}(t) \sin \left[ (\omega_{sig} - \omega_{LO})t + (\theta_{sig} - \theta_{LO})t + \theta_{IQ}(t) \right] \end{aligned} \quad (2.20)$$

Where  $R$  is the responsivity of the BPDs,  $P_{sig}$  is the signal power,  $P_{LO}$  is the local oscillator power,  $u_{IQ}(t)$  is the IQ signal optical field strength,  $(\omega_{sig} - \omega_{LO})$  is the frequency shift between signal and local oscillator,  $(\theta_{sig} - \theta_{LO})$  is the phase shift between signal and local oscillator,  $\theta_{IQ}(t)$  is the IQ phase of the optical signal field. The electrical RF waveforms ( $i_{x,y}$  and  $q_{x,y}$ ) are digitised using ADCs so that the detected field would be compatible to perform DSP.

The DSP starts with a digital low pass filter that eliminates the out-of-band noise and residuals from neighbouring WDM channels. The next stage of DSP is used to compensate for Chromatic dispersion by using Fast Fourier Transform (FFT) to convert a block of samples from the time domain to the frequency domain [67], then apply a phase correction ( $H(f)$ ) equivalent to the total dispersion accumulated along the system:

$$H(\omega, NL) = e^{\left[ -iD_c \frac{\lambda^2}{2\pi c} \frac{\omega^2}{2} NL + iS \left( \frac{\lambda^2}{2\pi c} \right)^2 \frac{\omega^3}{6} NL \right]} \quad (2.21)$$

The signal block is converted back from frequency domain to time domain using inverse FFT (iFFT). Clock recovery is used to interpolate the clock frequency of the ADC [68] [43]. Following that, a DSP stage is used to demultiplex and normalise the dual polarisation fields to compensate for polarisation random rotation due to PMD effects [13]. Finally, before decoding the QAM constellation to binary word, a phase and frequency recovery stage is used to compensate for the phase and frequency mismatch between the laser from the transmitter and the local oscillator laser at the receiver.

### 2.3.3 Optical Transmission Performance Merits

The true performance metric of optical transmission system is the Bit Error Rate (BER) of the demodulated signals. Pre-FEC BER gives an indication to the system designer to apply the appropriate coding rate (extra FEC overhead bits applied by the transmitter) to reduce the post FEC BER to form reliable communication channel. For example, a pre-FEC BER of  $3.15 \times 10^{-3}$  can be reduced to  $1 \times 10^{-15}$  after enforcing Hard-Decision Reed Solomon coding (HD-RS(255,239)) that has 6.69% coding overhead [69]. Pre-FEC BER of  $M$ -ary QAM can be identified as a function of SNR (per polarisation) as [70] (assuming Additive White Gaussian Noise, AWGN, channel):

$$BER = \frac{2 \left( 1 - \frac{1}{\sqrt{M}} \right)}{\log_2(M)} \operatorname{erfc} \left[ \sqrt{\frac{3 \log_2(M)}{2(M-1)}} SNR \right] \quad (2.22)$$

The  $Q$  factor of the received signal is also another performance metric and can be calculated from BER as follows:

$$Q = \frac{1}{2} \operatorname{erfc}^{-1} \left( \frac{BER}{\sqrt{2}} \right) \quad (2.23)$$

Monte-Carlo BER calculation requires an observation period that would have at least 100-bit errors, the observation period (or number of received symbols) can increase significantly for low BER systems. Error Vector Magnitude (EVM) is often used in numerical simulations and experimental demonstrations to quantify the performance of modulated signals, especially in error free systems. EVM is defined as the normalised average of vectoral distance between the received constellation point ( $S_n$ ) and the ideal constellation point ( $S_{0,n}$ ):

$$EVM = \sqrt{\frac{\frac{1}{N} \sum_{n=1}^N |S_n - S_{0,n}|^2}{\frac{1}{N} \sum_{n=1}^N |S_{0,n}|^2}} \quad (2.24)$$

EVM can relate to SNR factor as:

$$SNR = \frac{1}{(EVM)^2} \quad (2.25)$$

Equations 2.21-2.24 shows a correlation between all the performance metrics of optical transmission systems. A strong correlation between BER and EVM have been established in literature [71] which makes EVM as valid of a performance merit as BER.

## 2.4 Optical Fibre Nonlinearity Compensation Techniques

As mentioned before, the nonlinear Kerr effects cause energy conversion from one signal frequency to another, and results in a random interference that limits the propagating signal's SNR [46,47,72–75]. Many Kerr nonlinearity compensation techniques have been proposed and studied, such as: Digital Back Propagation (DBP) [14,15], Optical Phase Conjugation (OPC) [16], Optical Back Propagation (OBP) [17], Phase Conjugated Twin Wave (PCTW) [18], Phase Conjugated Pilot (PCP) coding [19].

DBP is a nonlinearity compensation technique that re-emulates the propagation of signal optical field propagation through the optical fibre and reverse its nonlinearities (by numerically solving the Nonlinear Schrodinger Equation, NLSE). DBP can be implemented in the transmitter [14], in the receiver [15], or both [76]. Performing DBP on a single detected channel from a WDM transmission system cannot fully recover the nonlinear Kerr noise [77] since the nonlinear inter-channel interference from neighbouring channels can be much larger than the nonlinear intra-channel interference which is recovered by the single channel DBP. To achieve full nonlinearity compensation, the receiver must have: coherent detection, full awareness of the link properties, sufficient sampling rate (or array of coherent receivers) to detect the full WDM signal field, and computational abilities to perform full field DBP [78].

OPC is an all-optical signal processing technique that performs spectral inversion (phase conjugation) which may compensate for the nonlinear interference accumulated along the transmission fibre [16]. OPC provides transparent (polarisation and modulation format independent) dispersion and nonlinear interference compensation technique. A full nonlinear noise compensation can be achieved by an OPC when deployed in quasi-lossless distributed Raman amplified system. A partial nonlinearity compensation (only intra-channel nonlinear noise) can be achieved when deploying mid-link OPC in discretely amplified transmission system [25–27,29,79] [X12]. Raman distributed amplification, with a short span length, and flattened dispersion slope fibre spans [80] can provide the power profile and dispersion symmetry required to achieve full nonlinearity compensation among optical modulated signals. The concept of OPC has been used in OBP by locating the OPC at the receiver side followed by HNLF and Dispersion Compensating Fibre (DCF) [17]. PCTW is a nonlinearity compensation technique that transmits multiplexed optical signal and its conjugate on two dimensions whether it is polarisation [18], frequency [81], or time [82]; and the receiver a simple coherent super-imposition of the signal and its conjugate may cancel the nonlinear Kerr effects [18] (assuming nonlinear effects are identical on the two dimensions used). PCTW is

not as computationally demanding as DBP, but it reduces the spectral efficiency of the system as it transmits redundant conjugated signals.

In this thesis, I will restrict my study on DBP and OPC assisted systems and their capabilities of compensating the nonlinear noise generated along long-haul optical fibre transmission systems.

### 2.4.1 Digital Backpropagation

The evolution of optical field along the optical fibre transmission system depends on the fibre parameters, power evolution, and the bandwidth of modulated signals. The propagation of dual polarisation optical signal in random birefringence optical fibre is governed by the NLSE (which is a generalised equation of the inhomogeneous nonlinear equation presented in equation 2.6):

$$\begin{aligned} \frac{\partial \vec{E}(z)}{\partial z} = & -\frac{1}{2}\alpha \vec{E}(z) \\ & +\beta' \frac{\partial \vec{E}(z)}{\partial t} -i \frac{\beta''}{2} \frac{\partial^2 \vec{E}(z)}{\partial t^2} + \frac{\beta'''}{6} \frac{\partial^3 \vec{E}(z)}{\partial t^3} + \dots + i(i)^m \frac{\beta^{(m)}}{m!} \frac{\partial^{(m)} \vec{E}(z)}{\partial t^{(m)}} \\ & +i \frac{8}{9} \gamma_0 \vec{E}(z) |\vec{E}(z)|^2 \end{aligned} \quad (2.26)$$

Where  $\vec{E}(z)$  is the optical field (full spectrum) vector (including both polarisations),  $\gamma_0$  is the intrinsic nonlinear factor of the optical fibre that can be defined as ( $\gamma_0=96\pi^3\chi/[cn^2\lambda A_{eff}]$ , [45]). This equation can be numerically solved through the discretisation of the optical fibre length to evaluate the numerical integration of the differential equation. The accuracy of the numerical integration depends on the number of steps per span used in the process.

Figure 2.11 shows a DBP assisted optical fibre transmission system. The figure shows that DBP is applied to the coherently received optical field in the digital domain, and then the conventional DSP is applied to get the final decoded bits. To perform DBP, the receiver should divide the transmission system into short steps of fibre ( $L_{step}$ ) so that the solution of equation 2.26 can be simplified to [83]:

$$\vec{E}(z+h,t) = iFFT \left[ FFT \left[ \vec{E}(z,t) \right] H(\omega, L_{step}) \right] e^{\left[ \frac{\alpha}{2} L_{step} - i \frac{8}{9} \gamma L_{step} \left( |E_x(z,t)|^2 + |E_y(z,t)|^2 \right) \right]} \quad (2.27)$$

This process is called Split Step Fast Fourier Transform that is used to solve the NLSE. The *FFT* can convert the signal samples from the time domain into the frequency domain, and *iFFT* converts the signal back to the time domain; this process is used to compensate for the accumulated dispersion in the given fibre step (defined in equation 2.21). The exponent in

equation 2.27 is used as a correction factor optical field amplitude and nonlinear phase shift compensating for the nonlinear Kerr effects in the fibre step. The negative value of nonlinear factor ( $\gamma_0$ ) indicates a reverse phase shift to recover the Kerr effects occurred during the forward propagation. If the transmission link uses distributed Raman amplification, then the attenuation factor  $\alpha$  (in equation 2.26) should be replaced by the power profile of the signal  $\log(\sqrt{G(z)})$  (as defined in equation 2.11).

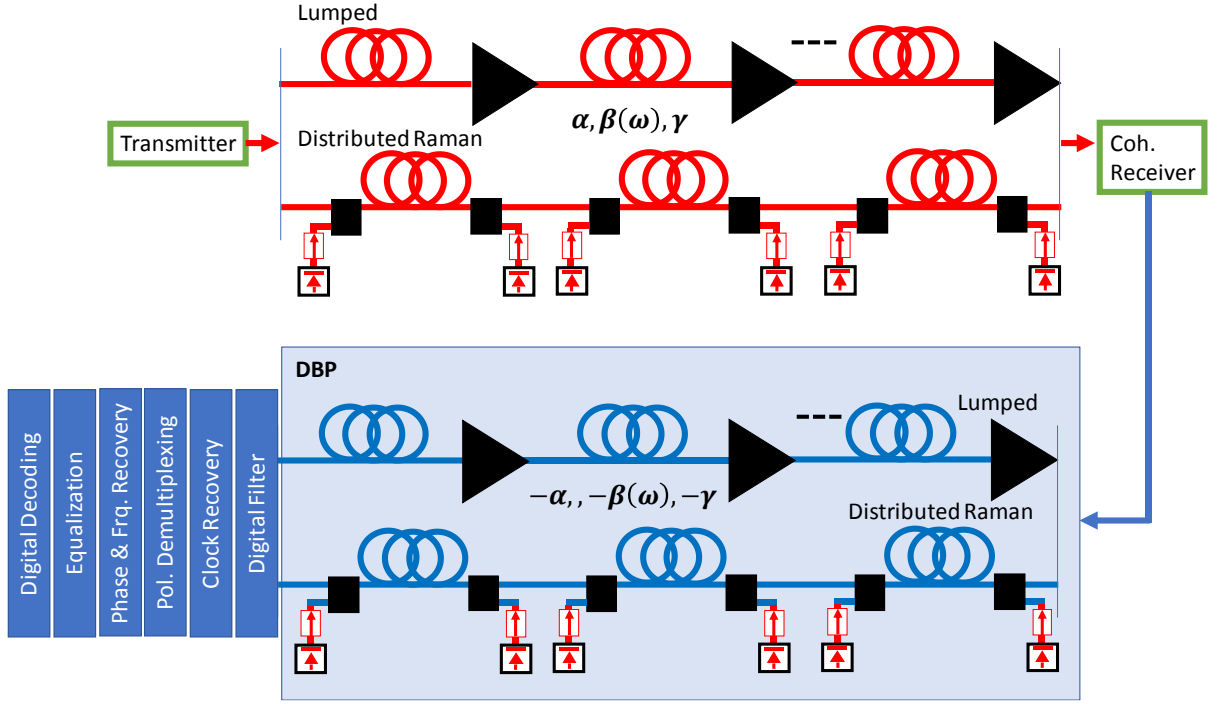


Figure 2.11: DBP assisted optical fibre transmission system.

Figure 2.11 shows the operations performed in DBP when using Split Step FFT, where the optical link is divided  $NL/L_{step}$  steps, each of length  $L_{step}$ . The NLSE solution over  $L_{step}$  consists of four processes: performing dispersion compensation for  $L_{step}/2$ , nonlinear phase correction for  $L_{step}$ , dispersion compensation for  $L_{step}/2$ , and signal power correction. As mentioned before, DBP requires the receiver to have full access to the coherent received signals from all the channels propagating through the system (which is called in literature as full field DBP [58]). Otherwise DBP would fully recover the Kerr nonlinear effects within the detected bandwidth while ignoring the nonlinear Kerr effects that originate from the other undetected WDM channels, which causes a limited capability of nonlinearity compensation.

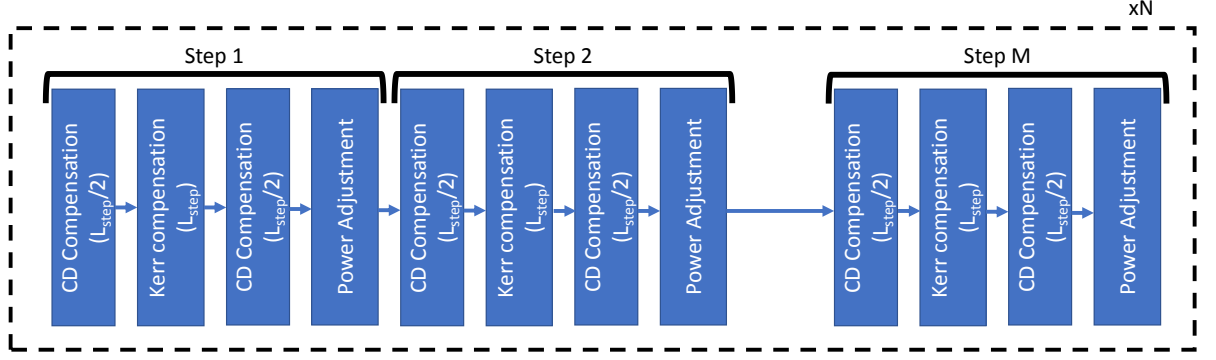


Figure 2.12: DBP using split-step Fourier method.

## 2.4.2 Optical Phase Conjugation

OPC performs an all-optical spectral inversion to generate conjugated signals. As FOPA, fibre-based OPC uses the nonlinear susceptibility properties of the fibre to create conjugated copy of the modulated signals, which can be realised using the high pumping power and HNLF. As the signal optical field ( $E_{Signal}$ ) propagates with high power pump(s) ( $E_{Pump1}$   $E_{Pump2}$ ) through the HNLF, an idler ( $E_{Idler}$ ) (phase conjugated copy of the signal) will be generated along the HNLF and can be theoretically written as:

$$\begin{aligned} E_{Idler} &= \eta E_{Pump1} E_{Pump2} E_{Signal}^* \\ \omega_{Idler} &= \omega_{Pump1} + \omega_{Pump2} - \omega_{Signal} \end{aligned} \quad (2.28)$$

where the nonlinear interaction between the signal ( $E_{Signal}$ ) and pumps ( $E_{Pump1}$  and  $E_{Pump2}$ ) (single pump, [ $\omega_{Pump1} = \omega_{Pump2}$ ]; or dual pump [ $\omega_{Pump1} \neq \omega_{Pump2}$ ]) generates the conjugated optical field ( $E_{Idler}$ ), with an implied frequency shift of ( $\omega_{Pump1} + \omega_{Pump2} - \omega_{Signal}$ ). The nonlinear Kerr generation efficiency ( $\eta$ ), in equation 2.28, can be found by solving the coupled inhomogeneous equations (assuming lossless HNLF and no pump depletion):

$$\begin{aligned} \frac{\partial E_{Idler}}{\partial z} &= i\gamma \left[ \begin{aligned} &|E_{Idler}|^2 E_{Idler} \\ &+ 2E_{Idler} \left( |E_{Pump1}|^2 + |E_{Pump2}|^2 + |E_{Signal}|^2 \right) \\ &+ 2E_{Pump1} E_{Pump2} E_{Signal}^* \exp(i\Delta\beta z) \end{aligned} \right] \\ \frac{\partial E_{Signal}}{\partial z} &= i\gamma \left[ \begin{aligned} &|E_{Signal}|^2 E_{Signal} \\ &+ 2E_{Signal} \left( |E_{Pump1}|^2 + |E_{Pump2}|^2 + |E_{Idler}|^2 \right) \\ &+ 2E_{Pump1} E_{Pump2} E_{Idler}^* \exp(i\Delta\beta z) \end{aligned} \right] \end{aligned} \quad (2.29)$$

The equation shows the nonlinear interactions among wave with itself (SPM, first term in each equation), among the two waves (XPM, second term in each equation), and among the three waves (FWM, third term in each equation). Equation 2.29 also shows that OPC can also

provide amplification to both the original signals as well as the conjugated signal (when  $2\gamma E_{Pump1}E_{Pump2}\exp(i\Delta\beta z) > 1$ ), the total gain and gain spectral properties can be found by solving the coupled inhomogeneous equations [10]. OPC can use other types of highly nonlinear mediums such as: Semiconductor Optical Amplifiers (SOA) [84] and Periodically Poled Lithium-Niobate (PPLN) waveguides [85]. OPCs filter the conjugated signals at the output of the HNLF to drop the remains of the high-power pump(s) and the original optical input signals, figure 2.13 shows the basic concept of the OPC that uses either single or dual pump.

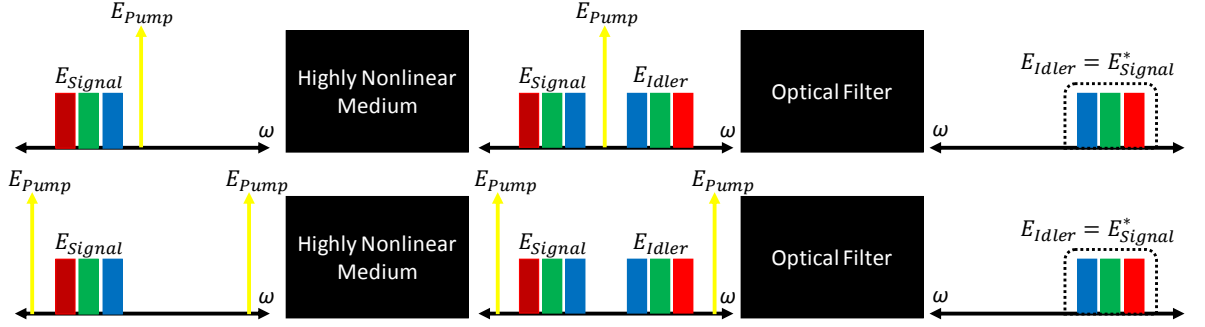


Figure 2.13: The concept of OPC.

OPCs should support the conjugation of dual polarisation optical field (polarisation insensitive OPCs). In single pump OPC, polarisation diversity loop is one of the solutions to achieve polarisation insensitive conjugation [86,87]. On the other hand, dual pump OPC can avoid the use of polarisation diversity loop by injecting two perpendicularly polarised pumps [88].

When deploying an OPC in transmission systems, the signal propagation along the first half of the link would be governed by the equation 2.26, at the mid-link point, all the signal would be conjugated through the OPC ( $E(z) \rightarrow E^*(z)$ ), so that the conjugates propagating through the second half of the link can be described by:

$$\begin{aligned} \frac{\partial \bar{E}(z)}{\partial z} = & -\frac{1}{2} \alpha \bar{E}(z) \\ & + \beta' \frac{\partial \bar{E}(z)}{\partial t} + i \frac{\beta''}{2} \frac{\partial^2 \bar{E}(z)}{\partial t^2} + \frac{\beta'''}{6} \frac{\partial^3 \bar{E}(z)}{\partial t^3} + \dots - i (i)^m \frac{\beta^{(m)}}{m!} \frac{\partial^{(m)} \bar{E}(z)}{\partial t^{(m)}} \\ & - i \frac{8}{9} \gamma_0 \bar{E}(z) |\bar{E}(z)|^2 \end{aligned} \quad (2.30)$$

From equation 2.26 and 2.30, we can see that the propagation of conjugated signals through the second half of the link would result a destructive accumulation of dispersion coefficients (even ordered,  $\beta''$ ,  $\beta''''$ , ...) which indicates the ability to compensate chromatic dispersion. Also, it can be seen that the accumulation of dispersion slope (odd order dispersion) cannot be compensated in OPC assisted transmission system. Deploying OPC in optical transmission systems can also provide nonlinearity compensation due to the fact that the conjugation has

converted the positive nonlinear fibre factor into a negative. But, the efficiency of nonlinearity compensation achieved by the OPC is highly dependent on the signal power profile along the transmission system. In the next chapter, I will discuss in detail on the modelling and quantification of the compensation efficiency achieved by the OPC when deployed in various optical fibre transmission systems.





# Chapter 3 : Optical Nonlinear Kerr Effects in Optical Transmission Systems

Contributions: [X4], [X15], and [X18].

The analytical modelling of nonlinear Kerr accumulation (SPM, XPM, and FWM) in transmission systems is important to analyse the SNR degradation of optical modulated signal propagating through these transmission systems. In literature, several closed form analytical models have been reported to characterise the accumulation of the nonlinear Kerr effects; these models were derived from the inhomogeneous equation (equation 2.6) to model the generation of nonlinear optical products. The analytical solution presented in [44] has described the power of nonlinear Kerr products generated by the end of a single span of optical fibre; the analytical model has formulated the relationship between the resulting nonlinear Kerr power and the power of mixing signals along with the physical properties of the fibre (length, attenuation constant, dispersion, and nonlinear factor) [45]. Discretely amplified multi-span optical transmission system (lumped system) impose signal power profile periodicity defined by the separation between EDFAs. The signal power profile periodicity and dispersion accumulation along the system result the power oscillation of the nonlinear Kerr product (as a function of phase mismatching  $\Delta\beta$ ); this oscillation in nonlinear Kerr product power was analytically formulated [89–91] and experimentally verified [92] to show that the oscillation frequency depends on the dispersion of the fibre and the number of the spans in the system. The dispersion of the optical fibre can have a huge impact on the nonlinear Kerr power behaviour, for example: a low dispersion accumulation enhances the bandwidth of highly efficient nonlinear Kerr interactions [45]. In-line dispersion compensation (using DCF) can be used to change the dispersion accumulation map, the deployment of the DCFs in the system can be in a uniform manner (DCF per span) or nonuniform manner [93–95]; the nonlinear Kerr products generated from such systems can still be described analytically by finding the coherent summation of the

Kerr fields generated from each fibre span [96,97]. In distributed Raman amplification, the non-constant exponential signal power variation ( $G(z)$ , in equation 2.10) makes the integration of the inhomogeneous equation harder to solve (in a closed form), so, a numerical integration (over fibre length) is required to describe the nonlinear Kerr effects [98].

The deployment of mid-link OPC (or multi-OPC) in optical transmission systems may compensate for the nonlinear Kerr interference among signals propagating through the system; the level of compensation depends on the symmetry of dispersion and power profile in reference to the point of conjugation [99]. The analytical description of the nonlinear Kerr power generated by the end of discretely amplified optical transmission system with mid-link OPC was described in [100] and I have experimentally verified it [X15]. Distributed Raman amplification entail a dynamic signal power profile identified by the pumping scheme of each span along the system, which may provide the necessary signal power profile symmetry (along the link) to achieve significant nonlinear Kerr compensation when deploying OPC. Although mid-link OPC can achieve full deterministic nonlinearity compensation, transmission system will still be limited by the non-deterministic nonlinearities which can be minimised by deploying symmetrically located multi-OPC along the system. The conditions of ideal nonlinearity compensation (using mid-link OPC) were identified [101], but an analytical descriptions of nonlinear Kerr power generated in a generic distributed Raman with single or multi-OPC systems were never identified.

In this chapter, I will recall the analytical derivation of the nonlinear Kerr power generated in dispersion managed and unmanaged lumped optical transmission system. I will rewrite the numerical integration [98] that identifies the nonlinear Kerr product power generated in distributed Raman systems, then I will propose and validate (both by simulation and experimental results) an analytical closed form approximation that can describe nonlinear Kerr product power generated in distributed Raman systems (by considering piecewise power profile approximation). Then, I will rederive the analytical description [100] of nonlinear Kerr product power to a generic closed form that can describe the nonlinearities generated in dispersion managed or unmanaged lumped system that deploys single or multi-OPC; this closed form will be verified both by simulation and experimental results. Finally, I will report on an analytical description of nonlinear Kerr product power for a generic distributed Raman transmission system that deploys single or multi-OPC; this analytical equation will be analysed and verified (with simulation results and experimental results) for distributed Raman systems that deploy 1<sup>st</sup> order pumping.

### 3.1 Nonlinear Kerr Effects in Discretely Amplified Transmission Systems

The analytical modelling of nonlinear Kerr products can be realised by solving the inhomogeneous equation (equation 2.6), where it describes the evolution of the optical field (spectrally located at  $\omega_F$ ) which coincides with the optical field generation from the nonlinear Kerr interaction between up to three other optical waves ( $\omega_i$ ,  $\omega_j$ , and  $\omega_k$ ), which results (recalling from equation 2.7) [44]:

$$E_F(z) = i \frac{\gamma_0 D}{3} E_q(0) E_r(0) E_s^*(0) e^{\left(\frac{\alpha}{2} z\right)} \left[ \frac{e^{[-\alpha + i\Delta\beta]z} - 1}{-\alpha + i\Delta\beta} \right] \quad (3.1)$$

where  $\gamma_0$  is the intrinsic nonlinear coefficient of the optical fibre ( $\gamma_0 = 96\pi^3 \chi / [cn^2 \lambda A_{eff}]$ , [45]). And the resulting nonlinear Kerr product power can be written as [44,45]:

$$P_F(z) = \left( \frac{D\gamma_0}{3} \right)^2 P_q P_r P_s \left[ \frac{\alpha^2 e^{(-\alpha z)} z_{eff}^2}{\alpha^2 + \Delta\beta^2} \right] \left[ 1 + \frac{4e^{(-\alpha z)} \sin^2(\Delta\beta z / 2)}{(1 - e^{(-\alpha z)})^2} \right] \quad (3.2)$$

where  $P_{i,j,k}$  is the power of the mixing waves  $i, j$ , and  $k$  launched into the fibre,  $z_{eff}$  is the effective fibre length ( $z_{eff} = [1 - \exp(-\alpha z)] / \alpha$ ). Equation 3.2 shows that the nonlinear Kerr product power scales quadratically with the nonlinear factor of the fibre ( $\gamma_0$ ), and the product of optical powers of the mixing waves ( $q, r, s$ ). The first squared bracket in equation 3.2 shows that the Kerr nonlinear product depends on the fibre attenuation constant, the effective length of the fibre, and the phase mismatching factor. The third term represents the coherent oscillation of the Kerr nonlinear products because of the phase mismatching accumulation during the propagation through the optical fibre.

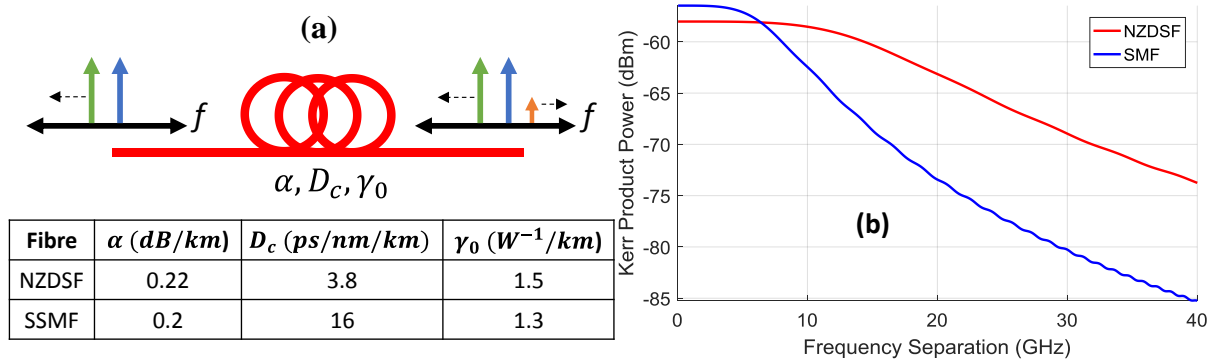


Figure 3.1: (a) 100km span optical system transmitting two CW lasers (0dBm each, spectrally located at 1555nm) through Non-Zero-Dispersion Fibre (NZDSF) or Standard Single Mode Fibre (SSMF). (b) The nonlinear Kerr product power as a function of frequency separation between the mixing CWs. [X1]

Figure 3.1 (a) shows a single span (100km) system that transmits two CW lasers (0dBm each, spectrally located at 1555nm) propagating through two types of optical fibres: Non-Zero

Dispersion Shifted Fibre (NZDSF) and SSMF. The spectral separation between two CW lasers was changed to observe the effect of phase mismatching on the power Kerr nonlinear product generated by the end of the fibre; as shown in figure 3.1 (b). The figure shows that nonlinear product power has the highest value at strongly phase matched region (low frequency separation,  $\Delta\beta \rightarrow 0$ ) for both types of fibre. As the frequency separation between CW lasers increases, the growth of phase mismatching ( $\Delta\beta$ , defined in equation (2.8)) between the CW lasers cause a degradation in the nonlinear product power which can be analytically concluded from first squared brackets in equation 3.2. At weakly phase matched mixing components (large frequency separation,  $\Delta\beta \gg 0$ ), the nonlinear product power generated in NZDSF show lower roll-off when compared to the product generated in SSMF; this is a result of the lower accumulated dispersion in NZDSF. A minor oscillation in the nonlinear product power can be observed at weakly phase matched region; this oscillation is generated from the last term in equation 3.2.

In a multi span system, an optical amplifier (often EDFA) is located at the end of each span to compensate for the signal power loss in the fibre span. In a symmetric uniform optical transmission system, all the spans of the system have the same length, and accordingly, all the in-line amplifiers will provide similar gain ( $G = \exp(\alpha L)$ ). The nonlinear Kerr field generated by the end of first span of a multi-span transmission link can be described by equation 3.1, the amplifier deployed by the end of the span compensates not only for the power loss of the mixing components (signals) but also the nonlinear product. Figure 3.2 shows a conceptual diagram of the accumulation of the nonlinear optical fields results in multi-span discretely amplified optical transmission system. The mixing fields at the input of each span ( $E_i(0)$ ,  $E_j(0)$ , and  $E_k(0)$ ) will change their phase according to phase mismatching accumulation from previous spans, which explains the phase shift factor  $\exp[i(\Delta\beta + \beta_F)(n-1)L]$  applied to the nonlinear Kerr field generated from the  $n^{th}$  span. The nonlinear Kerr field generated from the  $n^{th}$  span then propagates through the rest of the link which results a phase shift ( $\exp[i\beta_F(N-n)L]$ ) due to the propagation constant of the Kerr nonlinear field (which can be identified from equation (2.2)). The nonlinear Kerr fields generated from each span can then be coherently added to calculate the total power of the nonlinear product [91,96,97].

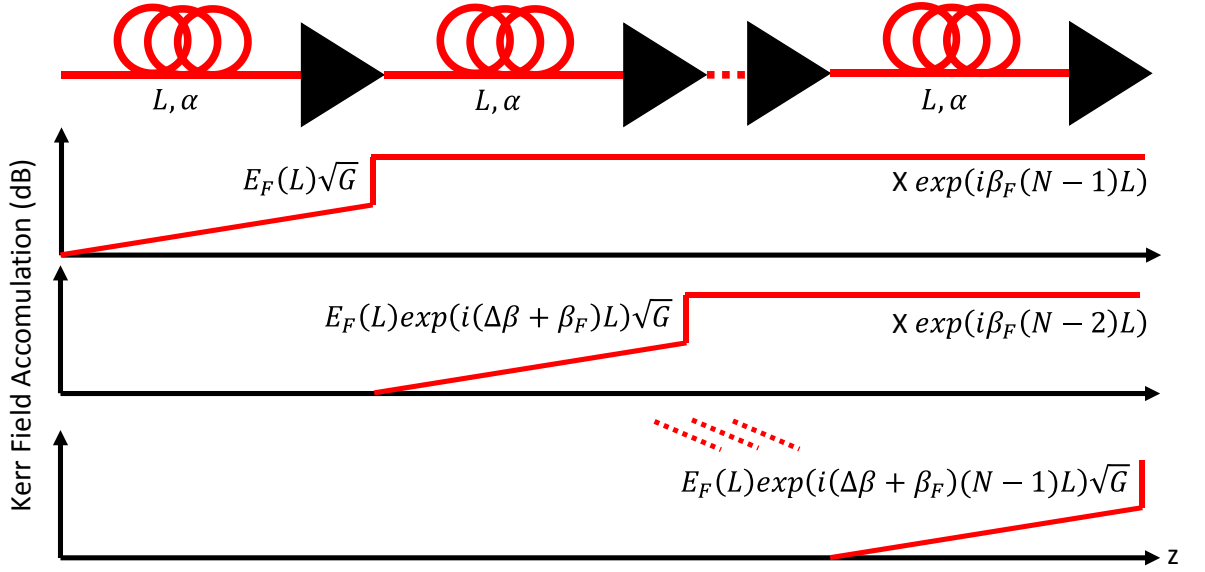


Figure 3.2: Nonlinear Kerr field accumulation map for multi-span optical transmission system. [XI]

From the previous analysis, we can theoretically formulate the nonlinear Kerr field generated from the  $n^{th}$  span and measured by the end of the transmission line as [91]:

$$E_F(L_n \rightarrow \text{end}) = i \frac{\gamma_0 D}{3} E_q(0) E_r(0) E_s^*(0) e^{(i\beta_F NL)} \left[ \frac{e^{([- \alpha + i\Delta\beta]L)} - 1}{-\alpha + i\Delta\beta} \right] e^{(i\Delta\beta(n-1)L)} \quad (3.3)$$

The total nonlinear Kerr field generated by the end of the transmission link can be calculated as the coherent summation of all the Kerr fields generated from each span in the link; this summation can be written as (for  $N$  identical spans each of length is  $L$ , and assuming that the amplifiers are black box amplifiers that has zero dispersion and nonlinear Kerr effects) [91]:

$$E_F(NL) = i \frac{\gamma_0 D}{3} E_q(0) E_r(0) E_s^*(0) e^{(i\beta_F NL)} \left[ \frac{e^{([- \alpha + i\Delta\beta]L)} - 1}{-\alpha + i\Delta\beta} \right] \sum_{n=1}^N e^{(i\Delta\beta(n-1)L)} \quad (3.4)$$

Accordingly, the nonlinear Kerr product power can be written as [89–91]:

$$P_F(NL) = \left( \frac{D\gamma_0}{3} \right)^2 P_q P_r P_s \left[ \frac{\alpha^2 L_{eff}^2}{\alpha^2 + \Delta\beta^2} \right] \left[ 1 + \frac{4e^{(-\alpha L)} \sin^2(\Delta\beta L / 2)}{(1 - e^{(-\alpha L)})^2} \right] \left[ \frac{\sin^2(\Delta\beta NL / 2)}{\sin^2(\Delta\beta L / 2)} \right] \quad (3.5)$$

Compared to equation 3.2, equation 3.5 introduces a new oscillating scaling term (the last term) which represents the phase mismatching effect accumulated along the cascaded amplifier chain. The oscillating term is expressed for a uniform system with identical spans, and is readily verified experimentally [92]. Figure 3.3 (a) shows a 5-span (each 100km) system that transmits two CW lasers (0dB each, spectrally located at 1555nm) through two types of optical fibre: NZDSF and SSMF. Figure 3.3 (b) shows the nonlinear Kerr product power as a function of

frequency separation between the two CWs. In the strongly phase matched region, the power of nonlinear Kerr product scales proportional to  $N^2$ , which can be concluded from the last term in equation 3.5. At the weakly phase matched region, the oscillating last term in equation 3.7 starts to degrade the power of the nonlinear Kerr product; this oscillation has a frequency proportional to the squared value of the frequency separation between the mixing two lasers (from the definition of  $\Delta\beta$ , equation 2.8). The figure also shows that the NZDSF oscillates in a slower pace compared to the SSMF system due to its lower value of dispersion.

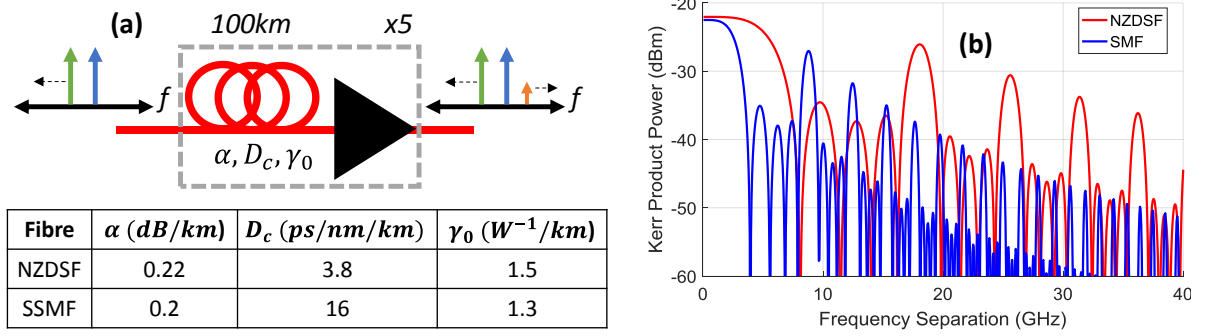


Figure 3.3: (a) 5x100km optical system transmitting two CW lasers (0dBm each, spectrally located at 1555nm) through NZDSF and SSMF. (b) Nonlinear Kerr product power as a function of frequency separation between the mixing components. [X1]

To experimentally verify equation 3.5, I have injected two tuneable CW lasers (3dBm each, combined by 3dB coupler, spectrally located at 1555nm) into a system of one and two 100km spans (Sterlite OH-LITE(E), ITU-T G.652.D, [102]). Then, I have measured the power of nonlinear Kerr product generated by the end of the system using a high resolution Optical Spectrum Analyser (OSA) (150MHz resolution), I have used the Hold Max feature to get continues measurement trace as the frequency separation between the two CW lasers was changed. An EDFA (with gain of 20dB) was used to compensate for the optical fibre span. Also, I have conducted numerical simulations of the system using VPITransmissionMaker v9.8. Figure 3.4 shows a comparison between the theoretical, simulation, and experimental results (for a single span (a) and two spans (b)[X15]) of the nonlinear Kerr product power as a function of the separation between the two CW lasers. The parameters used in the simulations and the theory were:  $D=3$ ,  $L=100\text{km}$ ,  $\gamma_0=1.3/\text{W/km}$ ,  $D_c=16.4\text{ps/nm}$ ,  $S=0$ , and  $P_q=P_r=P_s=0\text{dBm}$ . The simulation results show a perfect agreement with the analytical predictions for both single span and two spans. The experimental results show a margin of error of 0.5dB (at the peaks of nonlinear product power) compared to the analytical predictions. The mismatching between the analytical predictions and the experimental results at the nulls (of figure 3.4b)) can be explained by the limited resolution of the OSA in the experimental setup. In a single span system, the nonlinear product power starts at its highest value at frequency

separation less than 5GHz; then, as expected, the nonlinear product power is degraded due to the phase mismatching ( $\Delta\beta$ ) when the frequency separation is above 5GHz. The nonlinear product power generated from a single span system does not show power oscillation due of the fact that the last term of equation 3.5 is equal to one (no oscillation). On the other hand, a two-span system will cause nonlinear product power to oscillate as a function of the squared value of the frequency separation (because of the last term in equation 3.5). When comparing the single span and two spans systems, the maximum nonlinear product power (at low frequency separation) for a two-span system is 6dB (four times) higher than the power generated in a single span system; this increment can be reasoned by the last term in equation 3.5 which is simplified to  $N^2$  when  $\Delta\beta \rightarrow 0$ .



Figure 3.4: Nonlinear Kerr power as a function of the frequency separation between two CW lasers. (a) 100km system, (b) 2x100km system [X15].

In dispersion managed systems, the low dispersion accumulation in the system tends to enhance the nonlinear Kerr effects by extending the phase matching bandwidth, which can be seen from the difference in nonlinear Kerr power generated in SSMF and NZDSF shown in figures 3.1 and 3.3. If the system was deploying DCF span of fibre following SSMF span, then the nonlinear Kerr field accumulated along the system can be written (by following the analysis in figure 3.2) as [97] (assuming  $\exp(-\alpha L_{SSMF}) \ll 1$ ):

$$E_F(NL) = i \frac{\gamma_{SSMF} D}{3} E_q(0) E_r(0) E_s^*(0) e^{(i\delta\beta_F NL)} \left[ \frac{e^{([- \alpha + i\Delta\beta] L_{SSMF})} - 1}{-\alpha + i\Delta\beta} \right] \sum_{n=1}^N e^{(i(n-1)\delta\Delta\beta L)} \quad (3.6)$$

and power of the nonlinear Kerr product can be written as [97]:

$$P_F(NL) = \left( \frac{D\gamma_{SSMF}}{3} \right)^2 P_q P_r P_s \left[ \frac{\alpha^2 L_{eff}^2}{\alpha^2 + \Delta\beta^2} \right] \left[ 1 + \frac{4e^{(-\alpha L_{SSMF})} \sin^2(\Delta\beta L_{SSMF} / 2)}{(1 - e^{(-\alpha L_{SSMF})})^2} \right] \left[ \frac{\sin^2(\delta NL / 2)}{\sin^2(\delta L / 2)} \right] \quad (3.7)$$

where  $\delta$  is the ratio of the residual dispersion from the SSMF which can be written as:



$$\delta = \frac{\Delta\beta_{SMF}L_{SSMF} + \Delta\beta_{DCF}L_{DCF}}{\Delta\beta_{SMF}L_{SSMF}} \quad (3.8)$$

Other dispersion management maps require the reformulation of equation 3.6 by considering the accumulation of phase mismatching and nonlinear fields for each span. Figure 3.5 (a) shows a 5-span dispersion managed system, each span consists of 100km SSMF and varying length of DCF to show effect of residual dispersion ratio ( $\delta$ ). Figure 3.5 (b) shows verification of equation 3.7 (using simulation results) which shows the nonlinear Kerr product power generated from the mixing between two CW lasers (0dBm each, spectrally located at 1555nm) as a function of frequency separation. A fully dispersion compensated ( $\delta=0\%$ ) system shows a nonlinear response similar to the single span system but scaled by  $N^2$  (representing the last term in equation 3.7). A dispersion compensated system with residual chromatic dispersion ( $\delta>0\%$ ) tends to reintroduce oscillations in nonlinear product power generated from the weakly phase matched mixing components, as seen from figure 3.5(b). The higher the residual dispersion in the system ( $\delta$ ) leads to a higher frequency of nonlinear product oscillations as a function of the frequency separation between the mixing components. If the system was overcompensating the dispersion accumulation along the SSMF ( $\delta<0\%$ ), the nonlinear Kerr product power oscillations will have the same response as a system equivalent with undercompensated dispersion ( $|\delta|>0\%$ ); this can be concluded from the last term in equation. The figure shows that the minimisation of dispersion accumulation along the system leads to the enhancement of nonlinear Kerr power generation along the system.

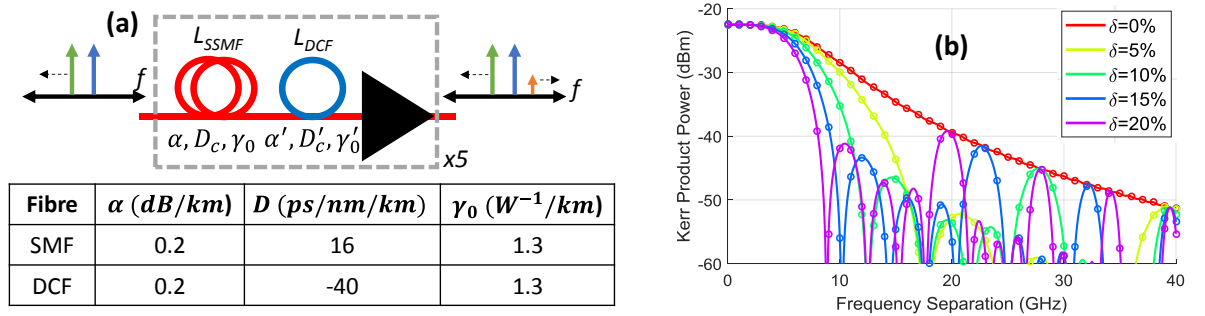


Figure 3.5: (a) Dispersion managed 5x100km optical system transmitting two CW lasers (0dBm each, spectrally located at 1555nm). (b) Nonlinear Kerr product power as a function of frequency separation between the mixing components, the different curves show various values of residual dispersion  $\delta$ . (solid lines) theoretical predictions, (open circles) simulation results. [X1]

## 3.2 Nonlinear Kerr Effects in Distributed Raman Transmission Systems

As explained in chapter 2, deploying distributed Raman amplification along optical fibre span imply the change of the signal power profile from constant exponent attenuation coefficient

(along the span) to a dynamic power profile with longitudinal change in attenuation/gain coefficient, described by equation 2.10. Dispersion management in distributed Raman transmission systems has been used either by incorporating DCF within the SSMF transmission span [103], or by adding separate Raman pumped DCF span [104]. Using a single Raman pump to amplify signals propagating through an optical span that contains SSMF and DCF changes the signal power profile along the span in equation 2.10 (shown in [103]), since the Raman gain factor for DCF is often higher than the Raman gain factor in SSMF. In this section, we will concentrate on the dispersion unmanaged distributed Raman systems because of the analytical simplicity. The non-constant exponential power variation in distributed Raman span imposes a difficulty in formulating a closed form solution to the inhomogeneous wave equation (equation 2.6, when replacing  $\alpha$  by  $\sqrt{G(z)}$ ). So, a numerical integration is required to find the nonlinear Kerr product power accumulated along the distributed Raman amplified span.

If I divide each distributed Raman amplified span into  $M$  sections (each with length= $l$ ) and follow the same solution criteria described in figure 3.2, I can rewrite the integration (presented in [98]) that describes the nonlinear Kerr power generated by the end of  $N$  distributed Raman spans as [X4]:

$$P_F(NL) = \left(\frac{D\gamma_0}{3}\right)^2 P_q P_r P_s \left| \sum_{k=1}^M \left[ \frac{e^{(g_k + i\Delta\beta)L_k} - 1}{g_k + i\Delta\beta} \right] \left[ \prod_{l=1}^{k-1} e^{(g_l + i\Delta\beta)L_l} \right] \right|^2 \left[ \frac{\sin^2(N\Delta\beta L/2)}{\sin^2(\Delta\beta L/2)} \right] \quad (3.9)$$

where  $L_k$  is the length of the  $k^{th}$  fibre section, and  $g_k$  represents the exponential gain/attenuation constant of the  $k^{th}$  section which can be defined as (assuming  $L_x = L/M$ ):

$$g_k = \frac{M}{L} \log \left[ G(kL/M) - G([k-1]L/M) \right] \quad (3.10)$$

where  $G(z)$  is the Raman power profile (described in equation 2.10). We can see that the last term in equation 3.9 remains unchanged (compared to equation 3.5, of discretely amplified system), whilst the terms in the squared brackets represents an approximated solution of the inhomogeneous wave equation over single distributed Raman span. The accuracy of equation 3.9 relies on the number of sections per span ( $M$ ), a higher number of sections would cause the constant exponent interpolation (equation 3.10) to get closer to the power profile curvatures as described in equation 2.10 and figure 2.4. Figure 3.6 shows the power of nonlinear Kerr product (generated from the mixing of two CW lasers, 0dBm each and spectrally located at 1555nm) as a function of frequency separation between the two CW lasers propagating through single span (a) and two spans (b); each span is 62km (SSMF) that deploy 1<sup>st</sup> order bidirectional Raman pumping ( $100\% > r_f > 0\%$ ) (with different  $r_f$  values). The figure compares the theoretical

predictions of equation 3.9 ( $M=31$ ,  $L_k=2\text{km}$ ) and simulation results (conducted in VPITransmissionMaker 9.8) [X4].

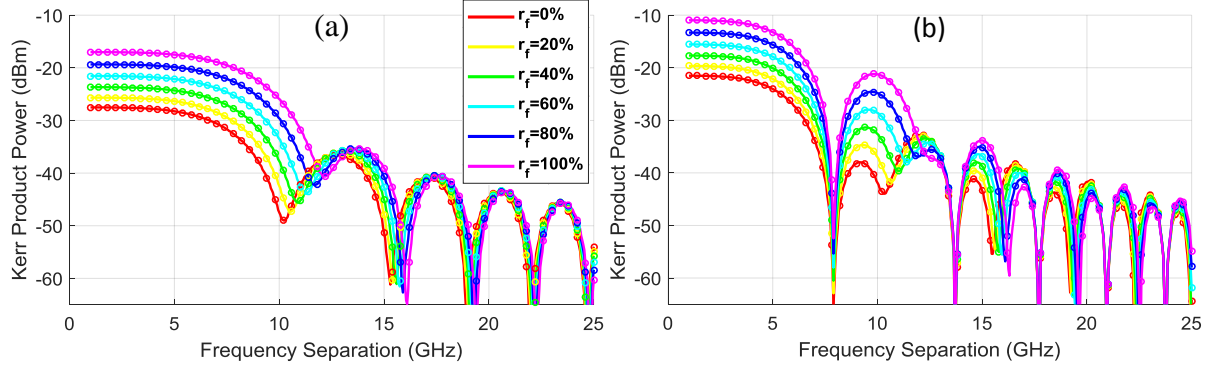


Figure 3.6: Nonlinear Kerr product power as a function of frequency separation between two CW lasers (0dBm each, spectrally located at 1555nm) propagating through single span (a) and two spans (b), each span is 62km that deploy 1<sup>st</sup> order bidirectional Raman pumping ( $100\% > r_f > 0\%$ ). (Solid lines) theoretical predictions resulted from equation 3.9, (open circles) simulation results. The color code represents different forward Raman pumping ratio ( $r_f$ ). [X4]

At low signal frequency separation ( $\Delta\beta \rightarrow 0$ ), the nonlinear Kerr product power increases gradually when the pumping scheme moves from full backward pumped ( $r_f=0\%$ ) to full forward pumped ( $r_f=100\%$ ) Raman spans, which is expected as the signal power along the span increases with  $r_f$  (as seen in figure 2.4). The nonlinear product generated by the end of a single span system (figure 3.6(a)) shows a power oscillation as a function of frequency separation due to the phase mismatching and power variation which are described by  $(./)^2$  in equation 3.9. As the frequency separation increases beyond 20GHz, the phase mismatching starts to dominate over the value of section gain ( $\Delta\beta > g_x$ ) which leads to a convergence in nonlinear Kerr product power oscillation (regardless of pumping scheme,  $r_f$ ) to become [X4]:

$$\begin{aligned}
 P_F(NL) &= \left( \frac{D\gamma_0}{3} \right)^2 P_q P_r P_s \left| \frac{e^{i\Delta\beta L} - 1}{i\Delta\beta} \right|^2 \left[ \frac{\sin^2(N\Delta\beta L / 2)}{\sin^2(\Delta\beta L / 2)} \right] \\
 &= \left( \frac{D\gamma_0}{3} \right)^2 P_q P_r P_s \left[ \frac{4 \sin^2(N\Delta\beta L / 2)}{\Delta\beta^2} \right]
 \end{aligned} \tag{3.11}$$

Equation 3.11 also represents the nonlinear Kerr product power for an ideal quasi-lossless distributed Raman amplification, which can be concluded by taking the limit of equation 3.9 as  $g_x \rightarrow 0$ . When moving from single span to two-span (figure 3.6 (b)) system, the nonlinear Kerr product power generated by strongly phase matched signals will quadruple (compared to the single spans system) since the last term of equation 3.9 can be simplified to become  $N^2$  at  $\Delta\beta \rightarrow 0$ . As the frequency separation increases, the last term in equation 3.9 starts to cause nonlinear product power to oscillate (as a function of frequency separation) while the original

oscillations (appeared in single span system) remain unchanged. Again, the simulation results presented in figure 3.6 matches the theoretical calculations.

To quantify the effects of number of sections ( $M$ ) used in equation 3.9 and the accuracy of representing the nonlinear Kerr power, I have plotted in figure 3.7 the Root Mean Squared (RMS) error of the calculated nonlinear Kerr power as a function of  $r_f$ . The nonlinear product power calculations were carried out by solving equation 3.9 with various number of sections  $M$ , the RMS error values were calculated relative to the solution of equation 3.9 when representing the 62km distributed Raman span with  $M=31$  sections ( $L_k=2\text{km}$ ). The figure shows that a higher number of sections, representing the distributed Raman span, result a lower error in the calculation of the nonlinear Kerr product power. A 16.5dB accuracy improvement can be achieved when using  $M=12$  when compared  $M=2$ .

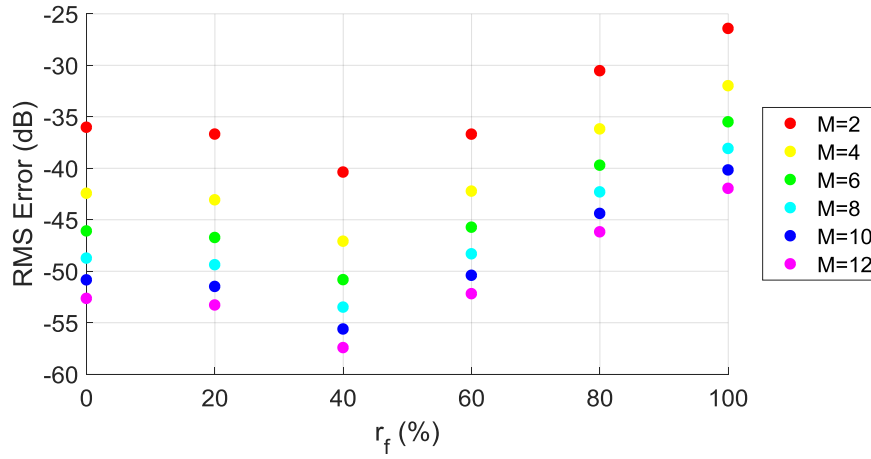


Figure 3.7: RMS error of nonlinear Kerr power as a function of forward Raman pumping ratio ( $r_f$ ). The RMS was calculated in reference to the calculation of ( $M=31$ ) over 50GHz bandwidth for different number of sections  $M=2, 4, 6, 8, 10$ , and 12.

The power profile of a strongly forward pumped Raman span ( $r_f=75\%$  to 100%) and strongly backward pumped Raman span ( $r_f=0\%$  to 25%) can be approximated by two distinguished sections each has constant exponential gain/loss coefficients. Figure 3.8 shows the two-section approximation of the Raman power profile, where the length of the first section ( $L_1$ ) is identified as the fibre length at which the longitudinal signal power evolution is equal to zero ( $dG(z)/dz=0$ ), while the length of the second section ( $L_2$ ) is the remaining span length. Following the previous definition, the length of the two sections can be derived from equation 2.10, which results [X18]:

$$L_1 = \left( \frac{1}{\alpha_p} \right) \log \left( \frac{\alpha_s \pm \sqrt{\alpha_s^2 - 4P_0^2 g_r^2 r_f (1-r_f) \exp(-\alpha_p L)}}{2g_r P_0 (1-r_f) \exp(-\alpha_p L)} \right) \quad (3.12)$$

$$L_2 = L - L_1$$

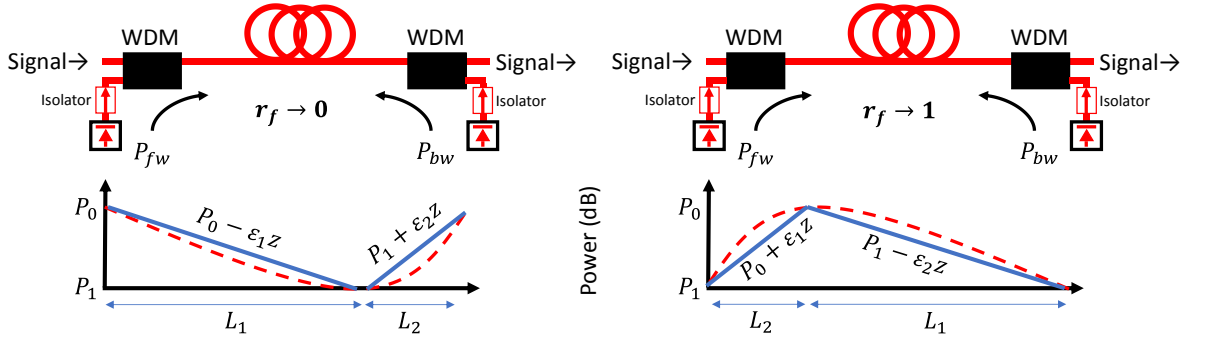


Figure 3.8: Two section approximation for distributed Raman power profile: (left) power profile in the case of dominating backward pump ( $r_f < 0.25$ ), and (right) is the case of dominating forward pump ( $r_f > 0.75$ ). [X18]

Choosing the value of constant gain/attenuation coefficients for the two sections ( $g_1$  and  $g_2$ ) can affect the approximation accuracy of representing the power profile. The constant exponent approximations described in figure 3.8 may appear inadequate, due to the strong curvature of the power evolution along the distributed Raman span. An optimised fitting factor  $k$  can be used to scale the gain/attenuation constants of the two sections which will provide a better approximation for the power profile. The fitting factor  $k < 1$  minimises the overestimation (in the two-section approximation) of the power profile when  $r_f \rightarrow 0$ , while  $k > 1$  minimises the underestimation of power profile when  $r_f \rightarrow 1$ . So, the gain attenuation/coefficients can be identified for the two sections as follows:

$$\begin{aligned} g_1 &= k \log[G(L_1)] / L_1 \\ g_2 &= -g_1 L_1 / (L - L_1) \end{aligned} \quad (3.13)$$

where the parameters  $k$  represents the fitting factor. Following the previous assumptions, the nonlinear Kerr product power can be approximated as:

$$P_F(NL) = \left( \frac{D\gamma_0}{3} \right)^2 P_q P_r P_s \left[ \frac{\sin^2(N\Delta\beta L/2)}{\sin^2(\Delta\beta L/2)} \right] \left| \frac{e^{(g_1 + i\Delta\beta)L_1} - 1}{g_1 + i\Delta\beta} + e^{(g_1 + i\Delta\beta)L_1} \frac{e^{(g_2 + i\Delta\beta)L_2} - 1}{g_2 + i\Delta\beta} \right|^2 \quad (3.14)$$

which can be rewritten as [X18]:

$$P_F(NL) = \left( \frac{D\gamma_0}{3} \right)^2 P_q P_r P_s \left[ \frac{\sin^2(N\Delta\beta L/2)}{\sin^2(\Delta\beta L/2)} \right] + \left[ \frac{\frac{(1 - e^{g_1 L_1})^2 + 4e^{g_1 L_1} \sin\left(\frac{\Delta\beta L_1}{2}\right)^2}{g_1^2 + \Delta\beta^2} + \frac{(1 - e^{g_2 L_2})^2 + 4e^{g_2 L_2} \sin\left(\frac{\Delta\beta L_2}{2}\right)^2}{g_2^2 + \Delta\beta^2}}{-2\Re\left\{ \frac{(e^{g_1 L_1} - e^{i\Delta\beta L_1})(e^{g_2 L_2} - e^{i\Delta\beta L_2})}{g_1 g_2 \pm i(|g_1| + |g_2|)\Delta\beta + \Delta\beta^2} \right\}} \right] \quad (3.15)$$

The upper sign (of  $\pm$ , in equation 3.15) refers to the system with dominated by backward pumping ( $r_f \rightarrow 0\%$ ) and the lower sign refers to the system with dominated by forward pumping ( $r_f \rightarrow 100\%$ ). In essence, equation 3.15 is identical to two copies of equation 3.5, one for each section, with an additional term representing the coherent addition of the nonlinear Kerr product powers generated by each section (third term in the second squared brackets of equation 3.15). Figure 3.9 (a) compares the theoretical calculations of nonlinear Kerr product power with 31-section approximation (using equation 3.9, verified by simulations in figure 3.6) and the theoretical results using the two-section approximation equation 3.15. Figure 3.9 (b) shows the two-section approximation and 31-section power profiles for:  $r_f=0\%$ , 20%, 80%, and 100% that corresponds to the nonlinear Kerr product power curves plotted in figure 3.9 (a). The lengths of the two sections and their gain/attenuation coefficients, in the two-section approximation, were calculated using equation 3.12 and equation 3.13, respectively. The gain fitting factor ( $k$ ) in equation 3.13 was optimised for each power profile to minimise the RMS error of the nonlinear product power curve when compared to the 31-section approximation (equation 3.9,  $M=31$ ). The resulting  $k$  values were 0.725, 0.876, 1.125 and 1.265 for  $r_f=0\%$ , 20%, 80%, and 100%, respectively. From figure 3.9, we can see that the two-section approximation shows an acceptable method to calculate the nonlinear Kerr product power in distributed Raman system with  $r_f \rightarrow 0\%$  or  $r_f \rightarrow 100\%$ . With an RMS error (in reference to the 31-section solution) values of -47dB ( $r_f=0\%$ ), -49dB ( $r_f=20\%$ ), -44.1dB ( $r_f=80\%$ ), and -38dB ( $r_f=100\%$ ); the two-section approximation represents an accuracy equivalent to the 8-section approximation as presented in figure 3.6.

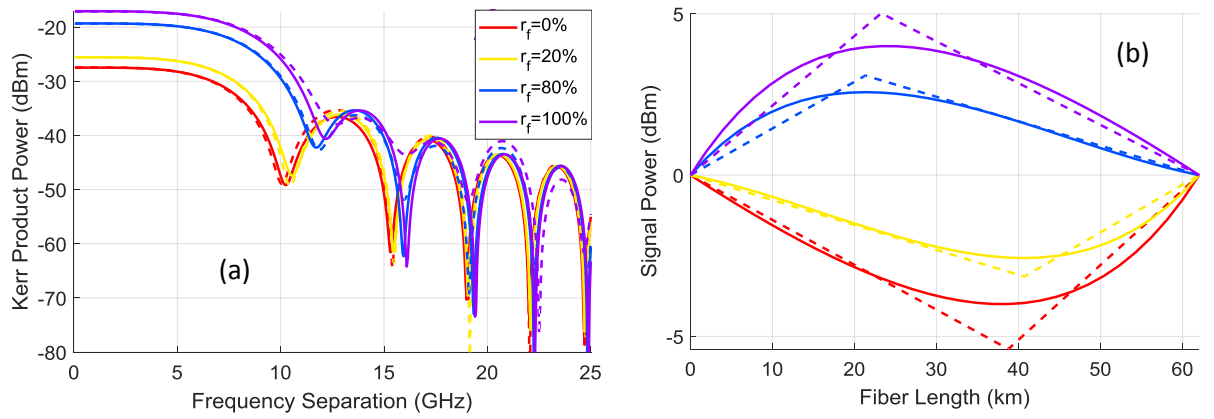


Figure 3.9: (a) Nonlinear Kerr product power as a function of frequency separation, (b) signal power profile. (solid lines) 31-section approximation, (dashed lines) two-section approximation.

To experimentally verify the two-section approximation, we have implemented Raman Fibre Laser (RFL) [105,106] that uses second order Raman pumping scheme. The power profiles due to second order Raman pumping of the span show lower signal power excursions along the span compared to the first order Raman pumping [60]. Figure 3.10 shows the experimental setup to measure the nonlinear product power generated from the mixing of two CW lasers (spectrally located at 1555nm), the counter propagating Raman pumps used in this setup were spectrally located at 1366nm [105]. A 62km of single mode fibre (G.652) was used in this experiment, two tuneable lasers ( $P_1$  and  $P_2$ ), and high resolution OSA. The table in figure 3.10 shows the pumping powers, forward pumping ratio ( $r_f$ ), and the power of input CW lasers.



Figure 3.10: Experimental setup of 2<sup>nd</sup> order distributed Raman span, the table shows the pumping powers, forward pumping ratio ( $r_f$ ), and the power of input CW lasers. [X18]

Figure 3.11 (a) shows the nonlinear product power as a function of frequency separation between the two CW lasers for different power profiles (listed in the table of figure 3.10), figure 3.11 (b) shows the signal power profile measured by Optical Time-Domain Reflectometer (OTDR) and our two-section approximation. Figure 3.11 shows that the occurrence of the first null in nonlinear Kerr product power shifts to higher frequency separation as  $r_f$  moves from 0% to 100%. The experimental results follow the same expected behaviour of matching phase performance at high frequency separation which has been concluded from figure 3.6(a).



*Figure 3.11: (a) Nonlinear Kerr product power as a function of frequency separation, (b) correspondent power profile along the distributed Raman span. (Solid lines) experimental measurement, (dashed lines) assumed power profile for the two-section approximation of profiles 1 to 4. [X18]*



*Figure 3.12: Nonlinear Kerr product power as a function of frequency separation between two CW lasers passing through 62km second order Raman pumped (at 1366nm) span with different  $r_f$  values listed in figure 3.10. [X18]*

To compare experimental results with the theory presented in equation 3.9 (multi section approximation), I have divided the Raman span into 31 sections and calculated  $g_i$  for each section according to the OTDR measurement. To verify the two-section approximation (equation 3.15), I have calculated  $g_1$  and  $g_2$  from dashed lines in figure 3.11(b). Figure 3.12



shows a comparison between the experimental results (of nonlinear Kerr power as function of frequency separation) and the theoretical predictions of 31-section approximation and the two-section approximation. In general, we can see good agreement (within 0.7dB margin of mismatching at the peaks) between the experimental results and the theoretical predictions from equations 3.9 and 3.15; the mismatch between the experimental results and the theoretical results at the nulls occur due to the limited resolution of OSA. The two-section approximation have a good matching with the 31-section approximation at the peaks, and have mismatching of 3.7dB at the first null; see the first null (red solid line and green dashed line) in “profile 3” of figure 3.12. [X18]

### 3.3 Nonlinear Kerr Effects in OPC-Assisted Discretely Amplified Transmission Systems

As mentioned before, installing OPC in optical transmission system can achieve compensation of linear and nonlinear impairments accumulated in the optical transmission fibre, the level of compensation depends on the dispersion and power profile symmetry along the system. The term “*dispersion and power profile symmetry*” was always mentioned [34,107–109] as a factor that significantly affect the nonlinear Kerr compensation that the OPC can achieve, but, a theoretical quantification was never established between the relation between symmetry and the nonlinear Kerr accumulation in OPC assisted systems. In this section, I will derive and analyse the accumulation of nonlinear Kerr effects in a generic OPC assisted (single- or multi-OPC), dispersion managed or unmanaged, discretely amplified transmission systems.

In literature, a few studies have investigated the benefits of installing multiple (symmetrically placed) OPCs along an optical transmission systems [110] [X9,X10]. The deployment of multiple OPCs divides the systems into multiple “*segments*” [X10], where the signals propagating along the even indexed segment would result a compensation of the nonlinearities and dispersion occur in the odd indexed segment. There are two approaches to install OPCs along a transmission link: single segmented spaced OPC [X10] and a double segmented spaced OPCs [110]; figure 3.13 shows example of 8-span system to that uses the two approaches of multi-OPC deployment (to create 4 segments in the system,  $N_{seg}=4$ ). In the single segmented spaced OPC deployment approach, shown in figure 3.13(top), the number of spans separating any two consecutive OPCs is the same number of spans separating the transmitter from the first OPC; and is the same number of spans separation between the last OPC and the receiver. In this deployment criteria, the number of segments along the system is defined as  $N_{seg}=N/(N_{OPC}+1)$ , where each segment contains  $N/N_{seg}$  spans. On the other hand, the double

segmented spaced OPC deployment approach, shown in figure 3.13(bottom), the number of spans separating any two consecutive OPCs is twice number of spans separating the transmitter from the first OPC; and also twice the number of spans separation between the last OPC and the receiver [110]. In this deployment criteria, the number of segments along the system is defined as  $N_{seg}=N/(2N_{OPC})$ , where each segment contains  $N/N_{seg}$  spans.

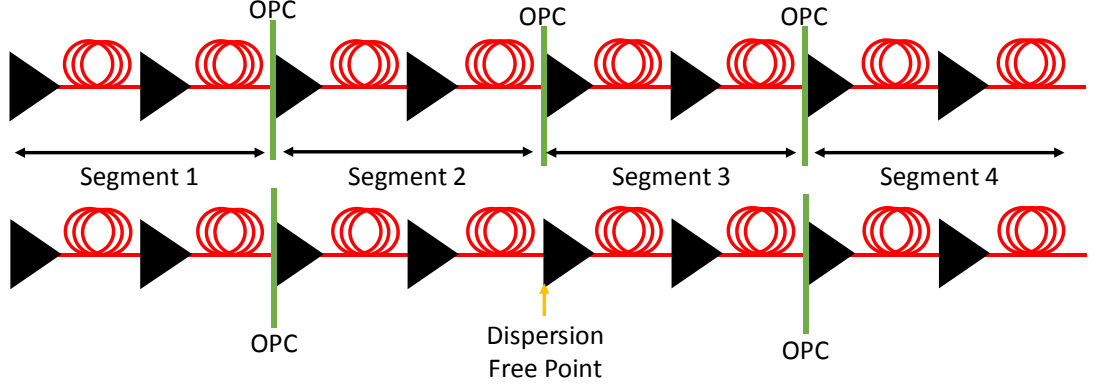


Figure 3.13: OPC deployment techniques. (top) single segment spaced OPCs, (bottom) double segment spaced OPCs.

In the OPC assisted system, the nonlinear Kerr optical field can be written as [X4]:

$$E_F(NL) = \frac{N_{seg}}{2} \left[ E_F(\text{even segment}) + [E_F(\text{odd segment})]^* e^{(i\delta\beta_F NL/N_{seg})} \right] \quad (3.16)$$

where the nonlinear Kerr field generated from any two consecutive segments can be represented by the terms inside the squared brackets (of equation 3.16), and the total nonlinear Kerr field generated in the system is simply the nonlinear Kerr field generated along two consecutive segments scaled by the number of segments divided by 2 ( $N_{seg}/2$ ). The nonlinear Kerr field generated from the odd indexed segment (of  $N/N_{seg}$  spans) can be written as (recall equation 3.4) [X4]:

$$E_F(\text{odd segment}) = i \frac{\gamma D}{3} E_q(0) E_r(0) E_s^*(0) e^{(i\delta\beta_F NL/N_{seg})} \left[ \frac{e^{([- \alpha + i\Delta\beta]L)} - 1}{- \alpha + i\Delta\beta} \right] \sum_{n=1}^{N/N_{seg}} e^{(i(n-1)\delta\Delta\beta L)} \quad (3.17)$$

Then this field is conjugated (\*) by the OPC and then propagates through the following (even indexed) segment (of  $N/N_{seg}$  spans) to accumulate the phase shift due to the propagation constant  $\beta_F$  (the second term in the squared brackets of equation 3.16) which can be written as:

$$\begin{aligned}
E_F \left[ (odd\ segment) \right]^* e^{(i\delta\beta_F NL/N_{seg})} \\
= -i \frac{\gamma D}{3} E_q^*(0) E_r^*(0) E_s(0) \left[ \frac{e^{([- \alpha - i\Delta\beta]L)} - 1}{-\alpha - i\Delta\beta} \right] \sum_{n=1}^{N/N_{seg}} e^{(-i(n-1)\delta\Delta\beta L)}
\end{aligned} \quad (3.18)$$

On the other hand, the mixing fields ( $q$ ,  $r$ , and  $s$ ) are phase shifted according to the accumulation of dispersion along the odd indexed segment ( $\exp(i\delta[\Delta\beta + \beta_F]NL/N_{seg})$ ), then, the mixing fields get conjugated and propagate through the even indexed segment to generate a nonlinear Kerr field (the first term in the squared brackets of equation 3.16) as **[X4]**:

$$\begin{aligned}
E_F (even\ segment) \\
= i \frac{\gamma D}{3} \left[ E_q(0) E_r(0) E_s^*(0) e^{(i\delta[\Delta\beta + \beta_F]NL/N_{seg})} \right]^* e^{(i\delta\beta_F NL/N_{seg})} \left[ \frac{e^{([- \alpha + i\Delta\beta]L)} - 1}{-\alpha + i\Delta\beta} \right] \sum_{n=1}^{N/N_{seg}} e^{(i(n-1)\delta\Delta\beta L)} \\
= i \frac{\gamma D}{3} E_q^*(0) E_q^*(0) E_s(0) e^{(-i\delta\Delta\beta NL/N_{seg})} \left[ \frac{e^{([- \alpha + i\Delta\beta]L)} - 1}{-\alpha + i\Delta\beta} \right] \sum_{n=1}^{N/N_{seg}} e^{(i(n-1)\delta\Delta\beta L)} \\
= i \frac{\gamma D}{3} E_q^*(0) E_q^*(0) E_s(0) e^{(-i\delta\Delta\beta L)} \left[ \frac{e^{([- \alpha + i\Delta\beta]L)} - 1}{-\alpha + i\Delta\beta} \right] \sum_{n=1}^{N/N_{seg}} e^{(-i(n-1)\delta\Delta\beta L)}
\end{aligned} \quad (3.19)$$

When substituting equation 3.17 and 3.19 into equation 3.16, the total accumulated nonlinear Kerr field generated along the system can be written as **[X4]**:

$$\begin{aligned}
E_F (NL) = i \frac{\gamma DN_{seg}}{6} E_q^*(0) E_r^*(0) E_s(0) \\
\left[ e^{(-i\delta\Delta\beta L)} \frac{e^{([- \alpha + i\Delta\beta]L)} - 1}{-\alpha + i\Delta\beta} - \frac{e^{([- \alpha - i\Delta\beta]L)} - 1}{-\alpha - i\Delta\beta} \right] \sum_{n=1}^{N/N_{seg}} e^{(-i(n-1)\delta\Delta\beta L)}
\end{aligned} \quad (3.20)$$

And the corresponding nonlinear Kerr product power ( $P=|E|^2$ ) can be written as **[X4]**:

$$\begin{aligned}
P_F (NL) = \frac{D^2 \gamma^2 N_{seg}^2}{36} P_q P_r P_s \left| e^{(-i\delta\Delta\beta L)} \frac{e^{([- \alpha + i\Delta\beta]L)} - 1}{-\alpha + i\Delta\beta} - \frac{e^{([- \alpha - i\Delta\beta]L)} - 1}{-\alpha - i\Delta\beta} \right|^2 \\
\frac{\sin^2 (N\delta\Delta\beta L / [2N_{seg}])}{\sin^2 (\delta\Delta\beta L / 2)}
\end{aligned} \quad (3.21)$$

Which can be simplified for fully dispersion compensated system ( $\delta=0$ ) as **[X4]**:

$$P_F (NL) = \frac{D^2 \gamma^2}{9} \frac{P_q P_r P_s N^2}{(\alpha^2 + \Delta\beta^2)^2} \left[ \alpha e^{-\alpha L} \sin(\Delta\beta L) + \Delta\beta (e^{-\alpha L} \cos(\Delta\beta L) - 1) \right]^2 \quad (3.22)$$

and for dispersion uncompensated system ( $\delta=1$ ) as [X4]:

$$P_F(NL) = \frac{D^2 \gamma^2 N_{seg}^2}{9} \frac{P_q P_r P_s}{(\alpha^2 + \Delta\beta^2)^2} \left[ \alpha (e^{-\alpha L} + 1) \sin\left(\frac{\Delta\beta L}{2}\right) + \Delta\beta (e^{-\alpha L} - 1) \cos\left(\frac{\Delta\beta L}{2}\right) \right]^2 \frac{\sin^2(N\delta\Delta\beta L / [2N_{seg}])}{\sin^2(\delta\Delta\beta L / 2)} \quad (3.23)$$

Equation 3.22 shows that dispersion managed system with ( $\delta=0$ ) that deploy OPC will have the same nonlinear Kerr response irrespective on the number of deployed OPCs along the link. A full per-span dispersion compensation implies that any point of conjugation (along the link) has zero accumulation of dispersion (phase mismatching), which: eliminates the nonlinear Kerr product power oscillation (as seen in figure 3.5(b)), and achieve the same frequency response of nonlinearity compensation (regardless on the number of spans on either side of the OPC) as the phase mismatching accumulations resets to zero by the end of each span. The nonlinear Kerr product power generated in dispersion uncompensated system, equation 3.23, increasing the number of OPCs along the system (increasing  $N_{seg}$ ) results in a linear scaling and reduction of the nonlinear Kerr product power oscillations resulted by the last term of equation 3.23. Equation 3.22 and 3.23 shows that deploying OPC in discretely amplified system provides full nonlinearity compensation efficiency. A full nonlinearity compensation efficiency can be achieved by the OPC in discretely amplified system when: deploying dispersionless transmission optical fibre ( $\beta''=0$ ), deploying lossless optical fibre (ideal distributed Raman system), or when deploying infinitely short span length ( $L \rightarrow 0$  and  $N \rightarrow \infty$ ). A Pre-OPC dispersion compensated stage has been suggested by [111,112] to improve the nonlinearity compensation efficiency of the OPC in discretely amplified system; this technique can be related to equation 3.21 by adding an optimised phase shift to the second term of the squared brackets to minimise its value. This technique can improve the nonlinearity compensation capabilities of the OPC but cannot fully compensate for the nonlinearities accumulated along the system [111]. The symmetric placement of the OPC in the system [85] can be analytically modelled by altering the upper limit of the summations in equation 3.17 and 3.19.

Figure 3.14 shows the nonlinear Kerr product power generated from two CW lasers (each 0dBm, spectrally located at 1555nm) as they propagate through 200km system; the system has used various uniform span lengths (distance between any two consecutive EDFAs) with and without mid-link OPC [X4]. The figure compares simulation results with the theoretical predictions calculated from: equation 3.5 for a system without OPC (red curves), equation 3.22

for fully dispersion compensated system with mid-link OPC (blue curves, left column), and equation 3.23 for dispersion uncompensated system with mid-link OPC (blue curves, right column). The simulations have used ideal lossless OPC which was simply a mathematical conjugation of the optical field. The fully dispersion compensated transmission system ( $\delta=0\%$ ) in the left column of figure 3.14, it can be seen that the nonlinear Kerr power generated in a link without mid-link OPC scales as a function of  $(NL_{eff})^2$  as the system uses shorter span length; which can be concluded from the analytical expression of equation 3.5. A minor oscillation starts to grow as the span length gets shorter which is generated from the second term of the squared bracket of equation 3.5. Installing a mid-link OPC, see figure 3.14 (left column), in a fully dispersion compensated system would result a strong nonlinearity compensation among strongly phase matched signals. The compensation of Kerr product power starts to fade away among weakly phase matched CW lasers, eventually, the nonlinear Kerr product power generated in OPC assisted system will converge to match the nonlinear Kerr product power generated in a system that does not deploy a mid-link OPC. The bandwidth of nonlinearity compensation in fully dispersion compensated transmission system grows slowly as the span length decreases (10GHz for 2x100km system to 17GHz for 16x12.5km system).



Aston University

Illustration removed for copyright restrictions

*Figure 3.14: Nonlinear Kerr product power as a function of frequency separation between two CW lasers (0dBm each, spectrally located at 1555nm) propagating through 200km lumped transmission system (with different span length). (left column) fully dispersion compensated system with 0% residual dispersion, (right column) dispersion uncompensated system. (red) without OPC, (blue) with mid-link OPC. (solid lines) theory, (open circles) simulation results. [X4]*

In dispersion uncompensated system without mid-link OPC (figure 3.14, right column), the nonlinear Kerr power generated from strongly phase matched CW lasers scales as a function of  $(NL_{eff})^2$  which results a growth in the nonlinear Kerr power as the system uses shorter span length, but the nonlinear Kerr power generated from weakly phase matched CW lasers oscillates as a function of  $(L_{eff} \sin(N\Delta\beta L/2) / \sin(\Delta\beta L/2))^2$ . The last term in equation 3.5 results nonlinear Kerr power degradation only matches the nonlinear Kerr power generated from fully dispersion compensated system when  $(\sin(N\Delta\beta L/2) / \sin(\Delta\beta L/2))^2 = N^2$ . For a system that deploys mid-link OPC and long span length (2x100km), we can see that full nonlinearity compensation is still achieved among strongly phase matched CW lasers; whilst the nonlinear Kerr product power peaks converges in the weakly phase matched region (at higher frequency separation) to match the nonlinear power generated in a system without OPC.

As the span length gets shorter (number of spans increase), the nonlinear Kerr power generated from a system that deploys mid-link OPC starts to oscillate at half the frequency of oscillation that appears in the system without OPC, which can be clearly seen in the systems that deploy more than 2 spans (see figure 3.14). This can be explained by the fact the frequency of the oscillating scaling factor  $(\sin(NL\delta\Delta\beta/[2N_{seg}]))$ , in equation 3.23) in a system with OPC is divided by  $N_{seg}$  (=2 in figure 3.14) when compared to the frequency of the oscillating scaling factor  $(\sin(NL\delta\Delta\beta/2))$ , in equation 3.7) in a system without OPC. A reduction in the span length will cause the second term in the squared brackets of equation 3.23 to be degraded by the factor  $(e^{-\alpha L} - 1)$ , this degradation will slow down the convergence to the nonlinear Kerr power generated in a system without OPC. As a result, a shorter span length in dispersion uncompensated system achieves higher nonlinear Kerr product power compensation (compared to fully dispersion compensated system), as can be clearly seen when comparing the right column with the left column of figure 3.14. In general, the simulation results show a good agreement with the theoretical predictions.

As can be clearly seen from equation 3.23, deploying multiple OPCs along dispersion uncompensated system discretely amplified system would result an inherent, per segment, dispersion compensation from the OPCs along the system. The per segment dispersion compensation (achieved by the deployment of multi-OPC) which reduce the oscillation frequency of the nonlinear Kerr power (last term in equation 3.23) leading to the enhancement of the accumulated nonlinearities along the system.



Illustration removed for copyright restrictions

*Figure 3.15: Nonlinear Kerr product power as a function of frequency separation between two CW lasers (0dBm each, spectrally located at 1555nm) propagating through 24x100km lumped transmission system with different number of equally spaced and symmetrically located OPCs (1OPC, 3OPCs, 5OPCs, and 7OPCs). (red) without OPC, (blue) with OPCs. [X4]*

Figure 3.15 shows the nonlinear Kerr product power as a function of the frequency separation between two CW lasers (0dBm each, spectrally located at 1555nm) passing through 24x100km dispersion uncompensated system, discretely amplified system that deploys various number of OPCs (1OPC, 3OPCs, 5OPCs, and 7OPCs). The figure plots the nonlinear Kerr product power generated in a system without OPC as a point of reference. The figure compares between the theoretical reductions and simulation results [X4]. The figure shows that increasing the number of OPCs in the system will lead to the broadening of the nonlinear Kerr power peaks which diminish the nonlinearity compensation achieved by only a single, mid-link, OPC. An ultimate OPC per span ( $N_{seg}=N$ ) would cause the system to act as a fully dispersion compensated system with a single OPC, as described by equation 3.22 and figure 3.14 (left column). Again, the simulation results match the theoretical predictions which further validates equation 3.23.

To experimentally verify equation 3.23, I have implemented 2x100km fibre transmission system with and without mid-link OPC that transmits two tunable CW lasers (5dBm each, spectrally located at 1553nm). A 3dB coupler was used to combine the two lasers and inject



them into the first fibre span. Two EDFAs (Gain=20dB) were deployed at the output of each span to compensate for their loss. By the end of the system, I have measured the nonlinear Kerr product power using a high resolution OSA (150MHz resolution) as the frequency separation between the two CW were swept from 0 to 20GHz. The OPC experimental implementation will be discussed in detail in chapter 5. Figure 3.16 shows a comparison between the theoretical predictions and the experimental results. The experimental results show a good agreement with the theoretical predictions within a margin of mismatching of less than 0.5dB (at the peaks), the mismatching (at the nulls) between the experimental results and theoretical predictions is attributed to the limited OSA resolution. For the case where a mid-link OPC is installed, we attribute the mismatching at low frequency separation to a slight mismatch in the pump dither, resulting in residual dithering components on the conjugated CW laser (which will be explained in chapter 5). When comparing the system without OPC with the system that deploys mid-link OPC, figure 3.16 (a) and (b), we can see that the mid-link OPC results a clear nonlinear Kerr power compensation at strongly phase matched CW lasers.



*Figure 3.16: Nonlinear Kerr power as a function between two CW lasers (5dBm each, spectrally located at 1553nm) passing through 2x100km transmission system. (a) without OPC, (b) with OPC. [X4] [X15]*

### **3.4 Nonlinear Kerr Effects in OPC-Assisted Distributed Raman Amplified Transmission Systems**

In distributed Raman transmission systems, the power profile plays a role in describing the nonlinear behaviour of the transmission system, as described in section 3.2. The introduction of OPC in distributed Raman amplified links alters the accumulation of nonlinear Kerr effects. Based on equation 3.9 and the derivation steps of equation 3.16 to equation 3.21, we can describe the nonlinear Kerr generated by the end of OPC- assisted, dispersion unmanaged, distributed Raman amplified system as [X4]:

$$P_F(NL) = \frac{D^2 \gamma^2 N_{seg}^2}{9} P_q P_r P_s \left| e^{(-i\Delta\beta L) \sum_{k=1}^M \left[ \frac{e^{(g_k + i\Delta\beta)L_k} - 1}{g_k + i\Delta\beta} \right] \left[ \prod_{l=1}^{k-1} e^{(g_l + i\Delta\beta)L_l} \right]} - \sum_{k=1}^M \left[ \frac{e^{(g_k - i\Delta\beta)L_k} - 1}{g_k - i\Delta\beta} \right] \left[ \prod_{l=1}^{k-1} e^{(g_l - i\Delta\beta)L_l} \right] \right|^2 \frac{\sin^2(N\Delta\beta L / [2N_{seg}])}{\sin^2(\Delta\beta L / 2)} \quad (3.24)$$

The equation still shows (as equation 3.21) oscillation  $(\sin(N\Delta\beta L / (2N_{seg}))^2 / \sin(\Delta\beta L / 2)^2)$  in the nonlinear Kerr product power. The term  $|\cdot|^2$  represents the nonlinear Kerr product power generated by two consecutive Raman span separated by an OPC. A multi OPC system still acts as dispersion compensation for each segment in the system, as can be seen from the last term in equation 3.24. Figure 3.17 (right) shows the theoretical evaluation of the nonlinear Kerr product power as a function of frequency separation between two CW lasers (0dBm each, spectrally located at 1555nm) propagating through 200km distributed Raman system with different span lengths, different Raman power profiles ( $r_f$ ), with OPC, and without OPC; the correspondent power profiles for each span length used along the system can be seen in Figure 3.17 (left) [X4]. From the figure, we can see that deploying long distributed Raman span length will have high signal power excursions along the system (a maximum of 9.2dB in the 100km span) and higher signal power variance as a function of  $r_f$  (a maximum of 14.8dB in the 100km span). The signal power variation (along the span and as a function of  $r_f$ ) gets smaller as the deployed span length gets shorter (maximum of 0.18dB and 0.36dB, respectively, for 12.5km span). As a result, the variation (as a function of  $r_f$ ) in the nonlinear Kerr product power among strongly phase matched signals is higher when deploying long span length, this variation (as a function of  $r_f$ ) fades away as the span length gets shorter, see the right column of figure 3.16. If we compare the nonlinear Kerr product power generated in an OPC assisted system with the system that does not deploy OPC, we can see that significant nonlinearity compensation occurs among strongly phase matched signals (regardless of the span length). The nonlinearity compensation starts to fade away as the frequency separation increases, especially for systems with long span length (100km). The nonlinear Kerr product power generated in OPC assisted system reaches its peak at frequency separation ranging around 8GHz (for 2x100km system), 12GHz (for 4x50km system), 17GHz (for 8x25km), and 25GHz (for 16x12.5km). The frequency at which the peak of the nonlinear product power (in a system with OPC) occur shifts to higher frequency as the curvature in the signal power profile is reduced along the system.

Those peaks also follow the frequency at which the nonlinear product power (in a system without OPC) changes non-uniformly as a function of  $r_f$ .

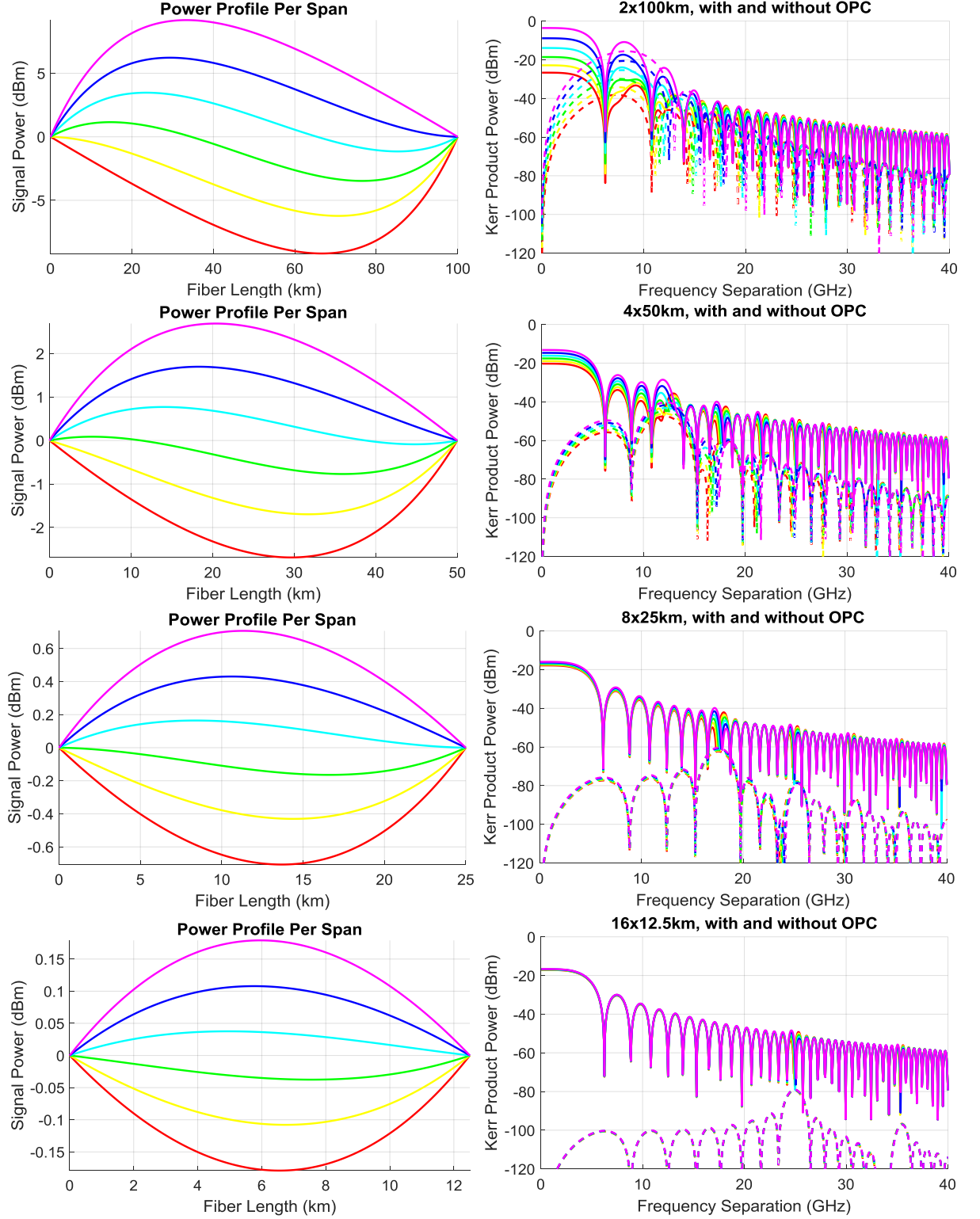


Figure 3.17: (left column) power profiles of distributed Raman with  $r_f$  ranging from  $r_f=0\%$  to  $100\%$  with a step of  $20\%$ . (right column) Nonlinear Kerr product power as a function of frequency separation between two CW lasers ( $0\text{dBm}$  each, spectrally located at  $1555\text{nm}$ ) propagating through  $200\text{km}$   $1^{\text{st}}$  order distributed Raman transmission system (with different span lengths). (solid lines) without mid-link OPC, (dashed lines) with mid-link OPC, the colour code indicates the power profile shown in the left column of the figure. [X4]

In general, as the frequency separation raise above the frequency separation at which the nonlinear Kerr product power reaches its maximum (in OPC assisted system), the nonlinear Kerr product power starts to decline at higher rate compared to the one generated in a system without OPC. The reasoning for this is the fact the value of  $\Delta\beta$  starts to dominate over gain/attenuation coefficients ( $g_x$ ) which gets the system to the state of OPC assisted quasi-lossless distributed Raman system that provide full compensation of the nonlinear Kerr effects:

$$\left| e^{(-i\Delta\beta L)} \frac{e^{i\Delta\beta L} - 1}{i\Delta\beta} - \frac{e^{-i\Delta\beta L} - 1}{-i\Delta\beta} \right|^2 = 0 \quad (3.25)$$

When comparing figure 3.17 to figure 3.14, we can see that the OPC can introduce higher nonlinear Kerr compensation in distributed Raman systems when compared to their equivalent of discretely amplified systems system, especially at shorter span lengths. For example, the nonlinear Kerr product power generated in OPC assisted 16x12.5km Raman system does not rise above -95dBm over the frequency separation ranging from 0 to 20GHz, while the equivalent lumped system shows a nonlinear Kerr product power at least 40dB higher than that value over the same frequency range. This shows a clear advantage of OPC assisted Raman system over OPC assisted discretely amplified transmission system. Figure 3.18 shows the validation of equation 3.24 using simulation results (with mid-link, single, OPC) conducted in VPITransmisisonMaker 9.8 [X4]. The simulation results show a good agreement with the theoretical predictions (considering  $M=L/2.5km$ ).

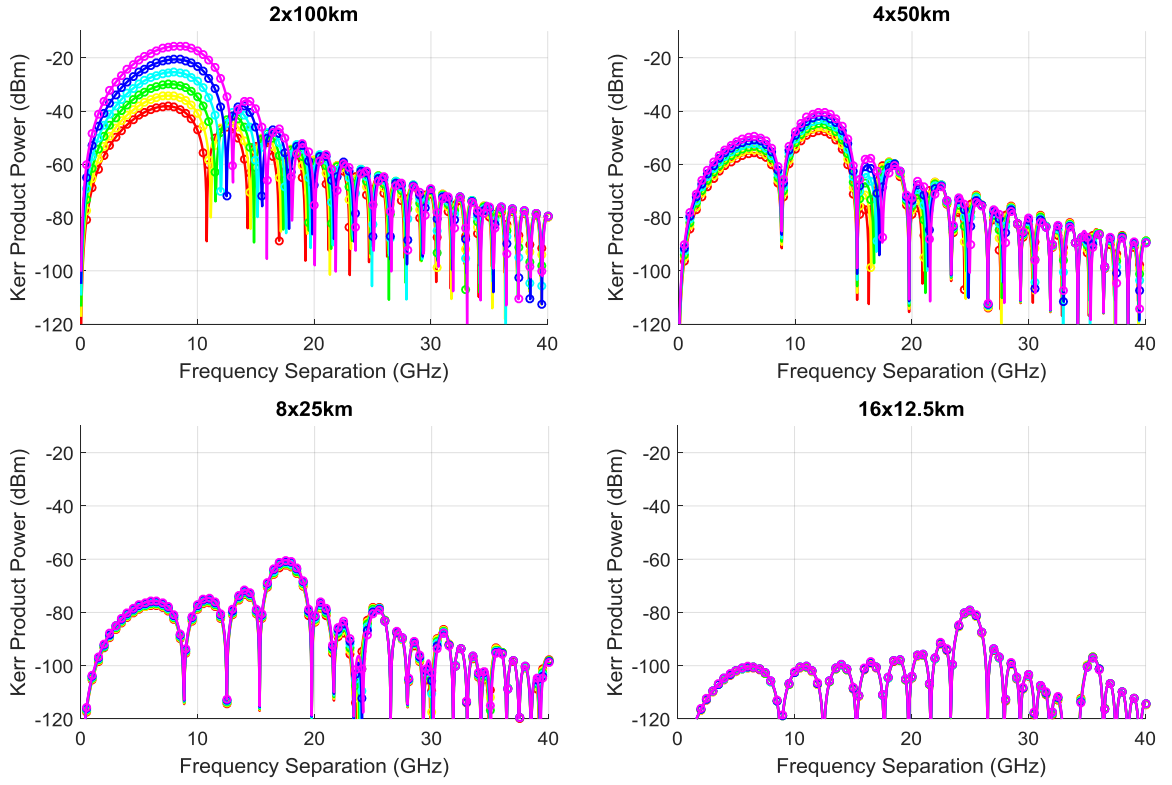


Figure 3.18: Verification of the curves in figure 3.17 using simulation results (with mid-link OPC). (solid lines) theoretical predictions, (open circles) simulation results. [X4]

The deployment of multi OPC in distributed Raman transmission system still causes a broadening of the nonlinear Kerr product power peaks (as seen in figure 3.15). Figure 3.19 shows a validation of equation 3.24, by considering multi-OPC ( $N_{seg} > 2$ ), using simulation results of nonlinear Kerr product power generated from two CW lasers (0dBm each) propagating through 24x50km distributed Raman system (considering different power profiles) with various number of OPCs. Again, the theoretical predictions match the simulation results. In this analysis, I have considered the first order Raman pumping but still equations 3.24 is still valid for generic Raman power profile, for example: higher order pumping [113,114], given that the correct  $g_i$  series was substituted in the equation.

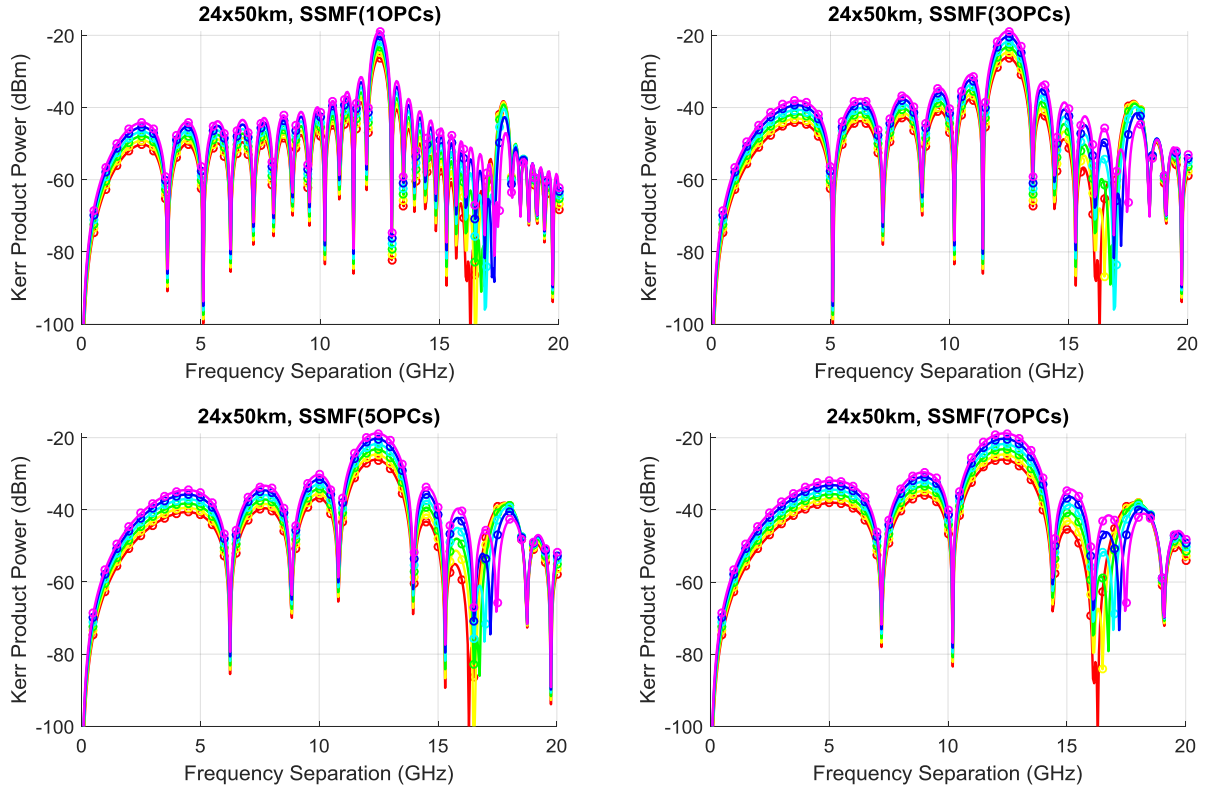


Figure 3.19: Nonlinear Kerr product power as a function of frequency separation between two CW lasers (0dBm each, spectrally located at 1555nm) propagating through 24x50km distributed Raman transmission system with different number of equally spaced and symmetrically located OPCs (1OPC, 3OPCs, 5OPCs, and 7OPCs). Colours represent different  $r_f$  values, same colour code as figure 3.16. [X4]

To experimentally validate equation 3.24, I have built a 2x50km distributed Raman transmission system and evaluated the nonlinear Kerr product generated from two CW lasers (6dBm each), as shown in figure 3.20 [X4]. A high-power Raman pump (located at 1455nm) was split equally to be injected (using a WDM) in the backward direction of the two 50km spans ( $r_f=0\%$ ). An isolator was used to prevent any remains of the Raman pump from passing through to the lasers or EDFAs. In between the two spans two paths were created: with and without OPC. In both paths an EDFA is used to restore the laser powers to 6dBm for each laser (9dBm output power). The path that deploys the OPC has used an EDFA pre-amplifier, band pass filters to eliminate out of band ASE noise (at the input and output of the OPC), a single fibre grating filtered high-power pump, and a highly nonlinear fibre ( $L=170\text{m}$ ,  $\lambda_0=1549.7\text{nm}$ ,  $\gamma = 14/\text{W/km}$ ). The OTDR measurements of power profile (shown as an inset to figure 3.20) were performed on both spans and compared with the theoretical power profile showing a good agreement.

~



Figure 3.20: Experimental setup to measure the nonlinear Kerr product power generated in 2x50km 1<sup>st</sup> order distributed Raman amplified system (with  $r_f=0\%$ ). Inset shows the theoretical and measured power profile of both 50km spans. [X4]



Figure 3.21: The nonlinear Kerr power as a function between two CW lasers passing through 2x50km backward pumped 1<sup>st</sup> order distributed Raman transmission system without OPC (a) with mid-link OPC (b). [X4]

Figure 3.21 shows the nonlinear Kerr product power generated along the experimental setup (without OPC (a) and with OPC (b)) as a function of the frequency separation between two CW lasers (6dBm each) propagating through the system. The experimental results show a good agreement with the theoretical predictions, with 0.8dB margin of mismatching, for both systems (without OPC (a) and with OPC (b)). The figure confirms the significant nonlinearity compensation over the full bandwidth of the measurement window.

## Summary and Conclusions

In this chapter, we have reviewed well-known equations that describes the nonlinear Kerr product power generated in discretely amplified and distributed Raman amplified optical transmission systems. We have shown that the nonlinear Kerr power generated in distributed Raman transmission system can be approximated by the multi-section approach, the accuracy

of the approximation modelling depends on the number of sections ( $M$ ) considered to describe the power profile. In section 3.2, I have introduced the two-section approximation that describes strongly forward pumped or strongly backward pumped distributed Raman transmission systems, the theoretical model has proved its validity using both experimental and simulation results.

In sections 3.3, I have introduced a generalised theoretical formula that describes the nonlinear Kerr product power accumulated along dispersion managed and unmanaged lumped system that deploy single or multi OPC; the closed form equations were validated both by experimental and simulation results. In section 3.4, I have introduced a theoretical model that describes the nonlinear Kerr power accumulated along OPC assisted dispersion uncompensated distributed Raman systems; this theoretical model was validated using numerical analysis and experimental results. The results have shown that deploying mid-link OPC in discretely amplified system may partially compensate for the accumulated nonlinearities along the system, which manifests in the full compensation of nonlinear products generated only among strongly phase matched signals ( $\Delta\beta \rightarrow 0$ ). The compensation efficiency achieved by the mid-link OPC (deployed in discretely amplified system) can be enhanced by shortening the amplifier spacing along the system (assuming uniform amplifier spacing). The nonlinearity compensation efficiency achieved from the deployment of mid-link OPC in distributed Raman systems is superior to the level of compensation efficiency achieved in the equivalent discretely amplified systems.

Finally, I have shown that the deployment of multiple OPCs may diminish the level of nonlinearity compensation achieved by a single, mid-link, OPC in any system (discretely amplified or distributed Raman). The periodic dispersion compensation that accompanies the deployment of multiple OPC enhances the generation of nonlinear Kerr effects by broadening the peaks of nonlinear Kerr power (reduction in the oscillation of nonlinear product power, as a function of frequency separation). The degradation in nonlinearity compensation efficiency does not mean that a multi-OPC system is always inferior to a single OPC system, since (as we will see in the next chapter) the multi-OPC minimises the non-deterministic nonlinear Kerr interactions.



# Chapter 4 : Nonlinear Performance Limits of Optical Transmission Systems

Contributions: [X1], [X2], [X5], [X6], [X7], [X12], [X17], and [X19].

Long-haul optical fibre transmission systems are designed to achieve a target distance reach and deliver maximum digital capacity. The design of long haul optical links considers both the linear and the nonlinear noise accumulation along the link; since the noise acts as a limiting factor to the maximum deliverable capacity, quality of performance, and the maximum distance reach. The nonlinear Shannon limit [20,115] identifies the spectral efficiency (bps/Hz) as a function of the SNR of the received optical signals [22]. The maximum performance limits and distance reach of a long-haul optical transmission system is directly dependent on a trade-off between of the linear noise, generated from inline optical amplifiers, and nonlinear noise, generated from signal interference due to nonlinear Kerr effects of the optical fibre.

The accumulation of nonlinear Kerr effects along the optical transmission system, shown in chapter 4, can be used to calculate the nonlinear noise that limits the performance of the modulated signals propagating through the optical transmission system. The accumulation of nonlinear effects can be deterministic, such as the signal-signal nonlinear interactions, and non-deterministic (stochastically random), such as: signal-signal nonlinear interactions with the presence of PMD effects [116] [X9] and the signal-noise nonlinear interactions [117] [X7,X10]. The calculation of nonlinear threshold (nonlinear noise limit) in optical transmission systems [46,48,73,118,119] requires performing a double integration (over the bandwidth of the modulated signal) of the analytical formula that represents the nonlinear Kerr product power generated from the nonlinear interaction of (up to) three optical waves (derived and validated for various systems in chapter 3). Closed form equations can be derived from the double integration [46,119,120] (under certain assumptions) to simplify the prediction of the accumulated nonlinear noise generated in an optical transmission system. DBP or OPC, can

compensate for the deterministic nonlinear Kerr effects accumulated along the system, which leads to the performance enhancement of such systems (when compared to the conventional Electronically Dispersion Compensated, EDC system). Whilst nonlinearity compensation techniques can compensate for deterministic nonlinear Kerr effects, these techniques cannot fully compensate for the non-deterministic nonlinear effects. The non-deterministic nonlinear Kerr products cannot be compensated, but they can be minimised by introducing multi-OPC which linearise the higher order accumulation of these nonlinear products [121][X6,X7,X9,X10]. The ultimate performance of optical transmission system that deploy nonlinearity compensation techniques is limited by the nonlinear signal-noise interactions, which can be reached when the system deploys zero-PMD fibre.

In this chapter, we will evaluate the theoretical performance limits of modulated signals propagating through various optical transmission systems. We have introduced a closed form equation that predicts the residual nonlinear noise ratio in OPC assisted discretely amplified system (that deploys long span length). This equation is validated in this chapter by simulation results and will be validated by experimental results in chapter 6. Also, we have derived closed form equations, validated by simulation results, that identify the non-deterministic signal-noise nonlinear interaction limit for modulated signals propagating through discretely amplified system and quasi-lossless distributed Raman systems. By numerically performing the double integration (over bandwidth) of equations: 3.7 (EDFA system without OPC), 3.9 (Raman system without OPC), 3.23 (OPC assisted EDFA system), and 3.24 (OPC assisted Raman system); we have been able to identify the performance limits of various simulated optical transmission systems. We will show that the nonlinearity compensation efficiency of OPC assisted discretely amplified optical transmission system is highly dependent on the bandwidth of the modulated signals, especially when long span length is used across the system. The results will also show that the deployment of multiple OPCs in a system limited by deterministic signal-signal nonlinear interactions will always perform worse than the system that deploys a single mid-link OPC. By comparing OPC assisted discretely amplified systems with OPC assisted distributed Raman system, we will show that the performance enhancement achieved in distributed Raman system is far superior to the enhancements achieved in discretely amplified systems.

## 4.1 Nonlinear Noise Generation Efficiency

In chapter 3, we have reported the analytical description of the nonlinear Kerr product generated due to the interaction among three optical spectral components (spectrally located at

$\omega_q$ ,  $\omega_r$ , and  $\omega_s$ ) and propagating through various transmission systems. When modulated signals propagate through the optical transmission system, the nonlinear Kerr interactions occur among all the spectral components that construct the signal. The bandwidth and the spectral shape of the modulated signals play a role in the calculation of the total nonlinear power generated due to the Kerr interactions. In the ideal case, optical transmission systems transmit spectrally efficient modulated signals covering the maximum optical bandwidth, i.e. Nyquist WDM or Orthogonal Frequency Division Multiplexed (OFDM) multicarrier banks. Such pulse shaping techniques construct a rectangular, flat top, spectrum where the optical power is equally divided among all the spectral components of the modulated signals. To calculate the total nonlinear noise generated among such signals, Nyquist WDM or OFDM, a double integration (over the bandwidth  $B_w$  of the signals) is required to include the phase mismatching effects on Kerr generation efficiency. The double integration sweeps the frequency separation between two optical waves ( $f_q$  and  $f_r$ ) and a reference frequency ( $f_s$ ) over the signal bandwidth to calculate the nonlinear noise generation efficiency [46,122]:

$$\eta = \frac{I_{NL}}{I_s^3} = \frac{1}{2} \int_{-B_w/2}^{B_w/2} \int_{-B_w/2}^{B_w/2} \frac{P_F(f_1, f_2)}{P_s^3} df_1 df_2 \quad (4.1)$$

where the scaling factor of 0.5 was added to correct the double counting of Kerr products along the integration, and  $I_x$  represents the power spectral density of the signal (W/Hz). The integration assumes a uniform power spectral density ( $I_s$ ) across the optical bandwidth, which result the cubic relation of the nonlinear noise power spectral density ( $I_{NL}$ ) and the signal power spectral density ( $I_s = P_s/B_w$ ). Fixing the reference frequency ( $f_s$ ) at the centre of the modulated signals simplifies the phase mismatching scaling factor (see equation 2.8) to be  $f_1 f_2$  instead of  $(f_q - f_s)(f_r - f_s)$ . By substituting the nonlinear Kerr power functions reported in chapter 3 into equation 4.1, the nonlinear noise generation efficiency can be written as (assuming zero dispersion slope):

- Discretely amplified transmission system [46]

$$\eta = 8\gamma^2 \int_0^{B_w/2} \int_0^{B_w/2} \left[ \frac{\alpha^2 L_{eff}^2}{\alpha^2 + (4\pi^2 \beta'' f_1 f_2)^2} \right] \left[ 1 + \frac{4e^{(-\alpha L)} \sin^2(2\pi^2 \beta'' L f_1 f_2)}{(1 - e^{(-\alpha L)})^2} \right] \left[ \frac{\sin^2(2\pi^2 \delta \beta'' N L f_1 f_2)}{\sin^2(2\pi^2 \delta \beta'' L f_1 f_2)} \right] df_1 df_2 \quad (4.2)$$

- OPC assisted discretely amplified transmission system

$$\eta = 2\gamma^2 N_{seg}^2 \int_0^{B_w/2} \int_0^{B_w/2} \left| e^{(-i\delta 4\pi^2 \beta'' f_1 f_2 L)} \frac{e^{([- \alpha + i4\pi^2 \beta'' f_1 f_2] L)} - 1}{-\alpha + i4\pi^2 \beta'' f_1 f_2} - \frac{e^{([- -\alpha - i4\pi^2 \beta'' f_1 f_2] L)} - 1}{-\alpha - i4\pi^2 \beta'' f_1 f_2} \right|^2 \left[ \frac{\sin^2(2\pi^2 \beta'' f_1 f_2 \delta N L / N_{seg})}{\sin^2(2\pi^2 \beta'' f_1 f_2 \delta L)} \right] df_1 df_2 \quad (4.3)$$

$$\eta|_{\delta=0} = 8\gamma^2 N^2 \int_0^{B_w/2} \int_0^{B_w/2} \left[ \frac{\alpha e^{-\alpha L} \sin(4\pi^2 \beta'' f_1 f_2 L) + 4\pi^2 \beta'' f_1 f_2 (e^{-\alpha L} \cos(4\pi^2 \beta'' f_1 f_2 L) - 1)}{\alpha^2 + (4\pi^2 \beta'' f_1 f_2)^2} \right]^2 df_1 df_2 \quad (4.4)$$

$$\eta|_{\delta=1} = 8\gamma^2 N_{seg}^2 \int_0^{B_w/2} \int_0^{B_w/2} \left[ \frac{\alpha (e^{-\alpha L} + 1) \sin(2\pi^2 \beta'' f_1 f_2 L) + 4\pi^2 \beta'' f_1 f_2 (e^{-\alpha L} - 1) \cos(2\pi^2 \beta'' f_1 f_2 L)}{\alpha^2 + (4\pi^2 \beta'' f_1 f_2)^2} \right]^2 \left[ \frac{\sin^2(2\pi^2 \beta'' N L f_1 f_2 / N_{seg})}{\sin^2(2\pi^2 \beta'' L f_1 f_2)} \right] df_1 df_2 \quad (4.5)$$

- Distributed Raman transmission system

$$\eta = 8\gamma^2 \int_0^{B_w/2} \int_0^{B_w/2} \left| \sum_{k=1}^M \left[ \frac{e^{(g_k + i4\pi^2 \beta'' f_1 f_2) L_k} - 1}{g_k + i4\pi^2 \beta'' f_1 f_2} \right] \left[ \prod_{l=1}^{k-1} e^{(g_l + i4\pi^2 \beta'' f_1 f_2) L_l} \right] \right|^2 \left[ \frac{\sin^2(2\pi^2 \beta'' N L f_1 f_2)}{\sin^2(2\pi^2 \beta'' L f_1 f_2)} \right] df_1 df_2 \quad (4.6)$$

- OPC assisted distributed Raman transmission system

$$\eta = 8\gamma^2 N_{seg}^2 \int_0^{B_w/2} \int_0^{B_w/2} \left| e^{(-i4\pi^2 \beta'' f_1 f_2 L)} \sum_{k=1}^M \left[ \frac{e^{(g_k + i4\pi^2 \beta'' f_1 f_2) L_k} - 1}{g_k + i4\pi^2 \beta'' f_1 f_2} \right] \left[ \prod_{l=1}^{k-1} e^{(g_l + i4\pi^2 \beta'' f_1 f_2) L_l} \right] - \sum_{k=1}^M \left[ \frac{e^{(g_k - i4\pi^2 \beta'' f_1 f_2) L_k} - 1}{g_k - i4\pi^2 \beta'' f_1 f_2} \right] \left[ \prod_{l=1}^{k-1} e^{(g_l - i4\pi^2 \beta'' f_1 f_2) L_l} \right] \right|^2 \left[ \frac{\sin^2(2\pi^2 \beta'' N L f_1 f_2 / N_{seg})}{\sin^2(2\pi^2 \beta'' L f_1 f_2)} \right] df_1 df_2 \quad (4.7)$$

- Ideal (quasi-lossless,  $\alpha=0$ ) distributed Raman transmission system [123]

$$\eta = 32\gamma^2 \int_0^{B_w/2} \int_0^{B_w/2} \frac{\sin^2(2\pi^2 \beta'' N L f_1 f_2)}{(4\pi^2 \beta'' f_1 f_2)^2} df_1 df_2 \quad (4.8)$$

- OPC assisted ideal (quasi-lossless,  $\alpha=0$ ) distributed Raman transmission system

$$\eta = 0 \quad (4.9)$$

In equations 4.2-4.9, the degeneracy factor  $D$  was substituted by a factor of 6 to represent the dominant non-degenerate FWM that occurs in modulated signals with large bandwidth. Due to the symmetry of nonlinear Kerr process as a function of phase mismatching, the integration limits were changed to start from 0 instead of  $-B_w/2$  and a scaling factor of 4 was accordingly added to the integrations. Numerical solutions of equations 4.2-4.9 generate the nonlinear noise generation efficiency of spectrally flat modulated signals propagating through the aforementioned systems by substituting systems parameters, such as: signal's bandwidth ( $B_w$ ), attenuation coefficient ( $\alpha$ ), chromatic dispersion of the fibre ( $\beta''$ ), residual dispersion ( $\delta$ ) in dispersion managed systems, number of spans ( $N$ ), span length ( $L$ ), number of segments in OPC assisted systems ( $N_{seg}$ ), and the power profile of distributed Raman system represented by ( $g_x$ ) series.

A few approximations have been reported in literature to provide a closed form solution to equation 4.2 which represents the nonlinear noise generation efficiency in discretely amplified transmission systems [46,47,119,122]. In these approximations, a long span length ( $\exp(-\alpha L) \ll 1$ ,  $L_{eff} = 1/\alpha$ ) was assumed to solve equation 4.2; which results [46]:

$$\eta \approx 8\gamma^2 \int_{B_0/2}^{B_w/2} \int_0^\infty \left[ \frac{1}{\alpha^2 + (4\pi^2 \beta'' f_1 f_2)^2} \right] \left[ N + 2 \sum_{n=1}^{N-1} (N-n) \cos(4\pi^2 n \delta \beta'' L f_1 f_2) \right] df_1 df_2 \quad (4.10)$$

$$B_0 = \max \left( B_{sc}, \frac{\alpha}{2\pi^2 |\beta''_{SMF}| B_w} \right)$$

When comparing equation 4.2 to equation 4.10, it can be seen that the integration limits were changed to achieve closed form solution. The upper limit of the internal integration was changed from  $B_w/2$  to  $\infty$  (assuming  $B_w > 50\text{GHz}$ ) since the nonlinear Kerr efficiency drops dramatically to ignorable value for large frequency separation  $f_l$ . On the other hand, the lower limit of the outer integration was replaced by the maximum correlated optical signal bandwidth ( $B_0/2$ ) defined as the maximum between the bandwidth of an OFDM subcarrier and the walk-off bandwidth [46]; the walk-off bandwidth is identified as the 3dB bandwidth of the maximum nonlinear Kerr response (strongly phase matched, check chapter 3) which is inversely proportional to the signal bandwidth and dispersion length of each span along the link. This approximation assumes that the phase estimation in the DSP can recover correlated intra channel nonlinear interference within the correlated optical bandwidth ( $B_0$ ). The oscillating scaling factor due to the phase mismatching accumulation along the spans,

$(\sin(\Delta\beta NL/2)/\sin(\Delta\beta L/2))^2$ , was expanded into a series of cosines. The complex functional analysis can be used to solve the first (internal) integration as [46]:

$$\int_0^\infty \frac{F(x)}{x^2 + a^2} dx = \frac{\pi}{2a} F(ia) \quad (4.11)$$

As  $\cos(x) = \text{Re}[\exp(ix)]$ , the internal integration can be solved as [46]:

$$\begin{aligned} \eta &= 8\gamma^2 \int_{B_0/2}^{B_w/2} \int_0^\infty \frac{1}{\left(4\pi^2 \beta'' f_2\right)^2} \left[ \frac{\text{Re} \left[ N + 2 \sum_{n=1}^{N-1} (N-n) \exp(i4\pi^2 n \delta \beta'' L f_1 f_2) \right]}{\left( \frac{\alpha}{4\pi^2 \beta'' f_2} \right)^2 + f_1^2} \right] df_1 df_2 \\ &= \frac{\gamma^2}{\pi |\beta''| \alpha} \left[ N + 2 \sum_{n=1}^{N-1} (N-n) \exp(-\alpha n \delta L) \right] \int_{B_0/2}^{B_w/2} \frac{1}{f_2} df_2 \end{aligned} \quad (4.12)$$

To simplify the final solution to [46]:

$$\eta = \frac{\gamma^2}{\pi |\beta''| \alpha} \left[ N + 2 \frac{e^{-\alpha \delta L} (N - 1 + e^{-\alpha \delta NL} - N e^{-\alpha \delta L})}{(e^{-\alpha \delta L} - 1)^2} \right] \log \left( \frac{B_w}{B_0} \right) \quad (4.13)$$

where  $\gamma^2 = \gamma_0^2$  for a single polarisation transmission, while  $\gamma^2 = 8\gamma_0^2/27$  for a dual polarisation transmission system with random birefringence optical fibres [47],  $\gamma_0$  is the intrinsic nonlinear factor of the fibre.. In a system where the frequency separation between channels is greater than the baud rate of the channels, nonlinear noise contributions from the spectral gaps between the signals must be excluded from the outer integration [124] which results a correction factor to the bandwidth inside the natural logarithm of equation 4.13. The second term of equation 4.13 illustrates the effect of residual dispersion in dispersion-managed discretely-amplified transmission systems.

Equation 4.3 represents the nonlinear noise generation efficiency accumulated along dispersion managed or unmanaged discretely amplified systems that deploy arbitrary number of symmetrically located OPC(s). Equations 4.4 and 4.5 simplify the mathematical expression when the system is either fully dispersion compensated ( $\delta=0$ ) or dispersion uncompensated ( $\delta=1$ ) systems, respectively. Apart from the numerical solution of equations 4.4 and 4.5 to find the nonlinear noise generation efficiency, an approximation can be made to calculate the residual nonlinearity relative to the nonlinear noise generation efficiency of a system without OPC. A simple approximation can be made if the double integration was performed on the ratio

of nonlinear Kerr power of a system with mid-link OPC to the nonlinear Kerr power generated in a system without OPC, as:

$$\frac{P^{w/OPC}}{P^{wo/OPC}} = \frac{4}{\alpha^2 + (4\pi^2 \beta'' f_1 f_2)^2} \frac{\sin^2(\pi^2 \beta'' f_1 f_2 NL)}{\sin^2(2\pi^2 \beta'' f_1 f_2 NL)} \frac{\left[ \alpha (e^{-\alpha L} + 1) \sin(2\pi^2 \beta'' f_1 f_2 L) + 4\pi^2 \beta'' f_1 f_2 (e^{-\alpha L} - 1) \cos(2\pi^2 \beta'' f_1 f_2 L) \right]^2}{\left[ (1 - e^{-\alpha L})^2 + 4e^{-\alpha L} \sin^2(2\pi^2 \beta'' f_1 f_2 L) \right]} \quad (4.14)$$

If long span length assumption was made ( $\exp(-\alpha L) \ll 1$ ,  $L_{eff} = 1/\alpha^2$ ), then the expression simplifies to:

$$\frac{P^{w/OPC}}{P^{wo/OPC}} = \frac{4}{\alpha^2 + (4\pi^2 \beta'' f_1 f_2)^2} \frac{\sin^2(\pi^2 \beta'' f_1 f_2 NL)}{\sin^2(2\pi^2 \beta'' f_1 f_2 NL)} \frac{\left[ \alpha \sin(2\pi^2 \beta'' f_1 f_2 L) - 4\pi^2 \beta'' f_1 f_2 \cos(2\pi^2 \beta'' f_1 f_2 L) \right]^2}{\left[ \alpha \sin(2\pi^2 \beta'' f_1 f_2 L) - 4\pi^2 \beta'' f_1 f_2 \cos(2\pi^2 \beta'' f_1 f_2 L) \right]^2} \quad (4.15)$$

The expression can be further simplified at strongly phase matched region of the nonlinear interaction, such that:  $4\sin^2(\Delta\beta NL/4)/\sin^2(\Delta\beta NL/2) \approx 1$ ,  $\sin(\Delta\beta NL/2) \approx 0$ , and  $\cos(\Delta\beta NL/2) \approx 1$ . These assumptions are clearly valid for strongly phase matched signals ( $\Delta\beta \rightarrow 0$ ), while in the weakly phase matched region, the generated nonlinear Kerr power generated in OPC assisted system is equal to the nonlinear Kerr power (at the peaks) generated in a system that does not deploy OPC, as shown in figure 3.14. If we apply such approximation, equation 4.15 can be simplified to:

$$\frac{P^{w/OPC}}{P^{wo/OPC}} \approx \frac{(4\pi^2 \beta'' f_1 f_2)^2}{\alpha^2 + (4\pi^2 \beta'' f_1 f_2)^2} \quad (4.16)$$

Figure 4.1 shows a comparison between the exact residual nonlinearity ratio (equation 4.15) and the proposed approximation (equation 4.16) as a function of  $f_1 f_2$  (assuming that  $f_1 = f_2$ ) [X12]. The figure shows that the residual nonlinearity ratio calculated from the approximation follows the trend of the exact expression (equation 4.15), but the approximation ignores the effect of phase mismatching shift introduced by the OPC (halving the frequency of Kerr power oscillation at large frequency separation). The sharp peaks in figure 4.1 correspond to the mismatching at the nulls of the nonlinear product power curves (check figure 3.14) which have



negligible nonlinear power when compared to the peaks of the nonlinear product power (check figure 3.14) that corresponds to the curved peaks of the red line (in figure 4.1) that match the blue line (in figure 4.1).

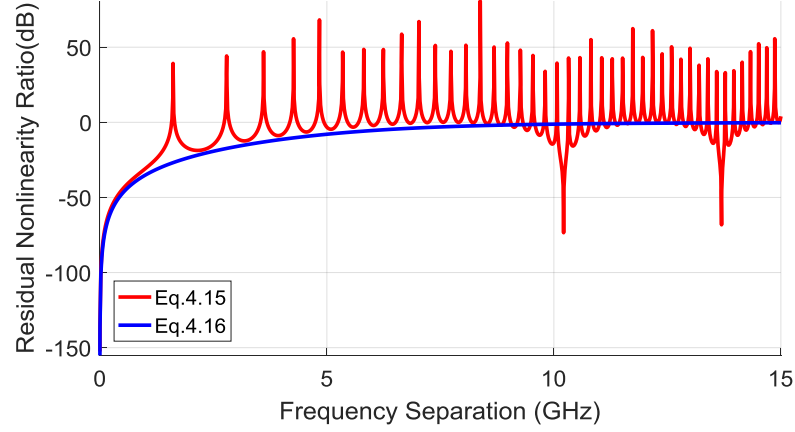


Figure 4.1: Nonlinear Kerr power ratio between discretely amplified system with mid-link OPC and a system without OPC. ( $N=30$ , fibre type: SSMF) [X12]

To calculate the residual nonlinear noise ratio (of a system with OPC to a system without OPC), we double integrate the approximated residual nonlinear power ratio (equation 4.16) and normalise it over the bandwidth of the signal as:

$$\begin{aligned}\kappa &\approx \frac{4}{B_w^2} \int_0^{B_w/2} \int_0^{B_w/2} \frac{(4\pi^2 \beta'' f_1 f_2)^2}{\alpha^2 + (4\pi^2 \beta'' f_1 f_2)^2} df_1 df_2 \\ &\approx \frac{4}{B_w^2} \int_0^{B_w/2} \int_0^{B_w/2} \frac{f_1^2}{\left(\frac{\alpha}{4\pi^2 \beta'' f_2}\right)^2 + f_1^2} df_1 df_2\end{aligned}\quad (4.17)$$

Where  $\kappa$  is the residual nonlinear noise in OPC assisted discretely amplified system. The internal integration can be solved as follows:

$$\kappa \approx \frac{4}{B_w^2} \int_0^{B_w/2} \frac{B_w}{2} - \frac{\alpha}{4\pi^2 |\beta_2| f_2} \tan^{-1} \left( \frac{2\pi^2 |\beta_2| f_2 B_w}{\alpha} \right) df_2 \quad (4.18)$$

, and the second integration as:

$$\kappa \approx \frac{4}{B_w^2} \left[ \frac{B_w^2}{4} - \frac{i\alpha}{4\pi^2 |\beta_2|} \left( Li_2 \left( \frac{-i\pi^2 |\beta_2| B_w^2}{\alpha} \right) - Li_2 \left( \frac{i\pi^2 |\beta_2| B_w^2}{\alpha} \right) \right) \right] \quad (4.19)$$

where  $Li_2(x)$  is the polylogarithm function of the second order [125]. Finally, the approximated residual nonlinear noise ratio can be written in closed form as [X2,X12]:

$$\kappa \approx 1 - \frac{2\alpha}{\pi^2 |\beta_2| B_w^2} \operatorname{asinh} \left( \frac{\pi^2 |\beta_2| B_w^2}{2\alpha} \right) \quad (4.20)$$

Figure 4.2 shows the residual nonlinear noise ratio (system with OPC to system without OPC) as a function the modulated signal bandwidth propagating through the system (discretely amplified, dispersion uncompensated, with large span length). The figure shows that the mid-link OPC can compensate well above 10dB of nonlinear noise generated from modulated signals with bandwidth below 20GHz propagating through the system. As the bandwidth of modulated signal raises above 20GHz, the compensation ratio of nonlinear noise falls to an ignorable value to reach the saturation point at 100GHz where the introduction of the OPC barely compensates for the nonlinear noise generated in the discretely amplified system. At this saturation point, the nonlinear noise generated from the weakly phase matched signals is much larger than the nonlinear noise generated from strongly phase matched signals (which was compensated for by the mid-link OPC).

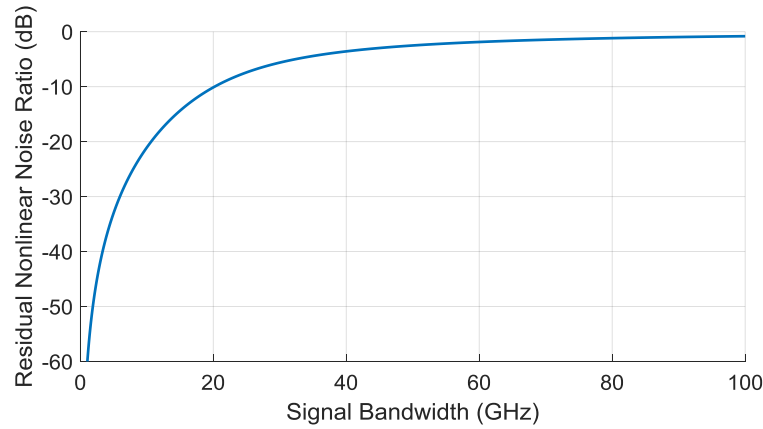


Figure 4.2: Residual nonlinear noise ratio (in dB) as a function the modulated signal bandwidth.

The nonlinear noise generated in ideal quasi-lossless distributed Raman transmission system (equation 4.8) can be solved the same way followed in equations 4.10 to 4.13. So, equation 4.8 can be rewritten as (assuming  $B_w > 50\text{GHz}$ ):

$$\eta = 32\gamma^2 \int_{B_0/2}^{B_w/2} \int_0^\infty \frac{\sin^2 \left( 2\pi^2 \beta'' L f_1 f_2 \right)}{\left( 4\pi^2 \beta'' f_1 f_2 \right)^2} df_1 df_2 \quad (4.21)$$

Using the complex functional analysis, the internal integral of equation 4.21 can be solved as:

$$\int_0^\infty \frac{\sin^2(ax)}{x^2} dx = \frac{\pi|a|}{2} \quad (4.22)$$

which results:

$$\begin{aligned} \eta &= \frac{2\gamma^2}{(\pi^2 \beta'')^2} \int_{B_0/2}^{B_w/2} \frac{\pi |2\pi^2 \beta'' L f_2|}{2f_2^2} df_2 \\ &= \frac{2\gamma^2 L}{\pi |\beta''|} \int_{B_0/2}^{B_w/2} \frac{1}{f_2} df_2 \end{aligned} \quad (4.23)$$

where  $L$  represents the total length of the ideal (quasi-lossless) distributed Raman link. Finally, the nonlinear noise generated under modulated signals propagating through an ideal (quasi-lossless) transmission system can be written in a closed form as [123] [X7]:

$$\eta = \frac{2\gamma^2 L}{\pi |\beta''|} \log(2\pi^2 |\beta''| L B_w^2) \quad (4.24)$$

The definition of  $B_0$  in equation 4.10 does not correctly reflect the nonlinear response in ideal quasi-lossless system ( $\alpha=0$ ). So, in equation 4.24 we have replaced  $L_{eff}=L/\alpha$  by the total length of the system ( $L$ ).

## 4.2 Nonlinear Noise Due to Signal-Noise Interactions

The nonlinear noise generation efficiency reported in the previous section identifies the nonlinear noise generated from signal-signal interaction. These signal-signal nonlinear Kerr interactions can be partially (as shown in equation 4.20, OPC assisted discretely amplified systems) or fully recovered either in the electronic domain (DBP [15]) or in the optical domain (OPC [16], e.g. OPC assisted ideal Raman shown in equation 4.9).

Ideal nonlinearity compensated transmission links (full field DBP, or OPC in quasi-lossless distributed Raman links) are limited by the non-deterministic nonlinear Kerr effects of signal-signal interaction due to the influence of Polarisation Mode Dispersion (PMD) [116] [X9]. The stochastic randomness of polarisation state accompanied with the PMD (phase shift between the two polarisation states) of the fibre leads to a random signal-signal (both polarisations) interactions which cannot be predicted by DBP [116]. Mid-link and multi-OPC can show higher improvements (compared to DBP system) since it reduces the signal-signal polarisation decorrelation length resulted by the random birefringence and PMD effects [X9]. These

random signal-signal nonlinear interactions are commonly refer to as non-deterministic nonlinear interactions [116]. The minimisation of PMD (ideally zero-PMD) in optical fibres unveils another non-deterministic Kerr effect due to the signal-noise nonlinear Kerr interactions (known as the Gordon-Mollenauer effect [126] or parametric noise amplification [X10]). In this thesis, we will concentrate on the signal-noise nonlinear Kerr interaction limit in full-field DBP and OPC assisted systems, as we believe it is the ultimate non-deterministic nonlinear limit of optical fibre systems that deploy ideal nonlinearity compensation techniques.

The nonlinear interaction between the modulated signals and ASE noise impose degeneracy factor change due to the fact that ASE spectral components are located under the signals frequency components to generate: signal-signal-signal, signal-signal-noise, signal-noise-noise, and noise-noise-noise nonlinear products. The degeneracy of these nonlinear interactions can be concluded from:

$$I_{sss,ssn,snm,nnn} = (I_Q + I_q)(I_R + I_r)(I_S + I_s)\eta \quad (4.25)$$

where  $I_Y$  is the power spectral density of the modulated signal spectral component  $Y$ , while  $I_y$  is the ASE noise power spectral density imposed under the  $Y$ th signal spectral component,  $\eta$  is the nonlinear noise generation efficiency (described in the previous section),  $I_{sss,ssn,snm,nnn}$  represents the power spectral density of nonlinear noise generated from the interactions among: signal-signal-signal, signal-signal-noise, signal-noise-noise, and noise-noise-noise interactions. Expanding equation 4.25 results:

$$\begin{bmatrix} I_{sss} \\ I_{ssn} \\ I_{snm} \\ I_{nnn} \end{bmatrix} = \begin{bmatrix} (I_p I_Q I_R) \\ (I_p I_Q I_r) + (I_p I_q I_R) + (I_p I_Q I_R) \\ (I_p I_q I_r) + (I_p I_Q I_r) + (I_p I_q I_R) \\ (I_p I_q I_r) \end{bmatrix} \eta \quad (4.26)$$

The first row in the squared bracket of equation 4.26 represents the nonlinear noise generated from signal-signal-signal interactions (as in the previous section) which can be fully compensated by nonlinear compensation techniques (if we assume zero PMD effects). The second row represents nonlinear noise generated from signal-signal-noise interaction [116,117] [X7,X9,X10,X19], the third and fourth rows represent the power spectral density of the nonlinear noise generated respectively from signal-noise-noise interactions and noise-noise-noise interactions and may usually be neglected. If we assume that the ASE noise power

spectral density is uniform across the amplification bandwidth and the modulated signals also have flats spectral shape, then the signal-signal-noise Kerr power spectral density have an extra degeneracy factor of 3 multiplied by the nonlinear noise generation efficiency (described in the previous section). So, the power spectral density of Kerr nonlinear noise generated from signal-signal-noise interaction due to the propagation of signals and ASE noise through  $N$  spans can be written as:

$$I_{ssn}^{1st-order}(n) = 3I_s^2 I_{ASE} \eta(n) \quad (4.27)$$

To analyse the accumulation of 1<sup>st</sup> order signal-noise nonlinear Kerr interactions (the 1<sup>st</sup> order distinction will be clarified later), we must follow signal propagation with ASE noise (added by each amplifier in the system). Figure 4.3 shows 4-span discretely amplified transmission system and the accumulation of signal- noise nonlinear noise in a system that uses ideal DBP (the blue side of the schematic) to fully compensate for the signal-signal-signal nonlinear interactions.

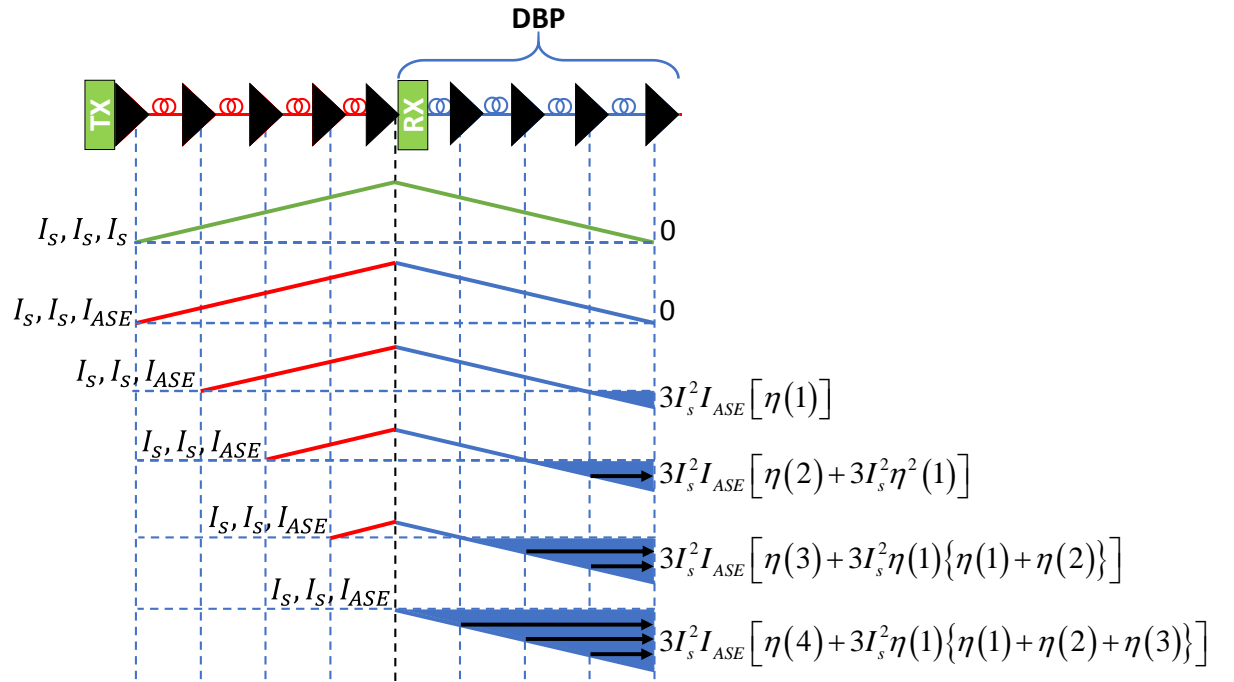


Figure 4.3: Kerr nonlinear noise accumulation in discretely amplified optical transmission system that deploys full field DBP. [X1]

As the signal-signal-signal nonlinear Kerr interactions are fully recovered using DBP, the nonlinear Kerr interactions between signals and ASE noise emitted from the first EDFA is also fully recovered by DBP due to the matching path of the co-propagation (in the optical domain) and the backpropagation (in the digital domain). The ASE noise generated from the second

amplifier propagate with signal for three spans and backpropagate (at the receiver) for four spans; this will result an over-compensation of the signal-noise interactions equivalent to one span ( $3I_s^2 I_{ASE} \eta(1)$ ), we will call this interaction as 1<sup>st</sup> order signal-noise interaction (represented by filled triangles in figure 4.3). The ASE noise generated from the third amplifier will co-propagate with signals over two spans and backpropagate (at the receiver) for four spans; this will result an over-compensation of the signal-ASE interactions to result 1<sup>st</sup> order interactions equivalent to two spans ( $3I_s^2 I_{ASE} \eta(2)$ ). Furthermore, by the end of the first overcompensated span the 1<sup>st</sup> order signal-noise interaction ( $3I_s^2 I_{ASE} \eta(1)$ ) will also interact with signals over the second overcompensated span to generate 2<sup>nd</sup> order signal-ASE interactions (represented by black arrows in figure 4.3). The 2<sup>nd</sup> order signal-noise interaction can be written (for  $n$  overcompensated spans) as:

$$I_{ssn}^{2nd-Order}(n) = 3I_s^2 \left[ 3I_s^2 I_{ASE} \eta(1) \right] \sum_{i=1}^{n-1} \eta(n) \quad (4.28)$$

The 2<sup>nd</sup> order signal-noise interactions result from a seed of 1<sup>st</sup> order signal-noise products interacting with modulated signals and it must be taken into account, since the 1<sup>st</sup> order signal-noise interactions can reach level of power higher than the power spectral density of the ASE noise generated from a single EDFA. The 2<sup>nd</sup> order signal-noise interactions (as it can be seen from equation 4.28) grows quartically as a function of the signal's power spectral density. The ASE noise added by the fourth and fifth EDFAs results signal-noise interactions (1<sup>st</sup> and 2<sup>nd</sup> order) due to the overcompensation of the DBP for three and four spans, respectively; leading to generate 1<sup>st</sup> order signal-noise interactions ( $I_{ssn}^{1st-order}(3)$  and  $I_{ssn}^{1st-order}(4)$ ) and 2<sup>nd</sup> order signal-noise interactions ( $I_{ssn}^{2nd-order}(3)$  and  $I_{ssn}^{2nd-order}(4)$ ).

The summation of all signal-noise nonlinear Kerr power spectral densities (including both 1<sup>st</sup> and 2<sup>nd</sup> order) can be mathematically formulated for a system with  $N$  spans and  $N+1$  EDFAs, which result the following total nonlinear generation efficiency due to signal-noise interactions ( $\eta_{ssn}$ ) [X1,X7]:

$$\eta_{ssn}(N) = \frac{I_{ssn}(N)}{I_s^2 I_{ASE}} = 3 \left[ \sum_{n=1}^N \eta(n) + 3I_s^2 \eta(1) \sum_{n=1}^N \sum_{i=1}^{n-1} \eta(i) \right] \quad (4.29)$$

where the first term represents the nonlinear noise generation efficiency of the 1<sup>st</sup> order signal-noise nonlinear interactions, and the second term represents the nonlinear noise generation efficiency of the 2<sup>nd</sup> order signal-noise nonlinear interactions. Equation 4.29 assumes that the

transmission system is uniform where all the spans have the same length and each amplifier in the system emits that same ASE power spectral density ( $I_{ASE}$ ). Equation 4.29 can be simplified for dispersion uncompensated transmission systems that uses large span length, where the second term of equation 4.13 can be simplified to become  $N$ . As a result, the nonlinear noise generation efficiency of signal-noise interactions can be simplified from the summation form to [X1,X7]:

$$\eta_{sn}(N) = \frac{3\gamma^2 N(N+1)}{2\pi\alpha|\beta''|} \left[ 1 + \frac{3\gamma^2 I_s^2 (N-1)}{\pi\alpha|\beta''|} \log\left(\frac{B_w}{B_0}\right) \right] \log\left(\frac{B_w}{B_0}\right) \quad (4.30)$$

The equation shows that the efficiency of 1<sup>st</sup> order signal-noise interactions grows quadratically with both the number of the amplifiers in the system and the signal power spectral density. On the other hand, the efficiency of 2<sup>nd</sup> order signal-noise interactions grow cubically with the number of spans and quartically with signal power spectral density.

In OPC assisted system, the OPC compensates for the nonlinear interactions among signal-signal or signal-noise as long as they are symmetrically propagating through the same number of spans on either side of the OPC. Figure 4.4 shows the nonlinear signal-signal and signal-noise interactions evolution along an 8-span system with (a) mid-link OPC and (b) 2-OPC system (double segmented OPC spacing). As seen from figure 4.4(a), a mid-link OPC breaks the 8 spans into two 4-span segments where the signal-signal nonlinear interactions are fully recovered. The nonlinear interactions between signals and ASE noise emitted from the first amplifier is also fully recovered since the signals and ASE propagate through two segments with the same length. The ASE noise generated from the second amplifier propagate with the signals through 3 spans in the first segment and four spans in the second segment, which result signal-noise interactions to be overcompensated over one span. The asymmetric segment size on both sides of the OPC results the ASE noise generated from the third, fourth, and fifth amplifiers to generate nonlinear signal-noise interactions equivalent to the overcompensation that the path imposes on signals propagating with ASE noise. The overcompensation of signal-noise interactions generated in the first segment contains 1<sup>st</sup> order signal-noise interactions (represented by the filled red triangles) and 2<sup>nd</sup> order signal-noise interactions (represented by the black arrows). At OPC, ASE noise generated from the OPC propagates with the signal along the second segment without any nonlinearity compensation, which results nonlinear signal-noise interaction of the 1<sup>st</sup> order and 2<sup>nd</sup> order along four spans. The accumulated signal-noise interactions along one segment (of four spans) can be calculated as shown in equation





Introducing 2 OPCs in the system (as shown in figure 4.4(b)) divides the transmission system into four segments (two spans/segment). When looking at the ASE noise generated from the second and third amplifier, we can see that the signal-noise interactions generated by the end of the link are generated due to the under-compensation of the nonlinear interactions between signals and ASE noise. On the other hand, the signal-noise interactions generated by the end of the link (originated from the second segment) are generated due to the over-compensation of the nonlinear interactions between signals and ASE noise. We can see that the nonlinear signal-noise interactions originated from the odd indexed segments are generated due to the under-compensation of the nonlinear interactions among signal and ASE noise, whilst the signal-noise interactions originated from the even indexed segments are generated due to the over-compensation of the nonlinear interactions among signal and ASE noise. When comparing figure 4.4(a) and (b), we can see that increasing the number of OPCs linearises the quadratic and cubic growth of the signal-noise interaction contributions by increasing the number of segments and decreasing the number of unique ASE noise sources per segment. From the analysis in figure 4.4, it can be easily concluded the total nonlinear noise generated from the signal-noise interactions can be written as [X7]:

$$\eta_{ssn}(N) = \frac{I_{ssn}(N)}{I_s^2 I_{ASE}} = 3N_{seg} \left[ \sum_{n=1}^{N/N_{seg}} \eta(n) + 3I_s^2 \eta(1) \sum_{n=1}^{N/N_{seg}} \sum_{i=1}^{n-1} \eta(i) \right] \quad (4.31)$$

Which shows that increasing the number of OPCs reduces the nonlinear interaction growth in signal-noise interactions in multi-OPC assisted systems. Equation 4.31 still applies to calculate the nonlinear signal noise interaction in DBP assisted system where the number of segments in the system is 1. Splitting DBP between the transmitter (nonlinearity pre-compensation of  $N/2$  span) and the receiver (nonlinearity post compensation of  $N/2$  spans) [76] would result a nonlinear signal-noise interactions equivalent to a system with mid-link OPC ( $N_{seg}=2$ ), which is lower than the signal-noise interactions generated in DBP assisted system fully implemented in the receiver side. When deploying 50% DBP (half link length) at the transmitter, then the signal-signal nonlinearities are fully recovered at the mid-link point while the signal-noise nonlinear interactions accumulate over the first half of the link (can be theoretically be described by  $\eta_{ssn}(N/2)$  of equation 4.29). Over the second half of the link, the signal-signal nonlinear interactions start to accumulate over  $N/2$  spans which will be compensated for by the 50% DBP implemented at the receiver. As for the nonlinear signal-noise interactions, it will accumulate over the second half of the link and can be theoretically described by  $\eta_{ssn}(N/2)$  of

equation 4.29. So, the total nonlinear signal-signal nonlinear interactions would be eliminated after the DBP at the receiver side, while the total signal-noise nonlinear interactions will be equal to  $2\eta_{ssn}(N/2)$  of equation 4.29; which is similar to the amount of signal-noise interactions generated in a mid-link OPC assisted system ( $N_{seg}=2$ ) which is described by  $\eta_{ssn}(N)$  of equation 4.31.

As mentioned before, a full deterministic signal-signal nonlinearity compensation of two consecutive segments (in an OPC assisted system) requires a system that deploys distributed Raman amplified systems. The ASE noise is generated along the optical fibre spans (as seen in equation 2.16 in section 2.2.2), unlike discretely amplified system that generate ASE noise discretely (by the end of each span) along the system. The calculation of the nonlinear noise generation efficiency generated from signal-noise interactions requires the conversion of the summations in equation 4.31 into integration over distance; where both  $I_{ASE}$  and  $\eta$  are defined as a function of fibre span length. In an ideal lossless distributed Raman transmission system, the ASE power spectral density is linearly generated along the span (as seen in equation 2.17 in section 2.2.2, [61]). So, an integration over the distance is required to calculate the efficiency of 1<sup>st</sup> order signal-noise interactions, and a double integration is required to calculate the efficiency of 2<sup>nd</sup> order signal-noise interactions. The nonlinear noise generation efficiency of these signal-noise interactions can be written for a system of  $N_{seg}$  segments as follows:

$$\begin{aligned}\eta_{ssn}^{1st-Order} &= N_{seg} \frac{I_{ssn}^{1st-Order}}{I_s^2 I_{ASE}} = N_{seg} \frac{6\gamma^2}{\pi\beta''} \int_0^{L/N_{seg}} z \log\left(2\pi^2 |\beta''| B_w^2 z\right) dz \\ &= \frac{3\gamma^2 L^2}{\pi\beta'' N_{seg}} \left[ \log\left(2\pi^2 |\beta''| \frac{L}{N_{seg}} B_w^2\right) - \frac{1}{2} \right]\end{aligned}\quad (4.32)$$

$$\begin{aligned}\eta_{ssn}^{2nd-Order} &= N_{seg} \frac{I_{ssn}^{2nd-Order}}{I_s^2 I_{ASE}} = N_{seg} \frac{18\gamma^4 I_s^2}{(\pi\beta'')^2} \int_0^{L/N_{seg}} \int_0^z x \log\left(2\pi^2 |\beta''| B_w^2 x\right) dx dz \\ &= N_{seg} \frac{18\gamma^4 I_s^2}{(\pi\beta'')^2} \int_0^{L/N_{seg}} \left[ \frac{z^2}{2} \log\left(2\pi^2 |\beta''| z B_w^2\right) - \frac{z^2}{4} \right] dz \\ &= \frac{3\gamma^4 I_s^2 (L)^3}{(\pi\beta'' N_{seg})^2} \left[ \log\left(2\pi^2 |\beta''| \frac{L}{N_{seg}} B_w^2\right) - \frac{5}{6} \right]\end{aligned}\quad (4.33)$$

Note that equations 4.32 and 4.33 are normalised over the ASE noise growth factor along the system ( $I_{ASE}=n_{sp}h\nu_0\alpha$ ). As a result, the total nonlinear noise generated from signal-noise interactions can be written as [X5,X6]:

$$\eta_{ssn}(N) = N_{seg} \frac{I_{ssn}(L/N_{seg})}{I_s^2 I_{ASE}} = \frac{3\gamma^2 L^2}{\pi |\beta''| N_{seg}} \left[ \log \left( 2\pi^2 |\beta''| \frac{L}{N_{seg}} B_w^2 e^{-1/2} \right) + \frac{I_s^2 \gamma^2 L}{\pi |\beta''| N_{seg}} \log \left( 2\pi^2 |\beta''| \frac{L}{N_{seg}} B_w^2 e^{-5/6} \right) \right] \quad (4.34)$$

This equation shows that increasing the number of OPCs in the quasi-lossless distributed Raman system (increasing number of segments) result a reduction of the 1<sup>st</sup> order signal-noise interactions by a factor of  $(1/N_{seg})$ , and reduction of the 2<sup>nd</sup> order signal-noise interaction by a factor of  $(1/[N_{seg}]^2)$ .

### 4.3 Performance of Coherently Detected Optical Modulated Signals

As shown in section 2.3.3, the performance (Q factor, BER, or EVM) of the received optical modulated signals is identified by the SNR; which is defined as the ratio between the signal power spectral density and the accumulated noise (linear ASE and nonlinear Kerr noise) along the system:

$$SNR = \frac{I_s}{NI_{ASE} + \kappa I_s^3 \eta + 3I_s^2 I_{ASE} \eta_{ssn}} \quad (4.35)$$

The noise terms in denominator of equation 4.35 represents, respectively, the linear ASE noise (defined in sections 2.2.1 and 2.2.2), the deterministic nonlinear signal-signal interaction (defined in section 4.1), and the non-deterministic nonlinear signal-noise interaction (defined in section 4.2). The deterministic nonlinear signal-signal nonlinear interactions ( $I_s^3 \eta$ ) is cubically dependent on the signal power spectral density; its effect is often dominant over the nonlinear noise generated from signal-noise interactions ( $I_s^3 \eta \gg 3I_s^2 I_{ASE} \eta_{ssn}$ ) in optical transmission system that does not deploy nonlinearity compensation systems ( $\kappa=1$ ). On the other hand, nonlinearity compensation (using DBP or OPC) can degrade (or fully eliminate) the deterministic nonlinear signal-signal interactions (second term in the denominator of equation 4.35). The residual deterministic nonlinearities ratio ( $\kappa \leq 1$ , defined in equation 4.17 for OPC assisted discretely amplified system) identifies whether the nonlinearity compensation technique implemented can reveal the dominance of nonlinear signal-noise interaction limit

(third term in the denominator of equation 4.35) over the residual nonlinear signal-signal interaction limit (second term in the denominator of equation 4.35). The residual deterministic nonlinear signal-signal interactions ( $\kappa$ ) can be equal to *zero*, when using full field DBP or OPC assisted quasi-lossless distributed Raman amplified system.

#### 4.4 Simulations, Verification, and Analysis

To verify the analytical equations presented in this chapter, we have conducted simulations that emulate the propagation of modulated optical signals through various transmission systems (discretely amplified, distributed Raman, with or without nonlinearity compensation: full field DBP or ideal OPC). The simulated systems were intended to unveil the dimensions of nonlinearity compensation in PMD free optical fibre transmission systems. The simulations were implemented using VPITransmissionMaker 9.5-9.8 to simulate the propagation in SSMF ( $\alpha=0.2\text{dB/km}$ ,  $\gamma_0=1.33\text{W/km}$ ,  $D_c=16\text{ps/nm/km}$ ,  $S=0$ ,  $T=300\text{K}$ ,  $g_r=0.37\text{W/km}$ , and ***PMD=0***). MATLAB was used to generate 28Gbaud PM-QPSK (Nyquist pulse shaped with 0% roll-off factor) signals and preforms DSP on the coherently received signals. VPI always used a sampling rate that equals 32 times the total baud rate of the modulated signals, and the split step size is defined so that the total nonlinear phase shift within the step is always less than  $0.05^\circ$ , to achieve an accurate simulation results. Distributed Raman transmission systems were calibrated so that the total Raman depolarised pumping power achieves 0dB net gain per span. The simulated OPC is an ideal OPC with zero insertion loss, implemented in MATLAB which simply conjugates the optical field blocks passed from VPI. In the simulated DBP assisted systems, we have used split-step method (with uniform DBP step size) to backpropagate the coherently detected field (full bandwidth) through the system with 120 steps per span, the number of steps was chosen so that any higher number of steps per span did not further compensate deterministic nonlinearities (of received modulated signal launched into the fibre with power deep in the nonlinear regime). The simulated lasers, at the transmitter, Raman pumps, and receiver sides were ideal (i.e. zero linewidth and zero RIN). To validate the analytical equations presented in this chapter, we have compared the simulated  $Q^2$  factor ( $=1/(EVM)^2$ , equation 2.24) of the received QPSK constellation with the analytical SNR predictions. MATLAB was used to calculate the nonlinear noise generation efficiency ( $\eta$  and  $\eta_{ssn}$ , with the parameters of the simulation marked in ***Bold*** earlier in this paragraph), and then use it in equation 4.35 to calculate SNR predictions (which equal to  $Q^2$  for QPSK modulated signal, equation 2.25).

#### 4.4.1 Discretely Amplified Systems

As we have seen in chapter 3, a mid-link OPC can compensate nonlinear Kerr effects in the strongly phase matched region when the span length deployed in the system is long ( $L > 50\text{km}$ ), while the nonlinearities at the weakly phase matched region remain uncompensated. A shorter span length allows the OPC to compensate nonlinearities in the weakly phase matched region (as shown in figure 3.14). Also, we have seen that deploying multiple OPCs can diminish the compensation efficiency of deterministic nonlinear impairments achieved by a single OPC, since the deployment of multi-OPC is equivalent to a dispersion managed system that enhance the nonlinear noise generation efficiency of the system (as shown in figure 3.15).

To visualise the performance improvement achieved by OPC assisted systems compared to conventional EDC systems, we have simulated a single channel (28Gbaud PM-QPSK) system propagating through 2400km link with various span lengths [X2]. The span lengths used in these simulations were: 100km [X17], 50km, 25km, 12.5km, and 6.25km. The EDFAs used in the system (to compensate for the span loss) had spontaneous emission factor ( $n_{sp}$ ) of 1.085 (equivalent to  $NF=3.36\text{dB}$  at  $G=20\text{dB}$ ) and used various number of symmetrically deployed double segment separated OPCs (No OPC, 1-OPC, 2-OPCs, and 3-OPCs).

Figure 4.5 shows the simulation results (filled dots) and the analytical prediction (solid lines) of received signal performance ( $Q^2=1/EVM^2$ ) as a function of the signal power ( $P_s=I_sB_w$ ) launched into the optical fibre spans. The analytical predictions were numerically calculated from: equation 4.2 ( $\eta$  without OPC), equation 4.3 ( $\eta$  with OPC), and equation 4.29 ( $\eta_{ssn}$  of signal-noise interactions); then the results were substituted in equation 4.35 to calculate SNR of the received signal. In the system of 24x100km (in figure 4.5(a)), we can see that the performance of EDC system (No-OPC) is dominated by the linear ASE noise when the signal power is ranging below 0dBm where increments in the signal power translate into an increment in the  $Q^2$  factor with a rate of  $+1\text{dB/dBm}_{(\text{signal power})}$ . The maximum performance ( $Q^2=14.4\text{dB}$ ) is reached at 0dBm after which the system enters the nonlinear regime, where the deterministic signal-signal nonlinear interaction starts to grow cubically as a function of signal power resulting a degradation of the  $Q^2$  factor with a rate of  $-2\text{dB/dBm}_{(\text{signal power})}$ . Introducing OPC into the system achieves partial compensation of the signal-signal nonlinear interactions to enhance the maximum achieved performance  $Q^2$  by 2.5dB, 1.9dB, and 0.6dB for systems with 1-OPC, 2-OPCs, and 3-OPCs, respectively. As concluded from chapter 4, figure 4.5(a) confirms that introducing more OPCs into discretely amplified system (with long span length)

degrades of the performance enhancement achieved by single OPC. Due to the per segment dispersion compensation that each OPC achieves, the nonlinear signal-signal interactions grow to diminish the nonlinearity compensation achieved by a single OPC. A 50km span length deployed in the system (figure 4.5(b)) further improves (compared to the 100km span system) the nonlinearity compensation achieved by the OPCs resulting performance enhancement of 5.7dB, 4.5dB, and 3.7dB for 1-OPC, 2-OPCs, and 3-OPCs, respectively. As the 50km span system, the 25km span system (figure 4.5(c)) still shows that introducing more than one OPC to the system degrades of the maximum performance of the OPC assisted system, but still the shorter span length (25km compared to the 50km and 100km) achieves further enhancement of the system performance reaching to 10.3dB, 9.8dB, and 8.9dB achieved by 1-OPC, 2-OPCs, and 3-OPCs, respectively. In the system that deploys 12.5km span length (figure 4.5(d)), the nonlinearity compensation efficiency achieved by 2-OPCs and 3-OPC precedes the compensation efficiency achieved by a single OPC where the performance (at the optimum launch power) of the system with 2&3 OPCs introduce 1.5dB further performance enhancement to the system that deploys a single OPC. At this point, the nonlinear efficiency of signal-signal interactions in an OPC assisted system reaches a comparable efficiency to the nonlinear signal-noise interactions.

When 6.25km span length is deployed in the system (figure 4.5(e)) further reduce the nonlinear signal-signal interactions to unveil the nonlinear signal-noise interaction limit where the increasing the number of OPCs reduce the nonlinear signal-noise interactions resulting enhancement of the maximum performance of the OPC assisted system. We can see that shortening the span length is one of the solutions to enhance the OPC's capability to compensate for the nonlinear signal-signal interactions. The theoretical calculations show a good agreement with the results obtained from the simulations, within a margin of mismatching of 0.4dB at the maximum  $Q^2$ . The nonlinear regime of figure 4.5(c&d) show an excessive  $Q^2$  degradation slope of -5dB/dBm<sub>(signal power)</sub> when the signal power is ranging above 7dBm; this can be explained by the nonlinear interactions between the signal and both the ASE noise as well as the uncompensated signal-signal nonlinearities, since these effects were not considered in the theory, the theoretical solid lines in figure 4.5(c&d) deviate from the simulation results at the nonlinear regime. This deviation does not degrade the theoretical predictions of the simulated system performance at the  $Q^2$  factor peak.



Aston University

Illustration removed for copyright restrictions

*Figure 4.5:  $Q^2$  as a function of signal power for discretely amplified 2400km transmission system that deploys various uniform span lengths and number of OPCs. [X2]*

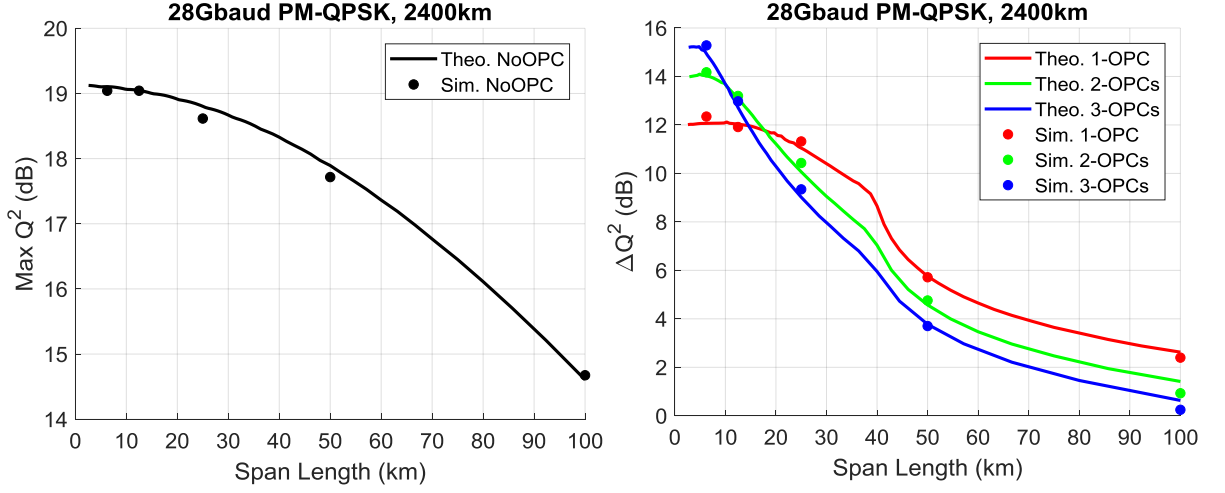


Figure 4.6: (a) The maximum  $Q^2$  factor, as a function of span length, can be achieved by single channel (28Gbaud) propagating through 2400km discretely amplified EDC system. (b) The improvement in the maximum  $Q^2$  factor can be achieved by 1-OPC, 2-OPCs, and 3-OPCs. [X2]

Figure 4.6 summarises the results from figure 4.5 by showing the maximum  $Q^2$  factor achieved by EDC system (a) and the performance improvement  $\Delta Q^2$  achieved by OPC (b) as a function of span length [X2]. The both parts of the figure compare the simulation results (filled dots) and the theoretical predictions (lines). Figure 4.6(a) shows that a shorter span length deployed along discretely amplified system can improve the performance of EDC systems (without OPC) by a factor of 4.4dB compared to a system that deploy 100km span length, which was concluded in [61,127]. On the other hand, the performance improvement achieved in OPC assisted discretely amplified systems, figure 4.6(b), shows that a single channel system with span length above 20km does not show full signal-signal nonlinearity compensation; which cause a degradation of the performance improvement when deploying more than one OPC. When deploying amplifier spacing less than 20km, the nonlinear signal-noise limit will be unveiled which gives that advantage to multi-OPC to show better performance improvement compared to a single OPC system.



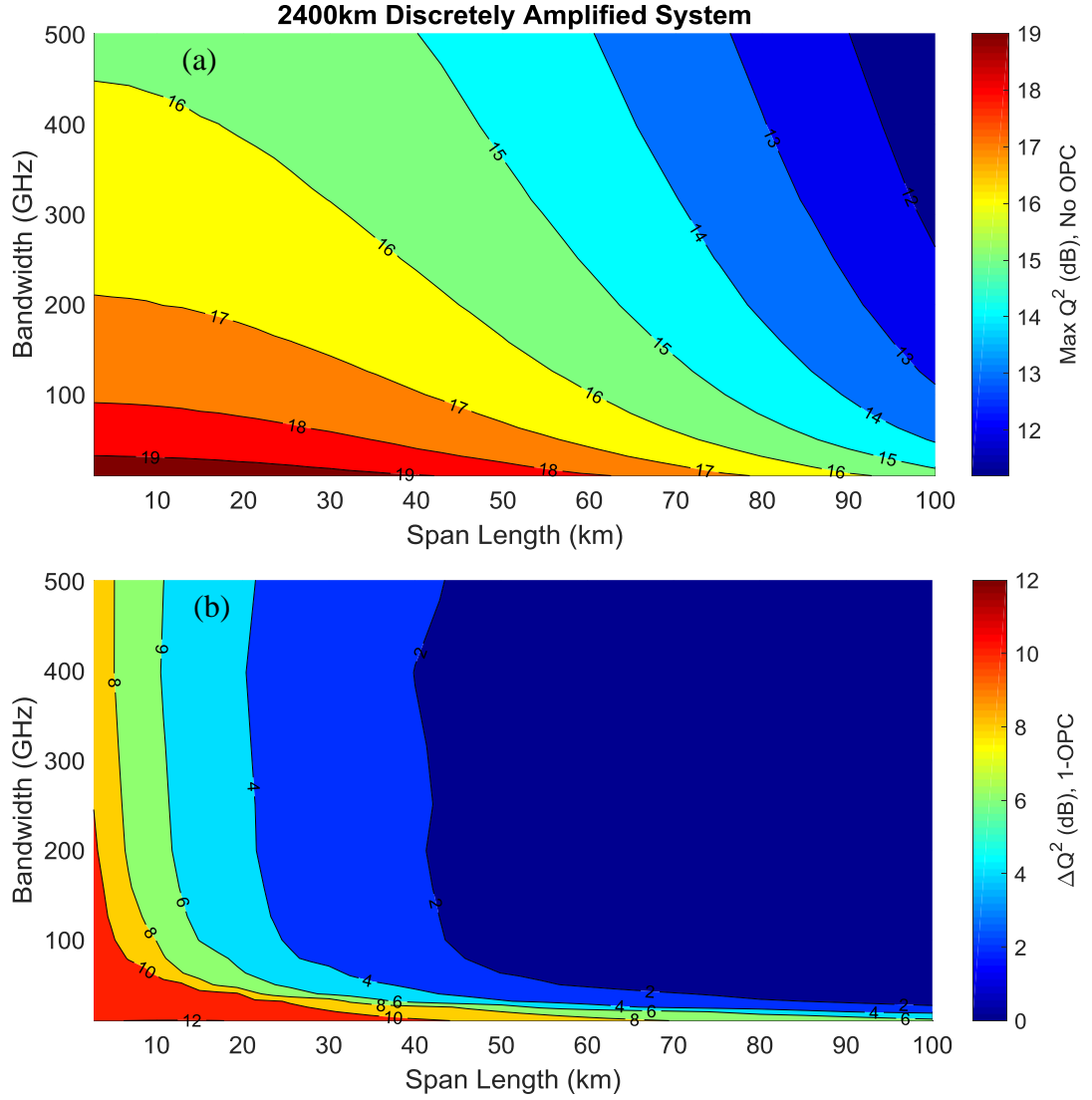


Figure 4.7: (a) Maximum  $Q^2$  factor, as a function of span length and bandwidth, can be achieved by the end of 2400km discretely amplified system without OPC. (b) Improvement in the maximum  $Q^2$  factor can be achieved by 1-OPC. [X2]

Figure 4.7 shows the theoretical numerical evaluation of the maximum  $Q^2$  factor of EDC system (a) as well as the improvement in  $\Delta Q^2$  factor that a single OPC achieves (b), both calculated at a total system length of 2400km and plotted as a function of span length and the bandwidth of the optical modulated signals [X2]. Figure 4.7(a) confirms that a shorter span length would result performance enhancement of EDC system. Furthermore, the shorter span length leads improvement of system performance enhancement when deploying mid-link OPC. When deploying long amplifier spacing ( $>70$ km), it can be seen that the improvement in  $Q^2$  (achieved by OPC) suddenly drops to 0dB as the signal bandwidth increases due to the dominance of signal-signal nonlinear interactions (generated from the uncompensated interactions among weakly phase matched signals). When the amplifier spacing is shorter than 16km, the deterministic nonlinear signal-signal interactions are significantly compensated by

the OPC to reveal the nonlinear limit of the signal-noise interactions where no further performance enhancement is possible unless multiple OPCs were deployed in the system (as shown in figure 4.6(b)). Signals with a bandwidth higher than 200GHz can achieve a 3dB improvement in  $Q^2$  (by OPC) only when the span length is around 35km, then the signal-signal nonlinear interactions starts to be degraded causing the improvement in  $Q^2$  to grow as the span length gets shorter than 30km. A system that deploys span length longer than 70km barely achieves any improvement in  $Q^2$  factor for signals with bandwidth above 100GHz.

To validate the closed form equations that approximate the nonlinear noise generation efficiency in discretely amplified system without OPC (equation 4.13) and with OPC (residual nonlinearity ratio, equation 4.20), we have changed the number of channels transmitted through the 24x100km system described before using: 1, 2, 4, 8, and 16 channels each with 28Gbaud (and channel spacing of 29GHz). Figure 4.8(a) shows the simulated and analytical results of  $Q^2$  factor as a function signal power spectral density ( $I_s$ ) launched into the system, figure 4.8(b&c) summarises figure 4.8(a) to show the maximum  $Q^2$  achieved by EDC system (b) and the improvement in  $Q^2$  that the OPC achieve (c) as a function of the bandwidth of the signal. The analytical curves were calculated from equations 4.13 and 4.20 and substituted into equation 4.35. The maximum  $Q^2$  factor achieved by EDC system is degraded as a function of signal bandwidth; this degradation is due to the nonlinear noise generation efficiency logarithmic growth as a function  $B_w^2$ . As shown in figure 4.8(c), deploying a mid-link OPC in discretely amplified transmission system (with long span length, 100km) can compensate only the nonlinear interactions in the strongly phase matched region while the weakly phase matched mixed signals remains, almost, unchanged which was shown in figure 4.2. As the signal bandwidth increases, the nonlinear interactions from the weakly phase matched signals become dominant over the compensated nonlinearities among the strongly phase matched signals. As a result, the nonlinearity compensation efficiency achieved by the OPC drops dramatically as a function of the signal bandwidth, as can be concluded from equation 4.20 and can be clearly seen from figure 4.8(c). The simulation results in figure 4.8 shows a good agreement, within 0.3dB margin of mismatching, validating the theoretical predictions made by the closed form approximations presented in equation 4.13 and 4.20. The approximations made in equations 4.13 and 4.20 are valid for long span lengths ( $\exp(-\alpha L) \ll 1$ ) at which the signal-signal interactions are dominating nonlinear noise generated in the system, and the multi-OPC approach would further degrade and nonlinearity compensation achieved by a single OPC (as shown in figure 4.5 and 4.6).



Figure 4.8: (a)  $Q^2$  as a function of signal power in 24x100km discretely amplified system. (b) maximum  $Q^2$  achieved by EDC system as a function of signal bandwidth, (c) the improvement in  $Q^2$  of mid-link OPC system as a function of signal bandwidth. [X2]

To check the capabilities of DBP assisted systems we have simulated 8x28Gbaud PM-QPSK (29GHz channel separation) signals propagating through 12x100km system that deploys: dispersion uncompensated system (only SSMF), NZDF ( $D_c=4\text{ps/nm/km}$ ), and per span dispersion managed system with residual dispersion ( $\delta$ ) of 5% of the SSMF chromatic dispersion (SSMF+DCF) [X1,X5]. The noise figure of the EDFAs in this system was 6dB and both the DCF and NZDSF had an intrinsic nonlinear factor ( $\gamma_0$ ) of 1.33/W/km. Figure 4.9 shows the  $Q^2$  factors of the received signal as a function of total optical signal power launched into the fibre, the figure compares the simulation results (dots) with theoretical predictions (lines). Equations 4.13 and 4.30 were used to calculate the nonlinear noise generation efficiency of signal-signal interactions and signal-noise interactions, respectively. The plotted theoretical curves of DBP assisted system uses only the 1<sup>st</sup> order signal-noise interactions (dashed lines), and uses both the 1<sup>st</sup> and 2<sup>nd</sup> order signal-noise interactions (dotted lines). It can be seen from the figure that lower accumulated chromatic dispersion along the link will lead to the degradation in system performance both for the case of receiver compensating only for chromatic dispersion and for the case of receiver compensating for nonlinearities using full field DBP. The figure shows that full field DBP can improve the  $Q^2$  factor by: 7dB for the SSMF link, 6dB for the NZDSF link, and 6.4dB for the 95% dispersion compensated SSMF. The improvements achieved by DBP are directly linked to the fact that DBP has fully recovered all the signal-signal nonlinear Kerr noise, but, it is clear from the figure that the transmission system is still limited by the signal-noise interactions. The theoretical SNR calculation that consider both the 1<sup>st</sup> and 2<sup>nd</sup> order signal-noise interactions represents more accurate prediction of the nonlinear regime of the DBP assisted system compared to the theoretical SNR

calculations that considers only the 1<sup>st</sup> order signal-ASE interactions. The 2<sup>nd</sup> order signal-noise interactions cause a degradation of the SNR with a rate of -3dB/dB<sub>(signal power)</sub>. In general, figure 4.9 shows a good agreement between the simulation results and the theoretical predictions, with 0.6dB margin of error.



Figure 4.9:  $Q^2$  as a function of the total launched optical signal power into a 12x100km discretely amplified system (EDFA noise figure of 6dB,  $B_w=224\text{GHz}$ ) with different dispersion maps: SSMF, NZDSF, SSMF+DCP with 5% residual dispersion. [X1,X5]

Figure 4.10 shows the  $Q^2$  factor as a function of distance of the same system that was described before, but the signal power was fixed to the optimum power (found at 1200km, of figure 4.9) [X1,X5]. The figure shows that the system that accumulates higher chromatic dispersion can achieve higher distance than a system with lower accumulation of fibre dispersion along the link. The  $Q^2$  difference (of EDC system) between the SSMF and the SSMF+DCF (with  $\delta=5\%$ ) starts with 2dB at 1000km distance, but this difference increases to almost 3dB as the distance reaches 5000km. This deviation can be explained by the fact that as the residual dispersion ( $\delta$ ) gets closer to 0%, the second term in equation 4.13 starts to scale the nonlinear power spectral density quadratically ( $N(N+1)/2$ ) instead of linearly ( $N$ ) for dispersion uncompensated transmission system ( $\delta=100\%$ ). For DBP system, it can be seen that the theoretical prediction considering only the 1<sup>st</sup> order signal-noise interaction can be inaccurate (at fixed signal power), especially when passing through higher number of spans, but including the 2<sup>nd</sup> order signal-ASE interactions will get the theoretical predictions to be accurate representation of the simulation results. As the number of spans in a DBP assisted transmission system increases, the performance of the EDC system matches the performance of the DBP assisted system; this is directly related to the fact that the signal-noise interactions grow in a quartic polynomial manner with the number of spans  $N$  (as it can be seen in equation 4.30). Figure 4.9 and figure 4.10 illustrate the importance of considering the 2<sup>nd</sup> order signal-noise Kerr nonlinear interactions to represent the nonlinear limit of ideal nonlinearity compensated transmission

systems. An optimisation of the signal power as a function distance can bring the simulated performance to match the dashed lines (considers only 1<sup>st</sup> order signal-noise interactions), since as seen from figure 4.9, the optimum  $Q^2$  factor achieved in DBP assisted system does not dramatically change whether 1<sup>st</sup> order only or both 1<sup>st</sup> and 2<sup>nd</sup> orders of signal-noise interactions were considered in the theoretical curves.



*Figure 4.10:  $Q^2$  as a function of distance (at optimum power identified by figure 4.9) of a discretely amplified system with  $L=100\text{km}$  with different dispersion maps: SSMF, NZDSF, SSMF+DCP with 5% residual dispersion. [X1,X5]*

#### 4.4.2 Distributed Raman Transmission Systems

As mentioned in chapter 3, nonlinearity compensation achieved in OPC assisted distributed Raman systems is always better when compared to an equivalent EDFA system. Distributed Raman amplification, especially when deploying shorter span length is used, gets the signal power profile closer to the ideal lossless Raman that is capable of achieving full signal-signal nonlinearity compensation. To test that, we have replicated the simulations conducted in figure 4.5 but with fully backward pumped distributed Raman ( $r_f=0\%$ , achieving 0dB net signal gain). Figure 4.11 shows the power profile along the optical fibre distributed Raman span. It can be seen that the shorter span length brings that system closer to the ideal lossless Raman system, for example, the 100km span length achieves signal power variation of 9.3dB long the span while the 6.25km span length shows a signal power variation of 0.045dB along the span. Figure 4.12 shows the simulation results (filled dots) and the theoretical predictions (solid lines) of  $Q^2$  factor (for 28Gbaud PM-QPSK) as a function of the signal power launched into the distributed Raman transmission system of length 2400km. The span lengths: 100km, 50km, 25km, 12.5km, and 6.25km were used in the simulated systems, power profiles per span is shown in figure 4.11. The theoretical calculations were obtained from equation 4.6 (signal-signal nonlinearities without OPC), equation 4.7 (signal-signal nonlinearities with OPC), equation 4.29 (signal-

noise nonlinearities), equation 2.15 (linear ASE noise); all were substituted in equation 4.35 to obtain the final  $SNR$ .

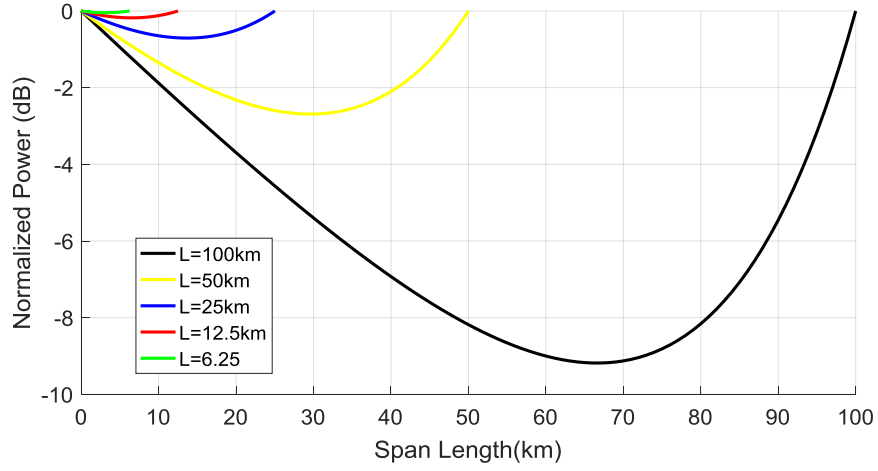


Figure 4.11: Normalised signal power as a function of span length, where the span is pumped with backward Raman pump achieving 0dB net gain.

The 24x100km system (figure 4.12(a)) shows that distributed Raman is still not giving OPC the power symmetry that is needed to fully compensate the signal-signal nonlinear interactions, which result the higher number of OPCs to always perform worse than a system with only one OPC. The level of improvement in  $Q^2$  factor achieved by a single OPC is still 1.8dB higher than the one achieved in the EDFA equivalent (figure 4.5(a)), while the 2- and 3-OPCs degrade the optimum  $Q^2$  factor achieved by a single OPC by 1.2 and 2dB, respectively. A 50km span length of distributed Raman, figure 4.12(b), is capable of compensating the signal-signal nonlinearities in OPC assisted system to match the signal-noise nonlinearities as the performance of the different number of OPCs achieve the same  $Q^2$  (at the optimum power) which is around 10dB better than EDC system. As expected, the residual signal-signal nonlinear interactions are degraded to unveil the signal-noise nonlinear limit of the system as the span length gets shorter than 50km (figure 4.12(c, d, and e)). Figure 4.12(c, d, and e) shows that the multi-OPC minimise the signal-noise nonlinear interaction to enhance the maximum  $Q^2$  factor achieved by the OPC assisted systems. In the simulated single channel system that deploy 25km, 12.5km, and 6.25km span length, it can be seen that the improvement in  $Q^2$  factor can reach 12dB, 14dB, and 15dB for distributed Raman system that deploy 1-OPC, 2-OPCs, and 3-OPCs. The level of performance enhancement achieved by OPC assisted system that deploys distributed Raman spans of 25km, 12.5km, and 6.25km hardly changes (between the mentioned span lengths) since the signal power variation along the link is always less than

0.8dB along the link which approaches the ideal lossless system (described by equations 4.24, 4.34).

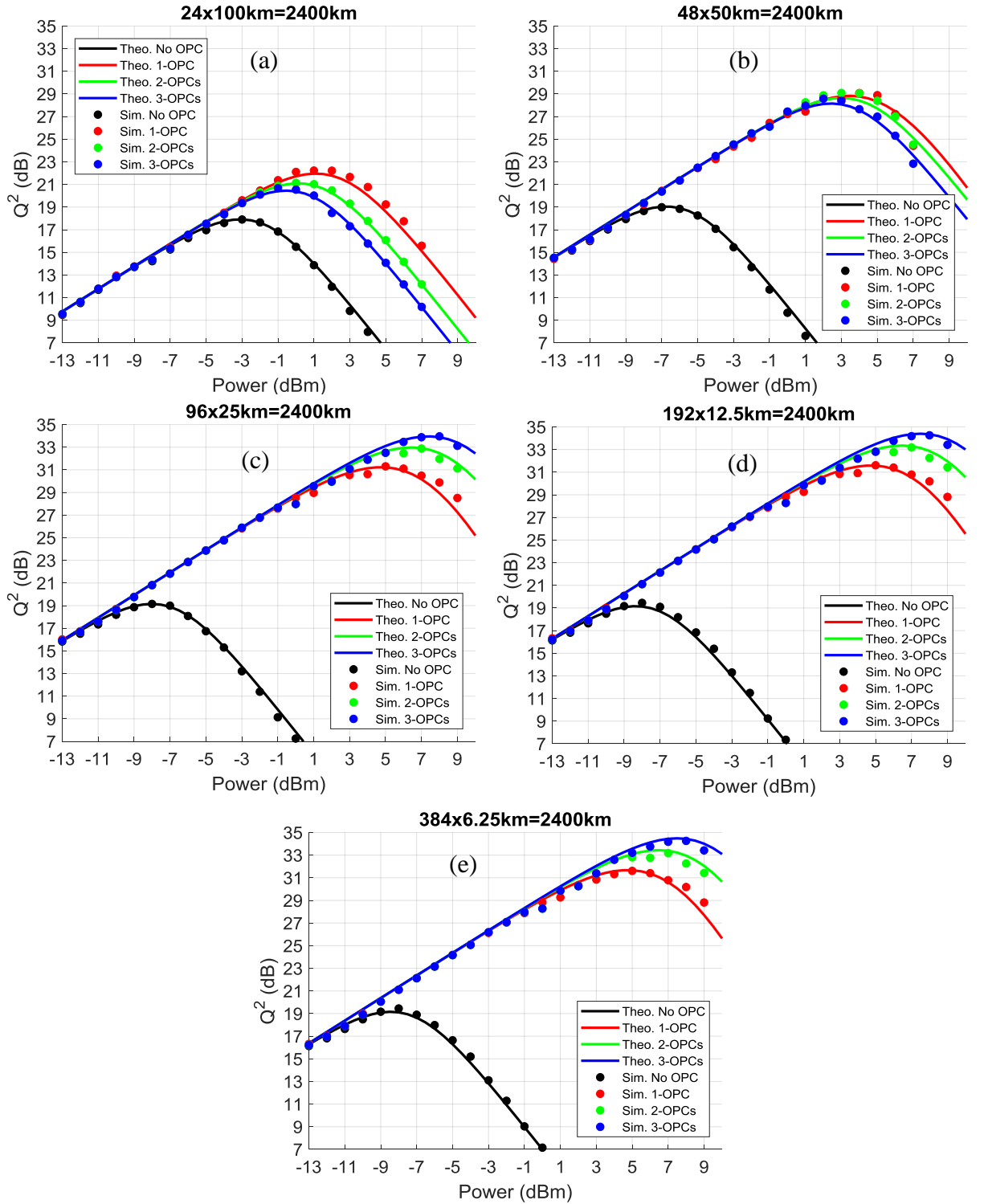


Figure 4.12:  $Q^2$  as a function of signal power for distributed Raman amplified 2400km transmission system that deploys various span length and number of OPCs. [X2]

Figure 4.13 summarises figure 4.12 to show the maximum  $Q^2$  achieved by EDC system (a) and the improvement (compared to EDC system) in optimum  $Q^2$  achieved by OPC assisted distributed Raman system (b). When comparing figure 4.13(a) and 4.6(a), it can be seen that distributed Raman system with long span length ( $>25\text{km}$ ,  $r_f=0\%$ ) performs better than the equivalent discretely amplified system. As the span length gets shorter than  $20\text{km}$ , the maximum performance of EDC discretely amplified system converges to match the maximum performance of the distributed Raman system (reaching  $19.15\text{dB}$ ), as we have chosen  $n_{sp}$  of the EDFAs so that the total ASE noise accumulated in discretely amplified system (with EDFAs  $G=1$ ) is equal to the total ASE noise generated along an ideal lossless distributed Raman system (described by equation 2.17). As for the OPC assisted distributed Raman systems, we can see that the signal-signal nonlinear noise is fully compensated, or at least much smaller than the nonlinear signal-noise interaction limit, when the span length shorter than  $30\text{km}$  (where multiple OPC further improve the performance). On the other hand, discretely amplified system need to deploy a span length shorter than  $5\text{km}$  to achieve this state.

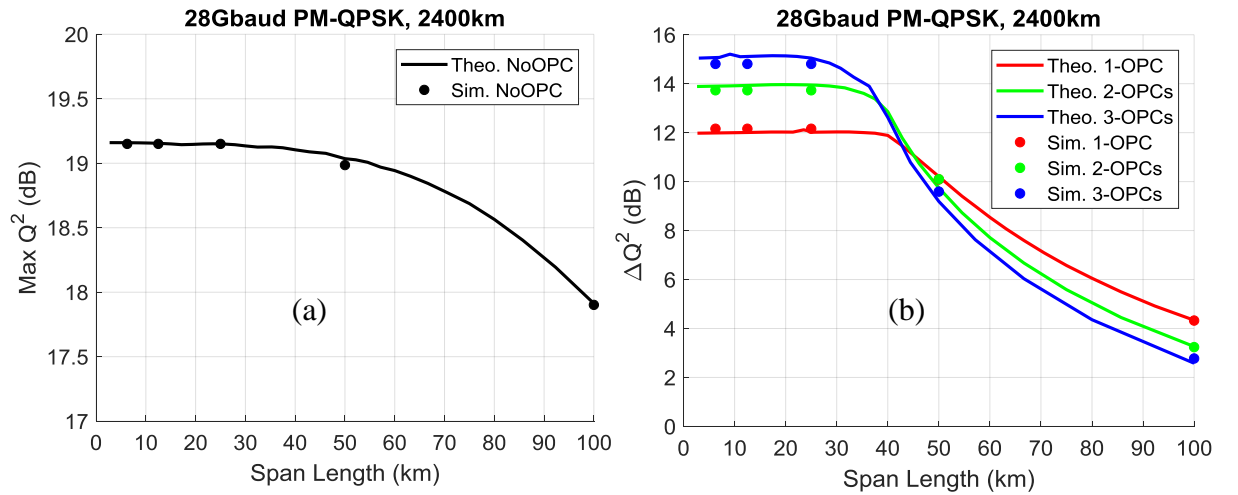


Figure 4.13: (a) The maximum  $Q^2$  factor, as a function of span length, can be achieved by 2400km distributed Raman amplified EDC system. (b) The improvement in the maximum  $Q^2$  factor can be achieved by 1-OPC, 2-OPCs, and 3-OPCs. [X2]

Figure 4.14 shows the numerical calculation of the maximum  $Q^2$  factor of EDC system (a) as well as the improvement in  $Q^2$  factor that a single OPC achieve (b), both calculated at a total system length of  $2400\text{km}$  (distributed Raman,  $r_f=0\%$ ) and plotted as a function of span length the bandwidth of the optical modulated signals. Figure 4.14(a) shows that EDC system maintains the previous conclusion that a shorter ( $<30\text{km}$ ) distributed Raman spans always performs better than longer span lengths, regardless of the bandwidth of the optical signals. Also, a span length shorter than  $30\text{km}$  achieves the maximum  $Q^2$  improvement of signals,



regardless of bandwidth, propagating through OPC assisted system, this span length is the point at which the signal noise interactions are dominant limiting factor at which a higher number of OPCs can further improve the system performance.

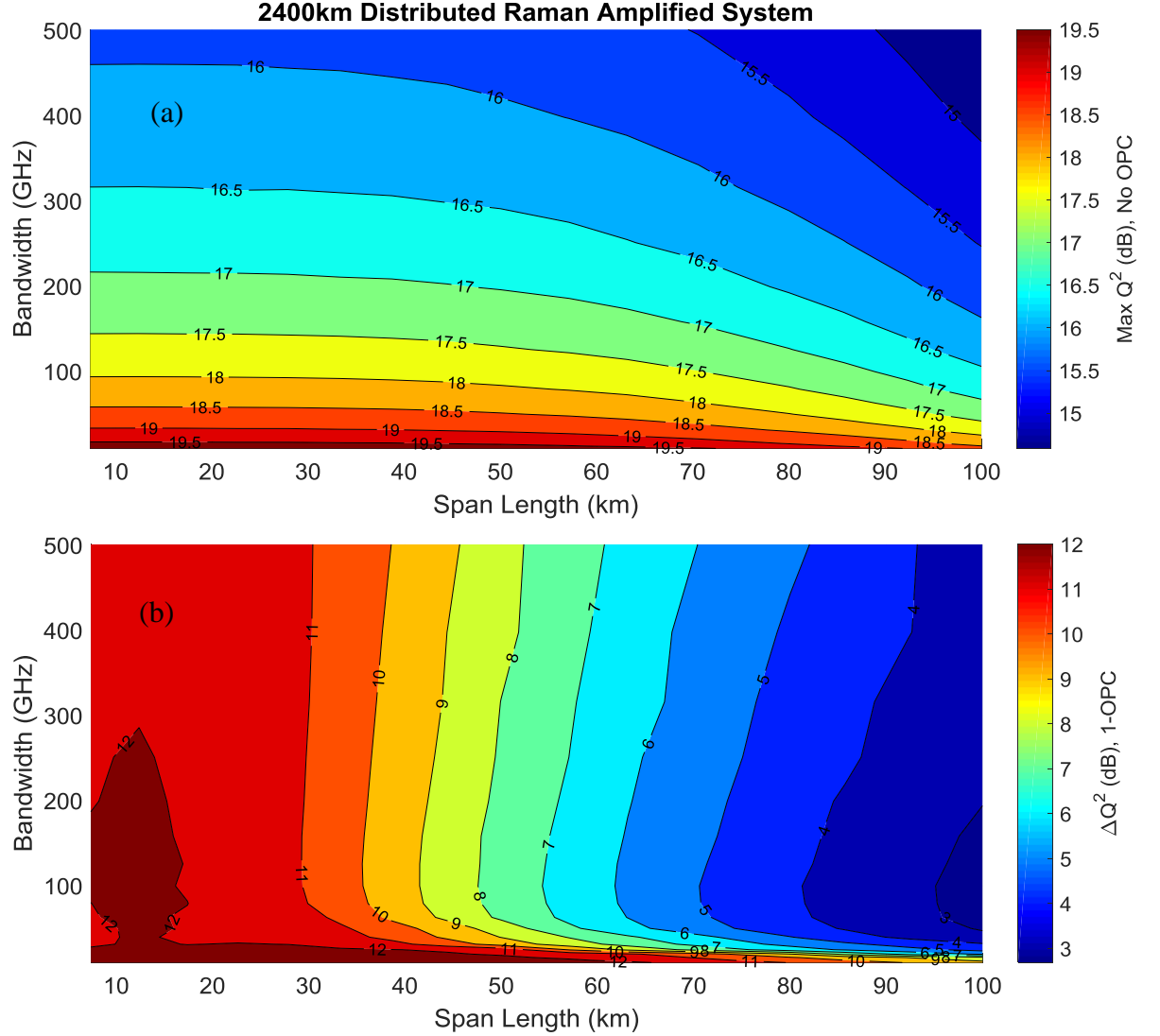


Figure 4.14: (a) Maximum  $Q^2$  factor, as a function of span length and bandwidth, can be achieved by the end of 2400km distributed Raman amplified system without OPC. (b) Improvement in the maximum  $Q^2$  factor can be achieved by 1-OPC. [X2]

To verify the analytical closed form approximations of ideal distributed Raman systems: equation 4.24 (signal-signal nonlinear noise) and 4.34 (signal-noise nonlinear noise), we have simulated the propagation of single channel (28Gbaud, PM-QPSK Nyquist 0%) propagating through 1200km system that deploys lossless SSMF ( $\alpha=0$ ). An AWGN (ASE noise) with power spectral density of  $1.1 \times 10^{-19}$  W/Hz was added to the system every 1km to emulate the linear ASE noise generation in quasi-lossless distributed Raman system (as described in equation 2.17). The level of ASE noise added in this simulation is 4 times larger than the ASE

noise of an ideal Raman system. Figure 4.15 shows simulation and theoretical predictions of  $Q^2$  as a function of signal power for a system that deploys EDC, DBP, 1-OPC, 2-OPCs, and 6-OPCs, the OPC deployment have used double segment separation between OPCs. In [X7] we have used the same setup but using single segment separated OPCs while here we have double segment OPC separation, to show that both types of OPC deployment techniques achieve the same performance enhancements. Again, the analytical predictions match the simulation results, within a margin of error of 0.5dB. A DBP assisted system can perform 8.5dB better than EDC system, while the OPC assisted system achieves  $Q^2$  improvements of: 10.5dB, 12.4dB, and 15.2dB when using 1-OPC, 2-OPC, and 6-OPCs. The maximum  $Q^2$  enhancement achieved by the OPCs in this simulation is 2dB worse than the enhancement achieved in figure 4.13 due to the fact that we have injected higher ASE noise in this simulation which linearly degrade the final SNR improvement. Again, the figure shows that the analytical presence of 2<sup>nd</sup> order signal noise interaction provides accurate representation of the nonlinear regime of the system.



*Figure 4.15:  $Q^2$  as a function of signal power for distributed Raman amplified 1200km transmission system that deploys various span length and number of OPCs. NLC: Nonlinearity Compensation (DBP or OPC). [X7]*

## Summary and Conclusions

In this chapter we have analyzed the calculation of the maximum performance can be achieved by discretely amplified and distributed Raman amplified coherent transmission systems and the capabilities of nonlinearity compensation achieved by OPC assisted and full field DBP assisted transmission system. By analytically formulating the nonlinear noise generation dynamics in these systems, we have successfully predicted the performance of optical transmission systems. The analytical equations presented in this chapter provide a tool that can

predict the maximum performance, distance reach, and the capacity achieved by the described transmission systems. This chapter has introduced a closed form equation, validated by simulation results, that predicts the residual nonlinear noise ratio in mid-link OPC assisted discretely amplified system with long amplifier spacing. Also, we have derived closed form equations, validated by simulation results, that identify the non-deterministic signal-noise nonlinear limit in optical systems that deploy ideal nonlinearity compensation techniques (DBP or OPC assisted quasi-lossless distributed Raman system).

In discretely amplified systems, we have shown that introducing multiple OPCs diminishes the nonlinearity compensation that can be achieved by a single OPC, especially when using large bandwidth optical signals propagating and the large amplifier spacing ( $>30\text{km}$ ). On the other hand, deploying short span lengths ( $<5\text{km}$ ) can achieve significant signal-signal nonlinear interactions to unveil the signal-noise interaction nonlinear limit. A discretely amplified transmission system that deploys NZDSF or deploys per span dispersion compensation, always performs worse than an SSMF system because of the fact that lower dispersion accumulation enhances the nonlinear noise generation efficiency [46]. A full field DBP deployment in the receiver side can fully compensate for the signal-signal nonlinear interactions to uncover the signal-noise interactions nonlinear limit, at which the DBP cannot further enhance the performance of the transmission system.

Distributed Raman transmission systems are always superior to their equivalent discretely amplified system when deploying OPC. OPC assisted 1<sup>st</sup> order distributed Raman amplified system can reach the signal-noise limit at sensible span length (around  $30\text{km}$ ). Deploying multiple OPCs along an optical transmission system that is limited by signal-noise interactions leads to achieve further performance improvement (when compared to a system deploying single OPC).

# Chapter 5 : Nonlinear Optical Fibre Devices

Contributions: [X13]

Fibre optical parametric amplification (FOPA) [10], optical phase conjugation (OPC) [10,128], and parametric comb generation [41] are few examples of all-optical signal processing techniques. These applications require a nonlinear medium (high susceptibility medium) to transfer photonic energy from a high-power pump(s) to achieve the targeted signal process: amplification, wavelength conversion, and generate multiple copies, respectively.

HNLFs can be used as a nonlinear medium to utilise the Kerr nonlinear process (see section 2.1.3(a)). Ideally, HNLF should achieve minimum phase mismatching accumulation ( $\Delta\beta \rightarrow 0$ ) over the bandwidth of operation, minimum SBS gain coefficient ( $g_B$ ), and maximum nonlinear coefficient ( $\gamma_0$ ). In reality, zero dispersion profile over broad optical bandwidth might be limited by the HNLF manufacturer standards, that's why a few techniques have been used to minimise dispersion accumulation along the nonlinear optical fibre device, such as: shortening the HNLF [129], cascading multiple HNLFs with varying Zero Dispersion Wavelengths (ZDW) [130], or cascading HNLF stages with dispersion compensating stages [41,131]. Those techniques require either high pumping power [129] or high precision engineering of the dispersion accumulation along the optical fibre nonlinear device [41,130]. As mentioned before SBS is one of the limitations of optical fibre nonlinear devices as it limits the total pumping optical power of the device, this effect can be minimised through dithering [53,132–134] which requires phase modulation of the pump wave(s) to broaden its spectral bandwidth. Dithering can be damaging to the conjugated signals (idler) in OPC, so a careful implementation of the dithering is required to prevent the broadening of the high-power pump from being transferred into the idlers.

This chapter presents the experimental implementation and characterisation of the dual-band-polarisation insensitive OPC and parametric comb generator. We will discuss our experimental implementation of the polarisation insensitive, dual-band, dual pump OPC that will be used in chapter 6 to realise OPC assisted optical transmission systems. Our characterisations of the

OPC analyze the polarisation dependent loss, nonlinear crosstalk, and the performance penalty imposed on phase conjugated optical signals produced from the OPC. The second section will present an experimental demonstration of a parametric comb generator that uses interferometric Wavelength Selective Switch (WSS) as a flexible dispersion management tool to optimise the flatness and bandwidth of comb lines generated at the output of the HNLF.

## 5.1 Dual-Band Optical Phase Conjugator, Design and Characterisation

A successful implementation of the OPC achieves polarisation independent phase conjugation and low insertion loss. The usage of perpendicular polarised dual pump in the implementation of the OPC [30] eliminates the need for polarisation diversity loop (used in the single pump OPCs [X8]) to achieve polarisation independent conjugation. The insertion loss of the OPC identifies whether an EDFA is needed to amplify conjugated signals at the output of the OPC, which will degrade the SNR of the conjugated signals due to the ASE noise emitted from the EDFA. Counter dithering [133] is considered to be one of the techniques used in dual pump OPC to minimise SBS effects which leads to the enhancement of the conversion efficiency (insertion loss) of the OPC.

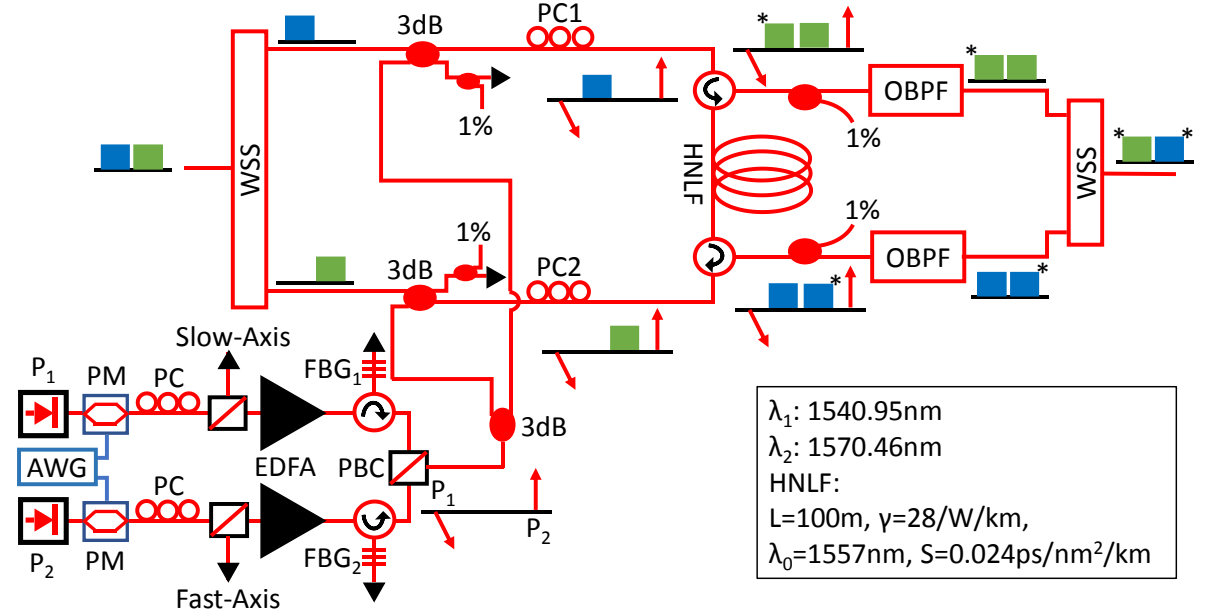


Figure 5.1: Experimental setup of dual band, polarisation insensitive, dual pump OPC.

Figure 5.1 shows our experimental setup of dual band OPC that uses two fibre lasers ( $P_1$  and  $P_2$ ) serving as the two pumps, those lasers were emitting at wavelengths 1540.95nm and 1570.46nm, respectively, with an ultra-low linewidth ( $<10\text{kHz}$ ) and Relative Intensity Noise (RIN) ( $-110\text{dBc/Hz}$ , at  $1\text{MHz}$ ). The two pump lasers were modulated (dithered) using optical

phase modulator (PM), a dual channel Arbitrary Wave generator (AWG) was used to generate two RF signals feeding the dithering phase modulators. After the dithering stage, the phase modulated pumps pass through polarisation realignment stage to align the polarisation of  $P_1$  and  $P_2$  on the fast axis and slow axis, respectively. This stage consists of polarisation controller (PC) and Polarisation Beam Splitter (PBS), the polarisation controllers were calibrated to minimise the laser power emitting from the slow axis port of the PBS (for  $P_1$ ) and from the fast axis port of the PBS (for  $P_2$ ). This stage ensures that the two pumps are perpendicularly polarised to realise the polarisation independency of the conjugation. The polarised lasers are then amplified using high power polarisation maintaining EDFAs (C-band PM-EDFA amplifies  $P_1$  and L-band PM-EDFA amplifies  $P_2$ ). A circulator and Fibre Bragg Grating (FBG) were used as a filter to eliminate the ASE noise generated from the EDFAs. The polarisation maintaining FBGs (FBG<sub>1</sub> reflects  $P_1$  and FBG<sub>2</sub> reflects  $P_2$ ) have a bandwidth of 1nm and reflectivity of 99.99%. The two polarised and filtered pumps were combined using Polarisation Beam Combiner (PBC) to maintain the state of perpendicularly polarised pumps. All fibre components from the polarisation realignment stage up to this point were polarisation maintaining components to ensure the stability of the polarisation state of the pumps. Finally, two copies of the polarised pumps were created (using 3dB splitter), each copy will be used to conjugate different band to realise the dual-band OPC.

At the input of the dual band OPC, we have used a WSS to split the input signals into two bands propagating on two different paths: short wavelength band (1541nm-1555.7nm) and long wavelength band (1555.7nm-1570.4nm). A 3dB coupler was used to combine each signal band with a copy of the perpendicularly polarised pumps. A polarisation controller was installed on each signal path to re-align the perpendicular pumps onto the principal axis of the HNLF, these polarisation controllers were critical optimisation tool to ensure polarisation independency of the conjugation process. The two bands combined with the pumps were directed into the HNLF ( $L=100\text{m}$ ,  $ZDW(\lambda_0)=1557\text{nm}$ ,  $\gamma_0=28/\text{W/km}$ ,  $S=0.024\text{ps/nm}^2/\text{km}$ ), counter propagating each other, and out of the HNLF using two circulators, as shown in figure 5.1. Each direction of propagation along the HNLF represents an independent OPC, in our case, we are using the two OPCs to conjugate two different bands. The circulators are installed to ensure the extraction of signals, conjugates and pumps after passing through the HNLF. Tuneable Optical Band Pass Filters (OBPFs) were used to remove the high-power pumps from the output of each OPC. Finally, a WSS was used at the output of the OPC to filter and combine the two conjugated bands (idlers).

Our implementation of the dual band OPC is a modified version of the configuration presented in [135], except our setup uses PBC to combine the two pumps which provides stability to the polarisation insensitive state of the OPC. Also, we deploy counter dithering [53,132–134] to minimise SBS effects to improve conjugation efficiency as higher pumping power was enabled. The polarisation independence of this OPC setup can be traced back to the fact that the nonlinear Kerr effects occur in the optical fiber is generated according to the following equation [44]:

$$\begin{aligned} E_i^x &= \eta \left[ E_1^x E_2^x E_s^{*x} + \frac{1}{3} \left( E_1^x E_2^x E_s^{*y} + E_1^x E_2^y E_s^{*x} + E_1^y E_2^x E_s^{*x} \right) \right] \\ E_i^y &= \eta \left[ E_1^y E_2^y E_s^{*y} + \frac{1}{3} \left( E_1^y E_2^y E_s^{*x} + E_1^y E_2^x E_s^{*y} + E_1^x E_2^y E_s^{*y} \right) \right] \end{aligned} \quad (5.1)$$

where  $\eta$  is the nonlinear Kerr field generation efficiency,  $E_s$ ,  $E_i$ ,  $E_1$ ,  $E_2$  are the optical field of signal, idler, pump1, and pump2, respectively. The superscript x and y represent the polarisation state of the optical field. Equation 5.1 shows that when having dual perpendicularly polarised pumps ( $E_1^x$  and  $E_2^y$ ), the nonlinear product idler results in the OPC is described by:

$$\begin{aligned} E_i^x &= \frac{\eta}{3} E_1^x E_2^y E_s^{*x} \\ E_i^y &= \frac{\eta}{3} E_1^x E_2^y E_s^{*y} \end{aligned} \quad (5.2)$$

Which indicates that the generated idlers (phase conjugated signal) contain both polarisations of the input signals (to be conjugated) which imply the polarisation independence of the phase conjugation of the OPC.

### 5.1.1 Counter Dithering and SBS Characterisation

To achieve the lowest SBS backscattered power of the pump (as it propagates along the HNLF), each dithering tone applied to the optical phase modulator should correspond to the generation of multi-tone pump laser where the optical power is equally divided among those tones. In other words, the RF voltage input to the phase modulator must be calibrated so that a single RF tone applied to the modulator corresponds to the generation of three optical tones (unsuppressed carrier and two sidebands) with matching optical power on each tone. In practice, the frequency response of the optical phase modulator limits the equal division of optical power among the generated optical tones. Figure 5.2 shows the measured RF spectrum of the dithered OPC pumps that were phase modulated with two-tone RF signal (60MHz and

600MHz) generated from the AWG. These plots were obtained from RF spectrum analyzer that was fed an RF signal generated from a photodiode that detected each pump. The frequency response of the modulated pumps does not show a balanced optical power division among the generated optical tones, this can be seen by comparing the RF tones located at positive frequency with RF tones located at negative frequency.

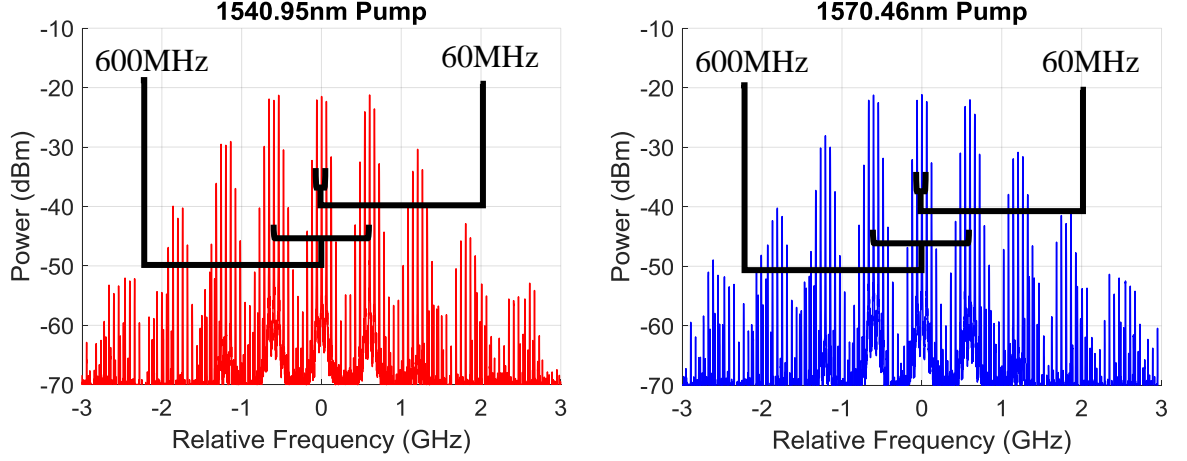


Figure 5.2: Frequency response of dithered OPC pumps. The x-axis represents the frequency relative to the CW laser frequency.

The imbalanced phase modulation of the OPC pumps implies that the optical power of the original laser would not be equally divided among the generated optical tones, leading the SBS to be triggered by the peak power among of the frequency components of each pump. Figure 5.3 shows the SBS measurement setup (a) and the SBS reflected power as function of pump input power to the HNLF (b). The SBS power was measured for both pumps with different dithering schemes (no dithering, 60MHz dithering, and 60+600MHz dithering). The output of the PBC, as shown in figure 5.3 (a), was connected to an isolator (to prevent damage from the high SBS reflected power). A 1% coupler to monitor was installed at the input of the HNLF to monitor the pump power (passed to the HNLF) and SBS power (reflected from the HNLF).

Figure 5.3 (b) shows that there is a reflected power that grows at a rate of 1dB/dB<sub>(power)</sub> which is induced from either the Rayleigh scattering of the HNLF or the back reflections of the splices along the path. The figure also shows that the power at which SBS backscattered light is dominant has expanded by 3.2dB when a single-tone (60MHz) dithering was applied on the pumps, while the two-tone (60MHz+600MHz) dithering have shown 8.7dB expansion. The SBS reflected power from P<sub>1</sub> is close to the SBS power reflected from P<sub>2</sub> which suggests that the optical power distribution among the dithering tones is similar on each OPC pump. Ideally, we should expect SBS threshold expansion by a factor 4.77dB per dithering tone (a factor of 3 per dithering tone). The experimental SBS threshold expansions of 3.2dB and 8.7dB for



60MHz and 60+600MHz dithered pumps, respectively. These SBS threshold expansions are 1.5dB and 0.85dB worse than the ideal case expectation, respectively; the non-flat frequency response of the optical phase modulators (as shown in figure 5.2) is the main reason behind the lower experimentally obtained SBS expansion values (shown in figure 5.3(b)).

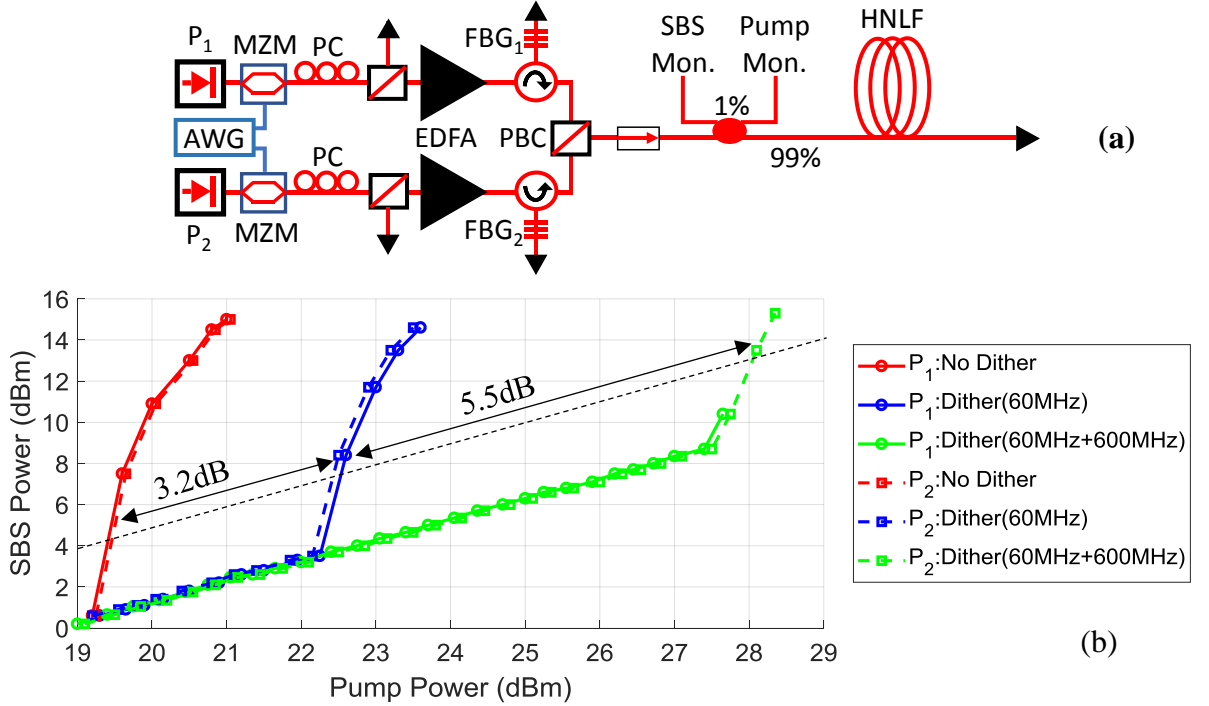


Figure 5.3: (a) SBS measurement setup, (b) SBS power as a function of pump power at the input of the HNLF.

Counter dithering indicates that the modulating RF signal for one pump is  $180^\circ$  phase shifted from the modulating RF signal for the other pump, which results in the cancellation of dithering tones on the conjugated signals at the output of the OPC. I have reverted the experimental setup to the original setup (figure 5.1) and injected two CW lasers (one on each OPC band: 1550nm and 1560.5) to the OPC and observed the spectral properties of the conjugated copies of each CW laser. Figure 5.4 shows the RF spectrum of photodiode-detected conjugated CW lasers at the output of the OPC. By adjusting the phase of the RF tones generated from the AWG, we have achieved 32dBc (dB relative to the carrier peak) suppression of the phase modulation sidebands transferred from the pumps to the conjugated CWs. The figure shows that both OPC bands have the same suppression ratio implying an identical response on both OPC paths. The residual counter dithering tones was hard to eliminate due to the unbalanced frequency response of the phase modulators (as shown in figure 5.2).

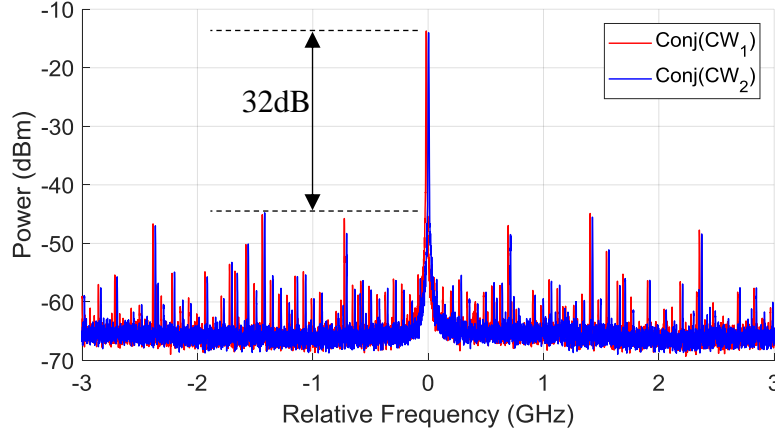


Figure 5.4: The frequency response of conjugated CW lasers (1550nm and 1560.5nm).

### 5.1.2 Polarisation Dependency of the Optical Phase Conjugator

The random birefringence and the PMD effects of the SMF components and HNLF will alter the perpendicularity of the two pumps, which might cause a large polarisation dependent loss occurring on the conjugated signals. The polarisation controllers (PC1 and PC2) were installed just before the HNLF to find the principal polarisation perpendicularity state of the two pumps. To calibrate the polarisation controllers (PC1 and PC2) to the desired condition, we have used depolarised spectrally shaped ASE noise band (1540nm to 1555.6nm) as an input to the OPC, see figure 5.5, and we have observed the optical spectrum generated on the output 1% monitor point on each OPC path (OPC1 that conjugates signals passing through PC1 and OPC2 that conjugates signals passing through PC2). The polarised ASE band (shown in figure 5.5) will be used later to test the polarisation dependent loss of the conjugated polarised ASE noise band. A polarisation controller (PC0) was installed at the input of the OPC to check the polarisation dependency of the conjugated signals as the PC0 was changed randomly.

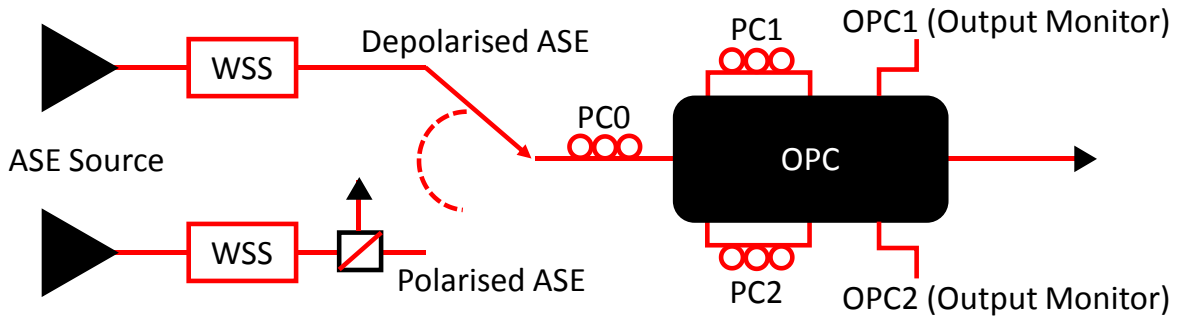


Figure 5.5: Polarisation independency calibration and testing setup.

At a given PC1 polarisation state, we have seen that the conjugation efficiency (idler power to signal power ratio at the output of the HNLF) of the depolarised ASE band changes as the state of PC0 was changing implying the existence of polarisation dependent conjugation efficiency,

as one of the polarisations of the ASE achieved higher conjugation efficiency than the other. The minimum conjugation efficiency of a depolarised ASE band corresponds to the state at which both polarisations of the ASE noise band were conjugated with equal efficiency (no polarisation dependent conjugation efficiency); this polarisation independency was observed as the conjugated ASE spectrum remained unchanging as PC0 state was randomly changed. Both PC1 and PC2 were calibrated to minimise the conjugation efficiency of the depolarised ASE band. Figure 5.6 shows the optical spectrum at the output monitor points (of OPC1 and OPC 2), we have used the OSA's HOLD MAX and HOLD MIN functions to observe the range of conjugation efficiency variation as PC0 was changed randomly. From figure (left side), it can be seen that both OPC paths (OPC1 and OPC2) have approximately the same spectral properties at the pumps were turned on. From the right side of the figure, we can see that the conjugated ASE band hardly changes (as PC0 was randomly changed) which indicates the polarisation independency that we wanted to achieve. The figure also shows that both OPCs have conjugation efficiency (the ratio of the idler power to the signal power at the output of the HNLF) ranging between -2.6dB to -0.6dB across the conjugated spectrum which indicates that the OPC will alter the flatness of the input signals to the OPC. This flatness issue can be solved by applying a spectral shape to the output WSS of the OPC which flattens the conjugated signals at the output of the OPC.

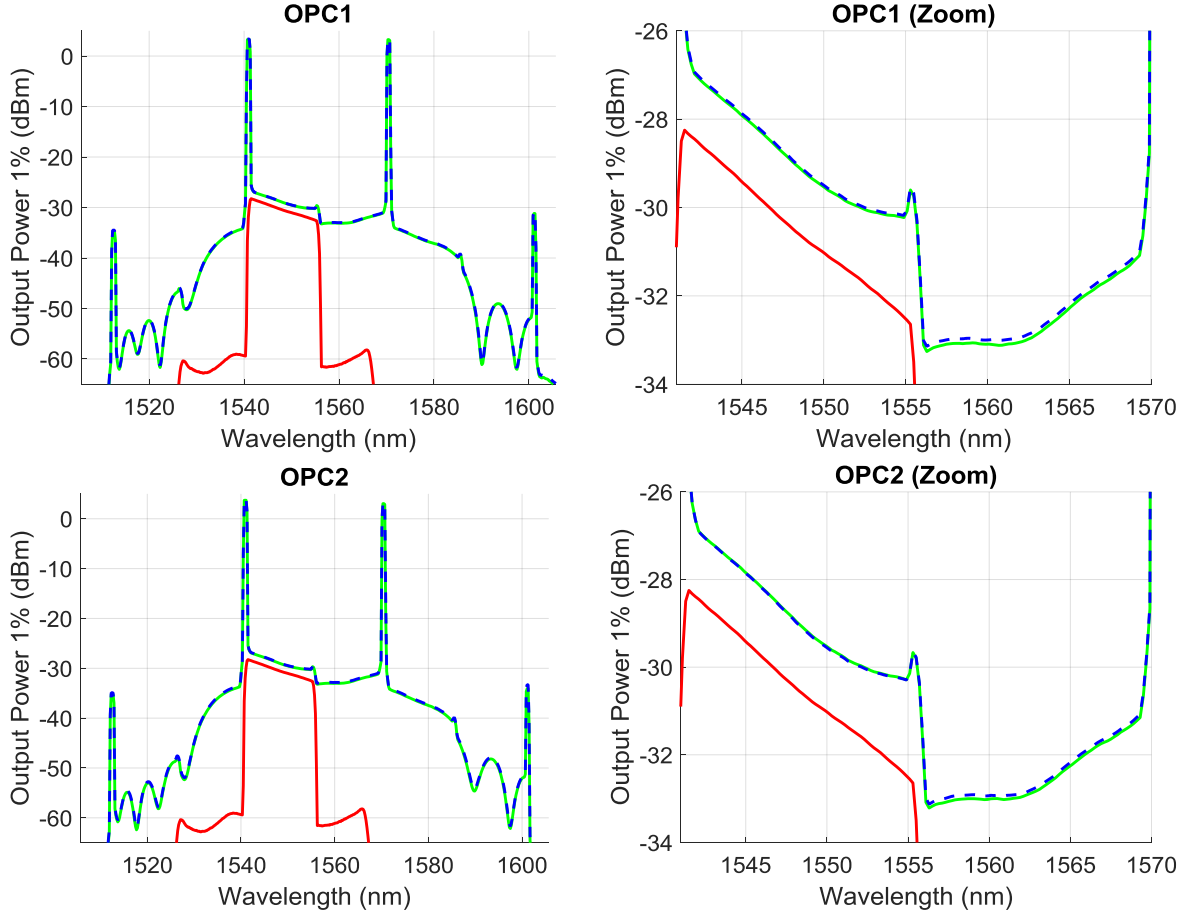


Figure 5.6: Optical spectrum observed at 1% monitor (of OPC1 and OPC2) when the input signal is depolarised ASE band. (red solid lines) indicates the spectrum as the pumps were turned off, (solid green lines) HOLD MIN optical spectrum with the pumps turned on after PC0 was randomly changed, (dashed blue lines) HOLD MAX optical spectrum with the pumps turned on after PC0 was randomly changed.

To measure the polarisation dependent loss of the two OPC paths, we have used the polarised ASE band as the input to each OPC. The polarised ASE band input was generated by filtering out one of the polarisations of the previously used ASE band using PBS (see figure 5.5). Figure 5.7 shows the output maximum and minimum optical spectrum (at the output monitor points) as PC0 was randomly changed. We can see that the polarisation dependent loss occurs at the conjugated ASE band ranges within 0.7dB. This polarisation dependent loss can be explained by the fact that we have used non-PM HNLF, the random birefringence of the HNLF will lead the perpendicularly polarised at the input of the HNLF to change their polarisation state randomly along the HNLF.

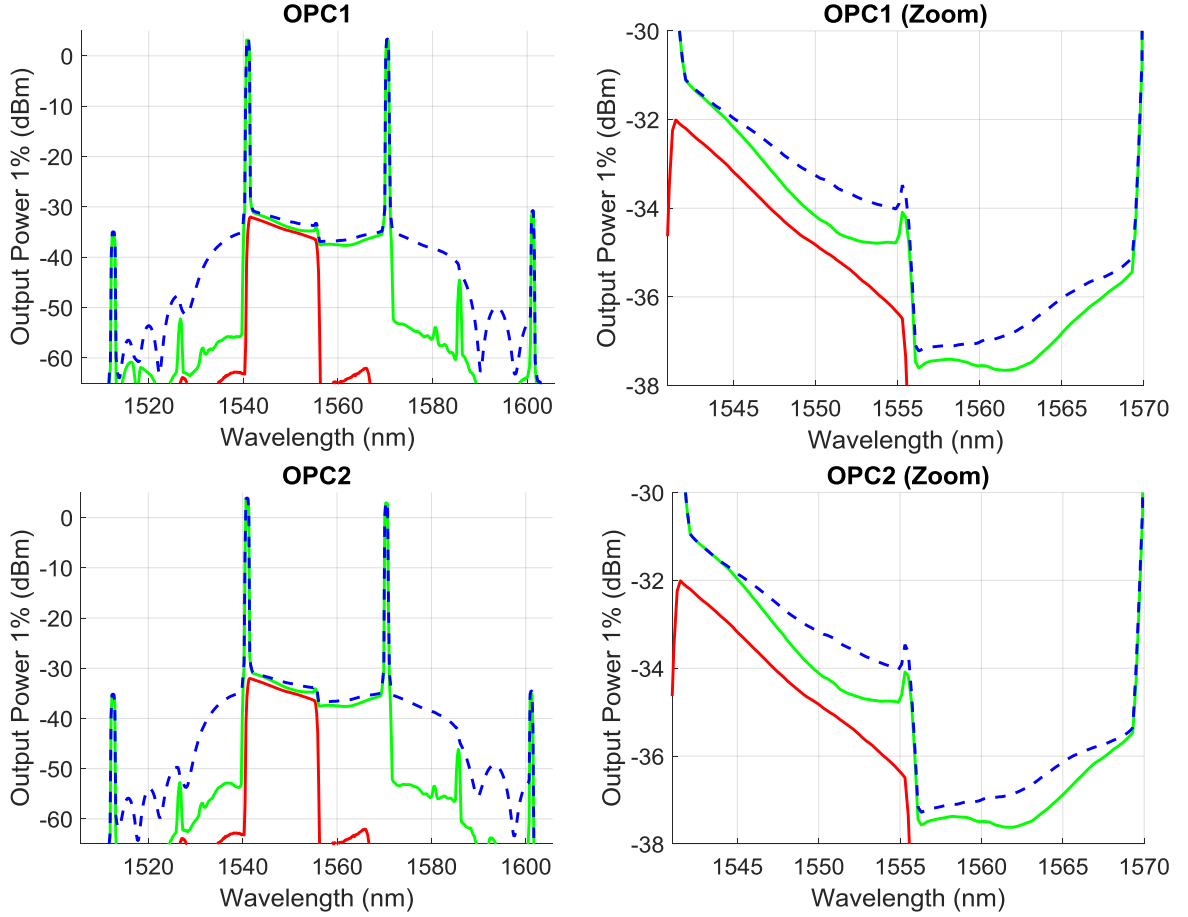


Figure 5.7: Optical spectrum observed at the OPC output 1% monitors (OPC1 and OPC2) when the input signal is polarised ASE band. (red solid lines) indicates the spectrum as the pumps were turned off, (solid green lines) HOLD MIN optical spectrum with the pumps turned on as PC0 was randomly changed, (dashed blue lines) HOLD MAX optical spectrum with the pumps turned on and PC0 was randomly changed.

### 5.1.3 Performance of Conjugated Modulated Optical Signals

The propagation of signals and pumps along the HNLFF not only generates the phase conjugated copies (idlers), but also generates unwanted interfering products that can severely impact the performance of the phase conjugated signals. Figure 5.8 shows the spectrum at the output monitor of the OPC when inserting 10dBm CW laser ( $\lambda_s=1552.5\text{nm}$ ,  $f_s=193.1\text{THz}$ ) into the OPC. From the figure, we can see that three different copies of the CW laser have been formed (between the two pumps). One of these copies is the desired phase conjugated copy generated from the non-degenerate FWM of the CW input signal with the two OPC pumps ( $f_i=f_{P1}+f_{P2}-f_s$ ). The other two CW copies (at  $f_{D1}$  and  $f_{D2}$ ) were generated due to the degenerate and non-degenerate FWM that occur between one of the pumps and the signal or the idler or both, where:

- The signal copy at  $f_{D1}$  is generated due to the degenerate FWM between the 1570.4nm pump and the input CW signal ( $f_{D1} = f_s + f_s - f_{P2}$ ), and the non-degenerate FWM between the 1540.94nm pump and both the signal and idler ( $f_{D1} = f_{P1} + f_s - f_i$ ).
- The signal copy at  $f_{D2}$  is generated due to the degenerate FWM between the 1570.4nm pump and the input CW signal ( $f_{D2} = f_i + f_i - f_{P1}$ ), and the non-degenerate FWM between the 1540.94nm pump and both the signal and idler ( $f_{D2} = f_{P2} + f_i - f_s$ ).

Since the idler is generated from the interaction of the input signal with the perpendicularly polarised counter dithered pumps, the power of the idler will be independent from the input signal polarisation state and will be cleared from the dithering effects of the two pumps (as shown in figure 5.4). On the other hand, the extra nonlinear products spectrally located at  $f_{D1}$  and  $f_{D2}$  will be broadened according to the dithering frequency response of the pump (as shown in figure 5.2) since they have been generated from the interaction of the signal or idler with only one of the pumps; we will refer to these products in the following text as “*the unwanted nonlinear products*”

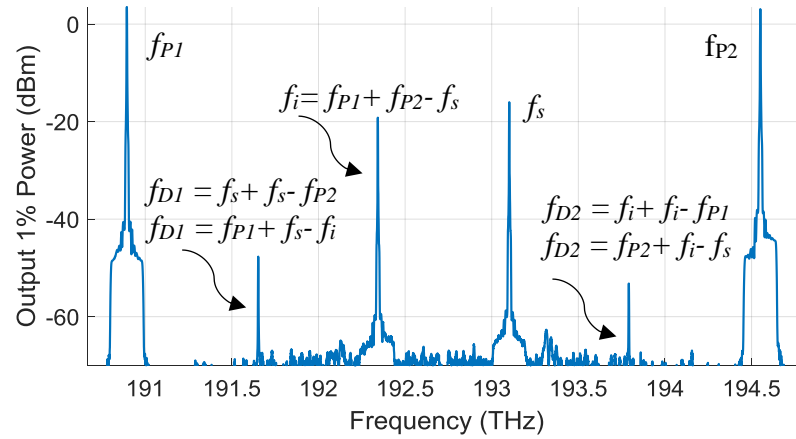


Figure 5.8: Optical spectrum (resolution: 0.02nm) at the output 1% monitor of the OPC, when a 10dBm CW laser is injected at the input of the OPC.

To check the frequency response of the unwanted nonlinear products generated in the OPC (on both paths, OPC1 and OPC2) we have swept the CW laser (10dBm) from 1544nm to 1567nm with 0.8nm (100GHz) step. Figure 5.9 shows the peaks of: signals (open circles), conjugates (open triangles), the unwanted nonlinear products generated at  $f_{D1}$  (filled circles), and the unwanted nonlinear products generated at  $f_{D2}$  (filled triangles). The figure shows that if the full bandwidth of the OPC was filled with signals (30nm), then the OSNR of the conjugated signals will be limited by the power of the unwanted nonlinear products (ranging between 24dB and 29dB in this case of 10dBm CW). The power of unwanted nonlinear products, posing as OSNR limiting factor, can be minimised by optimising the input power to the OPC; the output OSNR

of the conjugated signals would improve with a rate of +1dB/dB of input signal power until the ASE noise limits is reached.

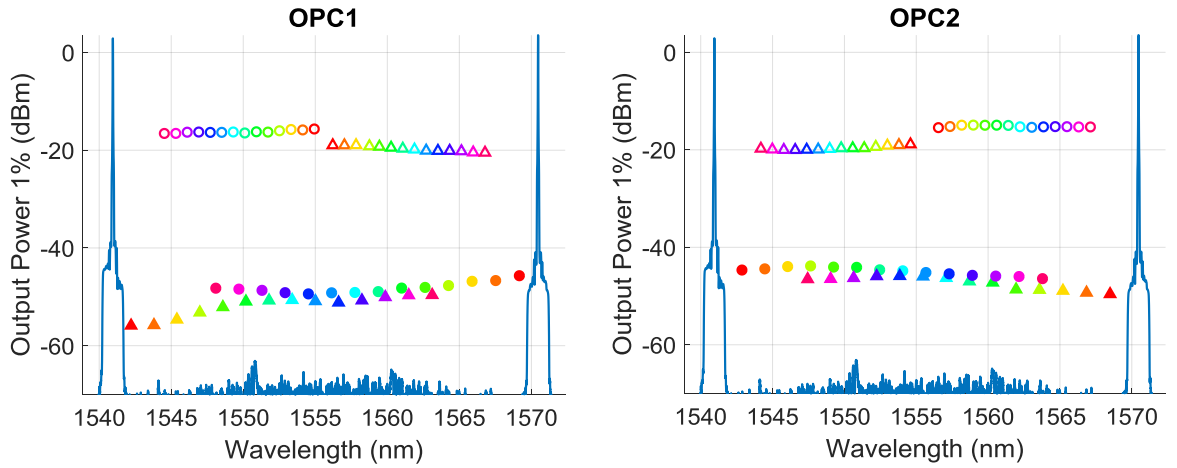


Figure 5.9: Optical spectrum (resolution: 0.02nm) at the output 1% monitor of the OPC, when a 10dBm CW laser is injected at the input of the OPC. CW laser was swept from 1544nm to 1567nm with 0.8nm (100GHz) step, the color code indicates the CW peaks resulted for each step.

The unwanted nonlinear interfering products (generated in the OPC) can be avoided from falling under the conjugated signals by limiting the total bandwidth to be conjugated by the OPC. Figure 5.10, shows two cases (a and b) at which the unwanted nonlinear products were avoided from interfering with the conjugated signals. From the figure, we can see that one third of the OPC bandwidth (separation between the two pumps) can be used if the unwanted nonlinear products wished to be avoided. As the unwanted nonlinear products were avoided, the local nonlinear interactions (among the signals or idlers) become dominating interfering products; these nonlinearities can be minimised by reducing signal power launched into the OPC until the ASE noise limit is reached. The local nonlinearities (among signals, among idlers, or among both signals and idlers) generated in the OPC are cubically dependent on the input power to the OPC, also, these nonlinearities are quadratically dependent on the bandwidth input signal band (as shown in [136,137]). We have chosen to use the central band (1552nm-1560nm, 1THz) for our experiments as it minimises the frequency shift of the conjugated signals from the original signal spectral locations, to avoid the effect of dispersion slope when deploying the OPC in transmission link

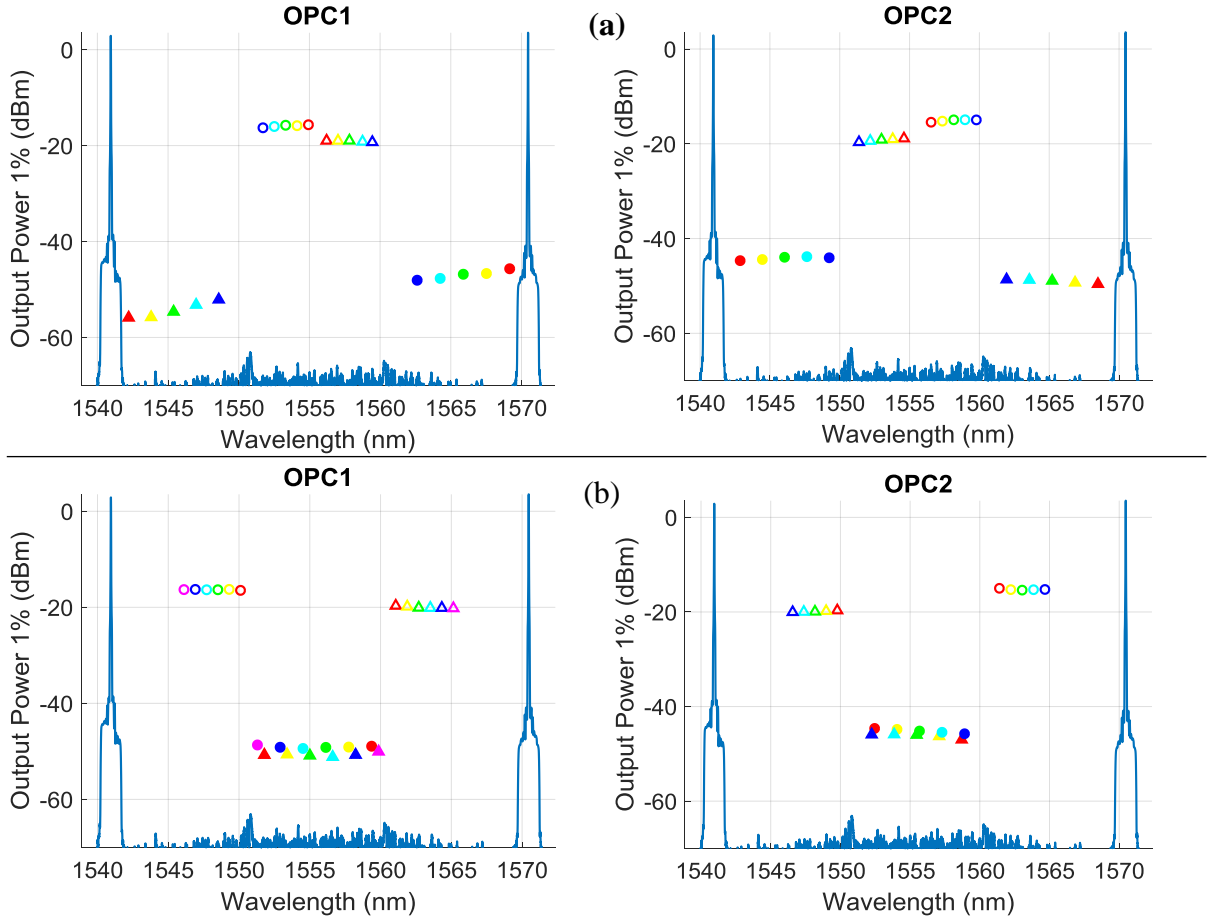


Figure 5.10: Interference-free conjugation (by limiting the signal bandwidth) tested by 10dBm CW laser. (a) central band (1552nm-1560nm), (b) outer band (1546nm-1550nm & 1551nm-1565nm).

Figure 5.11 shows the experimental setup that was used to test the performance of modulated signals to be conjugated using the previously described dual band OPC. In this setup, we have used eight lasers (linewidth<100KHz) on 50GHz grid, each four lasers construct an OPC band (first band: 192.25THz to 192.4THz, and second band: 193.05THz to 193.2THz). The even and odd indexed laser channels were separately modulated using dual-polarisation optical modulator (Tektronix OM5110). The modulators were fed by 28Gbaud PM-QPSK Nyquist pulse shaped with roll of factor of 0.2, the electrical signals were generated from an Arbitrary Waveform Generator (AWG: Keysight M8195A) operating at 56GSa/s and a  $2^{15}-1$  PRBS bit sequence. The AWG decorrelates the modulating data of X and Y polarisations by 4096 symbols. The two sets of modulated channels (even indexed and odd indexed) were decorrelated over 4m of optical fibre and combined using a 3dB coupler (400 PM-QPSK symbols), then was amplified to pass through the OPC or to bypassing the OPC to reach the noise loading coupler. The ASE noise loaded onto the signals was generated from an EDFA then spectrally shaped and flattened using a WSS. A Variable Optical Attenuator (VOA) was used to control the level of ASE noise added to the signals. A tunable band pass filter was used



to filter the targeted channels to be detected by the dual polarisation coherent receiver, which was running at a sampling frequency of 100GSa/s.

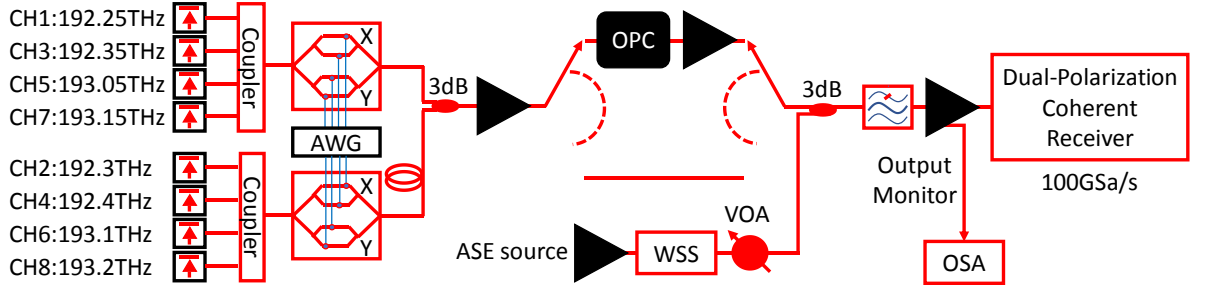


Figure 5.11: Back to back performance measurement setup, (with and without OPC).

Figure 5.12 shows the optical spectrum at the input and the output monitor points of the OPC (for each band). From the figure, we can see that the input WSS of the OPC (see figure 5.1) not only split the two bands (below and above 1555.7nm) but also filter out the ASE noise that falls in the idler (conjugates) band. The figure also shows that the unwanted nonlinear products (generated around 1547nm and 1564nm) were not interfering with the conjugated signals, and the conversion efficiency achieved at the output of the HNLF was -4dB. We found that the total OPC insertion loss (as it appears in figure 5.1) is 16dB including the flattening spectral profile applied on the output WSS.

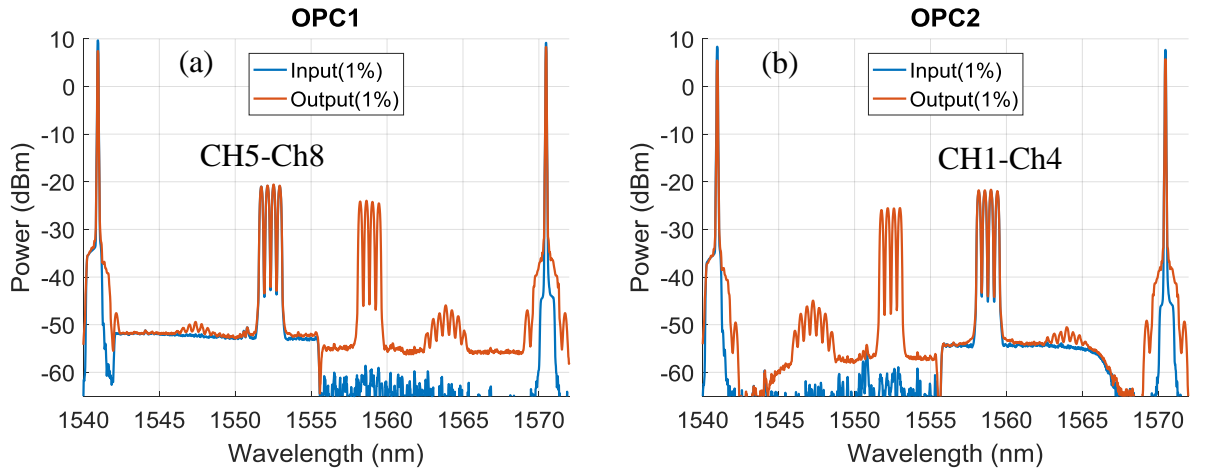


Figure 5.12: Optical spectrum at the input and output monitor points of the OPC (for both bands: OPC1 and OPC2). [X2]

We have tested the performance as a function of received Optical Signal to Noise Ratio (OSNR) which was measured from OSA (resolution 0.1nm, 12.5GHz) at the monitor point of the receiver EDFA, see figure 5.11. Figure 5.13(a) shows the  $Q^2$  factor of the received 28Gbaud PM-QPSK as a function of the received OSNR, (b) shows the BER a function of received OSNR. For the case of signals propagating through the OPC, we have measured the

performance of one channel from each band (Ch2 and Ch7). Each experimental point on the figure consists of the mean of measured  $Q^2$  factor (or BER) for 10 captures each has 500000 samples. The back to back measurement (bypassing the OPC) shows that QPSK signal quality factor grows in a rate of +1dB/dB<sub>OSNR</sub> when the OSNR is ranging between 10dB to 21dB and then the performance ( $Q^2$  factor) saturates to reach a quality factor of 21.35dB at the highest SNR (34.3dB) due to the transceiver noise. As the signals propagate through the OPC, we can see that the maximum received OSNR (x-axis) is degraded by 2.3dB which can be explained by the extra ASE noise added from the EDFA that compensates for the insertion loss of the OPC. The conjugated signals show a degradation of 0.7dB in Q factor compared to signals bypassing the OPC at OSNR=30dB. The nonlinear effects (in the HNLF) were not the degrading factor in the measurements plotted in figure 5.13, since the input power to the OPC was optimised to achieve the highest performance of the conjugated signals (as we will show next).

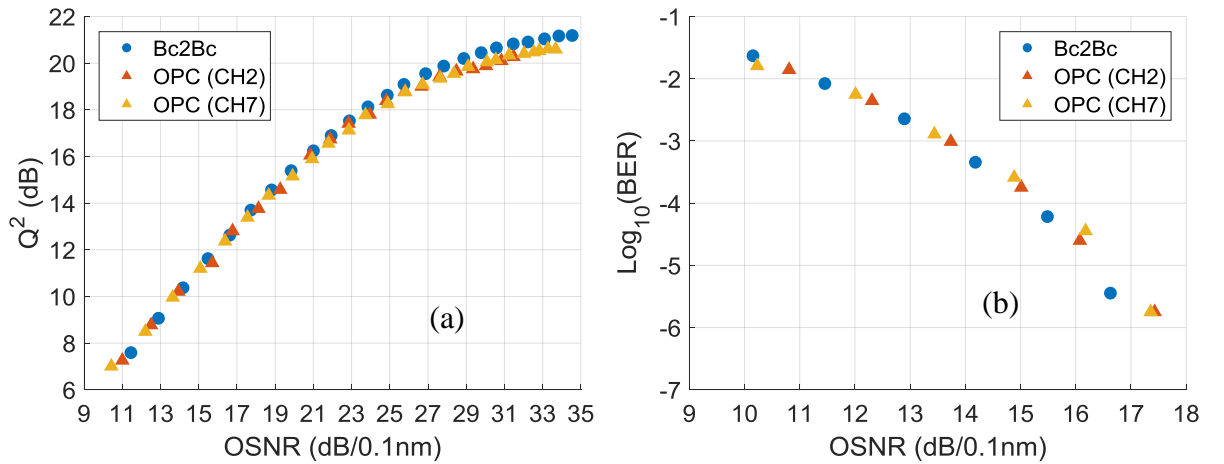


Figure 5.13: Receiver  $Q^2$  factor(a) and BER(b) as a function of OSNR.

The main performance limiting factors of the OPC are: the linear ASE noise (from inside the OPC), the OSNR penalty due to the insertion loss of the OPC, the counter dithering residual noise, and the nonlinear interference due to the propagation in the HNLF. The ASE noise can be generated from inside the OPC which is the ASE (from high power EDFAs) that passes through the FBGs, this ASE noise floor can be seen clearly in figure 5.12. To evaluate the contribution of each noise component to the performance of the conjugated signals, we have swept the input power to the OPC (when the loaded noise in figure 5.11 was turned off) and observed the changes in the performance of the conjugated signals. Figure 5.14 shows the  $Q^2$  factor as a function of input power (per channel) to the OPC, the maximum  $Q^2$  factor achieved in the back to back measurement was plotted as a reference point (blue line). We can see that

the  $Q^2$  factor of the conjugated signals degraded by the linear ASE noise when the input power to the OPC is lower than 2dBm/Ch, then the signal quality factor saturates to reach its maximum ( $Q^2=20.55\text{dB}$ ) around 7dBm/Ch. Finally, the nonlinear noise becomes dominant as the input power to the OPC is higher than 10dBm/Ch. In general, we can conclude that in this OPC design, the conjugated signals are facing 0.7dB degradation (when compared to back to back measurement) in the  $Q^2$  factor at the optimum input power. In general, we can see that we have built a successful polarisation independent dual band OPC with a small performance penalty of 0.7dB, and the performance of the two bands are equivalent.

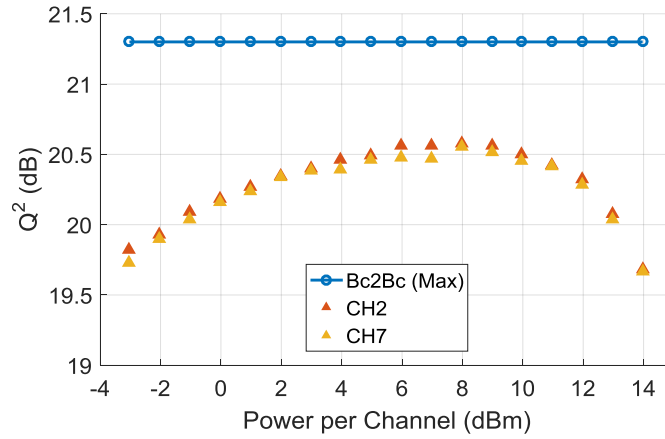


Figure 5.14: Received  $Q$  factor as a function of input power to the OPC.

In another experiment, we have tested the performance of 30x30Gbaud PM-QPSK modulated signals that pass through the OPC, this experiment achieves higher spectral efficiency when compared to the previous results (displayed in figure 5.13). In this setup, we have used 10 lasers, as shown in figure 5.15, these lasers were spectrally divided on both OPC bands (Band1:Ch1-5 and Band2:Ch6-10). The lasers within each OPC band are spectrally separated by 100GHz. The even indexed lasers are combined using 4x1 and 2x2 couplers, the same also applies to the odd indexed lasers. Both the even and odd indexed lasers were then combined using a 3dB coupler to be modulated later by an optical modulator fed by 30GHz clock. The modulator suppresses the laser carrier and generate two optical tones (two sidebands with 66GHz frequency separation) resulting 20 optical lines at the output of the phase modulator. We have chosen to operate the optical phase modulation with suppressed carrier to prevent the generation of higher optical tones from interfering with the sidebands generated from neighboring lasers. A 1x2 WSS was used to suppress the remaining unsuppressed carriers and segregate (to different output ports) the comb lines originated from even indexed lasers and the comb lines originated from odd indexed laser. At the output of each WSS port, the comb lines

were combined with the original laser (suppressed carriers in the comb path) using 70:30 optical coupler to create separated even indexed and odd indexed bands of 15 lines separated by 66GHz. The even indexed and odd indexed lines were modulated separately using Tektronix OM5110. The modulators were fed by 30Gbaud PM-QPSK Nyquist pulse shaped with roll off factor of 0.1, the electrical signals were generated from an Arbitrary Waveform Generator (AWG: Keysight M8195A) operating at 60GSa/s and a  $2^{15}-1$  PRBS bit sequence.

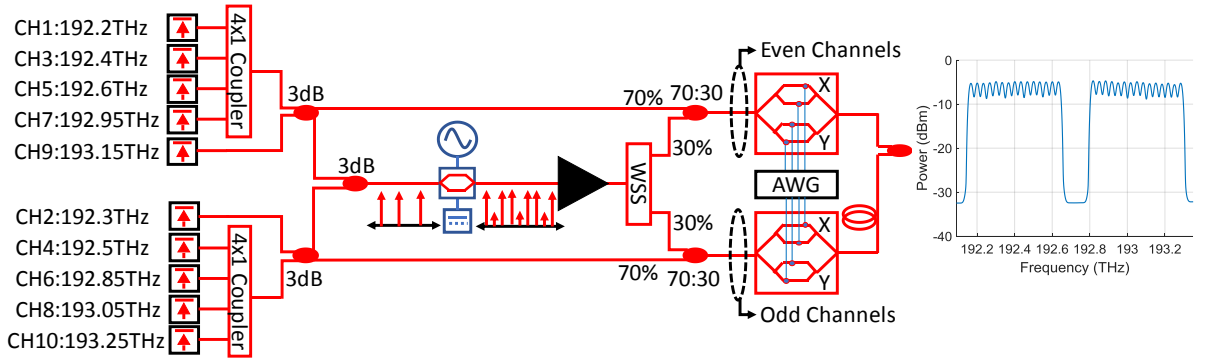


Figure 5.15: Experimental setup for spectrally efficient, comb-based transmitter system. [X3]

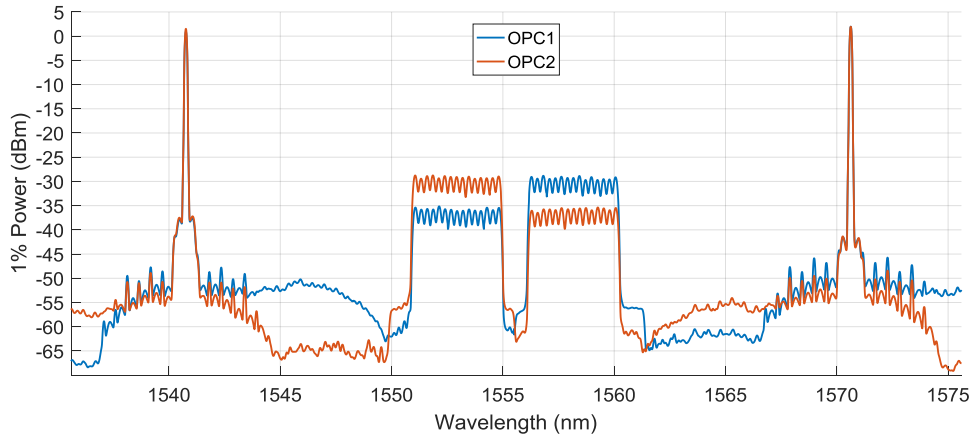


Figure 5.16: Optical spectrum at the output monitor points of the OPC (on both bands). [X3]

In this experiment, we had to reduce the OPC pumping power by 2dB (due to damage in the high power EDFA that amplified the 1570.4nm). As a result, the total OPC insertion loss became 20dB (including the spectral flattening applied by the WSS) due to the reduction of the conversion efficiency by 4dB. Figure 5.16 shows the optical spectrum at the output monitor points of each OPC while conjugating 30 modulated channels. From the figure, it can be seen that the modulated channels were conjugated with conversion efficiency ranging around -7dB with an acceptable flatness. The figure also shows that the unwanted nonlinear products (generated around 1547nm and 1564nm) were not interfering with the conjugated signals as their power roll off below the ASE noise floor at 1550nm and 1567nm.

Figure 5.17(a) shows the  $Q^2$  factor as a function of the received OSNR for signals in back to back setup and through the OPC, (b) shows the BER as a function of received OSNR. For the case of signals propagating through the OPC, we have measured the performance of the central channel from each band (Ch8 and Ch23). The back to back measurement (bypassing the OPC) shows that QPSK signal quality factor grows in a rate of 1dB/dB<sub>OSNR</sub> when the OSNR is ranging between 10dB to 15dB and then the performance ( $Q^2$  factor) saturates to reach a quality factor of 18.7dB at the highest OSNR (30.1dB) due to the transceiver noise and the interference from neighboring channels. As the signals propagate through the OPC, we can see that the maximum received OSNR (x-axis) has been degraded by 3-3.5dB which can be explained by the extra ASE noise added from inside the OPC and the EDFA that compensates for the insertion loss of the OPC. Due to the degradation of the conversion efficiency of the OPC, we have seen that the nonlinear regime of the OPC cannot be reached due to the limited output power of the booster EDFA (operated at 20dBm output power) located at the input of the OPC (shown in figure 5.11).

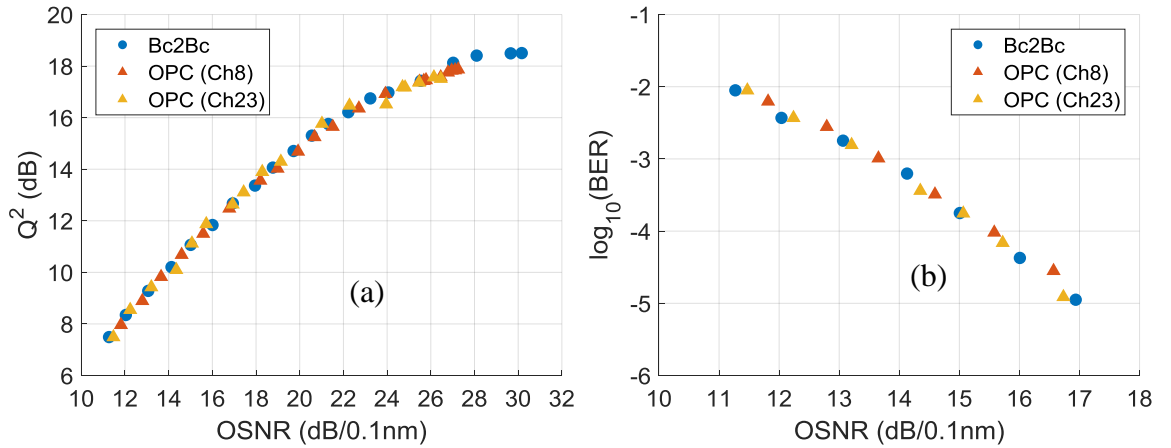


Figure 5.17: Receiver  $Q^2$  factor(a) and BER(b) as a function of OSNR.

Figure 5.18 shows the spectral properties (a) and the  $Q^2$  factor (b) of the modulated channels (back to back and conjugated through the OPC) at maximum OSNR. It can be seen, from figure 5.18(a), that the modulated signal propagating through the OPC shows a degradation in the maximum achieved OSNR ranging around 3.2dB, the spectral shape of the ASE noise indicates that ASE generated from the high power EDFA and leaked from the FBG (can be clearly seen in Figure 5.12) has contributed to the OSNR degradation at the output of the OPC. The performance ( $Q^2$ ) of the PM-QPSK modulated channels ranges around 18.8dB in back to back configuration, while the conjugated channels show a degradation 0.7dB in  $Q^2$  factor due to the

degradation of the OSNR. The variance in performance among the different channels ranges around 0.35dB to 0.5dB in both cases.

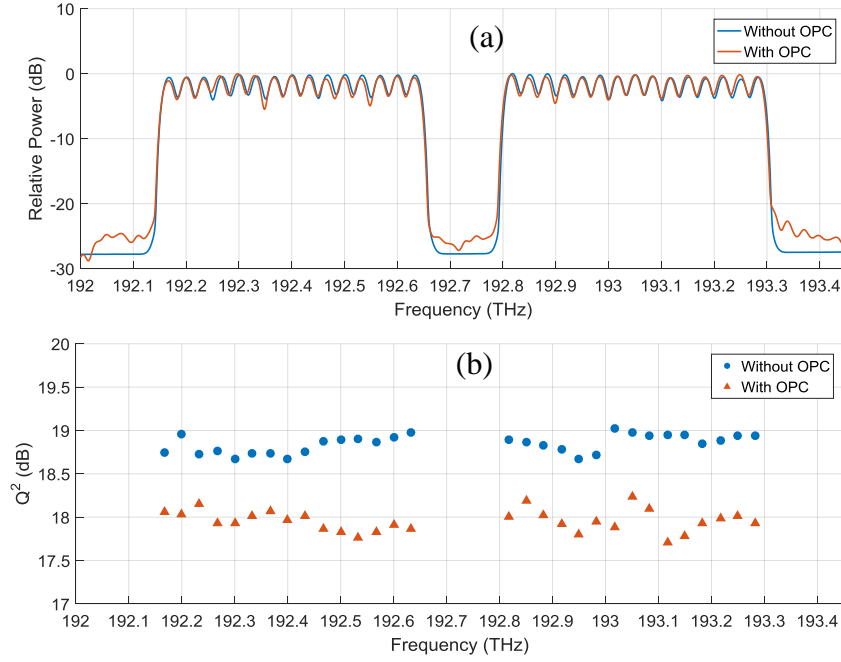


Figure 5.18: (a) Optical spectrum with and without OPC, at maximum OSNR. (b)  $Q^2$  of the individual channels with and without OPC, at maximum OSNR. [X3]

## 5.2 Comb Generator, Dispersion Optimisation Technique

Optical fibre comb generator is another application that uses the nonlinear Kerr properties of optical fibres to generate a large bandwidth of coherently synchronised and equally spaced optical frequency tones. Optical frequency combs were proposed to provide a solution to implement a coherent interference-free DWDM [138] and provide high level of coherence that allow for optical fibre nonlinearity compensation using full field Digital Back Propagation (DBP) [139]. Optical phase modulation has been used to generate optical combs, but this technique provides a limited bandwidth (number of lines) and poor flatness of the generated comb lines [140] which can be relatively improved by using cascaded phase modulators [141]. Cascaded optical fibre parametric mixers have been proposed [41] to generate ultra-wide bandwidth combs that spans C- and L-bands [142]. Parametric optical mixers are preferred to be used when seeded by coherent comb seed that triggers the Kerr effects of the HNLF to generate optical frequency lines over large bandwidth [142]. Cascaded optical parametric mixers suffer from the phase mismatching (dispersion) accumulation along the system which limits the flatness and the bandwidth of the generated combs [41,143], this technique require highly accurate installation of dispersion compensation stages (normally small piece of SSF)

between the highly nonlinear mixers (HNLFs). The dispersion compensating stages in the cascaded optical parametric mixers provide a rigid design that limits the capabilities of the comb to change the frequency separation between the comb lines [41]. A programmable optical processing technique have been proposed [144,145] to optimise the phase profile of the seed comb (dispersion pre-compensation) which provides a flexible technique to optimise the spectral shape (bandwidth and flatness) of the parametric generated comb. In this section, we will show that an interferometric WSS can perform dispersion pre-compensation to control the shape and bandwidth of the comb lines generated along the HNLF.

Figure 5.19 shows the experimental setup of single stage parametric comb regenerator that uses commercial (Pilot Photonics) comb source as a seed to the comb generator [X13]. The seed source generates 12-14 flat comb lines with reconfigurable frequency separation (using an RF clock), the experimental results displayed in this section have used 10GHz comb separation grid centered at 1550nm. At the output of the seed comb source we have used an interferometric WSS that will be responsible for the dispersion pre-compensation. A high power EDFA was used to amplify the seed comb lines and an optical band pass filter was used to filter the out of band ASE noise generated from the high power EDFA. A 70m HNLF was used as a nonlinear medium which has a nonlinear factor of  $\gamma_0=14/\text{W/km}$ ,  $\text{ZDW}(\lambda_0)=1551\text{nm}$ ,  $S=0.024\text{ps/nm}^2$ . A 1% monitor port was used to observe the output optical spectrum generated at the output of the HNLF.



*Figure 5.19: Experimental setup of comb regenerator. [X13]*

The relative phase among seed comb lines is critical to achieve parametric comb expansion, since the nonlinear Kerr interactions will act as coherent optical wave multiplication (equation 2.7). Also, the dispersion accumulation along the HNLF (figure 5.19) gradually changes the phase relation between mixing comb lines which will alter the flatness of the nonlinear Kerr process. We have set the output power of the EDFA to 31.5dBm and changed the phase profile applied to the seed comb lines (applied by the WSS) and observed the output generated comb lines at the output of the HNLF. Figure 5.20 shows the input comb lines with the phase profile applied to it (left side) and the output optical spectrum that was measured at the output of the

HNLf (using high resolution OSA, 150MHz). The figure clearly shows that the dispersion pre-compensation that the interferometric WSS applied dramatically change the generated comb lines at the output of the HNLf. When a -15ps/nm dispersion is emulated on the seed comb lines, the output comb expands to cover 1.5THz (150 lines) bandwidth with power variation of 16dB across the spectrum. An optimised dispersion of -25ps/nm shows the maximum comb expansion achieved by the HNLf which spans over 2.1THz (210 lines) with 11dB power variation. When we have further decreased the dispersion (applied by the WSS) to -35ps/nm, we have seen that the bandwidth of the generated comb lines starts to shrink back to 1.5THz with 16dB of power variation. This indicates that the WSS is over compensating the dispersion accumulation along the system.



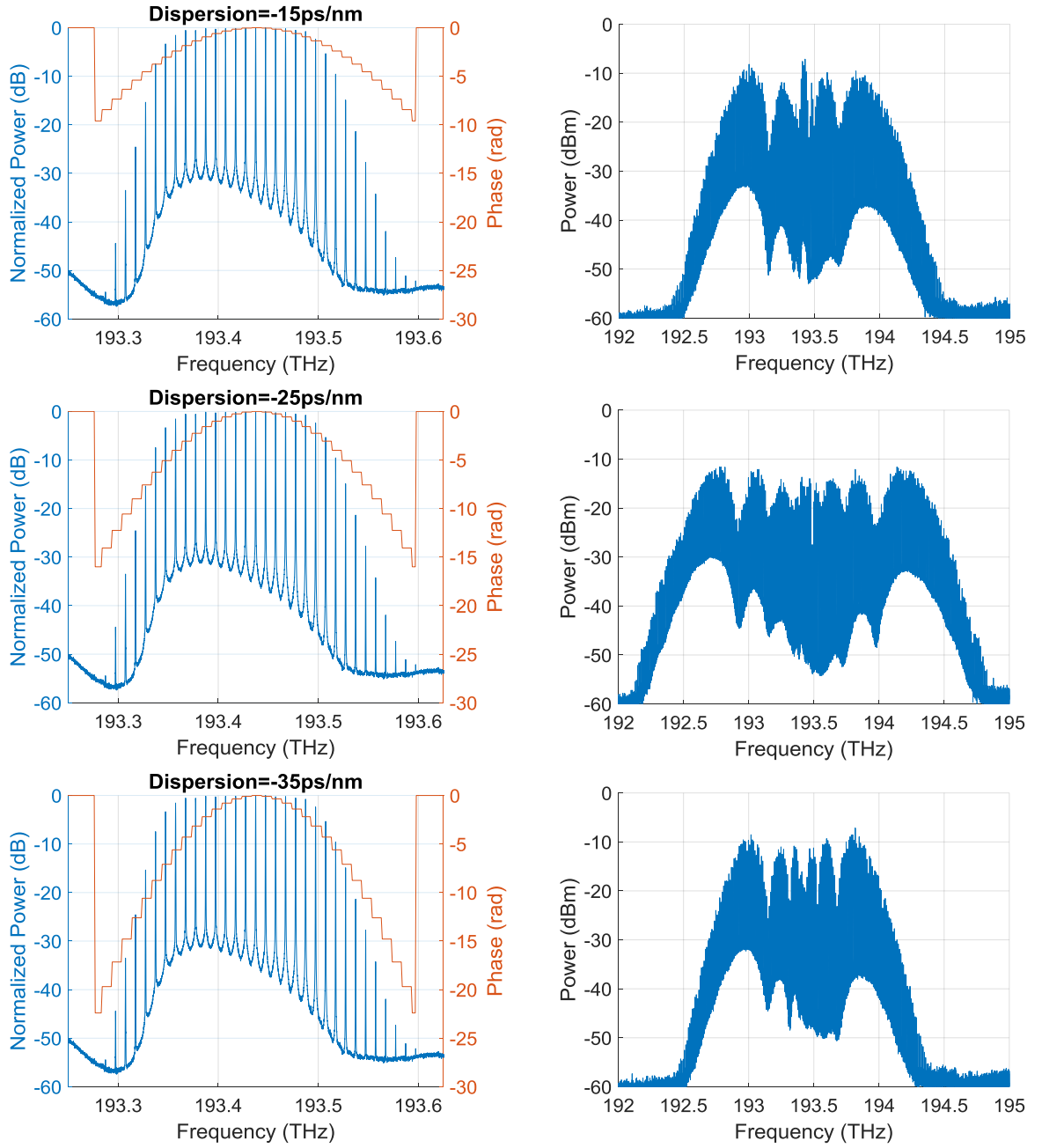


Figure 5.20: (left) Input Comb lines with the phase profile applied to the optical spectrum using the interferometric WSS. (right) output optical spectrum of the HNL (1%).

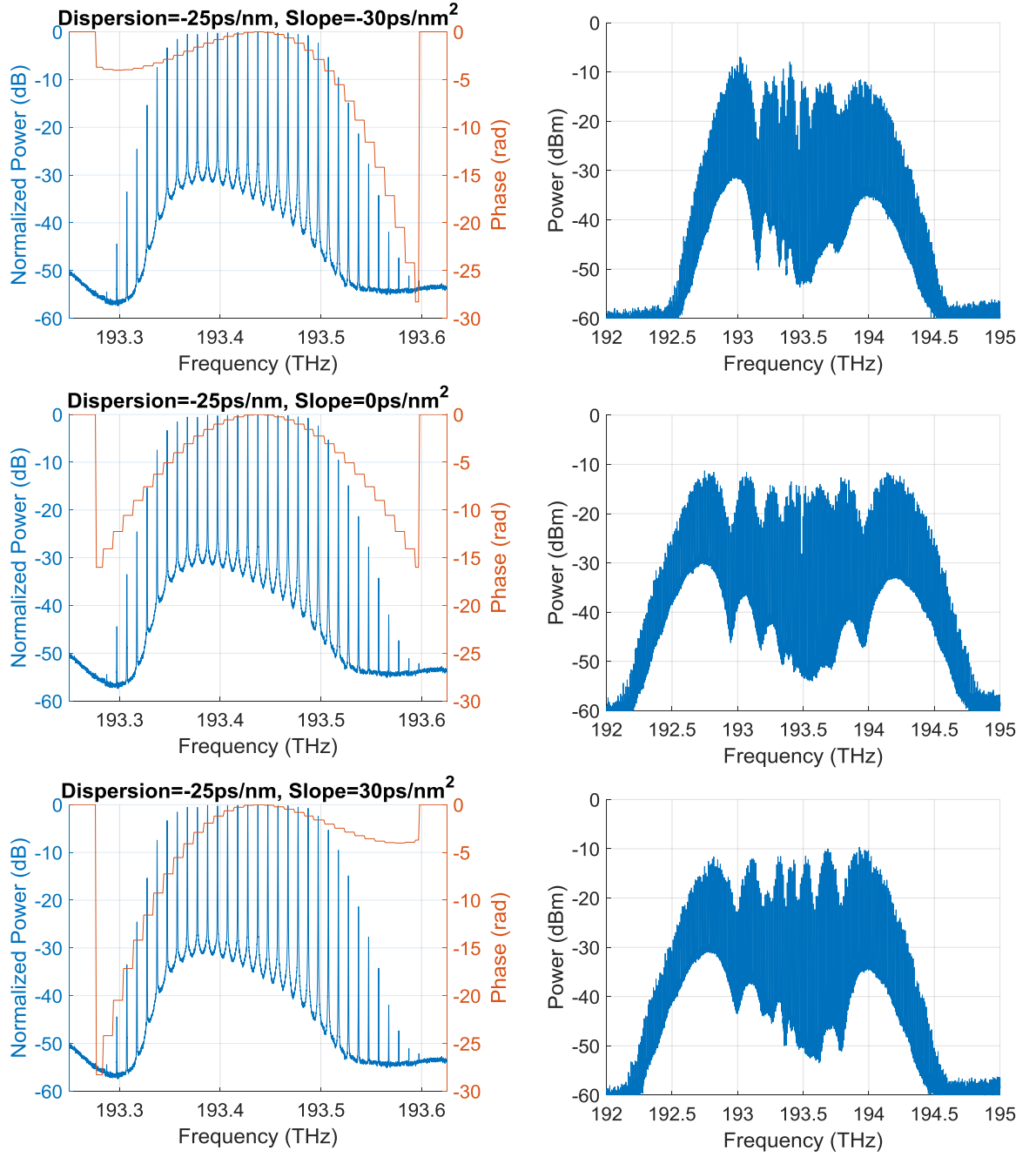


Figure 5.21: (left) Input Comb lines with the phase profile applied to the optical spectrum using the interferometric WSS. (right) the output optical spectrum of the HNLF (1%).

Figure 5.21 shows the effect of changing the dispersion slope compensation (enforced by the WSS) on the shape of the regenerated comb lines (at the output of the HNLF). The figure shows that only when the dispersion slope applied to the seed comb is in the order of  $\pm 30\text{ps/nm}^2$ , a significant degradation in the bandwidth and flatness of the generated comb lines by the end of the HNLF can be observed. When applying the pre-compensation dispersion slope ranging above  $30\text{ps/nm}^2$  the phase of the seed comb lines on the edge of the spectrum start to change which degrades the nonlinear Kerr generation efficiency achieved in the HNLF. This indicates

that the pre-compensation of the dispersion slope has no significant contribution to improve the bandwidth and the power variation across the generated comb lines. This can be explained by the fact that the dispersion slope pre-compensation is only applied on a small bandwidth of seed comb and would only affect the efficiency of first order nonlinear Kerr effects of the HNLF (the central 36 lines). The efficiency of higher order Kerr effects (beyond the central 36 lines) will be dictated by the local dispersion and dispersion slope accumulation along the HNLF, which explains the power rippling and noise floor of the comb lines across the spectrum.

Based on the previous observations, we can say that the pre-dispersion compensation using the interferometric WSS can only optimise the efficiency of the first order Kerr effects occurring along the HNLF, while the comb lines generated from higher order nonlinear effects will depend on the local accumulation of dispersion and dispersion slope along the HNLF. Figure 5.22 shows the generated comb lines (at the output of the HNLF) as the EDFA output power was changed (given that the WSS was applying -25ps/nm dispersion on the seed comb lines). We can see that increasing the power of seed comb lines would result in the expansion of the generated comb lines by the end of the HNLF. As the input power increases above 33.5dBm, the generated comb lines start to suffer from OSNR degradation due to the parametric noise amplification.

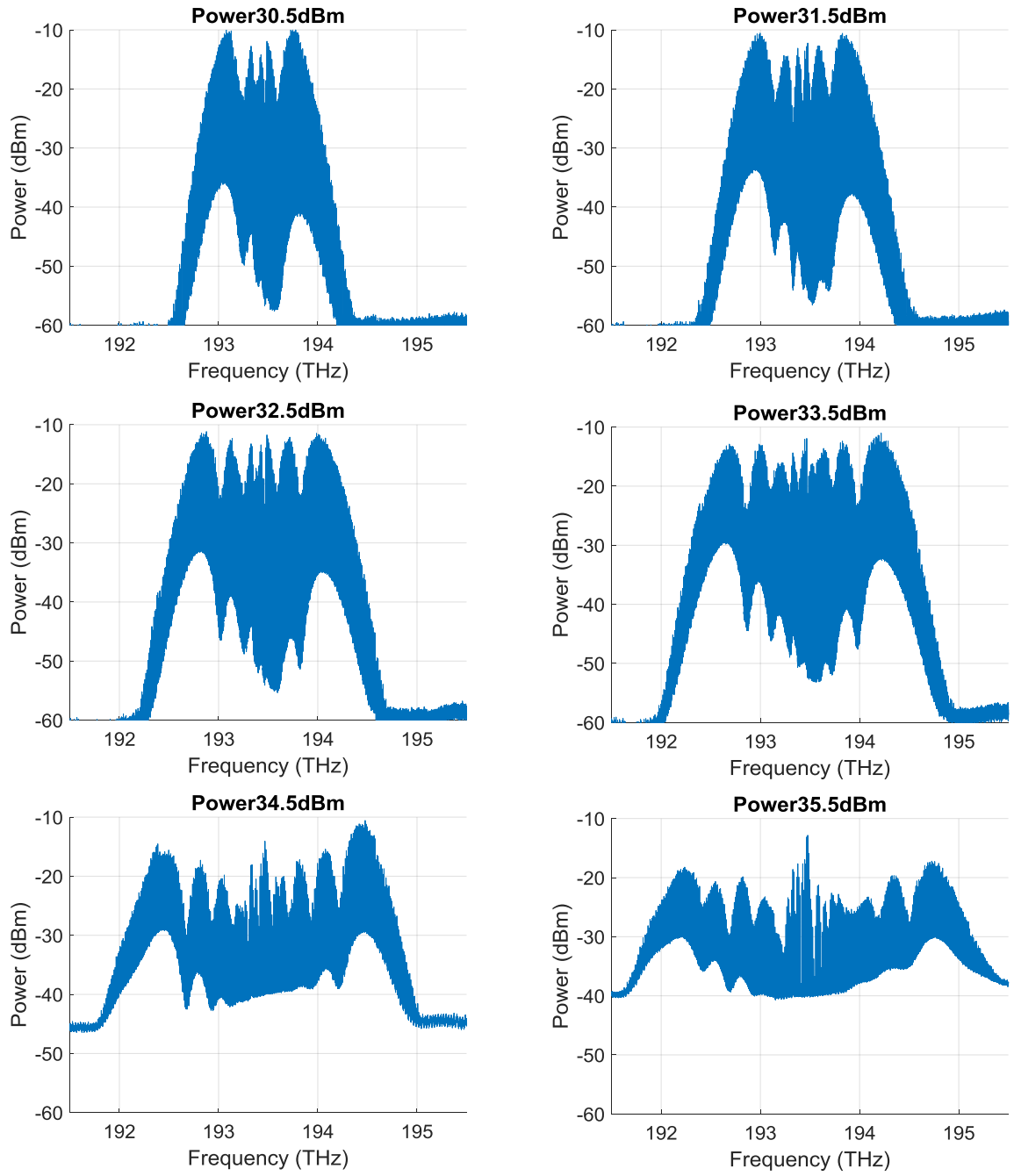


Figure 5.22: Regenerated comb lines (at the 1% output of the HNLF) for different input powers.

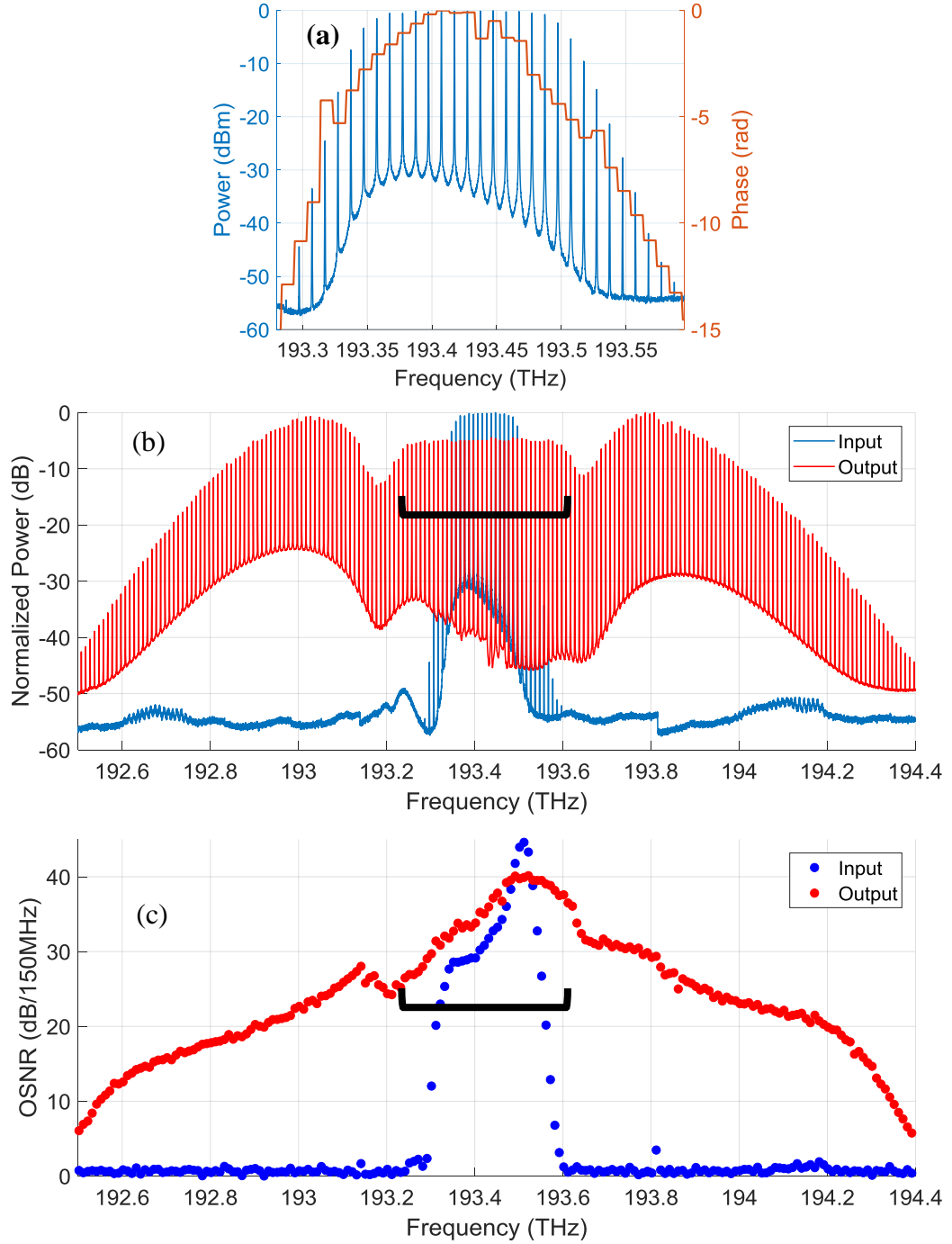


Figure 5.23: (a) phase profile applied to seed comb lines which was optimised to generate flat comb lines, (b) input and output spectrum of the comb generator, (c) the OSNR of input and output comb lines.

By optimising the individual phases of comb source lines (see figure 5.23(a)), we have achieved an expansion of the initial seed from 12 lines (with flatness of 1dB) to 38 lines (with flatness of 1dB), see figure 5.23 (b) [X13]. The optimisation was performed by changing the individual phase of each of the seed comb lines and observing the spectral properties of the generated comb at the output of the HNLF, aiming to generate the highest number of comb lines (at the output of the HNLF) with acceptable spectral flatness ( $<1\text{dB}$ ). It can be seen that

the side lobes of the regenerated comb cannot be eliminated since they are generated from higher order FWM at a phase mismatching state according to the local dispersion of the HNLF (due to the high dispersion slope of our fibre). The parametric ASE noise (modulation instability) floor variation between the side lobes can be explained by the fact that lower frequency side lobe is generated from the FWM at normal HNLF local dispersion ( $D_c > 0$ ), while the higher frequency side lobe is generated from the FWM at negative HNLF local dispersion ( $D_c < 0$ ) [41]. Figure 5.23 (c) shows that the OSNR of the generated comb lines is ranging between 25dB to 40.5dB, which indicates no significant OSNR degradation when compared to the seed comb lines.

## Summary and Conclusions:

We have shown our dual-band OPC design that uses counter dithered, perpendicularly polarised, dual-pump configuration. The counter dithering has allowed 8.7dB higher pumping power to be injected into the HNLF which leads to 17dB improvement of conversion efficiency (compared to non-dithered pump). The perpendicularly polarised pumps of the OPC eliminates the need for polarisation diversity loop to realise polarisation insensitive phase conjugation. From our measurements we have seen that the polarisation dependent loss of our OPC is ranging below 0.7dB. Both directions of propagation along the HNLF have been used to realise two independent OPCs (dual-band OPC). The OPC can produce unwanted nonlinear products that can degrade the OSNR of the conjugated signals, those unwanted products can be avoided by limiting the bandwidth signals to be conjugated. The OPC, with total insertion loss of 16dB and 20dB in both reported experiments, impose an OSNR penalty of 2dB to 3.5dB. We have reported two experiments to evaluate the OPC, 8x28Gbaud PM-QPSK (Nyquist roll-off of 0.2) and 30x30Gbaud PM-QPSK (Nyquist roll-off of 0.1); both experiments have shown consistent evaluation of the OPC showing degradation of 0.7dB in the  $Q^2$  imposed on the conjugated signals.

We have shown that the nonlinear response of single stage parametric generator can be optimised using an interferometric WSS that is capable of changing the individual phase of the seed comb. We have successfully expanded a seed comb (12 lines with flatness of 1dB) to 38 lines with in the same flatness restriction.



# Chapter 6 : Experimental Demonstration of Performance Enhancement in OPC-Assisted Transmission Systems

Contributions: [X2], [X3], and [X12].

As shown in chapter 4, OPC provides a promising solution to enhance the performance of optical transmission systems by compensating not only the even-ordered dispersion accumulation, but also the nonlinear noise accumulated along the system [16]. The nonlinear compensation efficiency that the OPC can achieve is highly dependent on the properties of the transmission system, such as: amplification technique, dispersion management map, fibre properties, span length, signal bandwidth, and the number of deployed OPCs.

In this chapter, I will report on experimental demonstrations of performance enhancement achieved by OPC assisted discretely amplified as well as distributed Raman transmission system. The results will show that nonlinearity compensation efficiency in OPC-assisted discretely amplified system is highly dependent on the bandwidth of the modulated signals, as predicted by the closed form equation 4.20. A 1.9dB improvement in optimum  $Q^2$  was achieved by the mid-link assisted discretely amplified system that delivers single channel per OPC band (2x28Gbaud PM-QPSK); this performance improvement is degraded to become 0.7dB for the same system that delivers four channels per OPC band (8x28Gbaud PM-QPSK). Also, this chapter will present the experimental demonstration of 72% reach (and performance) enhancement of 30x30Gbaud PM-QPSK (spectral efficiency 3.6bps/Hz) achieved by mid-link OPC assisted distributed Raman system. The 72% reach enhancement reported in this chapter is the highest experimental demonstration of reach enhancement achieved by mid-link OPC deployed in long haul optical transmission links (>1000km).



## 6.1 OPC-Assisted Discretely Amplified Transmission System

To verify the theory that predicts the nonlinear noise compensation efficiency achieved by OPC-assisted discretely amplified transmission system, we have implemented a recirculating loop to emulate discretely amplified transmission system with a span length of 100km, shown in figure 6.1[X2,X12]. The experimental setup uses the transmitter configuration discussed in figure 5.11 and the dual band OPC discussed in section 5.1. The modulated signals (output of the transmitter) passes through a 2x1 optical switch (SW1) into the recirculating loop; this switch fills the recirculating loop by modulated light and recirculate the light inside the loop to emulate a multi-span system. The number of emulated recirculations is defined by the duration that the light takes to travel through the wanted length (number of spans). A 3dB coupler was used to split the signal into two copies, one bypassing the OPC and one passing through the OPC to generate the conjugates of the two bands simultaneously. The OPC path contains two extra EDFAs that boost the signal power (entering the OPC) and balance conjugated signals power (exiting the OPC) to the signals power at the other switch port (of SW2), the total gain of these EDFAs matches the insertion loss of the OPC (16dB in this experiment). Polarisation controllers (PC) on each path were added and calibrated to minimise the effect of polarisation dependent loss of the optical switches. A second 2x1 optical switch (SW2) was used to switch between the signals (bypassing the OPC) and the conjugated signals (generated from the OPC), to emulate the deployment of mid-link OPC. At the output of SW2, an EDFA (with measured  $NF=6\text{dB}$ ) was used to boost the signal power to 20dBm after which the signal's power was controlled through digitally controlled Variable Optical Attenuator (VOA). After the VOA, signals were passed through 100km SSMF (Sterlite OH-LITE(E), ITU-T G.652.D [102]), then an EDFA with 14dBm output power was used to pre-compensate the insertion loss of the optical switches and the 3dB coupler (recirculating loop loss). At the mid-stage of the booster EDFA, we have used 3-dB splitter to pass the signal both to the loop and to coherent receiver path. A tunable Band Pass Filter (BPF) was used to filter the targeted channels to be detected by the dual polarisation coherent receiver (Tektronix OM4245, 100Gsamples/s). High precision Digital Delay Generators (DDG) were used to synchronise the optical switches (SW1 and SW2) to fill the loop, trap light in the loop, switch the conjugated light into the loop, and trigger the coherent receiver to capture the signal. A Gain Flattening Filter (GFF) was used to maintain the flatness of the signal propagating through the system.

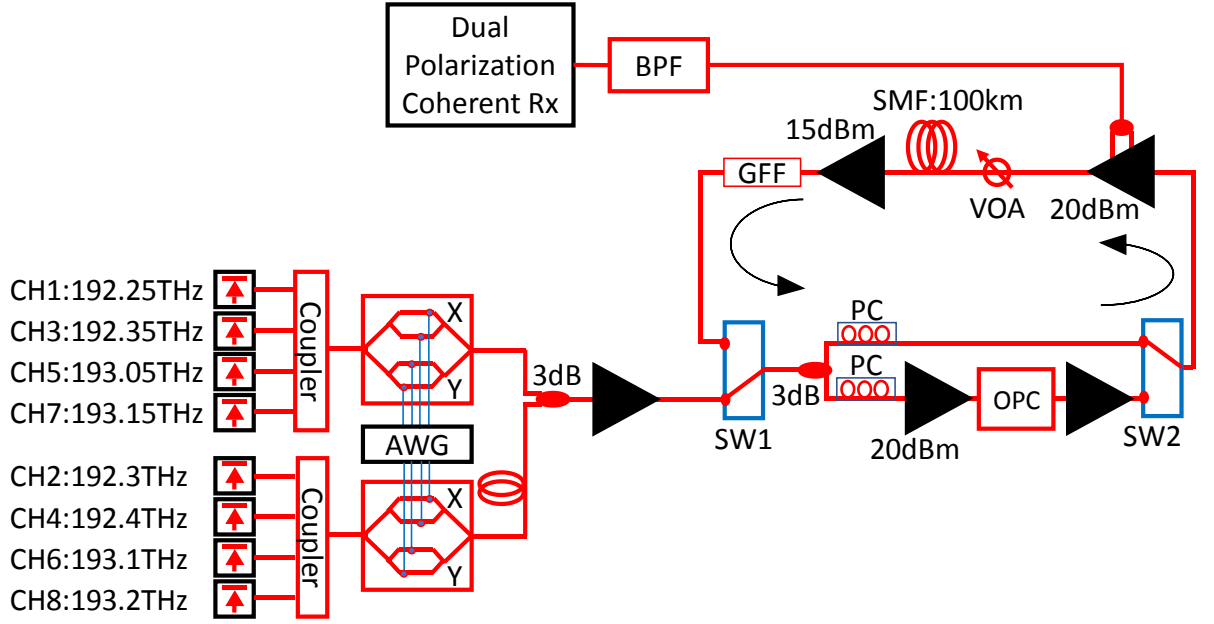


Figure 6.1: Experimental setup of OPC assisted discretely amplified transmission system.

The captured received signals were processed using the built-in DSP (of Tektronix OM4245); at which FIR filter was applied, constant modulus algorithm CMA (with 7 taps), dispersion compensation, and decoding was performed. The value of dispersion compensated in the DSP was dependent on the system length (number of spans) and whether a mid-link OPC was emulated in the link. In OPC-assisted system, the DSP compensates for the residual dispersion resulted from the dispersion slope and the wavelength shift resulted from the OPC. The receiver then calculates all the parameters that quantify the received signal quality, such as: BER (from the decoded bit sequence) and EVM (from the constellation). Each experimental result point, displayed in the following results, was calculated from the mean of  $Q^2 (=1/EVM^2)$  calculated from ten captures each containing 500000 samples.

Figure 6.2 shows  $Q^2$  for various number of channels per band measured at distance of 3000km (with and without OPC), as a function of signal power launched into the fibre (left column) and the constellation of the received signal at the optimum power for the system with and without OPC (right column) [X2,X12]. The experimental results display the performance of a channel from each signal band (Ch3 and Ch6) to show that the performance improvement is balanced across the two bands. The figure compares the experimental  $Q^2 (=1/EVM^2)$  with the theoretical SNR ( $=Q^2$ ) prediction calculated by: equation 4.13 (nonlinear noise generation efficiency without OPC), equation 4.20 (residual nonlinear noise ratio in OPC-assisted system), equation 4.35 (SNR). The parameters used in the theoretical evaluation were:  $NF=6\text{dB}$ ,  $\alpha=0.2\text{dB/km}$ ,  $D_c=17\text{ps/nm/km}$ ,  $\gamma_0=1.4\text{W/km}$ .

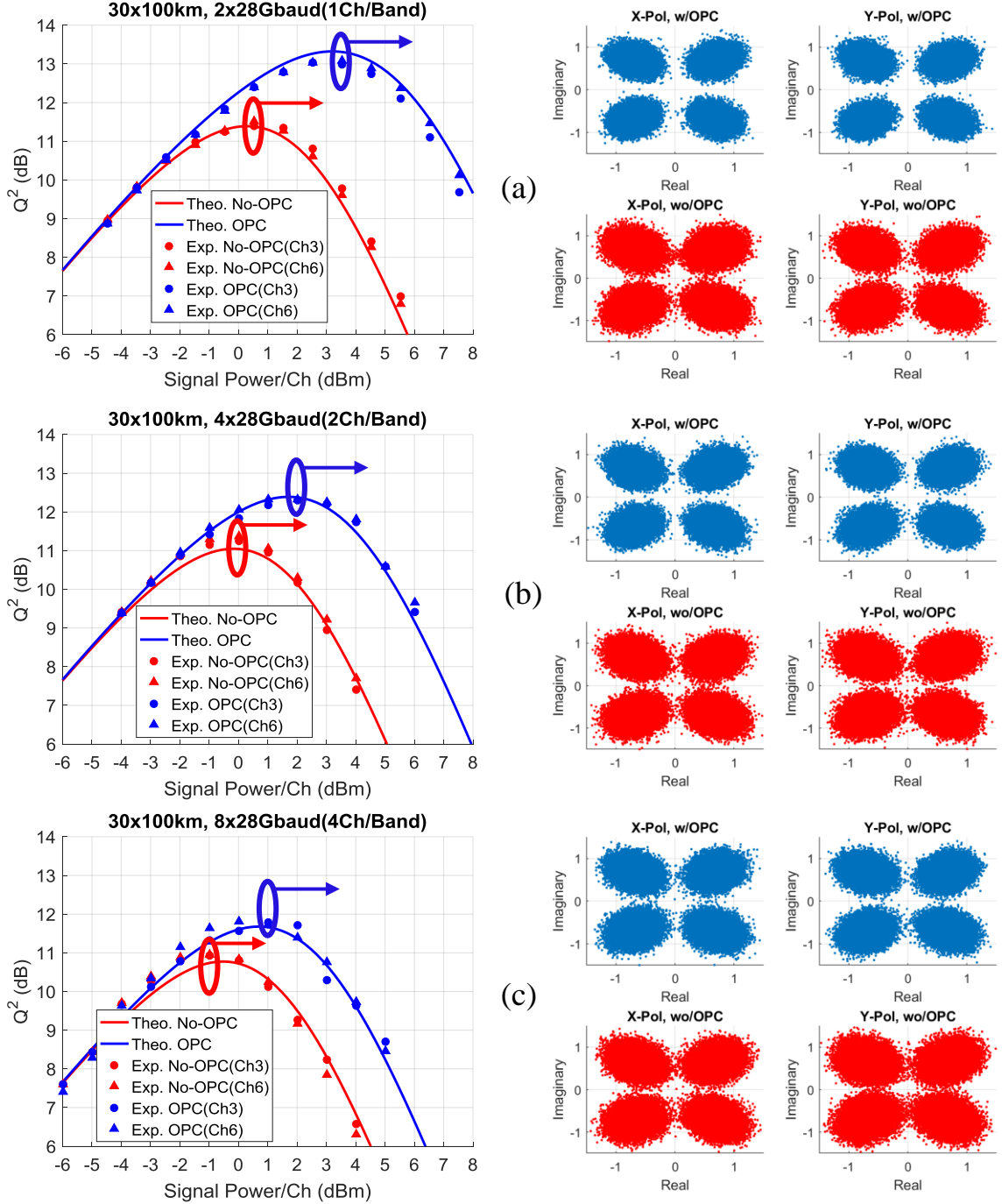


Figure 6.2:  $Q^2$  as a function of signal power (left column) and the received constellation at the optimum signal power (right column) measured at 3000km with and without OPC. The figure contains the results for 2 channels (a), 4 channels (b), and 8 channels (c).

When two signal channels (CH3 & CH6) are propagating through 3000km system, shown in figure 6.2(a), an EDC system (without OPC) reaches its maximum performance ( $11.4\text{dB}Q^2$ ) when the signal power is  $0.5\text{dBm}$  per channel, on the other hand, the system that deploys mid-link OPC reaches its maximum performance ( $13.2\text{dB}Q^2$ ) at  $3.5\text{dBm/channel}$ . The  $1.7\text{dB}$  improvement (on both channels) in optimum  $Q^2$  achieved by the mid-link OPC is a result of partial nonlinearity compensation of the intra-channel nonlinear interactions; which pushes the

nonlinear regime of EDC system to a higher signal power. When increasing the number of channels to four channels (CH3, CH4, CH5, and CH6; 2Channels/band), the improvement in  $Q^2$  achieved by the mid-link OPC is degraded from 1.8dB to 1dB, as shown in figure 6.2(b), which can be noticed from the received constellation at optimum signal power. Finally, an eight-channel system (CH1-8, 4 channels per band) further degrades the nonlinearity compensation efficiency leading the improvement in optimum  $Q^2$  achieved by mid-link OPC system to reach 0.7dB, as seen from figure 6.2(c). Figure 6.2 shows that increasing the number of channels propagating through the system not only degrades the optimum  $Q^2$  achieved by EDC system (11.4dB, 11.2dB, and 11dB for 1, 2, and 4 channels per band), but also degrades the nonlinearity compensation efficiency achieved by the OPC causing a degradation in the maximum  $Q^2$  improvement (1.8dB, 1dB, and 0.7dB for 1, 2, and 4 channels per band). The performance of both measured channels (from each band) propagating in both systems were close to each other and follow the theoretical predictions within a 0.4dB margin of error.

Figure 6.3 shows  $Q^2$  for various number of channels per band and measured at the optimum launched signal power (with and without OPC), as a function of distance (left column) and the constellation of the received signal at the distance marked by black circles (right column) [X2,X12]. The figure shows that the performance of OPC assisted systems are clearly superior to the EDC system at any given distance and any number of channels propagating through the system. The dual channel (single channel per band), shown in figure 6.3(a), propagating through mid-link OPC assisted system shows a performance enhancement of  $\sim 2\text{dB } Q^2$  at 4800km and reach enhancement of 43% (4800km to 7200km). As expected, the reach enhancement achieved by OPC assisted system degrades as the bandwidth of the modulated signals increases. The OPC assisted system that delivers 4 channels (2/band) and 8 channels (4/band) achieve reach enhancement ranging around 32% and 24%, respectively; see figure 6.3(b)&(c). The improvement in  $Q^2$  achieved by the OPC can be clearly seen in the constellations shown in the right column of figure 6.3. The experimental results show a good agreement with the theoretical predictions, within a margin of error of 0.4dB. The results displayed in figure 6.2 and figure 6.3 validate the closed form equation (equation 4.20) that represents the residual nonlinear noise ratio in mid-link OPC assisted discretely amplified systems with long span length.

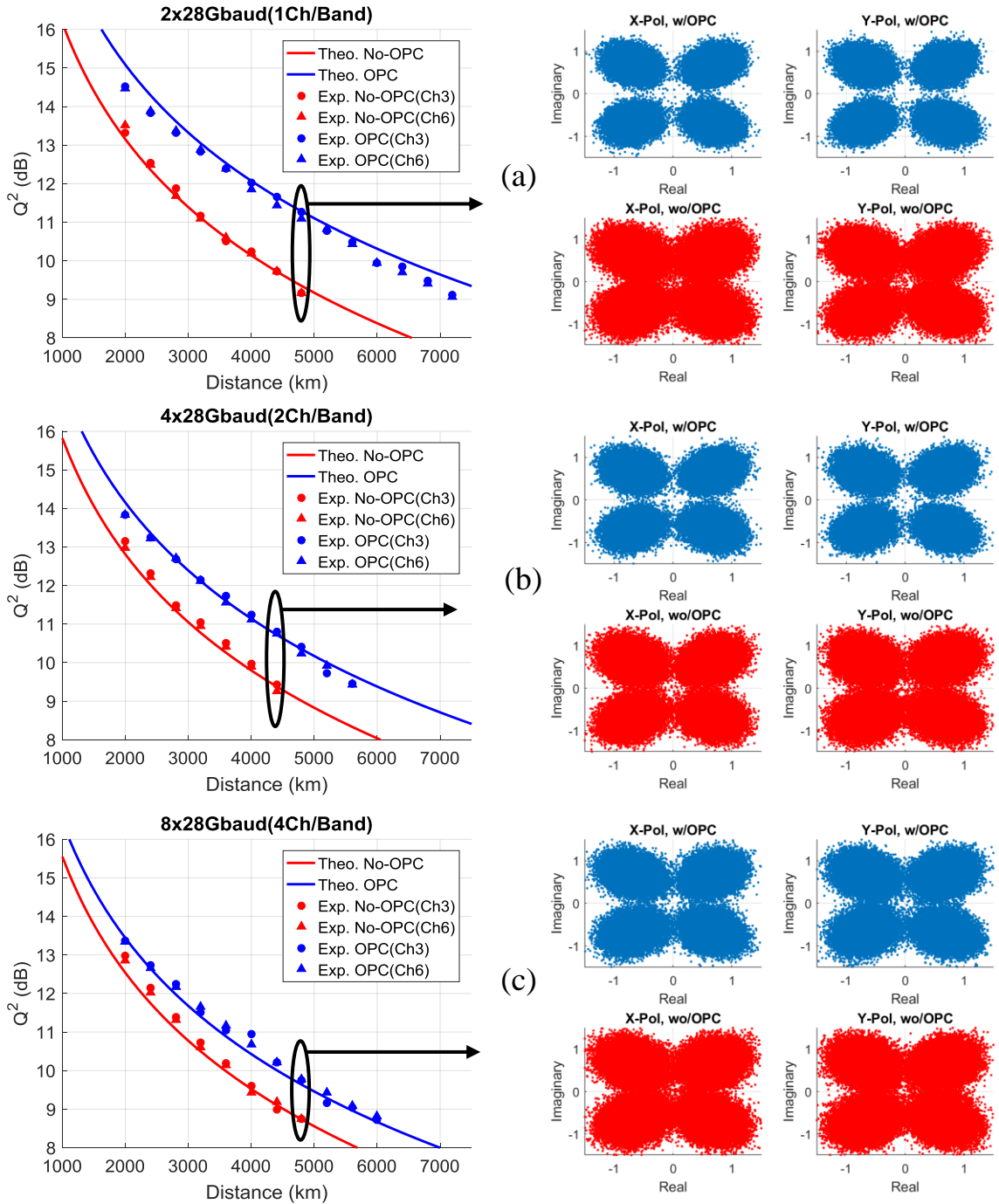


Figure 6.3: (left column)  $Q^2$  as a function of distance, (right column) received constellation at selected distance (the maximum of EDC system). The figure contains the results for 2 channels (a), 4 channels (b), and 8 channels (c).

Figure 6.4 shows the optical spectrum and the BER per channel measured at various distances (shown in the legends, with and without OPC) and various number of channels where the received BER is lower than  $2 \times 10^{-3}$  (compatible with FEC HD-RS(255,239)) [X2,X12]. The figure shows that the system that deploys mid-link OPC can reach higher distance compared to EDC system (achieving approximately the same BER). The level of reach enhancement achieved by mid-link OPC is highly dependent on the bandwidth (the number of channels) of

optical signals. As the number of channels changes: 2, 4, and 8 channels, the OPC enhance the maximum distance reach by 43%, 32%, and 24%, respectively, among all the channels propagation through the system (with a variance of 0.2dB in BER among channels). The experimental results displayed in figures 6.2 to 6.4 confirm the conclusions made in chapter 4, where we have explained that a mid-link OPC assisted discretely amplified transmission system (with large span length) achieves performance enhancement highly dependent on the bandwidth of the modulated signals.

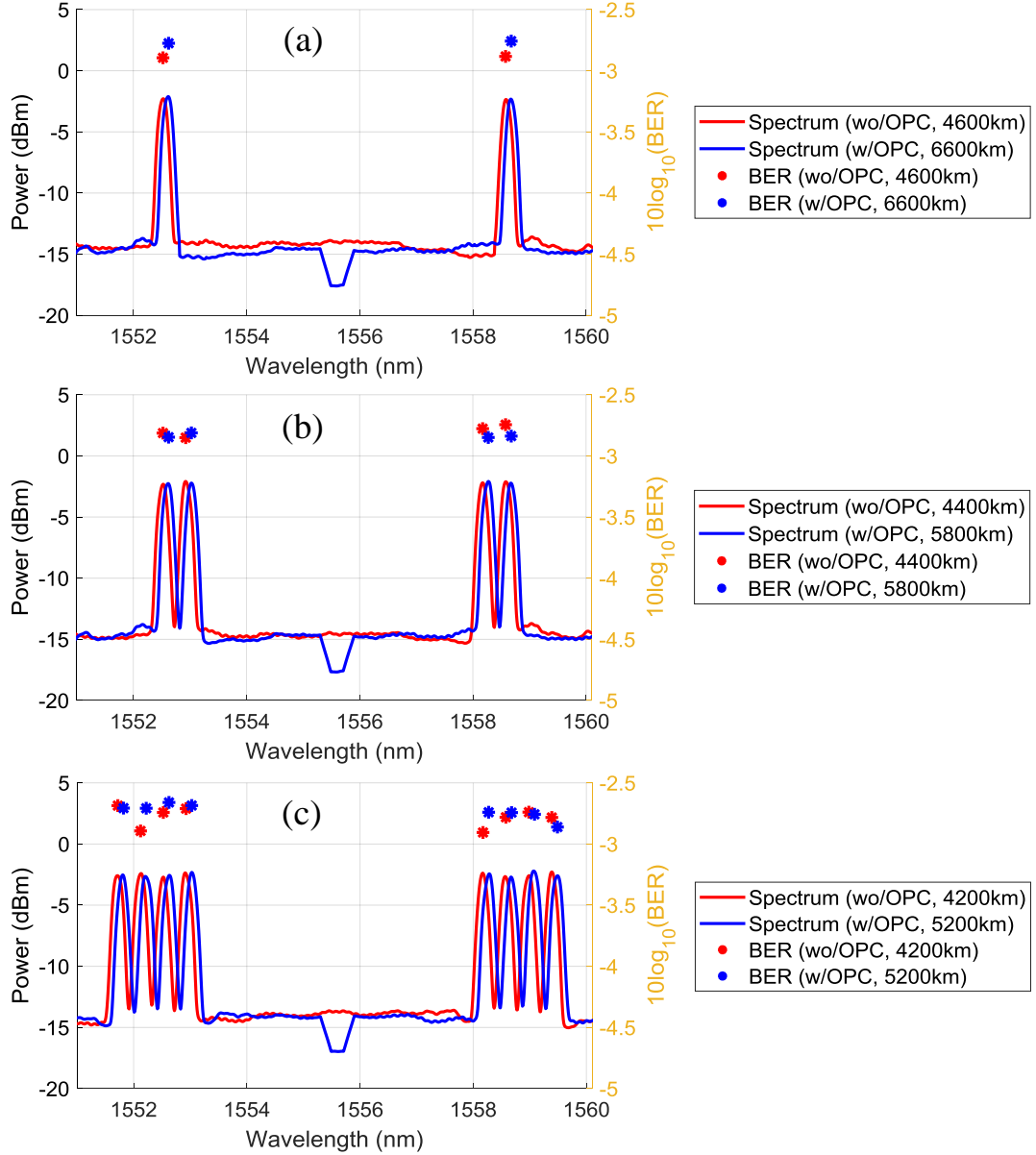


Figure 6.4: Optical spectrum and BER per channel at the maximum distance (at which  $\text{BER} > 2 \times 10^{-3}$ ), for 2-channel system (a), 4-channel system (b), and 8-channel system (c); with and without OPC.

Other experimental results reported in literature have shown the same trend [25–29] [X12]; which are summarised in table 6.1. Figure 6.5 summarises the improvement in  $Q^2$  (in dB, compared to EDC system) of those experiments [25–29] [X12] achieved by mid-link OPC

deployed in discretely amplified transmission systems. The general trend (even though the systems configurations were different) confirms that a higher bandwidth of modulated signal leads to degradation in the improvement in  $Q^2$  achieved by mid-link OPC.

Reference	Modulations	Grid (GHz)	Total Baud Rate (Gbaud)	Distance (km)	$\Delta Q^2$ (dB)
[25]	16-QAM	50	3x10(x2Bands)	2x100km+91.5km+DCM	~0.5
	64-QAM		3x10(x2Bands)	2x100km+91.5km+DCM	~1.7
[26]	QPSK	20	1x30	10x80km	0.2
	QPSK		10x30	10x80km	0
[27]	QPSK	100	8x28.5	62x83km	0
[28]	16-QAM	50	1x28	10x80km	1.3
	16-QAM		5x28	10x80km	0.9
[29]	16-QAM	50	1x28	10x80km	0.5
[X12], this work	QPSK	50	1x28(x2Bands)	48x100km	1.8
	QPSK		2x28(x2Bands)	44x100km	1
	QPSK		4x28(x2Bands)	42x100km	0.7

Table 6.1: Experimental demonstrations of OPC assisted discretely amplified transmission systems.

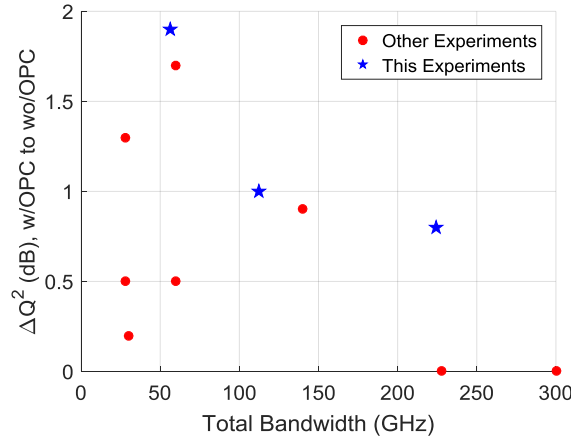


Figure 6.5: Comparison of improvement in  $Q^2$  of experimental coherent transmission systems, shown in table 6.1, that use mid-link OPC. [2]

## 6.2 OPC-Assisted Distributed Raman Transmission System

In this experiment, we have used the comb-based transmitter to generate 30x30Gbaud PM-QPSK (Nyquist roll off=0.1) channels, described in figure 5.15. Figure 6.6 shows the experimental setup used to emulate distributed Raman transmission system [X3]. This configuration uses two spans (each 50km) backwardly pumped by 1455nm 1<sup>st</sup> order Raman

pump (power profile shown in figure 3.20). An optical isolator was used at the input of each span to avoid any remains of Raman pump power from damaging the EDFAs. The power of signals injected into the two spans, inside the recirculating loop, was controlled by a single stage (constant gain) EDFAs. A 3dB splitter was used to take the signals from the loop to the coherent receiver (Tektronix OM4245, 100Gsamples/s) path. In this experiment, we have placed the GFF between the two distributed Raman spans to maintain the spectral flatness of the signals.

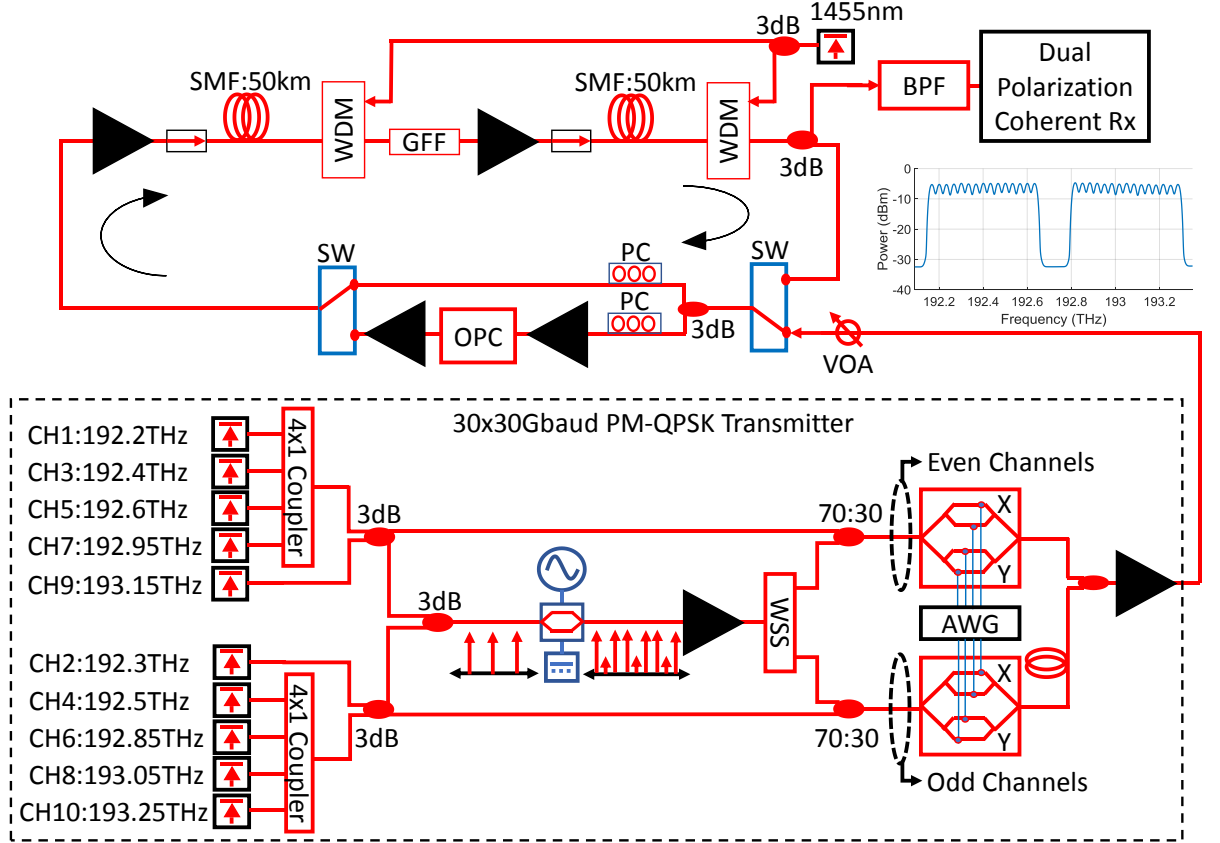


Figure 6.6: Experimental setup of OPC assisted distributed Raman amplified transmission system.

The power of the Raman pump was calibrated to achieve zero net signal gain at all measurements. The input power to the OPC was constant, 20dBm (controlled by the input EDFA), and the two EDFAs in the OPC path have compensated the insertion loss of the OPC which was 20dB. In this experiment we have used multiple OPCs to check whether we have achieved full compensation of deterministic signal-signal nonlinear interactions. The number of OPCs and their location along the emulated link was controlled by the DDG which changed the state of SW2 to pass the signal conjugates to the loop multiple times (each duration is an equivalent of single light recirculation). The OPCs were located symmetrically along the link with double segmented separation between any two consecutive OPCs.



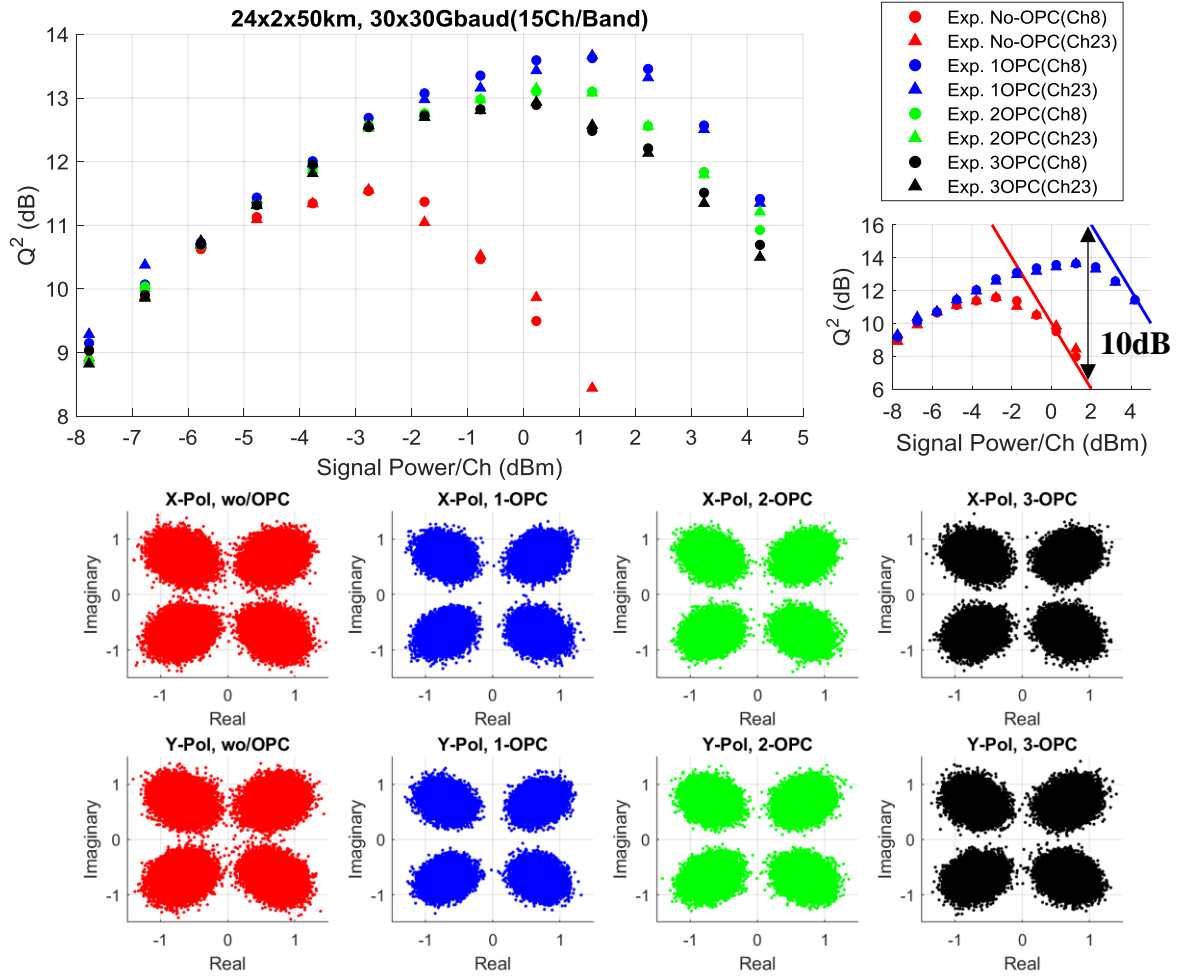


Figure 6.7:  $Q^2$  as a function of signal power and the received constellation at the optimum signal power measured at 2400km without OPC, 1-OPC, 2-OPC, and 3-OPC.

Figure 6.7 shows the experimental results of  $Q^2$  as a function of signal power launched into the distributed Raman amplified spans, the figure also shows the received signal's constellations at the optimum launched power for each system [X3]. The measurements displayed in figure 6.7 show the performance of the central channel of each band (channel 8 and channel 23) at distance of 2400km (24 recirculation, 48 spans) with various number of OPCs; No-OPC (EDC system), 1-OPC (two segments, each contains 24 spans), 2-OPCs (four segments, each contains 12 spans), and 3-OPCs (six segments, each contains 8 spans). The results shown in figure 6.7 show that the performance of EDC system reaches its maximum (11.6dB $Q^2$ ) at signal power ranging around -3dBm/Ch, while a system that deploys single mid-link OPC shows an improvement in the maximum  $Q^2$  factor by 2.1dB which is apparent in from the constellation of the received 30Gbaud PM-QPSK signal. The improvement in  $Q^2$ , and the nonlinear regime shift, of mid-link OPC link suggests that 90% (10dB) of the deterministic nonlinear signal-signal interactions were compensated by the OPC (as shown in the subfigure under the legend of figure 6.7); which result a system with higher tolerance of signal power by 4dB (compared

to EDC system). As the number of OPCs increase, 2 OPCs and 3 OPCs, the nonlinear limit of the power sweep is enhanced (appear at lower signal power) by 0.7dB and 1.1dB, respectively, when compared to the system that deploys only one OPC. As shown in the figure, the maximum performance ( $Q^2$ ) achieved by multi OPC system was degraded by 0.6dB and 0.8dB, respectively for 2-OPC and 3-OPC systems, when compared to the maximum performance achieved by single OPC system. This degradation in nonlinearity compensation (signal performance) as the number of OPC increase over single OPC suggests that the system is still limited by the deterministic nonlinear signal-signal interactions (the uncompensated 10% residual nonlinear noise in mid-link OPC system, as shown in figure 6.7).

As shown in chapter 6, an OPC assisted system that deploys 50km 1<sup>st</sup> order distributed Raman system cannot fully compensate for the signal-signal nonlinear interactions for a single channel, see figure 4.14(b). In a PMD-free system, simulated and numerically analysed systems in chapter 4, an OPC assisted system of 50km distributed Raman would have 0.3% residual nonlinear noise (of the nonlinear noise generated in EDC system) generated from the signal-signal nonlinear interactions. If we consider a nonzero-PMD system, the non-deterministic nonlinear signal-signal interactions dominate the nonlinear limit of the performance of OPC assisted system. According to [X9] (Fig.3), an optical fibre with PMD of 0.1ps/km<sup>2</sup> would result the performance enhancement achieved (in  $Q^2$ ) by mid-link OPC to be 5dB (compared to EDC system); where the system is limited by the non-deterministic signal-signal nonlinear interaction that is equivalent to 2.5% of the nonlinear noise generated in EDC system. In such ideal system (ideal lossless Raman and ideal OPC), the deployment of multiple OPCs would result an improvement in the performance compared to a system that depots only one OPC, as shown in [X9].

In our experimental setup that deploys an optical fibre with PMD=0.1ps/km<sup>1/2</sup> [102], a single mid-link OPC have compensated 90% of the nonlinear noise generated in EDC. The residual 10% of uncompensated nonlinear noise is four times higher than the residual nonlinear noise (2.5%) in an ideal PMD-limited system [X9]. This means that our experiment is operating in the deterministic nonlinear limit of signal-signal interactions, which causes the deployment of higher number of OPC to degrade the level of improvement achieve by only one OPC, which was explained in detail in the chapter 4. The uncompensated 10% of the deterministic nonlinear impairments in our experiment can be a result to many non-ideal reasons. For example, the polarisation dependent loss of the OPC and the optical switches (SW1&2) might cause the signal power on each polarisation to enter the fibre span with different powers each recirculation; this creates extra asymmetry of signal power profile along the emulated system

which degrades the nonlinearity compensation efficiency achieved by the OPC. Also, the dispersion slope of the optical fibre and the effect of the wavelength shift resulted from the OPC, which results different phase mismatching among the signals along different segments of the system.

Figure 6.8 shows the  $Q^2$  factor (for the central channel of each band, at optimum signal power) as function of distance for EDC system and a system that deploys a mid-link OPC [X3]. The figure shows a clear advantage of the OPC assisted system over the EDC system which appear in the form of enhancing the maximum distance reach by 72% of the distance achieved by EDC system. The constellations display shows the advantage in constellation quality (2.3dB $Q^2$ ) achieve by OPC at 4400km system.

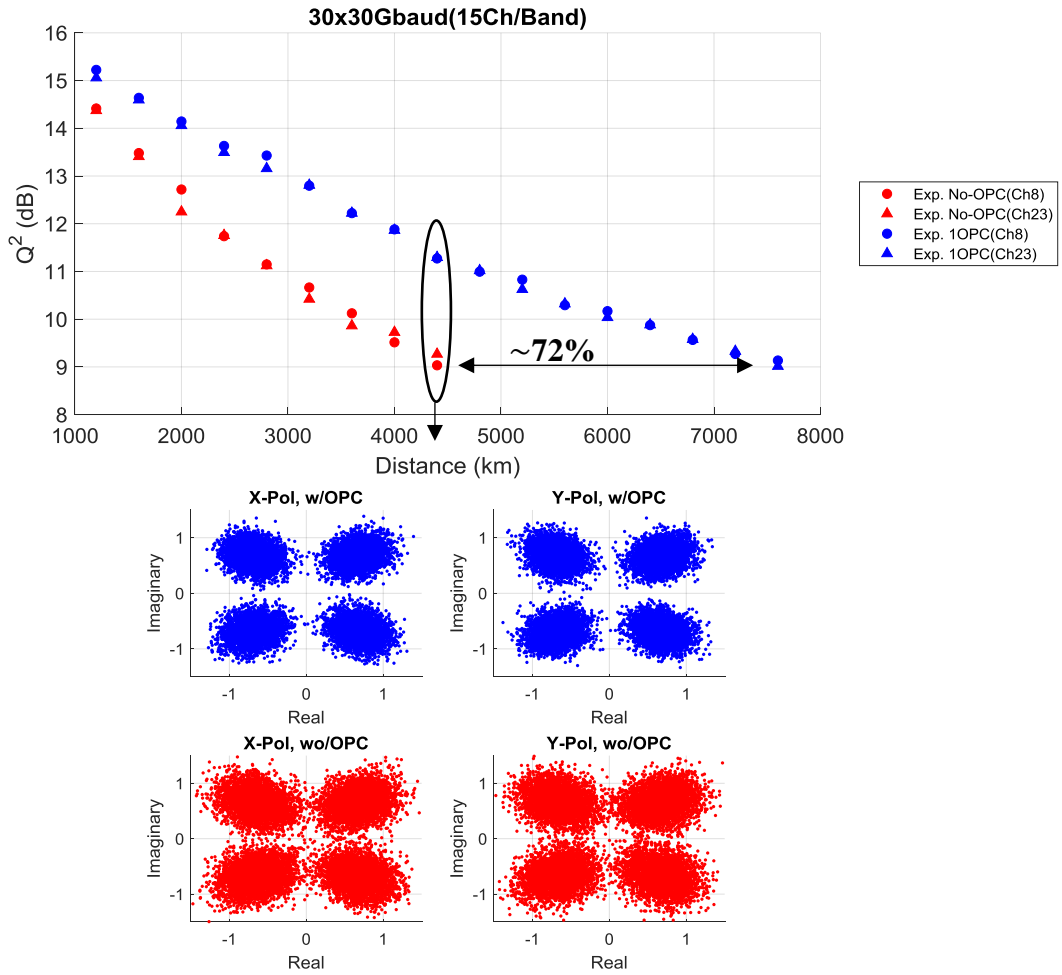


Figure 6.8:  $Q^2$  as a function of distance and received constellation at 4400km (the maximum of EDC system).

Figure 6.9 shows the optical spectrum and the BER achieved at the maximum distance (pre-FEC) to be compatible with HD-RS(255,239) [X3]. The results shown in figure 6.9 confirms the distance enhancement achieved by the OPC to expand the 4400km reach of EDC system to 7600km, at which the average BER of all the channels is approximately the same for both

system; this confirms a net distance enhancement of 72% due to the nonlinearity compensation achieved by a mid-link OPC. The figure shows that the reach enhancement is balanced across all the channels transmitted through the system (within a variance of 0.3dB).



Figure 6.9: Optical spectrum (resolution 0.1nm) and BER per channel of the received signals at the maximum distance of EDC system and mid-link OPC assisted system. [X3]

Table 6.2 summarises the key OPC assisted distributed Raman coherent systems reported in literature [27,30–35] [X8]. The most impressive performance enhancement (above 3dB) reported in literature was reported in [34] where the transmission system have used dispersion flattened NZDSF 12km span length (with counter propagating Raman pumps); this system is the closest to ideal lossless Raman system deploying OPC/span which have achieved  $5\text{dBQ}^2$ . Other systems lack the sufficient signal power symmetry due to the span length or the insertion loss of the WDM (the inject Raman pump) deployed between consecutive spans inside the recirculating loop.

Reference	Modulations	Grid (GHz)	Total Baud Rate (Gbaud)	Distance (km)	$\Delta Q^2$ (dB)
[30]	QPSK	50	8x32	36x100	~0.3
	16-QAM		1x32	9x100	~1.1
	16-QAM		8x32	9x100	~0.2
[31]	16-QAM	25	46x22.5(x2Bands)	48x80	~0.4
[32]	QPSK	25	24x12	12x12	~0.8
[33]	DQPSK	50	22x20	75x94.5(+DCF)	1.5
[27]	QPSK	100	8x28.5	96x83	1.2

[34]	16-QAM	25	4x12	2x12	5
[35]	16-QAM	25	1x12	2x12	2.5
	64-QAM		1x12	2x12	4
[X8]	16-QAM	100	1x60(x2Bands)	30x75	2
	16-QAM		2x60(x2Bands)	27x75	1.9
	16-QAM		3x60(x2Bands)	27x75	1.3
	16-QAM		4x60(x2Bands)	24x75	1
	16-QAM		5x60(x2Bands)	21x75	0.6
[X3], this work	QPSK	33	15x30(x2Bands)	88x50	2.3
* various FEC thresholds (at the maximum distance) have been reported in each experiment.					

Table 6.2: Experimental demonstrations of OPC assisted distributed Raman amplified transmission systems.

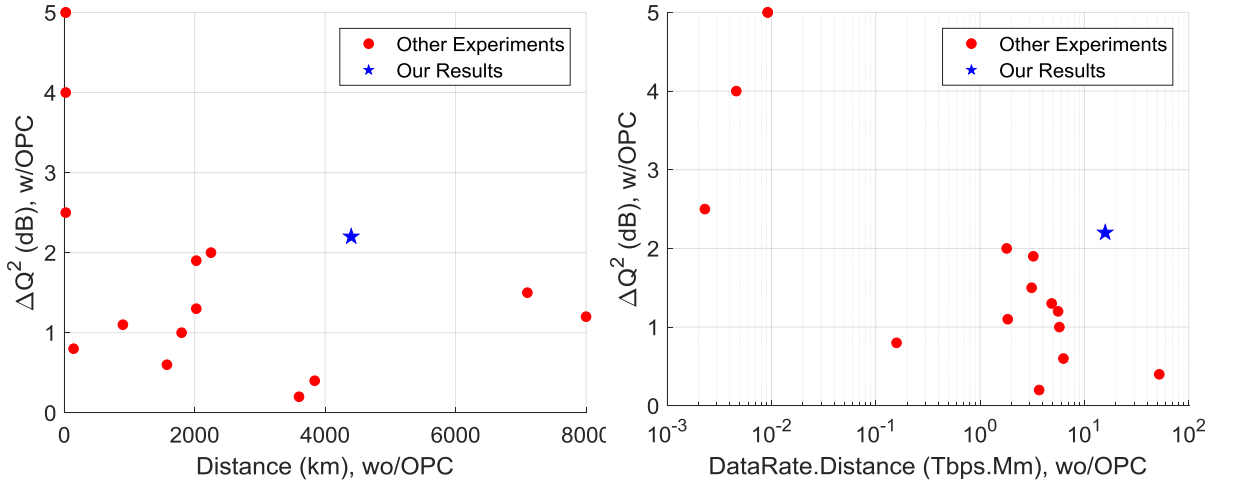


Figure 6.10: Comparison of improvement in  $Q^2$  of experimental coherent transmission systems, shown in table 6.2, that use optical phase conjugation. [X3]

Figure 6.10 visualises performance improvement (in  $Q^2$ ), achieved by experimental demonstrations reported in literature, as a function of maximum EDC distance (a) and as a function of the bitrate-distance product (b). Figure 6.10(a) shows that our experimental demonstration achieves the highest performance improvement ( $2.3\text{dB}Q^2$ ) over long-haul transmission system ( $>1000\text{km}$ ). Figure 6.10(b) shows that the results reported in [31] achieves higher data rate-distance product than our system, except that the maximum distance in [31] was measured at 20% FEC threshold ( $Q^2=5\text{dB}$ ) and the performance improvement achieved by the OPC is only  $0.5\text{dB}Q^2$  which is substantially lower than the performance achieved in our experiment ( $2.3\text{dB}Q^2$ ).

## Summary and Conclusion:

In this chapter, we have experimentally demonstrated the various advantages of the nonlinearity compensation using OPC deployed in discretely amplified and distributed Raman amplified system. We have validated the theoretical equation that represents the residual nonlinear noise ratio (compared to EDC system) achieved by OPC when deployed in discretely amplified system. We have shown that the nonlinearity compensation efficiency achieved by the OPC is highly dependent on the number of channels propagating through the system. The results have shown that the OPC enhances the distance reach of discretely amplified transmission system by 43%, 32%, and 24% for 2x112Gbps, 4x112Gbps, and 8x112Gbps signals.

In this chapter we have experimentally demonstrated that an OPC deployed in distributed Raman amplified transmission system can achieve significant nonlinearity compensation among large number of WDM signals (30x30Gbaud PM-QPSK signals, Spectral Efficiency=3.6bps/Hz). The distributed Raman amplification in the system has achieved 90% nonlinearity compensation of the deterministic signal-signal nonlinear interactions. We have shown that the implemented system is still limited by the uncompensated (10%) deterministic nonlinear signal-signal interactions; this conclusion was made based on the fact that the deployment of multiple OPCs, 2-OPCs and 3-OPCs, has reduced the level of performance enhancement (by 0.7dB and 1.1dB, respectively) when compared to the performance enhancement achieved by a single OPC. In general, we have demonstrated the highest reported reach enhancement of 72% (compared to EDC system) among long-haul experimental demonstrations reported in literature.



# Chapter 7 : Conclusions

In this thesis, we have investigated the nonlinear limits of long-haul coherent optical fibre transmission systems that deploy discrete or distributed amplification.

I have presented, for the first time, a theoretical description of nonlinear Kerr response of OPC assisted discretely amplified and OPC assisted distributed Raman amplified systems. The closed form equation (equations 3.22 and 3.23) can represent the nonlinear Kerr effects accumulated in dispersion managed and unmanaged discretely amplified optical transmission system that deploys arbitrary number of symmetrically deployed OPCs; this equation was validated using simulation and experimental results. The results have shown that deploying mid-link OPC in discretely amplified system can compensate for the nonlinear Kerr products generated among the strongly phase matched signals leaving the system limited by the nonlinear products generated among weakly phase matched signals. We have shown that the compensation efficiency achieved by the OPC can be enhanced by shortening the span length of the system. Also, we have presented the theoretical description of the nonlinear Kerr product accumulation in dispersion uncompensated distributed Raman systems with arbitrary power profile. The theoretical analysis, backed by simulation and experimental results, shows the superiority of nonlinearity compensation capabilities of mid-link OPC when deployed in distributed Raman system when compared to discretely amplified system. The theoretical basis that we have presented also have shown that the deployment of multiple OPCs might not always be the best choice as it enhances the nonlinear Kerr response of optical transmission systems (discrete or distributed).

I have used the theoretical equations that represent Kerr product accumulation (in chapter 3) to identify the nonlinear noise generation efficiency (in chapter 4) accumulated among optical modulated signals propagating along discretely amplified or distributed Raman amplified system that deploys arbitrary number of OPCs. The theoretical calculations of the nonlinear noise generation efficiency have helped us to predict the maximum performance can be achieved by various simulated optical transmission systems and the capabilities of performance enhancement can be achieved when deploying arbitrary number of OPCs. We have introduced



for the first-time closed form equations that represent the residual nonlinear noise ratio (relative to EDC system) achieved by mid-link OPC assisted discretely amplified system that deploy long span length ( $>70\text{km}$ ). Also, we have introduced an accurate closed form equation that represents the ultimate signal-noise interaction nonlinear limit of ideal, PMD free, optical transmission system that deploy ideal nonlinearity compensation techniques (full field DBP or OPC assisted quasi-lossless distributed Raman amplified systems). These closed form equations were validated by simulation results of modulated optical signals (PM-QPSK) propagating through various optical transmission systems to show their accuracy of prediction. We have established that the performance enhancement achieved by mid-link OPC assisted discretely amplified system (span length  $>70\text{km}$ ) is highly dependent on the bandwidth of the modulated signals propagating through the system. We have shown that introducing multiple OPCs in optical transmission systems limited by deterministic nonlinear signal-signal interactions will diminish the performance enhancement achieved by a single, mid-link, OPC. The numerical analysis and simulation results have shown that shortening the span length improves the nonlinearity compensation efficiency achieved by OPC assisted systems, the nonlinearity compensation efficiency achieved by distributed Raman amplified system is always superior to the discretely amplified system that deploy same span length. We have shown that increasing the number of OPCs linearises the accumulation of nonlinear signal-noise interactions, which leads to further performance enhancement when compared to mid-link OPC assisted system that is limited by the nonlinear signal-noise interactions.

We have experimentally implemented dual-band OPC design that uses counter dithered, perpendicularly polarised, dual-pump configuration. Both directions of propagation along the HNLF have been used to realise two independent OPCs (dual-band OPC). We have reported two experiments to evaluate the dual band OPC,  $8 \times 28\text{Gbaud}$  PM-QPSK (Nyquist roll-off of 0.2) and  $30 \times 30\text{Gbaud}$  PM-QPSK (Nyquist roll-off of 0.1); both experiments have shown consistent evaluation of the OPC showing and OSNR degradation of 2 to 3.5dB corresponding to  $0.7\text{dBQ}^2$  imposed on the conjugated signals. Also, we have experimentally demonstrated that the nonlinear response of single stage parametric generator can be optimised using an interferometric WSS by pre-compensating the phase mismatching accumulated along the optical fibre mixer (HNLF). We have successfully expanded a seed comb (12 lines with flatness of 1dB) to 38 lines within 1dB flatness.

Finally, we have experimentally demonstrated the various advantages of the nonlinearity compensation using OPC deployed in discretely amplified and distributed Raman amplified

system. The experimental results have shown that the OPC enhances the distance reach of discretely amplified transmission system by 43%, 32%, and 24% for 2x112Gbps, 4x112Gbps, and 8x112Gbps PM-QPSK signals. The degradation in reach enhancement, as the number of channels propagating through the system increased, has been explained by closed form equation that represents the residual nonlinear noise in OPC assisted discretely amplified system (presented in chapter 4). Also, we have reported the highest reported experimental reach enhancement of 72% (achieved by mid-link OPC when compared to EDC system) of distributed Raman amplified optical link.

## **Future Work**

In this thesis, we have studied the nonlinear limits of OPC assisted, PMD free, transmission systems. Further theoretical investigations on the nonlinear limits of OPC assisted transmission systems (discretely amplified and distributed Raman amplified) that deploy non-zero PMD transmission fibres.

A theoretical and experimental investigations on the benefits of using higher order distributed Raman amplification must be conducted. As the higher order Raman pumping provides more degrees of freedom to tailor the power profile of signals propagating along the system, higher symmetry can be achieved which will enable the OPC to achieve higher nonlinearity compensation (when compared to 1<sup>st</sup> order distributed Raman amplified systems at a given Raman pump spacing).

The experimental implications of dispersion slope and frequency shift (imposed by the OPC) on the nonlinearity compensation efficiency achieved by the OPC must be studied. This investigation must conclude the penalty on nonlinearity compensation efficiency as a function of the: dispersion slope of the fibre, length of the system, and frequency shift (generated in the OPC). Also, the effect of the local nonlinearities generated in the OPC on the total performance enhancement achieved by the OPC must be studied, which will suggest an optimisation of the number of the OPCs deployed along the system.



## References:

1. R. J. Essiambre and R. W. Tkach, "Capacity trends and limits of optical communication networks," *Proc. IEEE* **100**, 1035–1055 (2012).
2. A. D. Ellis, N. Mac Suibhne, D. Saad, and D. N. Payne, "Communication networks beyond the capacity crunch," *Philos. Trans. R. Soc. London A Math. Phys. Eng. Sci.* **374**, (2016).
3. A. Chraplyvy, "Plenary paper: The coming capacity crunch," in *2009 35th European Conference on Optical Communication* (2009), p. 1.
4. O. E. DeLange, "Optical heterodyne detection," *IEEE Spectr.* **5**, 77–85 (1968).
5. B. Glance, "Polarization independent coherent optical receiver," *J. Light. Technol.* **5**, 274–276 (1987).
6. D. Qian, M.-F. Huang, E. Ip, Y.-K. Huang, Y. Shao, J. Hu, and T. Wang, "101.7-Tb/s (370x294-Gb/s) PDM-128QAM-OFDM transmission over 3x55-km SSMF using pilot-based phase noise mitigation," in *2011 Optical Fiber Communication Conference and Exposition and the National Fiber Optic Engineers Conference* (2011), pp. 1–3.
7. D. N. Payne and L. Reekie, "Rare-earth-doped fibre lasers and amplifiers," in *Fourteenth European Conference on Optical Communication, ECOC 88 (Conf. Publ. No.292), Brighton* (1988), pp. 49–53.
8. R. H. Stolen, W. J. Tomlinson, H. A. Haus, and J. P. Gordon, "Raman response function of silica-core fibers," *J. Opt. Soc. Am. B* **6**, 1159 (1989).
9. R. Stolen and J. Bjorkholm, "Parametric amplification and frequency conversion in optical fibers," *IEEE J. Quantum Electron.* **18**, 1062–1072 (1982).
10. M. E. Marhic, *Fiber Optical Parametric Amplifiers, Oscillators and Related Devices* (Cambridge University Press, 2008).
11. G. Zeidler and D. Schicketanz, "Use of laser amplifiers in a glass-fibre communications system," *Radio Electron. Eng.* **43**, 675 (1973).
12. S. Beppu and M. Yoshida, "2048 QAM (66 Gbit/s) Single-Carrier Coherent Optical Transmission over 150 km with a Potential SE of 15.3 bit/s/Hz," *Opt. Express* **23**, 6–8 (2015).
13. S. J. Savory, "Digital filters for coherent optical receivers," *Opt. Express* **16**, 804 (2008).
14. K. Roberts, L. Strawczynski, M. O'Sullivan, and I. Hardcastle, "Electronic precompensation of optical nonlinearity," *IEEE Photonics Technol. Lett.* **18**, 403–405 (2006).
15. X. Li, X. Chen, G. Goldfarb, E. Mateo, I. Kim, F. Yaman, and G. Li, "Electronic post-compensation of WDM transmission impairments using coherent detection and digital signal processing," *Opt. Express* **16**, 880 (2008).
16. A. Yariv, D. Fekete, and D. M. Pepper, "Compensation for channel dispersion by

- nonlinear optical phase conjugation," *Opt. Lett.* **4**, 52 (1979).
17. S. Kumar and D. Yang, "Optical backpropagation for fiber-optic communications using highly nonlinear fibers.," *Opt. Lett.* **36**, 1038–40 (2011).
  18. X. Liu, a. R. Chraplyvy, P. J. Winzer, R. W. Tkach, and S. Chandrasekhar, "Phase-conjugated twin waves for communication beyond the Kerr nonlinearity limit," *Nat. Photonics* **7**, 560–568 (2013).
  19. S. T. Le, M. E. McCarthy, N. Mac Suibhne, a. D. Ellis, and S. K. Turitsyn, "Phase-conjugated pilots for fibre nonlinearity compensation in CO-OFDM transmission," in *2014 The European Conference on Optical Communication (ECOC)* (Ieee, 2014), pp. 1–3.
  20. A. D. Ellis, J. Z. J. Zhao, and D. Cotter, "Approaching the Non-Linear Shannon Limit," *J. Light. Technol.* **28**, 423–433 (2010).
  21. R.-J. Essiambre, "Overview of the Nonlinear Shannon Limit for Optical Fibers," in *Latin America Optics and Photonics Conference* (OSA, 2012), p. LM1C.1.
  22. C. E. Shannon, "A mathematical theory of communication," *Bell Syst. Tech. J.* **27**, 379–423 (1948).
  23. E. Desurvire, *Erbium-Doped Fiber Amplifiers : Principles and Applications* (Wiley, 1994).
  24. C. Headley and G. P. Agrawal, *Raman Amplification in Fiber Optical Communication Systems* (Elsevier, 2005).
  25. S. Yoshima, Y. Sun, Z. Liu, K. R. H. Bottrill, F. Parmigiani, D. J. Richardson, and P. Petropoulos, "Mitigation of Nonlinear Effects on WDM QAM Signals Enabled by Optical Phase Conjugation with Efficient Bandwidth Utilization," *J. Light. Technol.* **35**, (2017).
  26. M. Morshed, L. B. Du, B. Foo, M. D. Pelusi, B. Corcoran, and A. J. Lowery, "Experimental demonstrations of dual polarization CO-OFDM using mid-span spectral inversion for nonlinearity compensation," *Opt. Express* **22**, 10455–10466 (2014).
  27. I. Phillips, M. Tan, M. F. Stephens, M. McCarthy, E. Giacomidis, S. Sygletos, P. Rosa, S. Fabbri, S. T. Le, T. Kanesan, S. K. Turitsyn, N. J. Doran, P. Harper, and A. D. Ellis, "Exceeding the Nonlinear-Shannon Limit using Raman Laser Based Amplification and Optical Phase Conjugation," in *Optical Fiber Communication Conference* (2014), p. M3C.1.
  28. I. Sackey, F. Da Ros, J. Karl Fischer, T. Richter, M. Jazayerifar, C. Peucheret, K. Petermann, and C. Schubert, "Kerr Nonlinearity Mitigation: Mid-Link Spectral Inversion Versus Digital Backpropagation in 5×28-GBd PDM 16-QAM Signal Transmission," *J. Light. Technol.* **33**, 1821–1827 (2015).
  29. I. Sackey, R. Elschner, C. Schmidt-Langhorst, T. Kato, T. Tanimura, S. Watanabe, T. Hoshida, C. Schubert, and C. Schubert, "Novel Wavelength-Shift-Free Optical Phase Conjugator Used For Fiber Nonlinearity Mitigation in 200-Gb/s PDM-16QAM Transmission," in *Optical Fiber Communication Conference* (OSA, 2017), p. Th3J.1.
  30. H. Hu, R. M. Jopson, A. H. Gnauck, S. Randel, and S. Chandrasekhar, "Fiber nonlinearity mitigation of WDM-PDM QPSK/16-QAM signals using fiber-optic

- parametric amplifiers based multiple optical phase conjugations," *Opt. Express* **25**, 1618 (2017).
31. T. Umeki, T. Kazama, A. Sano, K. Shibahara, K. Suzuki, M. Abe, H. Takenouchi, and Y. Miyamoto, "Simultaneous nonlinearity mitigation in  $92 \times 180$ -Gbit/s PDM-16QAM transmission over 3840 km using PPLN-based guard-band-less optical phase conjugation.," *Opt. Express* **24**, 16945–51 (2016).
  32. K. Solis-Trapala, M. Pelusi, H. N. Tan, T. Inoue, and S. Namiki, "Optimized WDM Transmission Impairment Mitigation by Multiple Phase Conjugations," *J. Light. Technol.* **34**, 431–440 (2016).
  33. S. L. Jansen, D. Van Den Borne, P. M. Krummrich, S. Spalter, G.-D. Khoe, and H. De Waardt, "Long-haul DWDM transmission systems employing optical phase conjugation," *IEEE J. Sel. Top. Quantum Electron.* **12**, 505–520 (2006).
  34. K. Solis-Trapala, T. Inoue, and S. Namiki, "Signal power asymmetry tolerance of an optical phase conjugation-based nonlinear compensation system," in *2014 The European Conference on Optical Communication (ECOC)* (2014), p. 1–3 (We.2.5.4).
  35. S. Namiki, H. N. Tan, K. Solis-trapala, and T. Inoue, "Signal-transparent wavelength conversion and light-speed back propagation through fiber," in *Optical Fiber Communication Conference 2016* (2016), pp. 9–11.
  36. M. Tan, P. Rosa, M. A. Iqbal, I. Phillips, J. Nuño, J. D. Ania-Castanon, and paul harper, "RIN Mitigation in Second-Order Pumped Raman Fibre Laser Based Amplification," in *Asia Communications and Photonics Conference 2015* (OSA, 2015), p. AM2E.6.
  37. D. J. Richardson, J. M. Fini, and L. E. Nelson, "Space-division multiplexing in optical fibres," *Nat. Photonics* **7**, 354–362 (2013).
  38. G. P. Agrawal, *Nonlinear Fiber Optics* (Elsevier / Academic Press, 2007).
  39. Y. Tamura, H. Sakuma, K. Morita, M. Suzuki, Y. Yamamoto, K. Shimada, Y. Honma, K. Sohma, T. Fujii, and T. Hasegawa, "Lowest-Ever 0.1419-dB/km Loss Optical Fiber," in *Optical Fiber Communication Conference Postdeadline Papers* (OSA, 2017), p. Th5D.1.
  40. M. E. Marhic †, P. a. Andrekson, P. Petropoulos, S. Radic, C. Peucheret, and M. Jazayerifar, "Fiber optical parametric amplifiers in optical communication systems," *Laser Photon. Rev.* **9**, 50–74 (2015).
  41. E. Myslivets, B. P. P. Kuo, N. Alic, and S. Radic, "Generation of wideband frequency combs by continuous-wave seeding of multistage mixers with synthesized dispersion," *Opt. Express* **20**, 3331 (2012).
  42. D. N. O. Fiber and J. Tang, "The Multispan Effects of Kerr Nonlinearity and Amplifier Noises on Shannon Channel Capacity of a dispersion-free nonlinear optical fiber," *J. Light. Technol.* **19**, 1110–1115 (2001).
  43. Y. Stern, K. Zhong, T. Schneider, R. Zhang, Y. Ben-Ezra, M. Tur, and A. Zadok, "Tunable sharp and highly selective microwave-photonic band-pass filters based on stimulated Brillouin scattering," *Photonics Res.* **2**, B18 (2014).
  44. K. O. Hill, D. C. Johnson, B. S. Kawasaki, and R. I. MacDonald, "Cw Three-Wave

- Mixing in Single-Mode Optical Fibers," J. Appl. Phys. **49**, 5098 (1978).
45. N. Shibata, R. Braun, and R. Waarts, "Phase-mismatch dependence of efficiency of wave generation through four-wave mixing in a single-mode optical fiber," IEEE J. Quantum Electron. **23**, 1205–1210 (1987).
  46. X. Chen and W. Shieh, "Closed-form expressions for nonlinear transmission performance of densely spaced coherent optical OFDM systems.," Opt. Express **18**, 19039–54 (2010).
  47. W. Shieh and X. Chen, "Information Spectral Efficiency and Launch Power Density Limits Due to Fiber Nonlinearity for Coherent Optical OFDM Systems," Photonics Journal, IEEE **3**, 158–173 (2011).
  48. P. Poggiolini, G. Bosco, A. Carena, V. Curri, Y. Jiang, and F. Forghieri, "A Detailed Analytical Derivation of the GN Model of Non-Linear Interference in Coherent Optical Transmission Systems," arXiv:1209.0394 (2012).
  49. H. L. Fragnito, J. D. Marconi, and J. M. C. Boggio, "Experimental and Numerical Investigation of the SBS-Threshold Increase in an Optical Fiber by Applying Strain Distributions," J. Light. Technol. **23**, 3808 (2005).
  50. Y. Imai and N. Shimada, "Dependence of stimulated Brillouin scattering on temperature distribution in polarization-maintaining fibers," IEEE Photonics Technol. Lett. **5**, 1335–1337 (1993).
  51. K. Shiraki, M. Ohashi, and M. Tateda, "Performance of strain-free stimulated Brillouin scattering suppression fiber," J. Light. Technol. **14**, 549–554 (1996).
  52. K. Shiraki, M. Ohashi, and M. Tateda, "Suppression of stimulated Brillouin scattering in a fibre by changing the core radius," Electron. Lett. **31**, 668 (1995).
  53. J. B. Coles, B. P.-P. Kuo, N. Alic, S. Moro, C.-S. Bres, J. M. Chavez Boggio, P. a Andrekson, M. Karlsson, and S. Radic, "Bandwidth-efficient phase modulation techniques for stimulated Brillouin scattering suppression in fiber optic parametric amplifiers.," Opt. Express **18**, 18138–18150 (2010).
  54. G. Kalogerakis, M. E. Marhic, K. K.-Y. Wong, and L. G. Kazovsky, "Transmission of optical communication signals by distributed parametric amplification," J. Light. Technol. **23**, 2945–2953 (2005).
  55. T. J. Ellingham, L. M. Gleeson, and N. J. Doran, "Enhanced Raman Amplifier Performance Using Non-Linear Pump Broadening," in *2002 28TH European Conference on Optical Communication* (2002), Vol. 2, pp. 1–2.
  56. T. Tanaka, K. Torii, M. Yuki, H. Nakamoto, T. Naito, and I. Yokota, "200-nm Bandwidth WDM Transmission around 1.55  $\mu\text{m}$  using Distributed Raman Amplifier," in *2002 28TH European Conference on Optical Communication* (2002), Vol. 5, p. 1–2 (PD4.6).
  57. J. Yoshida, N. Tsukiji, T. Kimura, M. Funabashi, and T. Fukushima, "Novel concepts in 14XX-nm pump lasers for Raman amplifiers," in *ITCom 2002: The Convergence of Information Technologies and Communications, 2002, Boston, MA, United States* (International Society for Optics and Photonics, 2002), p. 169.
  58. R. H. Stolen, "Phase-matched three-wave mixing in silica fiber optical waveguides,"

- Appl. Phys. Lett. **24**, 308 (1974).
59. T. J. Ellingham, J. D. Ania-Castanon, R. Ibbotson, X. Chen, L. Zhang, and S. K. Turitsyn, "Quasi-lossless optical links for broad-band transmission and data processing," *IEEE Photonics Technol. Lett.* **18**, 268–270 (2006).
  60. J. C. Bouteiller, K. Brar, J. Bromage, S. Radic, and C. Headley, "Dual-order Raman pump," *IEEE Photonics Technol. Lett.* **15**, 212–214 (2003).
  61. R.-J. Essiambre, G. Kramer, P. J. Winzer, G. J. Foschini, and B. Goebel, "Capacity Limits of Optical Fiber Networks," *J. Light. Technol.* **28**, 662–701 (2010).
  62. J. Proakis and M. Salehi, *Digital Communications* (McGraw-Hill Education, 2007), Vol. 6.
  63. S. Benedetto and G. Bosco, "Channel Coding for Optical Communications," in *Optical Communication Theory and Techniques* (Kluwer Academic Publishers, 2005), pp. 63–78.
  64. I. P. Kaminow, T. Li, and A. E. Willner, *Optical Fiber Telecommunications V. Volume B, Systems and Networks* (Academic Press, 2008).
  65. K. Kikuchi, "Coherent Optical Communications: Historical Perspectives and Future Directions," in *High Spectral Density Optical Communication Technologies* (Springer Berlin Heidelberg, 2010), pp. 11–49.
  66. C. Laperle and M. OSullivan, "Advances in High-Speed DACs, ADCs, and DSP for Optical Coherent Transceivers," *J. Light. Technol.* **32**, 629–643 (2014).
  67. J. Leibrich and W. Rosenkranz, "Frequency Domain Equalization with Minimum Complexity in Coherent Optical Transmission Systems," in *Optical Fiber Communication Conference* (OSA, 2010), p. OWV1.
  68. F. Gardner, "A BPSK/QPSK Timing-Error Detector for Sampled Receivers," *IEEE Trans. Commun.* **34**, 423–429 (1986).
  69. ITU-T, *Forward Error Correction for High Bit-Rate DWDM Submarine Systems, Recommendation (G.975.1)* (n.d.).
  70. R. A. Shafik, M. S. Rahman, and A. R. Islam, "On the Extended Relationships Among EVM, BER and SNR as Performance Metrics," in *2006 International Conference on Electrical and Computer Engineering* (IEEE, 2006), pp. 408–411.
  71. R. Schmogrow, B. Nebendahl, M. Winter, A. Josten, D. Hillerkuss, S. Koenig, J. Meyer, M. Dreschmann, M. Huebner, C. Koos, J. Becker, W. Freude, and J. Leuthold, "Error Vector Magnitude as a Performance Measure for Advanced Modulation Formats," *IEEE Photonics Technol. Lett.* **24**, 61–63 (2012).
  72. A. Splett, C. Kurtzke, and K. Petermann, "Ultimate Transmission Capacity of Amplified Optical Fiber Communication Systems taking into Account Fiber Nonlinearities," in *19th European Conference on Optical Communication (ECOC)* (EPF, 1993), pp. 41–44.
  73. P. P. Mitra and J. B. Stark, "Nonlinear limits to the information capacity of optical fibre communications," *Nature* **411**, 1027–1030 (2001).
  74. J. Tang, "The Shannon channel capacity of dispersion-free nonlinear optical fiber



- transmission," *J. Light. Technol.* **19**, 1104–1109 (2001).
75. V. Curri, A. Carena, P. Poggiolini, G. Bosco, and F. Forghieri, "Evaluation of Non-Linear Interference in Uncompensated Links using Raman Amplification," *Eur. Conf. Exhib. Opt. Commun. We.2.C.5* (2012).
  76. D. Lavery, D. Ives, G. Liga, A. Alvarado, S. J. Savory, and P. Bayvel, "The Benefit of Split Nonlinearity Compensation for Single-Channel Optical Fiber Communications," *IEEE Photonics Technol. Lett.* **28**, 1803–1806 (2016).
  77. R. Dar and P. J. Winzer, "On the Limits of Digital Back-Propagation in Fully Loaded WDM Systems," *IEEE Photonics Technol. Lett.* **28**, 1253–1256 (2016).
  78. R. Maher, D. Lavery, D. Millar, A. Alvarado, K. Parsons, R. Killey, and P. Bayvel, "Reach Enhancement of 100% for a DP-64QAM Super-Channel using MC-DBP," in *Optical Fiber Communication Conference (OSA, 2015)*, p. Th4D.5.
  79. I. Sackey, F. Da Ros, M. Jazayerifar, T. Richter, C. Meuer, M. Nölle, L. Molle, C. Peucheret, K. Petermann, and C. Schubert, "Kerr nonlinearity mitigation in  $5 \times 28$ -GBd PDM 16-QAM signal transmission over a dispersion-uncompensated link with backward-pumped distributed Raman amplification," *Opt. Express* **22**, 27381 (2014).
  80. K. Solis-Trapala, T. Inoue, and S. Namiki, "Nearly-Ideal Optical Phase Conjugation based Nonlinear Compensation System," in *Optical Fiber Communication Conference (Osa, 2014)*, p. W3F.8.
  81. Y. Tian, Y. Huang, S. Zhang, P. R. Prucnal, and T. Wang, "112-Gb / s DP-QPSK Transmission over 7 , 860-km DMF using Phase-Conjugated Copy and Digital Phase-Sensitive Boosting with Enhanced Noise and Nonlinearity Tolerance," in *2013 Optical Fiber Communication Conference and Exposition and the National Fiber Optic Engineers Conference (OFC/NFOEC)* (2013), pp. 2–4.
  82. H. Eliasson, P. Johannisson, M. Karlsson, and P. a Andrekson, "Mitigation of nonlinearities using conjugate data repetition," *Opt. Express* **23**, 2392–2402 (2015).
  83. J. Shao, S. Kumar, and X. Liang, "Digital Back Propagation With Optimal Step Size for Polarization Multiplexed Transmission," *IEEE Photonics Technol. Lett.* **25**, 2327–2330 (2013).
  84. N. K. Dutta and Q. Wang, *Semiconductor Optical Amplifiers* (WORLD SCIENTIFIC, 2013).
  85. P. Minzioni, "Nonlinearity Compensation in a Fiber-Optic Link by Optical Phase Conjugation," *Fiber Integr. Opt.* **28**, 179–209 (2009).
  86. D. Caccioli, A. Paoletti, A. Schiffrini, A. Galtarossa, P. Griggio, G. Lorenzetto, P. Minzioni, S. Cascelli, M. Guglielmucci, L. Lattanzi, F. Matera, G. M. TosiBeleffi, V. Quiring, W. Sohler, H. Suche, S. Vehovc, and M. Vidmar, "Field Demonstration of In-Line All-Optical Wavelength Conversion in a WDM Dispersion Managed 40-Gbit/s Link," *IEEE J. Sel. Top. Quantum Electron.* **10**, 356–362 (2004).
  87. I. Sackey, F. Da Ros, T. Richter, R. Elschner, C. Meuer, C. Peucheret, K. Petermann, I. Sackey, F. Da Ros, T. Richter, and R. Elschner, "Design and performance evaluation of an OPC device using a dual-pump polarization-independent FOPA," in *2014 The European Conference on Optical Communication (ECOC)* (2014), p. 1–5 (Tu.1.4.4).

88. H. Hu, R. M. Jopson, a. H. Gnauck, M. Dinu, S. Chandrasekhar, C. Xie, and S. Randel, "Parametric Amplification, Wavelength Conversion and Phase Conjugation of a 2.048-Tbit/s WDM PDM 16-QAM Signal," *J. Light. Technol.* **8724**, 1286–1291 (2014).
89. A. D. Ellis and W. A. Stallard, "Four wave mixing in ultra long transmission systems incorporating linear amplifiers," in *IEE Colloquium on Non-Linear Effects in Fibre Communications* (1990), p. 6/1-6/4.
90. D. G. Schadt, "Effect of amplifier spacing on four-wave mixing in multichannel coherent communications," *Electron. Lett.* **27**, 1805 (1991).
91. K. Inoue, "Phase-mismatching characteristic of four-wave mixing in fiber lines with multistage optical amplifiers.," *Opt. Lett.* **17**, 801–803 (1992).
92. D. A. Cleland, A. D. Ellis, and C. H. F. Sturrock, "Precise modelling of four wave mixing products over 400 km of step-index fibre," *Electron. Lett.* **28**, 1171 (1992).
93. C. Kurtzke, "Suppression of fiber nonlinearities by appropriate dispersion management," *IEEE Photonics Technol. Lett.* **5**, 1250–1253 (1993).
94. M. E. Marhic, N. Kagi, T.-K. Chiang, and L. G. Kazovsky, "Optimizing the location of dispersion compensators in periodically amplified fiber links in the presence of third-order nonlinear effects," *IEEE Photonics Technol. Lett.* **8**, 145–147 (1996).
95. K. Nakajima, M. Ohashi, K. Shiraki, T. Horiguchi, K. Kurokawa, and Y. Miyajima, "Four-wave mixing suppression effect of dispersion distributed fibers," *J. Light. Technol.* **17**, 1814–1822 (1999).
96. W. Zeiler, F. Di Pasquale, P. Bayvel, and J. E. Midwinter, "Modeling of four-wave mixing and gain peaking in amplified WDM optical communication systems and networks," *J. Light. Technol.* **14**, 1933–1942 (1996).
97. K. Inoue and H. Toba, "Fiber four-wave mixing in multi-amplifier systems with nonuniform chromatic dispersion," *J. Light. Technol.* **13**, 88–93 (1995).
98. S. Radic, G. Pendock, a. Srivastava, P. Wysocki, and a. Chraplyvy, "Four-wave mixing in optical links using quasi-distributed optical amplifiers," *J. Light. Technol.* **19**, 636–645 (2001).
99. S. Watanabe and M. Shirasaki, "Exact compensation for both chromatic dispersion and Kerr effect in a transmission fiber using optical phase conjugation," *J. Light. Technol.* **14**, 243–248 (1996).
100. V. Pechenkin and I. J. Fair, "On Four-Wave Mixing Suppression in Dispersion-Managed Fiber-Optic OFDM Systems With an Optical Phase Conjugation Module," *J. Light. Technol.* **29**, 1678–1691 (2011).
101. S. Watanabe, M. Shirasaki, and T. Chikama, "Compensation for waveform distortion in a transmission fiber with loss by optical phase conjugation," *Electron. Commun. Japan, Part II Electron. (English Transl. Denshi Tsushin Gakkai Ronbunshi)* **79**, 773–779 (1996).
102. "[https://www.sterlitetech.com/new\\_pdf/pdf/op-product/OH-LITE\(E\)-Single-Mode-Optical-Fiber.pdf](https://www.sterlitetech.com/new_pdf/pdf/op-product/OH-LITE(E)-Single-Mode-Optical-Fiber.pdf)," .

103. R. Hainberger, T. Hoshida, T. Terahara, and H. Onaka, "Comparison of span configurations of Raman-amplified dispersion-managed fibers," *IEEE Photonics Technol. Lett.* **14**, 471–473 (2002).
104. B. Zhu, L. Leng, A. H. Gnauck, M. O. Pedersen, D. Peckham, L. E. Nelson, S. Stulz, S. Kado, L. Gruner-Nielsen, R. L. Lingle, S. Knudsen, J. Leuthold, C. Doerr, S. Chandrasekhar, G. Baynham, P. Gaarde, Y. Emori, and S. Namiki, "Transmission of 3.2 Tb/s (80x42.7 Gb/s) over 5200 km of UltraWave tm; fiber with 100-km dispersion-managed spans using RZ-DPSK format," in *2002 28TH European Conference on Optical Communication* (2002), Vol. 5, p. 1–2 (PD4.4).
105. M. Tan, P. Rosa, I. Phillips, and P. Harper, "Extended Reach of 116 Gb/s DP-QPSK Transmission using Random DFB Fiber Laser Based Raman Amplification and Bidirectional Second-order Pumping," in *Optical Fiber Communication Conference* (OSA, 2015), p. W4E.1.
106. M. Tan, P. Rosa, S. T. Le, I. D. Phillips, and P. Harper, "Evaluation of 100G DP-QPSK long-haul transmission performance using second order co-pumped Raman laser based amplification," *Opt. Express* **23**, 22181–22189 (2015).
107. P. Kaewplung and K. Kikuchi, "Simultaneous cancellation of fiber loss, dispersion, and Kerr effect in ultralong-haul optical fiber transmission by midway optical phase conjugation incorporated with distributed raman amplification," *J. Light. Technol.* **25**, 3035–3050 (2007).
108. D. Rafique and A. D. Ellis, "Nonlinearity compensation in multi-rate 28 Gbaud WDM systems employing optical and digital techniques under diverse link configurations.," *Opt. Express* **19**, 16919–16926 (2011).
109. L. Li, Y. Qiao, and Y. Ji, "Optimized optical phase conjugation configuration for fiber nonlinearity compensation in CO-OFDM systems," *Chinese Opt. Lett.* **9**, 60604 (2011).
110. M. H. Shoreh, "Compensation of Nonlinearity Impairments in Coherent Optical OFDM Systems Using Multiple Optical Phase Conjugate Modules," *J. Opt. Commun. Netw.* **6**, 549 (2014).
111. P. Minzioni and A. Schiffrini, "Unifying theory of compensation techniques for intrachannel nonlinear effects," *Opt. Express* **13**, 8460 (2005).
112. S. L. Jansen, D. Van Den Borne, B. Spinnler, S. Calabrò, H. Suche, P. M. Kummerich, W. Sohler, G. D. Khoe, and H. De Waardt, "Optical phase conjugation for ultra long-haul a phase-shift-keyed transmission," **24**, 54–63 (2006).
113. J. D. Ania-Castanon, "Quasi-lossless transmission using second-order Raman amplification and fibre Bragg gratings," *Opt. Express* **12**, 4372 (2004).
114. S. B. Papernyi, V. I. Karpov, and W. R. L. Clements, "Third-order cascaded Raman amplification," in *Optical Fiber Communication Conference and Exhibit* (Opt Soc. America, n.d.), p. FB4-1-FB4-3.
115. J.-C. Antona, "Key technologies for Present and Future Optical Networks," in *Presented at Topical Workshop on Electronics for Particle Physics Plenary Session 5* (2000).
116. G. Gao, X. Chen, and W. Shieh, "Influence of PMD on fiber nonlinearity

- compensation using digital back propagation.," *Opt. Express* **20**, 14406–18 (2012).
117. D. Rafique and A. D. Ellis, "Impact of signal-ASE four-wave mixing on the effectiveness of digital back-propagation in 112 Gb/s PM-QPSK systems.," *Opt. Express* **19**, 3449–54 (2011).
  118. J. Tang, "The channel capacity of a multispan DWDM system employing dispersive nonlinear optical fibers and an ideal coherent optical receiver," *J. Light. Technol.* **20**, 1095–1101 (2002).
  119. H. Louchet, A. Hodzic, and K. Petermann, "Analytical model for the performance evaluation of DWDM transmission systems," *IEEE Photonics Technol. Lett.* **15**, 1219–1221 (2003).
  120. G. Bosco, A. Carena, V. Curri, P. Poggiolini, and F. Forghieri, "Performance limits of nyquist-WDM and CO-OFDM in high-speed PM-QPSK systems," *IEEE Photonics Technol. Lett.* **22**, 1129–1131 (2010).
  121. C. J. McKinstrie, S. Radic, and C. Xie, "Reduction of soliton phase jitter by in-line phase conjugation.," *Opt. Lett.* **28**, 1519–1521 (2003).
  122. G. Bosco, V. Curri, a. Carena, P. Poggiolini, and F. Forghieri, "On the performance of nyquist-WDM terabit superchannels based on PM-BPSK, PM-QPSK, PM-8QAM or PM-16QAM subcarriers," *J. Light. Technol.* **29**, 53–61 (2011).
  123. G. Bosco, P. Poggiolini, a. Carena, V. Curri, and F. Forghieri, "Analytical results on channel capacity in uncompensated optical links with coherent detection: erratum," *Opt. Express* **20**, 19610 (2012).
  124. P. Poggiolini, "The GN Model of Non-Linear Propagation in Uncompensated Coherent Optical Systems," *J. Light. Technol.* **30**, 3857–3879 (2012).
  125. "<http://mathworld.wolfram.com/Polylogarithm.html>," .
  126. J. P. Gordon and L. F. Mollenauer, "Phase noise in photonic communications systems using linear amplifiers.," *Opt. Lett.* **15**, 1351–1353 (1990).
  127. A. D. Ellis and N. J. Doran, "Optical Link Design for Minimum Power Consumption and Maximum Capacity," in *39th European Conference and Exhibition on Optical Communication (ECOC 2013)* (Institution of Engineering and Technology, 2013), pp. 1068–1070.
  128. S. Watanabe, S. Takeda, and T. Chikama, "Interband wavelength conversion of 320 Gb/s (32×10 Gb/s) WDM signal using a polarization-insensitive fiber four-wave mixer," in *24th European Conference on Optical Communication* (Telefonica, n.d.), Vol. 3, pp. 83–87.
  129. V. Gordienko, M. F. C. Stephens, A. E. El-Taher, and N. J. Doran, "Novel broadband gain-spectrum measurement technique for Raman and parametric amplifiers," in *2017 Optical Fiber Communications Conference and Exhibition (OFC)* (2017), p. 1–3 (W2A.11).
  130. M. Lillieholm, P. Guan, M. Galili, M. S. Møller-Kristensen, L. Grüner-Nielsen, and L. K. Oxenløwe, "Optimization and characterization of highly nonlinear fiber for broadband optical time lens applications," *Opt. Express* **25**, 12566 (2017).

131. V. Ataie, E. Myslivets, B. P. P. Kuo, N. Alic, and S. Radic, "Spectrally equalized frequency comb generation in multistage parametric mixer with nonlinear pulse shaping," *J. Light. Technol.* **32**, 840–846 (2014).
132. M. Pelusi, K. Solis-Trapala, H. N. Tan, T. Inoue, and S. Namiki, "Multi-tone counter dithering of terabit/s polarization multiplexed signals for enhanced FWM with a single pump," in *2015 European Conference on Optical Communication (ECOC)* (IEEE, 2015), p. 1–3 (ID: 0369).
133. H. Nguyen Tan, T. Inoue, K. Tanizawa, S. Petit, Y. Oikawa, S. Takasaka, T. Yagi, and S. Namiki, "Counter-Dithering Pump Scheme for Cascaded Degenerate FWM Based Wavelength Converter," in *Optical Fiber Communication Conference* (Osa, 2014), p. W3F.4.
134. T. Torounidis, P. A. Andrekson, and B.-E. Olsson, "Fiber-optical parametric amplifier with 70-dB gain," *IEEE Photonics Technol. Lett.* **18**, 1194–1196 (2006).
135. S. Yoshima, Y. Sun, K. R. H. Bottrill, F. Parmigiani, P. Petropoulos, and D. J. Richardson, "Nonlinearity mitigation through optical phase conjugation in a deployed fibre link with full bandwidth utilization," in *2015 European Conference on Optical Communication (ECOC)* (IEEE, 2015), p. 1–3 (ID: 0682).
136. M. Morshed, L. B. Du, and A. J. Lowery, "Mid-Span Spectral Inversion for Coherent Optical OFDM Systems: Fundamental Limits to Performance," *J. Light. Technol.* **31**, 58–66 (2013).
137. M. Morshed, L. B. Du, A. J. Lowery, and A. S. Description, "Performance Limitation of Coherent Optical OFDM Systems with non-ideal Optical Phase Conjugation," in *IEEE Photonics Conference 2012, Burlingame, CA* (2012), pp. 394–395.
138. D. Hillerkuss, R. Schmogrow, T. Schellinger, M. Jordan, M. Winter, G. Huber, T. Vallaitis, R. Bonk, P. Kleinow, F. Frey, M. Roeger, S. Koenig, A. Ludwig, A. Marculescu, J. Li, M. Hoh, M. Dreschmann, J. Meyer, S. Ben Ezra, N. Narkiss, B. Nebendahl, F. Parmigiani, P. Petropoulos, B. Resan, A. Oehler, K. Weingarten, T. Ellermeyer, J. Lutz, M. Moeller, M. Huebner, J. Becker, C. Koos, W. Freude, and J. Leuthold, "26 Tbit s<sup>-1</sup> line-rate super-channel transmission utilizing all-optical fast Fourier transform processing," *Nat. Photonics* **5**, 364–371 (2011).
139. N. K. Fontaine, X. Liu, S. Chandrasekhar, R. Ryf, S. Randel, P. Winzer, R. Delbue, P. Pupalais, and A. Sureka, "Fiber Nonlinearity Compensation by Digital Backpropagation of an Entire 1.2-Tb/s Superchannel Using a Full-Field Spectrally-Sliced Receiver," *39th Eur. Conf. Exhib. Opt. Commun. (ECOC 2013)* 48–50 (2013).
140. S. Ozharar, F. Quinlan, I. Ozdur, S. Gee, and P. J. Delfyett, "Ultraflat Optical Comb Generation by Phase-Only Modulation of Continuous-Wave Light," *IEEE Photonics Technol. Lett.* **20**, 36–38 (2008).
141. J. Zhang, N. Chi, J. Yu, J. Zhu, Y. Shao, B. Huang, and L. Tao, "Generation of 113 coherent and frequency-lock multi-carriers using cascaded phase modulators and EDFA loop for Tb/s optical communication," in *2011 37th European Conference and Exhibition on Optical Communication* (2011), p. 1–3 (We.10.P1.07).
142. B. P. P. Kuo, E. Myslivets, V. Ataie, E. G. Temprana, N. Alic, and S. Radic, "Wideband parametric frequency comb as coherent optical carrier," *J. Light. Technol.* **31**, 3414–3419 (2013).

143. G. A. Sefler and K.-I. Kitayama, "Frequency comb generation by four-wave mixing and the role of fiber dispersion," *J. Light. Technol.* **16**, 1596–1605 (1998).
144. A. M. Clarke, D. G. Williams, M. A. F. Roelens, and B. J. Eggleton, "Reconfigurable Optical Pulse Generator Employing a Fourier-Domain Programmable Optical Processor," *J. Light. Technol.* **28**, 97–103 (2010).
145. X. Yang, D. J. Richardson, and P. Petropoulos, "Nonlinear Generation of Ultra-Flat Broadened Spectrum Based on Adaptive Pulse Shaping," *J. Light. Technol.* **30**, 1971–1977 (2012).